PROCEEDINGS
INTERNATIONAL SCHOOL OF PHYSICS «ENRICO FERMI»
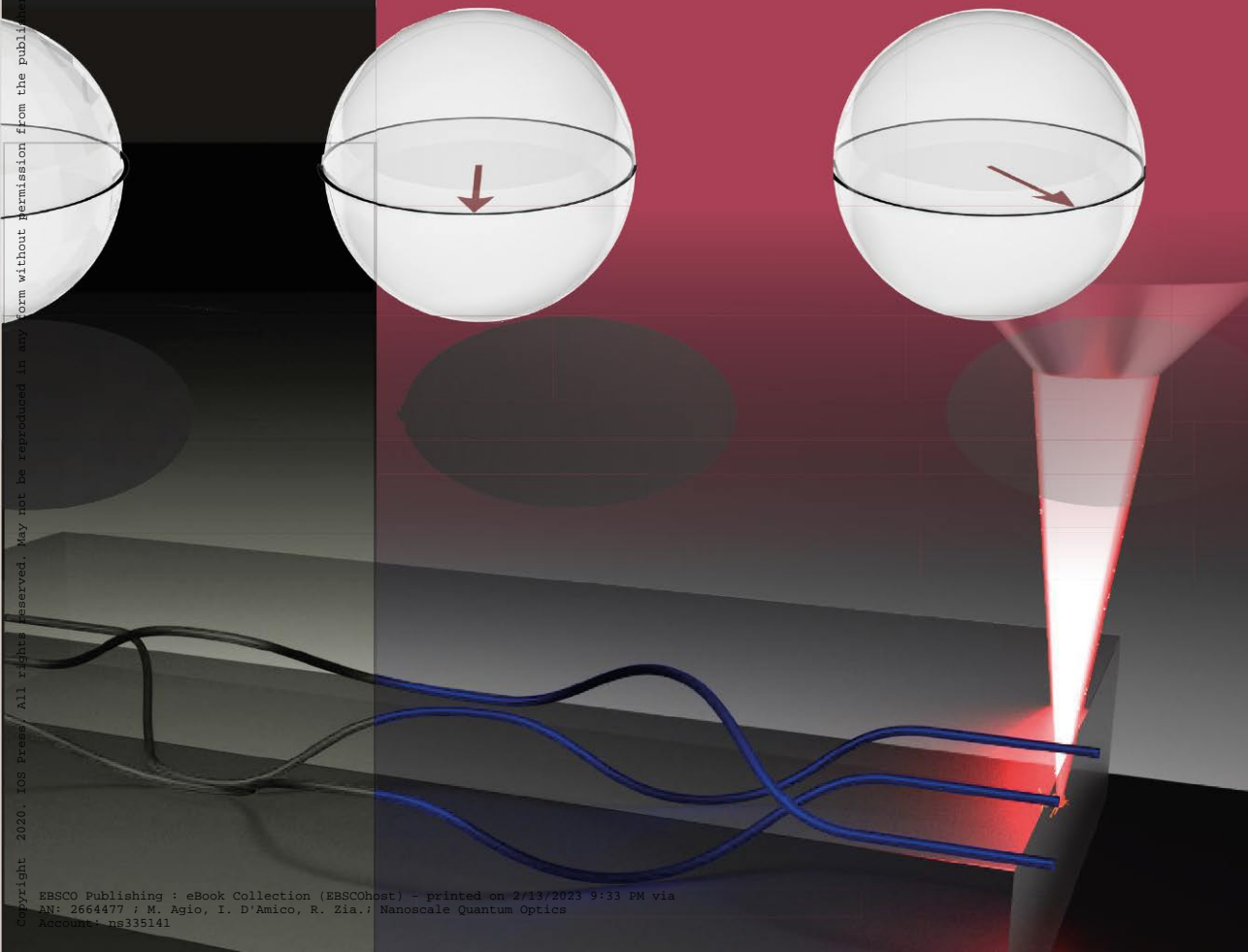
COURSE 204

Nanoscale Quantum Optics

edited by M. Agio, I. D'Amico, R. Zia and C. Toninelli

23 - 28 July 2018

Villa Monastero
Varenna, Lake Como

SOCIETÀ ITALIANA DI FISICA

———————

RENDICONTI

DELLA

SCUOLA INTERNAZIONALE DI FISICA

"ENRICO FERMI"

CCIV Corso

a cura di M. Agio, I. D'Amico e R. Zia
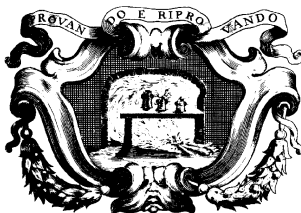
Direttori del Corso

e di

C. Toninelli

VARENNA SUL LAGO DI COMO

VILLA MONASTERO

23 – 28 Luglio 2018

Ottica quantistica a livello nanoscopico

2020

PROCEEDINGS

OF THE

INTERNATIONAL SCHOOL OF PHYSICS

"ENRICO FERMI"

COURSE 204

edited by M. AGIO, I. D'AMICO and R. ZIA

Directors of the Course

and

C. TONINELLI

VARENNA ON LAKE COMO

VILLA MONASTERO

23 – 28 July 2018

Nanoscale Quantum Optics

2020

Produced by the SIF Editorial Staff

Production Editor: Marcella Missiroli

Cover: see E. Polino, N. Spagnolo, F. Sciarrino, G. Corrielli, A. Crespi and R. Osellame, *Platforms for telecom entangled photon sources*, p. 85, and Friedemann Reinhard, *Nanoscale sensing and quantum coherence*, p. 145.

Graphic elaboration by Simona Oleandri

CONTENTS

The electronic version of volumes from 124 is available online at the IOS Press web site

`http://ebooks.iospress.nl/bookseries/proceedings-of-the-international`
`-school-of-physics-enrico-fermi`

Figures with colour source files will appear in colour in the online version.

SIF Members are granted free access to these volumes at
`https://members.sif.it`

For a complete list of published courses see
`https://en.sif.it/books/series/proceedings_fermi`

Preface

More than 60 people from all over the world, including students, researchers and lecturers, gathered in Varenna for the 204 Course of the International School of Physics "E. Fermi" dedicated to *Nanoscale Quantum Optics*. The course was organized in collaboration with the COST Action MP1403 "Nanoscale Quantum Optics", a network that involved 28 European countries and more than 500 researchers.

Recent developments aiming at the realization of new technologies based on quantum physics have been recognized by the European Commission as priorities, with the launch of the Quantum Technology Flagship Programme. These are, for example, new cryptographic techniques for security in telecommunications, new computing hardware that can solve problems so far inaccessible even to the latest generation of supercomputers, and new precision standards and sensors capable of measuring for instance extremely weak magnetic fields, with applications ranging from materials science to medical diagnostics. Nanoscale quantum optics combines these themes with nanophotonics, which addresses the control of light and its coupling with matter on a nanometer scale, a miniaturization comparable to the transition from valve-based electronics to integrated circuits. Structured materials provide confinement much beyond the wavelength scale, the interaction of light with nanoscale object offers novel means for interfacing light with different degrees of freedom, and quantum optics experiments are being upgraded in miniaturized nanophotonic platforms.

Based on such advances, the Course was therefore an opportunity to train new generations of scientists, who will have the privilege of doing research on topics that promise great innovations in science and technology.

This proceedings book contains the following lecture and seminars held during the school:

– "Basic concepts for quantum optics and quantum technologies", by I. D'Amico, introduces the background concepts.

– "Materials for quantum nanophotonics", by N. P. de Leon, outlines the requirements for a range of quantum nanophotonics applications, and describes the key material characteristics that affect physical properties related to these requirements.

– "Quantum optics and nonclassical light generation", by J. Vuckovic *et al.*, discusses the theoretical underpinnings of the seminal experiments in solid-state quantum optics.

– "Creating quantum correlations between quantum-dot spins", by M. Atatüre, describes how to generate nonlocal quantum correlations between electron spins in semiconductor quantum dots.

– "Platforms for telecom entangled photon sources", by F. Sciarrino *et al.*, reviews different platforms used to generate telecom-entangled photon pairs, focusing in particular on an integrated source realized by the femtosecond laser writing technique.

– "Quantum optics with single spins", by L. C. Bassett, describes the quantum-mechanical coupling between atom-like spin states and light, using the diamond nitrogen-vacancy (NV) center as a paradigm. Moreover, it explains various methods that serve as the basis for advanced protocols at the heart of many emerging quantum technologies.

– "Nanoscale sensing and quantum coherence", by F. Reinhard, summarizes concepts and techniques about single-qubit sensors, including an outlook to the major trends of the field.

– " Many-body physics and quantum simulations with strongly interacting photons", by D. G. Angelakis and Jirawat Tangpanitanon, focuses on interacting photons in superconducting circuits for quantum simulation of both in and out-of-equilibrium quantum many-body systems.

– "Nano-optomechanics", by E. Verhagen, introduces the basic physical description of optomechanical interactions at a tutorial level, and highlight several directions of current research.

In addition, among all poster contributions the following were selected for this book:

– "Photostable molecules on chip: a scalable approach to photonic quantum technologies", by M. Colaiutti *et al.*, presents the design and characterization of the evanescent coupling between dibenzoterrylene molecules and a ridge waveguide made of silicon nitride.

– "Environment spectroscopy with an NV center in diamond", by S. Hernández-Gómez *et al.*, describes in detail a method to spectroscopically characterize the spin bath around an NV center and identify the coherent coupling with the nearest nuclear spins.

– "Ultrafast photonic quantum correlations mediated by individual phonons", by S. Tarragó Vélez and C. Galland, outlines a new technique to prepare and measure the lifetime of the first phonon Fock state in diamond using single photon time-correlated Raman spectroscopy.

In this collection of chapters we hope the readers will find a valuable overview of the state-of-the-art and current trends in nanoscale quantum optics.

Mario Agio, Irene D'Amico, Costanza Toninelli and Rashid Zia

Italian Physical Society
INTERNATIONAL SCHOOL OF PHYSICS «E. FERMI»
COURSE 204
23 - 28 July 2018
VILLA MONASTERO – VARENNA, LAKE COMO

1) Giulia Mordini
2) Ramona Brigatti
3) Barbara Alzani
4) Niccolò Michieli
5) Reinier Van der Meer
6) Mauro Valeri
7) Andrea Geraldi
8) Ewold Verhagen
9) Niek van Hulst
10) Irene D'Amico
11) Mario Agio
12) Costanza Toninelli
13) Jelena Vuckovic
14) Rashid Zia
15) Maja Colautti
16) Yaseera Ismail
17) Isabella De Bellis
18) Monika Mycroft
19) Mackrine Nahra
20) Morgane Gandil
21) Maki Maeda
22) Priscila Romagnoli
23) Yunyun Dai
24) Sijia Gao
25) Haritha Kambalathmana
26) Caue Carvalho
27) Henk Snÿders
28) Santiago Tarrago Velez
29) Jodok Happacher
30) Sebastian Andersen
31) Mattia Mantovani
32) Zhe Xian (Zak) Koong
33) Marco Clementi
34) Friederike Klauck
35) Dario Cilluffo
36) Mariana Barros
37) Tetyana Shalomayeva
38) Richard Nelz
39) Marija Curcic
40) Andrea Cordaro
41) Francesca Urban
42) Carlotta Ciancico
43) Gabriele Frigenti
44) Martino De Carlo
45) Amy Skelt
46) Sahar Hejazi
47) Irina Komen
48) Simone Varo
49) Antonio Alessio Leonardi
50) Yadong Wang
51) Akshay Balgarkashi
52) Jan Olthaus
53) Daniel White
54) Subhojit Dutta
55) Sabyasachi Barik
56) Federico Andrea
Sabattoli
57) Gerard Queralto
58) Alessia Castellini
59) Huang Ding
60) Parvez Islam
61) Santiago Hernandez Gomez
62) Jake Southall
63) Alvaro Nodar Villa
64) Saverio Francesconi
65) Mikko Turunen
66) Lorenz Weiss
67) Thÿs Van Gogh

This page intentionally left blank

Basic concepts for quantum optics and quantum technologies

Irene D'Amico

Department of Physics, University of York - York, YO10 5DD, UK

International Institute of Physics, Federal University of Rio Grande do Norte - Natal, Brazil

Summary. — This introductory paper aims to provide a brief review of some basic concepts in quantum optics and quantum information, such as quantization of the electro-magnetic field, Fock and coherent states, quadrature operators, qubits and quantum gates, entanglement, Bell states and Bell inequality, mixed states and the density operator.

1. – Introduction

The field of nanoscale quantum optics (NQO) is rooted into quite different research areas: quantum optics, photonics, fundamentals of quantum mechanics, quantum information technologies, as well as low-dimensional condensed matter physics. Central to NQO are interacting many-body quantum system [1] strongly coupled to electromagnetic fields. These are some of the most difficult systems to be analysed experimentally and to be accurately treated via theoretical means, due to particle-particle interactions, to the necessity of treating light-matter interactions beyond linear response, to requirements for maintaining light, light-matter, and matter quantum conherence, etc. In the last couple of decades, these systems have also emerged as good prospective hardware for protocols

and devices relevant to quantum technologies [2]. Often NQO-related processes involve out-of-equilibrium dynamics far from the steady-state, and desired results may be hampered by interactions with the environment and other sources of noise and decoherence such as fields or temperature fluctuations. All of this makes NQO a complex field, which is growing under the hunger for technological achievements, and the stimuli of basic research quests and experimental challenges.

Further contributions in these proceedings will detail the progress in various NQO research topics; to support their understanding, this paper aims to briefly introduce some basic concepts relevant to quantum optics and to technologies derived from quantum information. In the first half of the paper we will review concepts important for quantum optics, such as the quantization of the electromagnetic field and Fock states (sect. **2**), coherent states (sect. **3**), quadrature operators and squeezed states (sect. **4**). These sections mainly follow related treatment by some well-known textbooks, as indicated. From sect. **5**, we will review some concepts relevant to quantum technologies: qubits and quantum gates (sect. **5**), quantum entanglement and Bell inequality (sect. **6**), "spin chains" as quantum buses (sect. **7**), and finally in sect. **8** the concepts of pure and mixed states and of the density operator.

2. – Quantization of the electromagnetic field and Fock states [3]

The cornerstone of quantum optics is the move from a classical description of electromagnetic fields to a full acknowledgement of the quantized nature of light and to the understanding of its consequences, especially in relation to the interaction between light and matter. The starting point is the quantization of the electromagnetic fields.

2‍.1. *Classical field, plane wave*. – We start by reviewing expressions for a classical electromagnetic field and consider a plane wave propagating in free space along the vector $\mathbf{k}$ with frequency ω_k. In CGS units, the corresponding electric and magnetic fields are, respectively,

$$(1) \qquad \mathbf{E}(\mathbf{r}, t) = \vec{\epsilon} E_0 \exp[i(\mathbf{k} \cdot \mathbf{r} - \omega_k t)] + \text{c.c.},$$

$$(2) \qquad \mathbf{B}(\mathbf{r}, t) = \frac{\mathbf{k} \times \vec{\epsilon}}{k} E_0 \exp[i(\mathbf{k} \cdot \mathbf{r} - \omega_k t)] + \text{c.c.},$$

where $k = \omega_k/c$ (with c the velocity of light), and $\vec{\epsilon} \perp \mathbf{k}$ is the polarization vector, and c.c. stays for "complex conjugate". We note that, when considering all possible modes, for each $\hat{k}$ there could be two orthogonal polarizations, $\vec{\epsilon}_{\mathbf{k},s}$, with $s = 1, 2$.

Given a volume V, the associated electromagnetic energy is

$$(3) \qquad U = \frac{1}{8\pi} \int_V [E^2(\mathbf{r}, t) + B^2(\mathbf{r}, t)] \mathrm{d}\mathbf{r},$$

leading, for a plane wave and up to fast oscillating terms, to

$$(4) \qquad U = \frac{1}{2\pi} |E_0|^2.$$

In the Coulomb gauge, the corresponding vector potential is given by

$$(5) \qquad \mathbf{A}(\mathbf{r},t) = \vec{\epsilon} A_0 \exp[i(\mathbf{k} \cdot \mathbf{r} - \omega_k t)] + \text{c.c.},$$

while E_0 becomes

$$(6) \qquad E_0 = i \frac{\omega_k}{c} A_0.$$

2˙2. *Generic classical field*. – We consider a travelling field within a cubic box of volume $V = L^3$. By expanding the field into plane waves and imposing periodic boundary conditions, the allowed $\mathbf{k}$-vectors are

$$(7) \qquad \mathbf{k} = 2\pi \frac{\mathbf{n}}{L},$$

with $\mathbf{n} = (n_x, n_y, n_z)$ and $n_i = 0, \pm 1, \pm 2 \ldots$, $i = x, y, z$. The vector potential is then

$$(8) \qquad \mathbf{A}(\mathbf{r},t) = \sum_{\text{allowed } \mathbf{k}; s=1,2} \frac{A_{\mathbf{k}s}}{\sqrt{V}} \vec{\epsilon}_{\mathbf{k}s} \exp[i(\mathbf{k} \cdot \mathbf{r} - \omega_k t)] + \text{c.c.},$$

with $A_{\mathbf{k}s}$ determining the specific field. Plane waves are orthogonal, so that the associated electromagnetic energy (3) becomes a summation of terms similar to (4) over the complete set of allowed $\{\mathbf{k}\}$. Then, using eq. (6), we obtain

$$(9) \qquad U = \frac{1}{2\pi} \sum_{\text{allowed } \mathbf{k}; s=1,2} \left(\frac{\omega_k}{c} \right)^2 |A_{\mathbf{k}s}|^2.$$

This equation expresses the energy of the electromagnetic field within the volume V as a sum of modes.

2˙3. *Quantization of the electromagnetic field*. – We associate each mode in the field to a quantum of energy $\hbar \omega_k$, with $\{n_{\mathbf{k}s}\}$ the number of quanta in the field. The total energy in the field can then be written as

$$(10) \qquad U = \sum_{\text{allowed } \mathbf{k}; s=1,2} \hbar \omega_k n_{\mathbf{k}s}.$$

A direct comparison between eqs. (9) and (10) then gives

$$(11) \qquad n_{\mathbf{k}s} = \frac{\omega_k}{2\pi \hbar c^2} |A_{\mathbf{k}s}|^2.$$

Next we associate U with the Hamiltonian operator $\hat{H}$, and the fields $\mathbf{A}$, $\mathbf{E}$, $\mathbf{B}$ to operators; $n_{\mathbf{k}s}$ becomes the number operator $\hat{n}_{\mathbf{k}s} = \hat{a}^\dagger_{\mathbf{k}s} \hat{a}_{\mathbf{k}s}$, with $\hat{a}^\dagger_{\mathbf{k}s}$, $\hat{a}_{\mathbf{k}s}$ creation and

annihilation operators for the mode $\mathbf{k}s$. Finally the average occupation number is now given by the Bose statistics

$$(12) \qquad \langle \hat{n}_{\mathbf{k}s} \rangle = \frac{1}{\exp \frac{\hbar \omega_k}{k_B} - 1} \, .$$

With these assumptions, and using eq. (11) we derive the relation

$$(13) \qquad \hat{A}_{\mathbf{k}s} = \sqrt{\frac{2\pi \hbar c^2}{\omega_k}} \hat{a}_{\mathbf{k}s},$$

from which we obtain the expressions for quantized fields

$$(14) \qquad \mathbf{A}(\mathbf{r}, t) = \sum_{\text{allowed } \mathbf{k}; s=1,2} \sqrt{\frac{2\pi \hbar c^2}{V \omega_k}} \vec{\epsilon}_{\mathbf{k}s} \hat{a}_{\mathbf{k}s} \exp[i(\mathbf{k} \cdot \mathbf{r} - \omega_k t)] + \text{h.c.}$$

$$(15) \qquad \mathbf{E}(\mathbf{r}, t) = i \sum_{\text{allowed } \mathbf{k}; s=1,2} \sqrt{\frac{2\pi \hbar \omega_k}{V}} \vec{\epsilon}_{\mathbf{k}s} \hat{a}_{\mathbf{k}s} \exp[i(\mathbf{k} \cdot \mathbf{r} - \omega_k t)] + \text{h.c.}$$

$$(16) \qquad \mathbf{B}(\mathbf{r}, t) = i \sum_{\text{allowed } \mathbf{k}; s=1,2} \sqrt{\frac{2\pi \hbar \omega_k}{V}} \frac{\mathbf{k} \times \vec{\epsilon}_{\mathbf{k}s}}{k} \hat{a}_{\mathbf{k}s} \exp[i(\mathbf{k} \cdot \mathbf{r} - \omega_k t)] + \text{h.c.},$$

where h.c. stands for "hermitian conjugate". Equations (14), (15), and (16) describe measurable operators. We note that, due to the choice of CGS units, electric and magnetic fields have the same prefactor.

As photons are bosons, creation and annihilation operators obey the bosonic commutation relations

$$(17) \qquad [\hat{a}_{\mathbf{k}s}, \hat{a}_{\mathbf{k}'s'}^{\dagger}] = \delta_{\mathbf{k}\mathbf{k}'} \delta_{s,s'},$$

$$(18) \qquad [\hat{a}_{\mathbf{k}s}, \hat{a}_{\mathbf{k}'s'}] = 0.$$

To obtain the correct form for the Hamiltonian, we need to substitute the quantized form of the fields (14), (15), and (16) into eq. (3) and use the bosonic commutation relations. The result is

$$(19) \qquad \hat{H} = \sum_{\text{allowed } \mathbf{k}; s=1,2} \frac{1}{2} \hbar \omega_k \left(\hat{a}_{\mathbf{k}s}^{\dagger} \hat{a}_{\mathbf{k}s} + \hat{a}_{\mathbf{k}s} \hat{a}_{\mathbf{k}s}^{\dagger} \right)$$

$$(20) \qquad = \sum_{\text{allowed } \mathbf{k}; s=1,2} \hbar \omega_k \left(\hat{n}_{\mathbf{k}s} + \frac{1}{2} \right).$$

Equation (20) shows that, even in the absence of quanta in the field, the corresponding energy is non-zero, and given by $\sum_{\text{allowed } \mathbf{k}; s=1,2} \frac{1}{2} \hbar \omega_k$, the zero-point energy. We note

that, by applying the quantization procedure directly to the classical results (9) —which assumes all fields components to commutes— there would have been no zero-point energy.

2'4. *Fock states and their properties.* – The eigenstates $|n_{\mathbf{k}s}\rangle$ of the number operator $\hat{n}_{\mathbf{k}s}$ are known as Fock states. For a single mode $\mathbf{k}s$ we can then write

$$(21) \qquad \hat{n}_{\mathbf{k}s}|n_{\mathbf{k}s}\rangle = n_{\mathbf{k}s}|n_{\mathbf{k}s}\rangle,$$

where $n_{\mathbf{k}s} = 0, 1, 2, \ldots \infty$. State $|0_{\mathbf{k}s}\rangle$ is the vacuum state and contains no quanta of the electromagnetic field. State $|n_{\mathbf{k}s}\rangle$ can be generated by the vacuum state as

$$(22) \qquad |n_{\mathbf{k}s}\rangle = \frac{1}{\sqrt{n_{\mathbf{k}s}!}}(\hat{a}_{\mathbf{k}s}^{\dagger})^{n_{\mathbf{k}s}}|0_{\mathbf{k}s}\rangle.$$

Fock states form a complete set of orthogonal states, and it can be shown that

$$(23) \qquad \hat{a}_{\mathbf{k}s}|n_{\mathbf{k}s}\rangle = \sqrt{n_{\mathbf{k}s}}|n_{\mathbf{k}s} - 1\rangle,$$

$$(24) \qquad \hat{a}_{\mathbf{k}s}^{\dagger}|n_{\mathbf{k}s}\rangle = \sqrt{n_{\mathbf{k}s} + 1}|n_{\mathbf{k}s} + 1\rangle.$$

When considering multimode fields, the related Fock states will be given by the product state of the single mode ones

$$(25) \qquad |\{n_{\mathbf{k}s}\}\rangle = \Pi_{\mathbf{k};s}|n_{\mathbf{k}s}\rangle.$$

The application of a specific mode annihilation or creation operator will then result in

$$(26) \qquad \hat{a}_{\mathbf{k}s}|\{n_{\mathbf{k}s}\}\rangle = \sqrt{n_{\mathbf{k}s}}|n_{\mathbf{k}s} - 1\rangle\Pi_{\mathbf{k}';s' \neq \mathbf{k};s}|n_{\mathbf{k}'s'}\rangle,$$

$$(27) \qquad \hat{a}_{\mathbf{k}s}^{\dagger}|\{n_{\mathbf{k}s}\}\rangle = \sqrt{n_{\mathbf{k}s} + 1}|n_{\mathbf{k}s} + 1\rangle\Pi_{\mathbf{k}';s' \neq \mathbf{k};s}|n_{\mathbf{k}'s'}\rangle.$$

3. – Coherent states

3'1. *Coherence in classical light* [4]. – For classical fields, coherence describes the "stability" of light. For example interference phenomena can be observed as long as the frequency of light is stable and its spread is small enough. We can classify coherence into temporal (or longitudinal) coherence and spatial (or transverse) coherence. A coherence time τ_c is associated to the temporal coherence, with $\tau_c \approx 1/\Delta\omega$, with $\Delta\omega$ the light spectral width. A coherence length can then be defined as $L_c = c\tau_c$. The coherence time (length) corresponds to the time (path) during which the wave train has a stable phase.

3'2. *Quadrature operators and Fock states in the quadrature space* [3]. – For a field represented by a plane wave, E_0 is a complex number, and, importantly, both its amplitude and phase can be measured experimentally.

As previously seen, in quantum optics E_0 corresponds to the annihilation operator $\hat{a}_{\mathbf{k}s}$, which is not Hermitian; it is then custom to consider instead the two Hermitian quadrature operators([1])

$$(28) \qquad \hat{X} = \frac{\hat{a}_{\mathbf{k}s} + \hat{a}_{\mathbf{k}s}^{\dagger}}{\sqrt{2}},$$

$$(29) \qquad \hat{Y} = \frac{\hat{a}_{\mathbf{k}s} - \hat{a}_{\mathbf{k}s}^{\dagger}}{i\sqrt{2}},$$

which inherit from (17) and (18) the commutation relation

$$(30) \qquad [\hat{X}, \hat{Y}] = i.$$

The above relation tells us that $\hat{X}$ and $\hat{Y}$ are related by canonical commutation relations, so that $\hat{Y}$ can be formally written as the momentum associated to $\hat{X}$ in the quadrature space, $\hat{Y} = -i\partial/\partial\hat{X}$. Because of (30), Heisenberg uncertainty relation will apply, so that

$$(31) \qquad \Delta\hat{X}\Delta\hat{Y} \geq \frac{1}{2},$$

where $(\Delta\hat{X})^2 = \langle\hat{X}^2\rangle - \langle\hat{X}\rangle^2$ and similarly for $\hat{Y}$.

Formally the commutation relations (17), (18), and (30) are the same that we encounter when we move from the first to the second quantization of a particle trapped by a one-dimensional harmonic potential. It is not surprising then, that when we wish to express Fock states in quadrature space we formally obtain the eigenstates of the one dimensional harmonic oscillator

$$(32) \qquad \psi_{n_{\mathbf{k}s}}(X) = \langle X|n_{\mathbf{k}s}\rangle$$

$$(33) \qquad = (2^{n_{\mathbf{k}s}} n_{\mathbf{k}s}! \sqrt{\pi})^{-\frac{1}{2}} H_{n_{\mathbf{k}s}}(X) \exp\left(-\frac{X^2}{2}\right).$$

The uncertainty relation (31) then becomes

$$(34) \qquad \Delta\hat{X}\Delta\hat{Y} = n_{\mathbf{k}s} + \frac{1}{2},$$

with $(\Delta\hat{X})^2 = (\Delta\hat{Y})^2 = n_{\mathbf{k}s} + \frac{1}{2}$, which shows that the vacuum state corresponds to the minimum uncertainty relation.

We note that the mean value of the quadrature operators calculated for Fock states is always zero, due to the orthogonality of Fock states. However from the existence of,

---

([1]) We note that the coefficients entering the definition of $\hat{X}$ and $\hat{Y}$ may vary slightly depending on the chosen text.

for example, single-mode lasers, we expect quantum mechanics to allow for well-defined amplitude and phase for the electromagnetic field: there must exist a set of "special" quantum states which satisfy this requirement. Indeed these states are called "coherent states" [5].

3˙3. *Coherent states and their properties* [3]. – Coherent states are defined by the requirement that $E_0 = \langle \hat{a}_{\mathbf{k}s} \rangle$ be finite. They are the eigenvectors of $\hat{a}_{\mathbf{k}s}$, satisfying the relation

$$(35) \qquad \hat{a}_{\mathbf{k}s}|\alpha_{\mathbf{k}s}\rangle = \alpha_{\mathbf{k}s}|\alpha_{\mathbf{k}s}\rangle,$$

where $\alpha_{\mathbf{k}s}$ is a complex number. The intensity of a coherent field, an observable, will then be proportional to $|E_0|^2$, that is to the mean value of the number operator over the relevant coherent state

$$(36) \qquad |E_0|^2 = \langle \alpha_{\mathbf{k}s}|\hat{a}_{\mathbf{k}s}^{\dagger}\hat{a}_{\mathbf{k}s}|\alpha_{\mathbf{k}s}\rangle$$

$$(37) \qquad \qquad = |\alpha_{\mathbf{k}s}|^2.$$

The corresponding mean value of the quadrature operators becomes

$$(38) \qquad \langle \alpha_{\mathbf{k}s}|\hat{X}|\alpha_{\mathbf{k}s}\rangle = \sqrt{2}\Re\alpha_{\mathbf{k}s},$$

$$(39) \qquad \langle \alpha_{\mathbf{k}s}|\hat{Y}|\alpha_{\mathbf{k}s}\rangle = \sqrt{2}\Im\alpha_{\mathbf{k}s}.$$

It can be shown (see, *e.g.*, [3]) that coherent states can be written in terms of Fock states as

$$(40) \qquad |\alpha_{\mathbf{k}s}\rangle = \exp\left(-\frac{1}{2}|\alpha_{\mathbf{k}s}|^2\right) \sum_{n_{\mathbf{k}s}=0}^{\infty} \frac{\alpha_{\mathbf{k}s}^{n_{\mathbf{k}s}}}{\sqrt{n_{\mathbf{k}s}!}}|n_{\mathbf{k}s}\rangle.$$

Equation (40) implies that if the field is in a coherent state, the probability of measuring a Fock state state is given by the Poisson distribution

$$(41) \qquad p_{n_{\mathbf{k}s}} = |\langle n_{\mathbf{k}s}|\alpha_{\mathbf{k}s}\rangle|^2 = \exp(-|\alpha_{\mathbf{k}s}|^2)\frac{(|\alpha_{\mathbf{k}s}|^2)^{n_{\mathbf{k}s}}}{n_{\mathbf{k}s}!},$$

with variance and mean given by $|\alpha_{\mathbf{k}s}|^2$.

Coherent states form a complete set, but they are *not* orthonormal. In fact

$$(42) \qquad \langle \alpha_{\mathbf{k}s}|\beta_{\mathbf{k}s}\rangle = \exp\left(\alpha_{\mathbf{k}s}^{*}\beta_{\mathbf{k}s} - \frac{1}{2}|\alpha_{\mathbf{k}s}|^2 - \frac{1}{2}|\beta_{\mathbf{k}s}|^2\right),$$

so that any coherent state can be expressed in terms of other coherent states. Importantly, coherent states have always minimum uncertainty relationship, independently from $\alpha_{\mathbf{k}s}$, *i.e.* $\Delta\hat{X}\Delta\hat{Y} = 1/2 = (\Delta\hat{X})^2 = (\Delta\hat{Y})^2$. Because of this, they are the best

quantum-mechanical analogue of the classical single-mode field: coherent states describe wave packets that, subject to free evolution of the field, change phase but do not change shape nor variance:

$$(43) \qquad |\alpha_{\mathbf{k}s}\rangle \xrightarrow{\hat{H}=\hbar\omega(\frac{1}{2}+\hat{a}^{\dagger}_{\mathbf{k}s}\hat{a}_{\mathbf{k}s})} \exp\left(-i\frac{\omega}{2}t\right)\left|\exp\left(-i\frac{\omega}{2}t\right)\alpha_{\mathbf{k}s}\right\rangle,$$

so that, under free dynamics, $\Delta\hat{X}(t)\Delta\hat{Y}(t) = 1/2 = (\Delta\hat{X})^2(t) = (\Delta\hat{Y})^2(t)$.

3'4. *Coherent states and the displacement operator* [6]. – By using eqs. (22) and (40), it can be shown that coherent states are displacements of the vacuum state

$$(44) \qquad |\alpha_{\mathbf{k}s}\rangle = \left[\exp\left(-\frac{1}{2}|\alpha_{\mathbf{k}s}|^2\right)\exp(\alpha_{\mathbf{k}s}\hat{a}^{\dagger})\exp(-\alpha^{*}_{\mathbf{k}s}\hat{a})\right]|0\rangle$$

$$(45) \qquad = D(\alpha_{\mathbf{k}s})|0\rangle,$$

where $D(\alpha_{\mathbf{k}s})$ is the displacement operator of amplitudes $\hat{a}$ and $\hat{a}^{\dagger}$, that is

$$(46) \qquad D^{-1}(\alpha_{\mathbf{k}s})\hat{a}D(\alpha_{\mathbf{k}s}) = \hat{a} + \alpha_{\mathbf{k}s},$$

$$(47) \qquad D^{-1}(\alpha_{\mathbf{k}s})\hat{a}^{\dagger}D(\alpha_{\mathbf{k}s}) = \hat{a}^{\dagger} + \alpha^{*}_{\mathbf{k}s}.$$

Importantly, $D(\alpha_{\mathbf{k}s})$ is unitary, with $D^{\dagger}(\alpha_{\mathbf{k}s}) = D(-\alpha_{\mathbf{k}s}) = [D(\alpha_{\mathbf{k}s})]^{-1}$. Using the Baker-Campbell-Hausdorff formula, one can show that

$$(48) \qquad D(\alpha_{\mathbf{k}s}) = \exp\left(-\frac{1}{2}|\alpha_{\mathbf{k}s}|^2\right)\exp(\alpha_{\mathbf{k}s}\hat{a}^{\dagger})\exp(-\alpha^{*}_{\mathbf{k}s}\hat{a})$$

$$(49) \qquad = \exp(\alpha_{\mathbf{k}s}\hat{a}^{\dagger} - \alpha^{*}_{\mathbf{k}s}\hat{a})$$

$$(50) \qquad = \exp\left(-\frac{1}{2}|\alpha_{\mathbf{k}s}|^2\right)\exp(-\alpha^{*}_{\mathbf{k}s}\hat{a})\exp(\alpha_{\mathbf{k}s}\hat{a}^{\dagger}).$$

4. – Quadrature operators in quantum optics [6]

Let us consider the homogeneous single-mode electric field

$$(51) \qquad \mathbf{E}(t) = i\sqrt{\frac{2\pi\hbar\omega_k}{V}}\vec{\epsilon}_{\mathbf{k}s}\left[\hat{a}_{\mathbf{k}s}\exp(-i\omega_k t) - \hat{a}^{\dagger}_{\mathbf{k}s}\exp(i\omega_k t)\right].$$

By substituting in it $\hat{a}_{\mathbf{k}s} = (\hat{X}+i\hat{Y})/\sqrt{2}$ and $\hat{a}^{\dagger}_{\mathbf{k}s} = (\hat{X}-i\hat{Y})/\sqrt{2}$, we obtain

$$(52) \qquad \mathbf{E}(t) = -2\sqrt{\frac{\pi\hbar\omega_k}{V}}\vec{\epsilon}_{\mathbf{k}s}\left[\hat{Y}\cos(\omega_k t) - \hat{X}\sin(\omega_k t)\right]$$

$$(53) \qquad \overset{\omega\to-\omega}{=} -2\sqrt{\frac{\pi\hbar\omega_k}{V}}\vec{\epsilon}_{\mathbf{k}s}\left[\hat{Y}\cos(\omega_k t) + \hat{X}\sin(\omega_k t)\right].$$
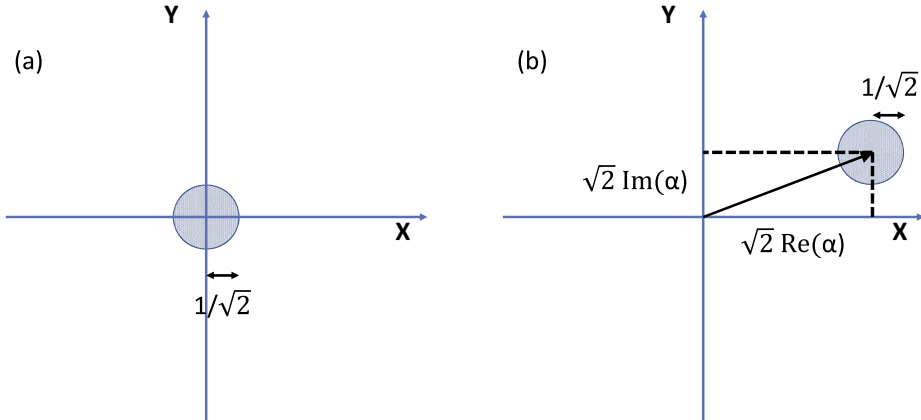
Fig. 1. – (a) Vacuum state $|0\rangle$ represented in quadrature space. (b) Coherent state $|\alpha\rangle$, with α complex, in quadrature space. Both states have minimum uncertainty $1/\sqrt{2}$.

Equation (53) clarifies that the operators $\hat{X}$ and $\hat{Y}$ correspond to the quadratures of the quantized electric field, with phase difference $\pi/2$. Measurement of these observables will then provide all necessary information on the characteristics of the quantized light. Similarly, plotting these quadratures will help better understanding (as well as visualizing) of the characteristics of different states of light, *e.g.* Fock's *versus* coherent states. We give some simple examples below.

4`1. *Examples of visualization of quantum states of light*. – To visualize a quantum state of light $|\psi\rangle$ using the quadrature operators, we plot its measurable properties $X = \langle\psi|\hat{X}|\psi\rangle$ and $Y = \langle\psi|\hat{Y}|\psi\rangle$, which give the position of the state *in the quadrature space*, as well as the corresponding standard deviations $\Delta\hat{X}$ and $\Delta\hat{Y}$ which give an indication of the state is spread.

In fig. 1a the vacuum quantum state $|0\rangle$ is visualized. For this state $\langle 0|\hat{X}|0\rangle = 0$ and $\langle 0|\hat{Y}|0\rangle = 0$, while $\Delta\hat{X} = 1/\sqrt{2} = \Delta\hat{Y}$, corresponding to minimum uncertainty.

In fig. 1b a coherent quantum state $|\alpha\rangle$ is visualized. From eqs. (38) and (39), it follows that $\langle\alpha|\hat{X}|\alpha\rangle = \sqrt{2}\Re\alpha$ and $\langle\alpha|\hat{Y}|\alpha\rangle = \sqrt{2}\Im\alpha$, while still $\Delta\hat{X} = 1/\sqrt{2} = \Delta\hat{Y}$.

Comparison between fig. 1a and fig. 1b graphically demonstrates that indeed coherent states are displacements of the vacuum state, in fact $D^{-1}(\alpha)\hat{X}D(\alpha) = \hat{X} + \sqrt{2}\Re\alpha$ and $D^{-1}(\alpha)\hat{Y}D(\alpha) = \hat{Y} + \sqrt{2}\Im\alpha$.

4`2. *Squeezed states* [6]. – Given two Hermitian operators $\hat{A}$ and $\hat{B}$ with commutation relation $[\hat{A}, \hat{B}] = i\hat{C}$, their expectation values will satisfy the uncertainty relationship $\Delta A\Delta B \geq |\langle\hat{C}\rangle|/2$. A quantum state is then a "squeezed" state if, for one of the observables (say $\hat{B}$), the relationship $(\Delta B)^2 < |\langle\hat{C}\rangle|/2$ is satisfied. In addition, if $\Delta A\Delta B = |\langle\hat{C}\rangle|/2$ is also satisfied, the state is an "ideal" squeezed state. The reduction of quantum fluctuations in the expectation value of one operator must be compensated by an increase in the other, so that the uncertainty relationship still holds.
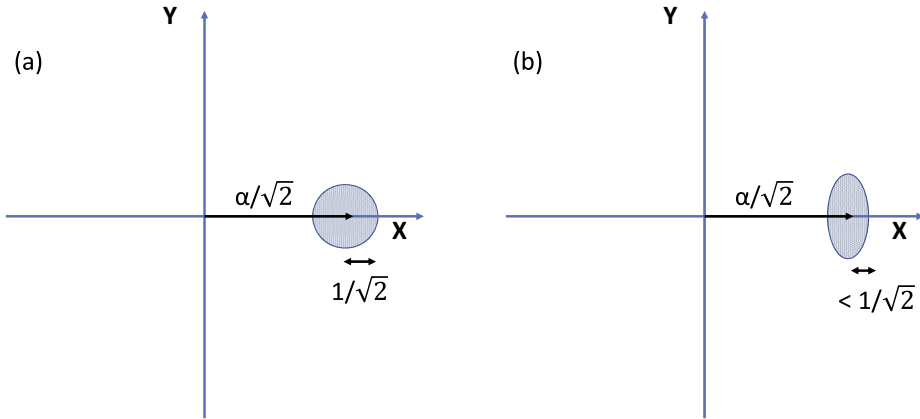
Fig. 2. – (a) Coherent state $|\alpha\rangle$, with $\alpha \in \Re$, represented in quadrature space. (b) The coherent state $|\alpha\rangle$ of panel (a) is squeezed along the X direction in quadrature space.

Coherent states may be squeezed by applying appropriate operators, see *e.g.* [6]. In fig. 2 a coherent state with $\alpha \in \Re$ (panel (a)) is squeezed along X (panel (b)). The use of squeezed states may improve measurements; this is the case, *e.g.* for interferometric measurements of gravitational waves.

5. – Elementary building blocks for quantum technologies: quantum bits and quantum gates

Focus on quantum information and related quantum technologies [2] has exponentially increased in the last 20 years, leading to side-by-side progress of related theory and experimental concepts and techniques, as well as to substantial investments by many Countries worldwide.

At the core of quantum information there is the concept of "quantum bit" or "qubit", the quantum equivalent of the familiar unit of classical information, the bit. A qubit is a quantum two-level system, with basis states $|0\rangle$ (or $|\uparrow\rangle$) and $|1\rangle$ (or $|\downarrow\rangle$). At difference with its classical counterpart, and according to the principles of quantum mechanics, a qubit can be in any linear superposition of its basis states, with its generic state being

$$(54) \qquad\qquad |\Psi\rangle = \alpha|0\rangle + \beta|1\rangle,$$

with $\alpha, \beta \in \mathbb{C}$ and $|\alpha|^2 + |\beta|^2 = 1$. Each qubit must be isolated enough to be well-defined as a two-level system; at the same time, it must be possible to change its state in a controllable way —*e.g.* via electromagnetic fields or direct coupling other qubits— to perform input/output operations and/or quantum logic gates. In matrix quantum mechanics, qubits are represented by two-entry column vectors. For example, in the

standard basis, state (54) becomes

$$(55) \qquad |\Psi\rangle = \begin{pmatrix} \alpha \\ \beta \end{pmatrix}.$$

Quantum gates acting on a single qubit are then 2×2 matrices and two-qubit gates 4×4 matrices. In principle universal computation can be realized by using one and two-qubit gates alone [7].

Similar to their classical counterpart, a sequence of quantum logic gates performs a computational algorithm; however the opposite may not be true as there exist quantum computation methods which are not based on quantum gates, notably "one-way quantum computing" [8]. The latter is based on an entangled network of qubits; these qubits are measured in such a way to produce the desired computation output, but without explicitly performing a series of gates. In this case quantum gates between qubits may be used to produce the initial computational resource, entanglement.

6. – Quantum entanglement

6˙1. *Entangled and unentangled states*. – Quantum entanglement is a purely quantum mechanical feature and accounts for part of a system quantum correlations [7]. Here we will examine the concept of bi-partite entanglement: we will consider a quantum system S formed by two subsystems, generally referred to as A and B, and define under which conditions A and B are —or not— entangled.

Let us start by considering a two-spin (two-qubit) system in the overall quantum state

$$(56) \qquad |\psi\rangle_{AB} = (\alpha|\uparrow\rangle + \beta|\downarrow\rangle)_A(\gamma|\uparrow\rangle + \delta|\downarrow\rangle)_B$$

$$(57) \qquad = |\Psi\rangle_A|\Psi\rangle_B.$$

As shown above, $|\psi\rangle_{AB}$ can be factorized in a state $|\Psi\rangle_A$ describing spin A by a state $|\Psi\rangle_B$ describing spin B, which means $|\psi\rangle_{AB}$ is a "product state". States like $|\Psi\rangle_{AB}$ are not entangled. From the information perspective this implies that if we measure the state of spin A no information is gained on spin B. In fact, whichever the result from measuring spin A, $|\Psi\rangle_B$ remains unaffected and so does the probability of obtaining any possible result from measuring B.

However if we consider the overall state given by

$$(58) \qquad |\psi\rangle'_{AB} = (\alpha|\uparrow\rangle_A + \beta|\downarrow\rangle_A)|\downarrow\rangle_B + \gamma|\downarrow\rangle_A|\uparrow\rangle_B,$$

we find that it is not possible to write it as a product state: $|\Psi\rangle'_{AB}$ is then an entangled state. If we now measure system A and obtain, let us say, $|\downarrow\rangle_A$, we see that this measurement affects the state of B, changing the probability of obtaining $|\uparrow\rangle_B$ (now $|\gamma|^2/(|\gamma|^2 + |\beta|^2)$) or $|\downarrow\rangle_B$ (now $|\beta|^2/(|\gamma|^2 + |\beta|^2)$) from a measurement of B. This shows that there is a correlation between the state of system A and the state of system B.
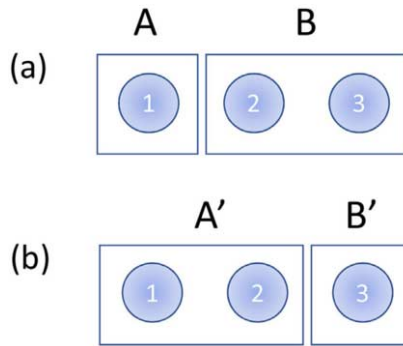
Fig. 3. – Two different partitions for the same ensemble of three particles.

The two-spin states

$$(59) \qquad |\Phi\rangle^+ = \frac{1}{\sqrt{2}}[|\uparrow\rangle_A|\uparrow\rangle_B + |\downarrow\rangle_A|\downarrow\rangle_B],$$

$$(60) \qquad |\Phi\rangle^- = \frac{1}{\sqrt{2}}[|\uparrow\rangle_A|\uparrow\rangle_B - |\downarrow\rangle_A|\downarrow\rangle_B],$$

$$(61) \qquad |\Psi\rangle^+ = \frac{1}{\sqrt{2}}[|\uparrow\rangle_A|\downarrow\rangle_B + |\downarrow\rangle_A|\uparrow\rangle_B],$$

$$(62) \qquad |\Psi\rangle^+ = \frac{1}{\sqrt{2}}[|\uparrow\rangle_A|\downarrow\rangle_B - |\downarrow\rangle_A|\uparrow\rangle_B].$$

are known as "Bell states" and are maximally entangled: this means that measuring one of the subsystems determines completely the state of the other. Bell's states represent an alternative basis for a two-qubit system, and are often used within quantum technology protocols. An instructive example is the one-qubit teleportation protocol [7].

Entanglement is naturally abundant in solid-state systems, while is it relatively difficult to entangle photons. In addition to quantum computation, it is a fundamental resource for certain quantum cryptography protocols, quantum sensing, quantum simulation, and quantum metrology.

6˙2. *Entanglement in systems with multiple degrees of freedom*. – Quantum systems are usually more complex than just two spins, for example they may include more than two particles. In this case the entanglement of the system will depend on the partition chosen. To understand this concept, let us consider three spin-$\frac{1}{2}$ particles in the state $|\Psi_{123}\rangle = |\Psi\rangle_1|\Phi\rangle_{23}^+$ and the partitions sketched in fig. 3. It is clear that, when considering partition (a), the subsystems are not entangled; however as particles two and three are maximally entangled, partition (b), which "separates" them, will result in non-zero entanglement.

Realistic systems are even more complex, and they usually include qualitatively different degrees of freedom. For example even a system of just two electrons would be characterized by their positions, momenta, and charges, in addition to their spins. When discussing entanglement, it is then very important to specify which degrees of freedom are considered, as, for the same overall system state, specific degrees of freedom may be entangled while others may not.

An example of this situation is the ground state of two non-interacting electrons, e_A and e_B, trapped by an harmonic potential. The overall wave function will be given by

$$(63) \qquad |\psi_{AB}\rangle = b e^{-a r_A^2} e^{-a r_B^2} |\Phi\rangle^-,$$

where a is proportional to the characteristic frequency of the harmonic oscillator and b is a normalization constant. Clearly if the spatial degrees of freedom r_A and r_B are considered, $|\psi_{AB}\rangle$ is not entangled. However if the spin degrees of freedom are considered, the two electrons are maximally entangled, as they are in the Bell state $|\Phi\rangle^-$.

A more complex example is given by comparing the behaviour of the average single-site entanglement *versus* the spatial entanglement for the one-dimensional Hubbard model [9, 10]. The single-site entanglement describes the entanglement of one site with the rest of the chain [11], while the spatial entanglement [12] refers to the entanglement between the spatial degrees of freedom of the particles. When considering the behaviour with respect to particle-particle interaction strength, the spatial entanglement is zero (minimum) for non-interacting particles, while the single-site entanglement is maximum. The two types of entanglement behave in a qualitative opposite way for most interaction strengths [9,10].

6˙3. *Entanglement and Bell's inequality.* – A main difference between quantum mechanics and our familiar "classical" world is that classically we assume that physical properties of objects are independent of measures, and that measures simply reveal the properties. For example if a car is blue, our intuition and experience tell us that it was blue even before we looked at it and, unless repainted, it will continue to remain blue.

On the contrary, the "collapse of the wave function" postulate of quantum mechanics implies that the act of measurement affects a system's properties. For example let us consider a particle not in the eigenstate of the relevant observable: measuring its position will localize it or measuring its energy give to this a specific value, while before the measurement it had a nonzero probability to be found elsewhere in space or to have a different energy. Quantum mechanics provides rules by which we can predict the probability of a certain measurement outcome but, with respect to measurement, it is not a deterministic theory.

In classical mechanics a probabilistic measurement outcome is associated to incomplete knowledge of the system at hand; a natural question is then if it is the same for quantum mechanics: are there "hidden variables" such that their knowledge could restore a deterministic theory of quantum measurement? Einstein, Podolsky and Rosen argued that this was the case [13]. However in 1964 John Stewart Bell came up with an outstanding proposal, and suggested an experiment for which quantum mechanics and

local-hidden-variable theories were giving different predictions [14]: incredible but true, the completeness of quantum mechanics could now be tested experimentally.

Bell proposed to measure specific observables and showed that a certain linear combination of the results had an upper bound when calculated using local hidden variable theory (Bell's inequality [7, 14]). Bell's inequality is derived under the "classical" assumptions of realism (physical properties have definite values which exist independently of observation) and locality (it is possible to set up laboratory conditions, *e.g.* distance between experimental set-ups, such that measurements done by experimenter A cannot influence measurements done by experimenter B). However, if the properties measured belong to entangled particles shared between experimenters A and B, this inequality is violated, and, as a consequence, either the hypothesis of realism or the one of locality, or both, are incorrect.

Hence, measuring if Bell's inequality is, or not, satisfied verifies if entanglement is an actual property of nature, at least up to the local-hidden-variable theory. Existence of entanglement means that measuring a subsystem A may indeed alter the state of a different subsystem B, even if A and B are not coupled to each other by the overall system Hamiltonian.

Bell's inequality has been tested multiple times [15-24], and especially in the last couple of decades [16-24]: in this period renewed interest in the fundamentals of quantum mechanics was sparkled by the surge of quantum information theory and, at the same time, technological advancements made it possible to design ever more sophisticated and accurate experiments.

So far experimental evidence supports the results from quantum mechanics and shows that entanglement is a quantum resource which goes beyond classical properties.

7. – "Spin chains" as eclectic quantum buses

Entanglement is a resource for many quantum technologies; however, to provide entanglement to the related protocols it may be necessary not only to generate it, but also to create specific entangled states, transport entanglement where needed, distribute it to different parties, detect it, and/or store it for later use.

Depending on the protocol, various methods and different hardware have been proposed to these aims. For example, when dealing with long distances, *e.g.* for quantum communication, entangled photons are usually the medium of choice: they can be generated, for example, using quantum dots, and then transported or distributed using optical fibers.

However within an electronic device there is often the necessity of transporting information resources between shorter distances, for example between different processors. Devices for quantum technologies are no exception and it is clear that it would be advantageous if these internal "quantum buses" could transfer faithfully not only simple qubits, but also entanglement. Even better if they could also manipulate entanglement in useful ways, actively contributing to the protocols themselves. This is the context in which it has emerged the concept of "spin chains" as quantum buses to transfer and manipulate

information and entanglement over mid-to-short distances (for early developments of the use of spin chains within quantum technologies see, *e.g.*, ref. [25]).

Spin chain here refers to a network of spins —not necessarily a linear chain— whose dynamics is governed by a lattice Hamiltonian such as the Heisenberg [26], Ising [27], Hubbard [28], Su-Schrieffer-Heeger [29], or the XY-Hamiltonian [25] models. In the context of quantum technologies, and at difference somewhat with previous studies, the use of these models focuses mainly on finite chains, non-equilibrium dynamics, entanglement-related properties, robustness against imperfections, and topological properties.

Originally developed to treat strongly correlated electronic systems, spin-chain Hamiltonians turned out to be very versatile, and can be applied to describe a variety of quantum systems, from chains of nanostructures [30-32], to arrays of cold atoms [33], trapped ions [34] strings of fullerenes [35], photonic systems [36,37], etc. Applications to specific physical systems may require inclusion of additional perturbative terms in the Hamiltonian, for example to describe system-specific decoherence mechanisms or typical fabrication defects (see *e.g.* ref. [38]).

Spin chains have been very fruitful for designing protocols to generate, transport, distribute, and store entanglement [39-46]. This includes knitting and distributing cluster states [47-50], which are relevant for one-way quantum computation. Importantly, spin chains can be engineered such that their evolution under their natural Hamiltonian may transport quantum information without spoiling it (perfect state transfer (PST) [32,51-53]), produce and/or distribute different types of entangled states between relatively far-apart parties [43-50]. With the addition of light-touch control protocols, spin chains whose natural dynamics produces entanglement can be made able to store it afterwards [43, 45]. Various of these protocols have been proven to be fast with respect to relevant decoherence mechanism and robust against fabrication defects (see *e.g.* [38, 43, 44]).

8. – The density operator

8$\cdot$1. *Why do we need a density operator?*. – So far we have described a quantum system using a coherent superposition of state vectors, *e.g.*

$$(64) \qquad |\psi\rangle_{AB} = \alpha_A|\Psi\rangle_A| + \alpha_B|\Psi\rangle_B.$$

However this state is an idealization when compared to the actual states prepared and analysed experimentally. In these, there will always be some statistical uncertainty due to imperfections (*e.g.*, in the procedure to prepare the quantum state), finite temperature effects, unwanted interactions of the quantum state with the environment, etc. We then need a description of a quantum state that, in addition to including quantum mechanical uncertainties, accounts for classical statistical uncertainty. This is provided by the density operator $\hat{\rho}$ [7].

Quantum mechanics can be formulated in terms of the density operator, and, in addition, the related formalism allows for an easier description of situations where classical

statistical uncertainty is present (*e.g.* experiments), and can be extended to describe open systems and decoherence processes, all of which is crucial when dealing with protocols and devices for quantum technologies.

8˙**2.** *Ensembles of quantum states: mixed and pure states.* – The density operator formalism is convenient to describe quantum systems whose state is not fully known. Suppose that, *e.g.* due to imperfections in fabrication methods, a quantum system is in the state $|\psi_i\rangle$ with probability p_i. Then the ensemble $\{p_i, |\psi_i\rangle\}$ is called an ensemble of pure states. The density operator for this quantum system is defined as

$$(65) \qquad \hat{\rho} = \sum_i p_i |\psi_i\rangle\langle\psi_i|,$$

with $\sum_i p_i = 1$, as for any classical probability. This is at difference with the quantum uncertainty expressed by the coefficients in eq. (64) where instead $\sum_i |\alpha_i|^2 = 1$. If at least two of the p_i coefficients in (65) are different from zero, we refer to $\hat{\rho}$ as to a "mixed state". If the state of the system is not affected by classical uncertainties, then we refer to it as a "pure state", and its density operator is given by

$$(66) \qquad \hat{\rho} = |\psi\rangle\langle\psi|.$$

8˙**3.** *Characterization of a density operator.* – A density operator is Hermitian, $\hat{\rho}^\dagger = \hat{\rho}$.

An Hermitian operator $\hat{\rho}$ is a density operator associated to some ensemble $\{p_i, |\psi_i\rangle\}$ if and only if it satisfies the conditions

- $\mathrm{Tr}\{\hat{\rho}\} = 1$ (trace condition);

- $\hat{\rho}$ is a positive operator, which means that, for any arbitrary state $|\phi\rangle$, it satisfies $\langle\phi|\hat{\rho}|\phi\rangle \geq 0$ (positivity condition);

- $\mathrm{Tr}\{\hat{\rho}^2\} \leq 1$, with $\mathrm{Tr}\{\hat{\rho}^2\} = 1$ if and only if $\hat{\rho}$ is a pure state.

8˙**4.** *Separable mixed states.* – Previously we have defined entanglement for a pure state: with respect to a specific partition, a state which cannot be factorized is entangled. Here we extend this definition to mixed states.

A mixed state $\hat{\rho}$, describing the bipartition A and B of the overall system, is separable (*i.e.* not entangled) if and only if it can be written as a linear combination of pure product states such as

$$(67) \qquad \hat{\rho}_{AB} = \sum_i p_i |A_i\rangle\langle A_i| \otimes |B_i\rangle\langle B_i|.$$

Here $|A_i\rangle$ and $|B_i\rangle$ are vector states describing subsystems A and B respectively, and $0 \leq p_i \leq 1$ with $\sum_i p_i = 1$. Vectors within $\{|A_i\rangle\}$ or $\{|B_i\rangle\}$ do not need to be orthogonal. As the definition of separable states implies, different pure-state ensembles may be represented by the same density operator.

REFERENCES

[1] Gerald D. Mahan, *Many-Particle Physics* (Springer, New York) 2000.

[2] Acin A. *et al.*, "The quantum technologies roadmap: a European community view," *New J. Phys.*, **20** (080201) 2018.

[3] Agarwal G. S., *Quantum Optics* (Cambridge University Press) 2013.

[4] Fox M., *Quantum Optics, Oxford Master Series in Atomic, Optical, and Laser Physics* (Oxford University Press) 2006.

[5] Glauber R. J., *Phys. Rev. Lett.*, **10** (1963) 84; *Phys. Rev.*, **131** (1963) 2766.

[6] Scully M. O. and Zubairy M. S., *Quantum Optics* (Cambridge University Press) 2008.

[7] See, for example, Nielsen M. A. and Chuang I.L., *Quantum Computation and Quantum Information* (Cambridge University Press) 2000.

[8] Dan E. Browne and Hans J. Briegel, "One-way Quantum Computation - a tutorial introduction", arXiv:quant-ph/0603226.

[9] Coe J. P., Franca V. V. and D'Amico I., *Phys. Rev. A*, **81** (2010) 052321.

[10] Coe J. P., Franca V. V. and D'Amico I., *Europhys. Lett.*, **93** (2011) 10001.

[11] Larsson D. and Johannesson H., *Phys. Rev. A*, **73** (2006) 042320.

[12] See, *e.g.*, Coe J. P., Sudbery A. and D'Amico I., *Phys. Rev. B*, **77** (2008) 205122.

[13] Einstein A., Podolsky B. and Rosen N., "Can Quantum-Mechanical Description of Physical Reality Be Considered Complete?" *Phys. Rev.*, **47** (1935) 777.

[14] Bell J. S., *Physics Physique Fizika*, **1** (1964) 195.

[15] See *e.g.*, Aspect A., *Nature*, **398** (1999) 189 and references therein.

[16] Rowe M. A. *et al.*, *Nature*, **409** (2001) 791.

[17] Salart D. *et al.*, *Phys. Rev. Lett.*, **100** (2008) 220404.

[18] Marissa G. *et al.*, *Nature*, **497** (2013) 227.

[19] Larsson J.-A. *et al.*, *Phys. Rev. A*, **90** (2014) 032107.

[20] Christensen B. G. *et al.*, *Phys. Rev. Lett.*, **111** (2013) 130406.

[21] Marissa G. *et al.*, *Phys. Rev. Lett.*, **115** (2015) 250401.

[22] Lynden K. Shalm *et al.*, *Phys Rev Lett.*, **115** (2015) 250402; Handsteiner J. *et al.*, *Phys. Rev. Lett.*, **118** (2017) 060401.

[23] Rosenfeld W. *et al.*, *Phys. Rev. Lett.*, **119** (2017) 010402.

[24] The BIG Bell Test Collaboration, *Nature*, **557** (2018) 212.

[25] Bose S., *Contemp. Phys.*, **48** (2007) 13.

[26] See *e.g.*, Nolting W. and Ramakanth A., *Heisenberg Model* in *Quantum Theory of Magnetism* (Springer, Berlin, Heidelberg) 2009.

[27] Ising E., "Beitrag zur Theorie des Ferromagnetismus," *Z. Phys.*, **31** (1925) 253.

[28] Gutzwiller M. C., *Phys. Rev. Lett.*, **10** (1963) 159; Kanamori J., *Prog. Theor. Phys.*, **30** (1963) 275; Hubbard J., *Proc. R. Soc. A*, **276** (1963) 237; Hubbard J., *Proc. R. Soc. A*, **281** (1964) 401.

[29] Su W. P., Schrieffer J. R. and Heeger A. J., "Solitons in polyacetylente," *Phys. Rev. Lett.*, **42** (1979) 1698.

[30] Irene D'Amico, *Microelectronics J.*, **37** (2006) 1440.

[31] Pierre Barthelemy and Lieven M. K. Vandersypen, *Ann. Phys.*, **525** (2013) 808.

[32] Nikolopoulos G. M., Petrosyan D. and Lambropoulos P., *J. Phys. Condens. Matter*, **16** (2004) 4991.

[33] See *e.g.*, Christian Gross and Immanuel Bloch, *Science*, **357** (2017) 995.

[34] Islam R. *et al.*, *Nat. Commun.*, **2** (2011) 377.

[35] Twamley J., *Phys. Rev. A*, **67** (2003) 052318.

[36] Gräfe M., Heilmann R., Perez-Leija A., Keil R., Dreisow F., Heinrich M., Moya-
      Cessa H., Nolte S., Christodoulides D. N. and Szameit A., *Nat. Photon.*, **8** (2014)
      791.
[37] Chapman R. J., Santandrea M., Huang Z., Corrielli G., Crespi A., Yung M.,
      Osellame R. and Peruzzo A., *Nat. Commun.*, **7** (2016) 11339.
[38] Ronke R., Spiller T. P. and D'Amico I., *Phys. Rev. A*, **83** (2011) 012325.
[39] Spiller T. P., D'Amico I. and Lovett B. W., *New J. Phys.*, **9** (2007) 20.
[40] Sahling S., Remenyi G., Paulsen C., Monceau P., Saligrama V., Marin C.,
      Revcolevschi A., Regnault L. P., Raymond S. and Lorenzo J. E., *Nat. Phys.*,
      11 (2015) 255.
[41] Banchi L., Bayat A., Verrucchi P. and Bose S., *Phys. Rev. Lett.*, **106** (2011) 140501.
[42] Apollaro T. J. G., Lorenzo S., Sindona A., Paganelli S., Giorgi G. L. and
      Plastina F., *Phys. Scr. T*, **165** (2015) 014036.
[43] Wilkinson K. N., Estarellas M. P., Spiller T. P. and D'Amico I., *Quantum Inf.
      Comput.*, **18** (2018) 247.
[44] Estarellas M. P., D'Amico I. and Spiller T. P., *Phys. Rev. A*, **95** (2017) 042335.
[45] Irene D'Amico, Brendon W. Lovett and Timothy P. Spiller, *Phys. Rev. A*, **76**
      (2007) 030302.
[46] Alastair Kay, *New J. Phys.*, **19** (2017) 043019.
[47] Clark S. R., Alves C. M. and Jaksch D., *New J. Phys.*, **7** (2005) 124.
[48] Clark S. R., Klein A., Bruderer M. and Jaksch D., *New J. Phys.*, **9** (2007) 202.
[49] Yung M.-H. and Bose S., *Phys. Rev. A*, **71** (2005) 032310.
[50] Ronke R., D'Amico I. and Spiller T. P., *Phys. Rev. A*, **84** (2011) 032308.
[51] Christandl M., Datta N., Ekert A. and Landahl A. J., *Phys. Rev. Lett.*, **92** (2004)
      187902.
[52] Christandl M., Datta N., Dorlas T. C., Ekert A., Kay A. and Landahl A. J.,
      Phys. Rev. A, **71** (2005) 032312.
[53] Plenio M. B., Hartley J. and Eisert J., *New J. Phys.*, **6** (2004) 36.

Materials for quantum nanophotonics

NATHALIE P. DE LEON(*)

Department of Electrical Engineering, Princeton University - Princeton, NJ, USA

Summary. — Engineering coherent systems is a central goal of quantum science, quantum optics, and quantum information processing. For quantum nanophotonics applications, it is particularly important to design and control systems that exhibit coherent optical transitions and long spin coherence times. This review outlines the requirements for a variety of quantum nanophotonics applications, and describes the key material properties that affect physical properties related to these requirements.

There has been an explosion of activity in the field of quantum nano-optics and quantum nanophotonics over the past two decades. Broadly, this area encompasses a large number of applications and research areas organized around controlling light-matter interactions at the single-photon or single-atom level in solid-state systems. Building on pioneering work in the cold atom community in the 80s and 90s using high-finesse cavities to control atom-photon interactions [1], significant progress has recently been made in engineering atom-like systems in the solid state that can interact strongly with light and store quantum information for long periods of time. Such systems generally comprise a defect or molecule that has well-defined, localized electronic states with narrow, selective optical transitions. These narrow optical transitions form a manifold that isolates a good two-level system for strong light-matter interactions, and in some cases they can

---

(*) E-mail: npdeleon@princeton.edu

be used to initialize or read out the ground electronic state. Although these features are natural elements of cold atoms, interactions with a solid-state environment can lead to decoherence of the optical transition, as well as the ground-state electronic spin. Engineering atom-like systems in the solid state by creating defects or structures that do not suffer from environment-induced decoherence is a central goal of the field.

1. – Desiderata for applications in quantum nano-optics

Here we will outline a few research areas in quantum nano-optics, and enumerate the key desiderata for each application. Many of the key desiderata are overlapping, and therefore lead to universal properties to engineer or search for in a quantum system.

1˙1. *Single-photon sources*. – The simplest quantum system is a two-level system with degrees of freedom that can be coherently manipulated. If these two levels are separated by an optical transition frequency, this system can couple strongly to light. Reciprocally, if a two-level system can strongly absorb a photon, in can also emit photons efficiently. There is a rich field of research and applications aimed at using such quantum systems to control and manipulate light. One such application is as single-photon sources for quantum communication and quantum computing. The main requirements for single-photon sources is that they are pure in that they should emit one photon at a time, and transform-limited in that they do not exhibit dephasing beyond the linewidth determined by the Fourier relationship between the wavepacket duration and the spread in frequency. It is also helpful for single-photon sources to be bright; most applications will have a key metric that scales with the rate of single photons. Finally, a typical requirement is that single photons be identical in polarization, frequency, and spatial mode. For quantum systems, the key desiderata therefore are that they exhibit a relatively short excited state lifetime to increase the rate of single-photon emission, are highly optically coherent, do not have parasitic emission that leads to background, and that they do not exhibit changes or drift in the optical transition frequency, known as spectral diffusion. It is also convenient if they exhibit a small static inhomogeneous distribution so that they can be scaled.

1˙2. *Using quantum systems to control light*. – Another field of research is building single-photon switches and transistors by achieving high cooperativity between a quantum system and a photon mode, for example using cavity QED. The atom-photon interaction can be parametrized by g, κ, and γ, where g is the single-photon Rabi frequency that scales inversely with the mode volume as $g \propto \frac{1}{\sqrt{V}}$, κ is the cavity decay rate that scales inversely with the quality factor of the cavity, and γ is the bare spontaneous emission rate of the atom. The enhancement of the atom-photon interaction is given by the cooperativity, $\frac{g^2}{\kappa\gamma}$. When g is the largest parameter, such systems will exhibit strong coupling, in which the photon coherently transfers between the atom and the cavity. In the absence of this condition, the cooperativity gives the Purcell enhancement factor of the spontaneous emission rate. In order to realize the full enhancement, the optical

transition dipole of the atom should be coherent, similar to the requirement of optical coherence for single-photon sources.

1˙3. *Quantum networks*. – There are several theoretical schemes to extend the range of quantum networks using quantum repeaters [2], in which single photons are entangled with quantum memories and then used to distribute entanglement among these quantum memories at remote nodes. This entanglement can then be used as a resource for teleportation [3]. For such applications, the key desiderata are a long-lived quantum memory in the form of a spin with long coherence time, an efficient spin-photon interface, high collection efficiency, and high optical coherence.

1˙4. *Enhanced collection efficiency from a quantum system*. – There is a broader class of applications in which the most important figure of merit is simply the photon collection efficiency. For example, for nanoscale quantum sensing with NV centers in diamond, the sensitivity scales with the number of photons collected per unit time, and nanophotonic devices can be used to enhance the total collection efficiency. Furthermore, small quantum computers with optical readout can generally benefit from higher collection efficiency, motivating integration into nanophotonic devices.

2. – Examples of physical systems

Solid-state quantum systems can be ordered in terms of their degree of spatial localization. Strain quantum dots are typically 10–100 nm, and their electronic wave functions are primarily determined by the band structure of the surrounding host. Shallow donors in semiconductors have wave functions with a spatial extent of a few nm, and they resemble hydrogenic orbitals that comprise the periodicity of the underlying lattice. Deep defects and impurities such as color centers in diamond have angstrom scale wave functions, and they resemble atomic or molecular orbitals.

Other systems that are used in quantum optics that are beyond the scope of this overview include cold neutral atoms, which have been used as model systems in cavity QED, trapped ions, which have been deployed in remote entanglement generation [4], superconducting qubits, which have been an especially fruitful playground for cavity QED and quantum optics in the microwave regime [5], and molecules such as terrylene [6], which have a strong optical dipole but generally do not have spin degrees of freedom.

2˙1. *Quantum dots*. – Quantum dots consist of islands of heteroepitaxially grown materials in a semiconductor, where the island geometry results from strain due to lattice mismatch. The most commonly studied system is InAs in GaAs. The smaller band gap of InAs allows for free carrier confinement within the InAs, and the small spatial extent of the InAs island leads to a large charging energy for electrons, which gives rise to a discrete density of states. These electronic states can be used as quantum memories, and the optical exciton can be used as an interface for photons. Because these systems have such a large optical dipole ($\tau \approx 100$ ps, quantum efficiency near unity), they are ideal systems for cavity QED experiments, and have been used as a model system

for a number of quantum optics demonstrations [7]. However, the rapidly fluctuating hyperfine field resulting from stiochiometric nuclear spins in GaAs limits quantum dot spin coherence to less than 100 ns, limiting the utility of quantum dots for quantum memories. Furthermore, despite significant efforts to improve growth homogeneity, the static inhomogeneous distribution of the optical transition frequency can be quite large, tens of nanometers, which hampers their application as single-photon sources.

2˙2. *Shallow donors*. – Shallow donors are impurities in semiconductors that are energetically close to the band edge, such as phosphorous in silicon. They would ionize to be dopants at room temperature, but at sufficiently low temperature the electron or hole remains bound to the impurity atom in hydrogenic orbitals. These systems exhibit excellent spin coherence, $T_1 \approx 100\,\text{s}$, $T_2 \approx 1\,\text{s}$ at $4\,\text{K}$ for isotopically purified silicon [8]. However, because they are so close to the band edge, optical transitions are highly ionizing. Most work on resonant excitation of shallow donors is performed on donor-bound excitons rather than the optical transitions of the shallow donor itself [9]. Some recent work has shown that chalocogen donors in silicon, which are energetically deeper, can exhibit spin-selective optical transitions in the mid infrared, but their quantum efficiency is unknown [10].

2˙3. *Defects and impurities*. – Atomic and atom-like defects in solid-state hosts are one of the leading experimental platforms for quantum information processing [11]. They offer the possibility of excellent quantum coherence, enabling long quantum bit storage times, and efficient and stable optical transitions that can be used to manipulate and sense the qubit states. Furthermore, some of these systems can function under ambient conditions and at room temperature, enabling their use as precise and versatile sensors. Several defects have been intensively studied for these qualities over the last decade, most notably the nitrogen vacancy (NV) center in diamond [12], which has a spin T_1 of around $10\,\text{ms}$ at room temperature, and hours at cryogenic temperatures in high-purity diamond. The NV center also has transform-limited optical transitions, but the zero phonon line only comprises a few percent of the total emission, limiting the total effective quantum efficiency. More recent work has expanded the list of known candidates for quantum applications to group-IV vacancies in diamond, such as the negative [13] and neutral [14] silicon vacancy, and divacancies in SiC [15]. The negatively charged SiV center exhibits more favorable optical properties than the NV center, but also has much shorter spin coherence at $4\,\text{K}$. The neutral SiV has longer spin coherence and excellent optical coherence with high apparent quantum efficiency, but spin-dependent fluorescence has not yet been observed.

The types of defects that can be deployed in quantum technologies can be broadly grouped into three categories: color centers (*e.g.* NV and SiV defects in diamond or vacancy complexes in SiC), transition metals (*e.g.* Ti, Cr, V, etc.) and rare-earth ions (*e.g.* Nd, Er, etc.). The latter two are interesting because they can be doped into a wide range of host crystals with significant (in the case of transition metals) or minor (in the case of rare earths) alteration of their properties. For rare earth ions in

particular, the submerged f shells are protected from the surrounding lattice, and $T_1 \approx$ milliseconds is achievable below $1\,\mathrm{K}$ [16]. However, the T_2 is typically much shorter, around microseconds because known host materials for efficient rare-earth ion incorporation contain stoichiometric nuclear spins. Although rare-earth ions have very high quantum efficiency, the optical transitions between f orbitals are forbidden because the orbitals have the same parity, so they are very weak; the optical-excited-state lifetime is typically milliseconds to hundreds of milliseconds. Recent work has achieved detection of single rare-earth ions, either by confocal microscopy [17] or Purcell enhancement of the emission rate using nanophotonics [18].

3. – Optical coherence and interactions with the environment

First, let us parametrize atom-photon interactions in general to identify the ideal case, following the treatment in [19]. Using the density operator and optical Bloch equations, the susceptibility χ of a medium of perfect two-level atoms, with ground state $|1\rangle$ and excited state $|2\rangle$, can be written as

$$(1) \qquad \chi = i\frac{N}{V}\frac{\mu^2}{\hbar\epsilon_0}(\rho_{11} - \rho_{22})\frac{1}{\gamma_{12} - i\delta}\,,$$

where $\frac{N}{V}$ is the density of the medium, μ is the optical transition dipole, $\gamma_{12} = \frac{\gamma_1 + \gamma_2}{2}$ is the average decay rate out of the two levels, δ is the detuning of the optical drive from the resonant transition, and $\rho_{nn'}$ are elements of the density matrix:

$$(2) \qquad \hat{\rho} = \rho_{11}|1\rangle\langle 1| + \rho_{12}|1\rangle\langle 2| + \rho_{21}|2\rangle\langle 1| + \rho_{22}|2\rangle\langle 2|\,.$$

We can rewrite eq. (1) in terms of the spontaneous emission rate, γ given by the Einstein A coefficient

$$(3) \qquad \gamma = \frac{\mu^2}{3\pi\epsilon_0\hbar}\left(\frac{2\pi}{\lambda}\right)^3$$

to the following:

$$(4) \qquad \chi = i\frac{3}{8\pi^2}\frac{N}{V}\lambda^3(\rho_{11} - \rho_{22})\frac{\gamma}{\gamma_{12} - i\delta}\,.$$

On resonance where $\delta = 0$, we can write the linear susceptibility by considering $\rho_{11} = 1$, $\rho_{22} = 0$, which assumes that all the population is in the ground state, and the drive is weak,

$$(5) \qquad \chi_0 = i\frac{3}{8\pi^2}\frac{N}{V}\lambda^3\frac{\gamma}{\gamma_{12}}\,.$$

So the linear susceptibility is purely imaginary. Physically, this means the medium is absorptive, with no refraction. The electric field $\mathcal{E}$ will propagate through this medium as

$$(6) \qquad \mathcal{E}(x) = \mathcal{E}(0)e^{(-Im[\chi]+iRe[\chi])kx/2}.$$

We also know, from Beer's Law, that

$$(7) \qquad |\mathcal{E}|^2 = I(x) = I(0)e^{\frac{-N\sigma x}{2}},$$

where eq. (7) is simply Beer's law written in terms of the absorption cross section per atom σ. Comparing to our expression for χ above, this gives

$$(8) \qquad \sigma = \frac{3}{4\pi}\lambda^2 \frac{\gamma}{\gamma_{12}}.$$

When $\gamma = \gamma_{12}$, the absorption cross section is on the order of λ^2! This means that a *single atom* can absorb a diffraction-limited photon. This condition where $\gamma = \gamma_{12}$ is referred to as *radiative broadening*. This requires that the optical transition has perfect quantum efficiency and that the linewidth $\Delta\nu$ is transform-limited, *i.e.* $\Delta\nu = \frac{1}{2\pi\tau}$ where τ is the excited state lifetime. In other words, there should be no linewidth broadening from non-radiative processes or spectral diffusion.

There are a number of interactions with the host that can lead to broadening beyond radiative broadening.

- First, if optical absorption results from absorption of a photon and a phonon, this will give a broad linewidth for the phonon excited state. These processes can generally be suppressed by cooling down to cryogenic temperatures, freezing out the thermal population of phonons.

- Second, if the optical emission results from emission of a photon and a phonon, the emitted photon will be shifted to the red and the linewidth will inherit the characteristics of the phonon lifetime, which gives rise to broad phonon sidebands.

- Third, the difference in energy levels between $|1\rangle$ and $|2\rangle$ can change due to interactions with electric, strain, or magnetic fields, leading to fluctuations in the optical transition frequency known as spectral diffusion. Changes in the electric field can arise from fluctuating trapped charges in the host, and this interaction comes from the difference in static dipole moment for the ground and excited states. This consideration leads the a natural strategy of searching for quantum defects that have no permanent electric dipole moment, in order to make them insensitive to fluctuating electrostatic fields. Fluctuations in magnetic fields from nearby nuclear spins can also lead to spectral diffusion if the ground and excited states have different hyperfine couplings. Since the hyperfine interaction is typically small (kHz–MHz scale), this is generally only relevant for very narrow-linewidth emitters, such as rare-earth ions.

4. – Spin coherence and interactions with the environment

In order to parametrize magnetic interactions with the host environment, let us start by writing down the Zeeman Hamiltonian for a spin $\vec{\sigma}$ in a magnetic field $\vec{B}$:

$$(9) \qquad \hat{H} = -\frac{1}{2}\hbar\gamma\vec{\sigma}\cdot\vec{B},$$

where γ is the gyromagnetic ratio given by $\gamma = \frac{g\mu_B}{\hbar}$. If we start with the spin in a superposition, $|\psi(t=0)\rangle = \frac{1}{\sqrt{2}}(|0\rangle + |1\rangle)$, we can solve the time-dependent Schrödinger equation in the presence of an external magnetic field aligned with the quantization axis, $B = B_0\hat{z}$:

$$(10a) \qquad i\hbar\frac{\partial}{\partial t}|\psi(t)\rangle = \hat{H}|\psi(t)\rangle,$$

$$(10b) \qquad |\psi(t)\rangle = \frac{1}{\sqrt{2}}\left(|0\rangle + e^{i\gamma B_0 t}|1\rangle\right).$$

The time-dependent phase corresponds to Larmor precession of a spin around the Bloch sphere. For an oscillating, AC magnetic field $B = B_1\cos\omega t\hat{x}$, we can solve the time-dependent Schrödinger equation in a rotating frame at the Larmor frequency, $|\psi^*(t)\rangle = e^{i\omega_L \sigma_z t/2}|\psi(t)\rangle$, and then apply the rotating-wave approximation to eliminate rapidly oscillating terms. When $\omega = \omega_L$, this leads to a magnetic resonance, and the resulting approximation for the Hamiltonian is given by

$$(11) \qquad H'(t) = \hbar\Omega\sigma_x,$$

where $\Omega = \frac{\gamma B_1}{2}$ is the Rabi frequency.

4.1. Dephasing. – Spins that experience inhomogeneous static magnetic fields will pick up different phases over time. These effects are generally referred to as T_2^* processes. Static inhomogeneity can give rise to ensemble linewidth broadening, while slowly varying fields can lead to spectral diffusion of the magnetic resonance. In addition to inhomogeneities in the applied field over the volume of the sample, there can also be sources of inhomogeneity intrinsic to the sample, such as strain gradients. Another dominant source of dephasing is hyperfine interactions with nuclear and electronic spins in the host material. Nuclear spins in particular can have exceptionally long spin-lattice relaxation times, so they will look like a very slowly varying magnetic field.

4.2. Decoherence. – It turns out that inhomogeneities in low frequency fields are relatively easy to cancel out using a Hahn echo pulse sequence. Remaining sources of decoherence can arise from high frequency magnetic, electric, or strain fields. The coherence time limited by these processes is referred to as T_2. This is a poorly defined term in that the measured T_2 can depend on what pulse sequences you apply, and can even be extended by driving the noise bath directly.

The impact of nuclear spins in the host material on the coherence time of the quantum defect will therefore depend on the density of nuclear spins. Nuclear spin-nuclear spin interactions can lead to short nuclear spin T_1, which gives rise to a rapidly fluctuating magnetic noise bath that is difficult to decouple from. This is generally true for materials in which the predominant isotopes have nonzero nuclear spin, such as III-V compounds. In materials with a small minority of nuclear spinful isotopes, like diamond or silicon, the natural abundance of nuclear spins give rise to a slowly varying bath that can be cancelled out effectively with Hahn echo and other dynamical decoupling sequences. Another subtlety is that nuclear spin flip-flops can be suppressed by a frozen core effect, in which nuclear spins see a gradient in the magnetic field due to proximity to an electron spin, causing them to be out of resonance with one another. This can lead to enhanced T_2 over what would be naively estimated from the nuclear spin density.

Other paramagnetic impurities in the host material with net electron spin can lead to faster decoherence. For example, when the quantum defect of interest is at sufficiently high density, spin-spin flip-flop interactions of nearest neighbors will look like a changing magnetic field for the central spin. This phenomenon is known as "instantaneous diffusion." Achieving long T_2 is therefore in principle conceptually simple, in that it requires a host material with nuclear spin-zero isotopes, free of paramagnetic electronic impurities.

However, it is possible to create a particular quantum defect that exhibits shorter T_2 than would be expected from the host spin bath. For example, if there is a phonon-mediated orbital relaxation, and these different orbitals experience different effective magnetic fields from the environment because of differing spin-orbit or spin-spin coupling, this orbital relaxation can also lead to decoherence. In such systems, although the spin T_1 is long, and the host material is free of paramagnetic impurities, the fluctuating effective magnetic field from orbital effects will lead to a drastically shortened T_2. This mechanism is responsible for the short T_2 observed in the negatively charged group-IV vacancies in diamond, for example.

4˙3. *Spin-lattice relaxation*. – For a spin in vacuum, spin relaxation arises from equilibration with the blackbody environment. Since the density of states at low frequencies is so small, this rate is essentially zero (10^{13} years at $10\,\mathrm{MHz}$!). In a solid, these spin relaxation times are much faster because of interactions with phonons. Because of this, T_1 relaxation is often referred to as *spin-lattice relaxation*. Phonons cannot flip the spin directly because they do not have a direct magnetic component. Indirectly, they can influence the spin relaxation by perturbing the lattice, which can look like a varying magnetic field via spin-orbit coupling. This leads to the prescription that long T_1 is typically achieved with either low spin-orbit coupling (low mass atoms) or low orbital-lattice coupling (for example, with buried electron shells in d or f orbitals).

The microscopic mechanisms for T_1 processes were extensively characterized in the middle of the 20th century [20]. The rates will depend on the density of states of phonons at the relevant energy scale, so stiff lattices with high Debye temperatures will allow for longer T_1. A non-exhaustive list follows:

- A direct process is one in which a single phonon can induce a spin flip from one sublevel to another. This should be linear in temperature at high temperatures, and when the temperature is small compared to the energy splitting between spin sublevels, it is exponentially activated.

- An Orbach process is a two-phonon process via an intermediate excited state. The T_1 relaxation rate will be exponential with temperature, with an activation energy given by the energy position of the excited state.

- A Raman process is also a two-phonon process via a virtual state. The temperature dependence is typically an odd power of temperature, and the exponent depends on the exact conditions.

It is generally true that different processes will dominate at different temperatures, depending on the available phonons and excited states. For example, it is common for a given quantum defect to have crossover temperatures between direct, Orbach, and Raman processes, where Raman processes dominate at the highest temperatures because of the large density of available phonons.

5. – Prospects for quantum technologies

Only a handful of quantum defects and atom-like systems have been thoroughly characterized and explored, and there are many more possibilities for new systems to achieve better metrics than those that are currently known. Here I will briefly highlight a few considerations for integration with nanoscale devices, which will be critical for deployment in any scalable quantum technology.

- In order to achieve long T_1, the most important criteria is the selection of the host material and the detailed interactions of the quantum system with phonons. Optimizing this desideratum together with the demands of nanofabrication and device functionality will be a central challenge in any search for new quantum systems.

- For long T_2, in addition to selecting a material that is free of nuclear spins, the host material must also be free of other electronic defects. The relevant length scale is set by spin-spin interactions with impurities; for spin $1/2$ electrons, $g = 2$, this scale is typically around $1\,\mathrm{kHz}$ at $30\,\mathrm{nm}$. In other words, paramagnetic impurities at the $100\,\mathrm{ppb}$ level will limit the spin coherence time to 1 millisecond. This poses a grand challenge in purifying materials for quantum applications. Only a few materials have been purified to ppb background impurity concentrations: silicon, germanium, diamond, and a few others that are used as scintillators.

- For nanophotonic applications, the device dimensions will typically be on the order of tens to hundreds of nanometers in order to confine a single optical mode. The

purity and surface termination at these nanofabricated surfaces presents a significant challenge for future integration of quantum systems. Two areas of active research are 1) to find quantum systems that are insensitive to noise at the surface, and 2) to better control the surface termination.

REFERENCES

[1] BIRNBAUM K. M., BOCA A., MILLER R., BOOZER A. D., NORTHUP T. E. and KIMBLE H. J., *Nature*, **436** (2005) 87.

[2] DUAN L.-M., LUKIN M. D., CIRAC J. I. and ZOLLER P., *Nature*, **414** (2001) 413.

[3] WEHNER S., ELKOUSS D. and HANSON R., *Science*, **361** (2018) 6412.

[4] HUCUL D., INLEK I. V., VITTORINI G., CROCKER C., DEBNATH S., CLARK S. M. and MONROE C., *Nat. Phys.*, **11** (2015) 37.

[5] DEVORET M. H. and SCHOELKOPF R. J., *Science*, **339** (2013) 1169.

[6] HWANG J., POTOTSCHNIG M., LETTOW R., ZUMOFEN G., RENN A., GÖTZINGER, S. and SANDOGHDAR V., *Nature*, **460** (2009) 76.

[7] ENGLUND D., FARAON A., FUSHMAN I., STOLTZ N., PETROFF P. and VUCKOVIC J., *Nature*, **450** (2007) 857.

[8] TYRYSHKIN A. M., TOJO S., MORTON J. J. L., RIEMANN H., ABROSIMOV N. V., BECKER P., POHL H., SCHENKEL T., THEWALT M. L. W., ITOH K. M. and LYON S. A., *Nat. Mater.*, **11** (2011) 143.

[9] LO C. C., URDAMPILLETA M., ROSS P., GONZALEZ-ZALBA M. F., MANSIR J., LYON S. A., THEWALT M. L. W. and MORTON J. J. L., *Nat. Mater.*, **14** (2014) 490.

[10] SIMMONS S., arXiv:1606.03488v1 (2016).

[11] AWSCHALOM D. D., BASSETT L. C., DZURAK A. S., HU E. L. and PETTA J. R., *Science*, **339** (2013) 1174.

[12] JELEZKO F. and WRACHTRUP J., *Phys. Status Solidi a: Applications and Materials Science*, **203** (2006) 3207.

[13] SIPAHIGIL A., EVANS R. E., SUKACHEV D. D., BUREK M. J., BORREGAARD J., BHASKAR M. K., NGUYEN C. T., PACHECO J. L., ATIKIAN H. A., MEUWLY C., CAMACHO R. M., JELEZKO F., BIELEJEC E., PARK H., LONCAR M. and LUKIN M. D., *Science*, **354** (2016) 847.

[14] ROSE B. C., HUANG D., ZHANG Z.-H., STEVENSON P., TYRYSHKIN A. M., SANGTAWESIN S., SRINIVASAN S., LOUDIN L., MARKHAM M. L., EDMONDS A. M, TWITCHEN D. J., LYON S. A. and DE LEON N. P., *Science*, **361** (2018) 60.

[15] KOEHL W. F., BUCKLEY B. B., HEREMANS F. J., CALUSINE G. and AWSCHALOM D. D., *Nature*, **479** (2011) 84.

[16] PROBST S., ROTZINGER H., USTINOV A. V. and BUSHEV P. A., *Phys. Rev. B*, **92** (2015) 014421.

[17] KOLESOV R., XIA K., REUTER R., JAMALI M., STÖHR R., INAL T., SIYUSHEV P. and WRACHTRUP J., *Phys. Rev. Lett.*, **111** (2013) 120502.

[18] DIBOS A. M., RAHA M., PHENICIE C. M. and THOMPSON J. D., *Phys. Rev. Lett.*, **120** (2018) 243601.

[19] LUKIN M. D., *Modern atomic and optical physics II, Harvard University physics* on line lecture notes.

[20] SHRIVASTAVA K. N., *Phys. Status Solidi B*, **117** (1983) 437.

Quantum optics and nonclassical light generation

RAHUL TRIVEDI, DANIIL LUKIN and JELENA VUCKOVIC

E. L. Ginzton Laboratory, Stanford University - Stanford, California 94305, USA

Summary. — This paper will focus on the theoretical and experimental study of light-matter interaction in photonic structures. We will therefore start by describing quantum optical models of optical cavities and waveguides. Then we will describe the basic physics behind light matter interactions, and provide a theoretical analysis of the phenomena that result from it. Finally, we will describe single-photon sources, their characterization and introduce solid-state platforms that can be employed for their implementation. Throughout this paper, we have tried to provide a sound and complete description of the theoretical underpinnings of the seminal experiments in quantum optics. Detailed derivations of some of the results employed in the main text have been provided in the appendices.

1. – Quantum description of electromagnetic fields

Quantum description of electromagnetic fields is an essential part of the study of light-matter interactions; even very fundamental effects such as spontaneous emission cannot be explained with a classical model of electromagnetic fields. This section attempts to give an overview of quantum optical models used for describing electromagnetic fields in systems that support a discrete set of modes (*e.g.* lossless cavities) as well as in systems that support a continuum of modes (*e.g.* waveguides).

29

1`1. *Lossless cavities: Systems with discrete modes.* – Lossless optical cavities are often an interesting mathematical model to understand the behaviour of a number of optical systems. An ideal lossless cavity can be formed by enclosing a lossless permittivity distribution within a perfect electrical conductor (PEC) or a perfect magnetic conductor (PMC). It is well known in classical electromagnetic theory that such a system supports a discrete set of modes $\mathbf{E}_n(\mathbf{x})$ at frequencies ω_n which satisfy the following generalized eigenvalue equation [1]:

$$(1) \qquad \nabla \times \nabla \times \mathbf{E}_n(\mathbf{x}) = \frac{\omega_n^2}{c^2} \varepsilon(\mathbf{x}) \mathbf{E}_n(\mathbf{x}),$$

where $\varepsilon(\mathbf{x})$ is the permittivity distribution inside the cavity, and $\mathbf{E}_n(\mathbf{x})$ satisfy the PEC or PMC boundary conditions at the boundaries of the cavity. Quantum optically, it is easy to show that each of these cavity modes behaves like a harmonic oscillator [2] — more concretely, the physics of the n-th cavity mode are governed by the Hamiltonian H_n:

$$(2) \qquad H_n = \omega_n a_n^\dagger a_n,$$

where a_n is the annihilation operator for the mode which satisfies the commutation relations $[a_n, a_m^\dagger] = \delta_{n,m}$ and $[a_n, a_m] = 0$. The Hamiltonian for the dynamics of all the cavity modes taken together is simply a sum of the Hamiltonians H_n:

$$(3) \qquad H = \sum_n H_n = \sum_n \omega_n a_n^\dagger a_n.$$

We note that in the Heisenberg picture, this Hamiltonian along with the commutation relationships mentioned above imply a time-harmonic evolution of the operators $a_n(t)$ — in particular, the solution of $\mathrm{d}a_n(t)/\mathrm{d}t = -\mathrm{i}[a_n(t), H(t)] = -\mathrm{i}\omega_n a_n(t)$ is simply $a_n(t) = a_n(0)\exp(-\mathrm{i}\omega_n t)$. This is consistent with the classical dynamics of optical cavities, wherein the amplitude of the n-th cavity mode (which is the classical variable corresponding to the operator a_n) oscillates in time at frequency ω_n.

The electric field at a point $\mathbf{x}$ inside the cavity is now described by a Hermitian operator $\mathbf{E}(\mathbf{x})$ given by

$$(4) \qquad \mathbf{E}(\mathbf{x}) = \sum_n \left(\frac{\hbar\omega_n}{2\varepsilon_0 \mathcal{N}_n} \right)^{1/2} (\mathbf{E}_n(\mathbf{x})a_n + \mathbf{E}_n^*(\mathbf{x})a_n^\dagger),$$

where $\mathcal{N}_n$ is the normalization factor for the n-th mode defined by

$$(5) \qquad \mathcal{N}_n = \int \varepsilon(\mathbf{x})|\mathbf{E}_n(\mathbf{x})|^2 \mathrm{d}^3\mathbf{x}.$$

The electric-field operator in the Heisenberg picture is given by

$$(6) \qquad \mathbf{E}(\mathbf{x}, t) = \sum_n \left(\frac{\hbar \omega_n}{2 \varepsilon_0 \mathcal{N}_n} \right)^{1/2} (\mathbf{E}_n(\mathbf{x}) a_n \exp(-\mathrm{i} \omega_n t) + \mathbf{E}_n^*(\mathbf{x}) a_n^\dagger \exp(\mathrm{i} \omega_n t)).$$

An important point to note about the electric-field operator is that there is a separate operator for each point $\mathbf{x}$ in the cavity — unlike quantum mechanics where the position of the particle is itself an operator, the spatial position in quantum optics merely plays the role of an index upon which an electric-field operator can be defined.

The quantum states of light in cavities can be most conveniently represented in the Fock state basis. Consider only the Hilbert space of a single cavity mode — a complete basis for this space is given by the states $|n\rangle$ constructed via

$$(7) \qquad |n\rangle = \frac{1}{\sqrt{n!}} (a^\dagger)^n |0\rangle \quad \forall \, n \in \{0, 1, 2 \ldots\},$$

where a is the annihilation operator for the cavity mode and $|0\rangle$ is the lowest-energy state of the cavity mode, often referred to as the vacuum state (its defining property is the fact that it is in the null space of the annihilation operator $a|0\rangle = 0$). It is straightforward to show that the state $|n\rangle$ is an eigenstate of the cavity Hamiltonian $\omega a^\dagger a$ with eigenenergy $n\omega$. These states are also orthonormal ($\langle n|m\rangle = \delta_{n,m}$) and complete (*i.e.* any allowed quantum state of the cavity can be expressed as their superposition). The eigenstates of the Hilbert space of all the cavity modes taken together can be easily constructed by performing a tensor product of Fock states for different cavity modes:

$$(8) \qquad |n_1, n_2, n_3 \ldots\rangle = |n_1\rangle |n_2\rangle |n_3\rangle \ldots = \prod_k \frac{1}{\sqrt{n_k!}} (a_k^\dagger)^{n_k} |\mathrm{vac}\rangle,$$

where $|\mathrm{vac}\rangle$ is the vacuum state of all the cavity modes taken together. Note that these states are, by construction, orthonormal and complete. Furthermore, they are eigenstates of the Hamiltonian H defined in eq. (3) with eigenenergy $n_1\omega_1 + n_2\omega_2 + n_3\omega_3 \ldots$. In almost all problems, it is more convenient to define the N-photon subspace of the cavity — this is defined as the space spanned by states of the form given in eq. (8) with $n_1 + n_2 + n_3 \ldots = N$. As an explicit example of the construction of these subspaces, consider a cavity with two modes — the ($N = 1$)-photon subspace then comprises of the states of the form $a_0|1, 0\rangle + a_1|0, 1\rangle$ where a_0 and a_1 are complex numbers which satisfy $|a_0|^2 + |a_1|^2 = 1$. The $N = 2$ photon subspace comprises of states of the form $a_0|2, 0\rangle + a_1|0, 2\rangle + a_{1,0}|1, 1\rangle$, where $|a_0|^2 + |a_1|^2 + |a_{1,0}|^2 = 1$. Higher-order photon subspaces can be constructed using a similar procedure.

An important property of Fock states, which is easily verified, is that the expectation of the annihilation operator a_n or the creation operator $a_n^\dagger$ vanish, and by extension the expection of the electric-field operator (eq. (6)) vanishes irrespective of the "energy" of the state. Consequently, the Fock states by themselves are not "classical" states of light,

in which one might expect the average electric field inside the cavity to become stronger with the energy of the state. The closest approximation of a classical state of light is the coherent state $|\alpha_1, \alpha_2, \alpha_3 \ldots\rangle$ defined by

$$(9) \qquad |\alpha_1, \alpha_2, \alpha_3 \ldots\rangle = \prod_k \mathcal{D}_k(\alpha_k) |0\rangle,$$

where $\mathcal{D}_k(\alpha_k)$ is the displacement operator for the k-th cavity mode defined by

$$(10) \qquad \mathcal{D}_k(\alpha_k) = \exp(\alpha_k a_k^\dagger - \alpha_k^* a_k).$$

Since the Fock states form a complete basis for the cavity mode, the coherent state can be expressed as a superposition of Fock states. In particular, a simple expression for $\mathcal{D}_k(\alpha_k)|0\rangle$ can be formed by using the Zassenhaus formula together with the commutation relationships for the cavity annihilation operators:

$$
\begin{aligned}
(11) \qquad \mathcal{D}_k(\alpha_k) |0\rangle &= \exp(-|\alpha_k|^2/2) \exp(\alpha_k a_k^\dagger) \exp(-\alpha_k^* a_k) |0\rangle \\
&= \exp(-|\alpha_k|^2/2) \sum_{n_k=0}^\infty \frac{\alpha_k^{n_k}}{n_k!} (a_k^\dagger)^{n_k} |0\rangle \\
&= \exp(-|\alpha_k|^2/2) \sum_{n_k=0}^\infty \frac{\alpha_k^{n_k}}{\sqrt{n_k!}} |0, 0, \ldots n_k, 0 \ldots\rangle.
\end{aligned}
$$

The coherent states defined in eq. (9) are eigenstates of the annihilation operator a_k:

$$(12) \qquad a_k |\alpha_1, \alpha_2, \alpha_3 \ldots\rangle = \alpha_k |\alpha_1, \alpha_2, \alpha_3 \ldots\rangle.$$

This can easily be verified using eq. (11). An immediate consequence of this property is that the expectation value of the electric-field operator resembles a "classical" electric field — in particular, note that

$$(13)$$
$$\langle\alpha_1, \alpha_2, \alpha_3 \ldots| \mathbf{E}(\mathbf{x}, t) |\alpha_1, \alpha_2, \alpha_3 \ldots\rangle = \sum_k \left(\frac{2\hbar\omega_k}{\varepsilon_0 \mathcal{N}_k}\right)^{1/2} \mathrm{Re}[\mathbf{E}_k(\mathbf{x})\alpha_k \exp(-\mathrm{i}\omega_k t)],$$

which, barring a normalization constant, resembles a harmonic field that classical cavities support if initialized with some energy at $t = 0$. Moreover, it can be shown that the standard deviation in the electric field $[\langle\mathbf{E}^2(\mathbf{x}, t)\rangle - \langle\mathbf{E}(\mathbf{x}, t)\rangle^2]^{1/2}$ becomes increasingly smaller compared to the expectation value of the electric field as the amplitudes of the coherent state, α_k, is increased, which further motivates the fact the coherent states are a good approximation of classical states of light.

1˙2. *Single-mode waveguide: System with a continuum of modes.* – Together with optical cavities, optical waveguides form the basic building blocks of quantum information processing systems. However, unlike optical cavities, optical waveguides can no longer be described with a discrete set of modes, rather they are described by a continuum of modes. For simplicity, in this section, we will focus only on describing the quantum optics of a single-mode optical waveguide — extension to multi-mode optical waveguides is straightforward. Most of the analysis presented here closely follows section II of [3].

As is well known in the classical theory of optical waveguides, a single-mode waveguide (with direction of propagation being the z-axis) can be described by modes of the form $\mathbf{E}_\beta(\boldsymbol{\rho}) \exp(\mathrm{i}\beta z)$, where β is the propagation constant, $\mathbf{E}_\beta(\boldsymbol{\rho})$ is the electric-field mode profile and $\boldsymbol{\rho} \equiv (x, y)$ is the coordinate in the transverse plane of the waveguide. Such a mode is supported at a specific frequency $\omega(\beta)$ which depends on the propagation constant (the relationship between ω and β is often refered to as the dispersion relation of the waveguide mode). $\mathbf{E}_\beta(\boldsymbol{\rho})$ and $\omega(\beta)$ satisfy the following generalized eigenvalue equation [1]:

$$(14) \qquad (\nabla_T + \mathrm{i}\beta\hat{z}) \times (\nabla_T + \mathrm{i}\beta\hat{z}) \times \mathbf{E}_\beta(\boldsymbol{\rho}) = \frac{\omega^2(\beta)}{c^2}\varepsilon(\boldsymbol{\rho})\mathbf{E}_\beta(\boldsymbol{\rho}).$$

Quantum optically, an optical waveguide can be modelled with a continuum of harmonic oscillators — each mode of the waveguide can be described by an annihilation operator a_β which satisfies the commutation relationship $[a_\beta, a_{\beta'}^\dagger] = \delta(\beta - \beta')$ and $[a_\beta, a_{\beta'}] = 0$. The Hamiltonian governing the dynamics of the quantum state of the waveguide can then be expressed as

$$(15) \qquad H = \int_{-\infty}^{\infty} \omega(\beta)a_\beta^\dagger a_\beta \mathrm{d}\beta.$$

The electric field at each point on the waveguide is described by a Hermitian operator given by

$$(16) \qquad E(\mathbf{x}) = \int_{-\infty}^{\infty} \left(\frac{\hbar\omega(\beta)}{2\varepsilon_0\mathcal{N}(\beta)}\right)^{1/2} [a_\beta\mathbf{E}_\beta(\boldsymbol{\rho}) \exp(\mathrm{i}\beta z) + a_\beta^\dagger\mathbf{E}_\beta(\boldsymbol{\rho}) \exp(-\mathrm{i}\beta z)],$$

where

$$(17) \qquad \mathcal{N}(\beta) = \int \varepsilon(\boldsymbol{\rho})|\mathbf{E}_\beta(\boldsymbol{\rho})|^2 \mathrm{d}^2\boldsymbol{\rho}.$$

Note that a negative value of β corresponds to a mode propagating in $-z$-direction. In most experimentally relevant systems, the waveguide mode is excited in a narrow band of frequencies around an operating frequency ω_0. The theoretical analysis of these systems can be greatly simplified by assuming that the dispersion relationship $\omega(\beta)$ can be well

approximated by two linear dispersions around ω_0, $\omega_+(\beta)$ for the forward-propagating modes $(\beta > 0)$ and $\omega_-(\beta)$ for the backward-propagating modes $(\beta < 0)$:

$$(18a) \qquad \omega_+(\beta) = \omega_0 + v_G(\beta - \beta_0) \iff \beta_+(\omega) = \beta_0 + \frac{\omega - \omega_0}{v_G},$$

$$(18b) \qquad \omega_-(\beta) = \omega_0 - v_G(\beta + \beta_0) \iff \beta_-(\omega) = -\beta_0 - \frac{\omega - \omega_0}{v_G},$$

where v_G is the group velocity of the waveguide mode, and β_0 is the propagation constant corresponding to ω_0. The Hamiltonian can then be approximated by

$$(19) \qquad H \approx \int_0^\infty \omega_+(\beta) a_\beta^\dagger a_\beta \mathrm{d}\beta + \int_{-\infty}^0 \omega_-(\beta) a_\beta^\dagger a_\beta \mathrm{d}\beta$$

and the electric-field operator can be approximated by

$$(20) \qquad \mathbf{E}(\mathbf{x}) \approx \mathbf{E}_+(\mathbf{x}) + \mathbf{E}_-(\mathbf{x}),$$

where

$$(21a) \qquad \mathbf{E}_+(\mathbf{x}) = \left(\frac{\hbar\omega_0}{2\varepsilon_0 \mathcal{N}(\beta_0)}\right)^{1/2} \mathbf{E}_{\beta_0}(\boldsymbol{\rho}) \int_0^\infty a_\beta \exp(-\mathrm{i}\beta z)\mathrm{d}\beta + \text{h.c.},$$

$$(21b) \qquad \mathbf{E}_-(\mathbf{x}) = \left(\frac{\hbar\omega_0}{2\varepsilon_0 \mathcal{N}(-\beta_0)}\right)^{1/2} \mathbf{E}_{-\beta_0}(\boldsymbol{\rho}) \int_{-\infty}^0 a_\beta \exp(-\mathrm{i}\beta z)\mathrm{d}\beta + \text{h.c.}$$

Finally, it is customary to express the Hamiltonian and the electric-field operators as an intergal over frequency ω as opposed to the propagation constant β. To do so, we define an annihilation operator f_ω for the forward-propagating mode at frequency ω and an operator b_ω for the backward-propagating mode at frequency ω via

$$(22) \qquad f_\omega = \frac{a_{\beta_+(\omega)}}{\sqrt{v_G}} \quad \text{and} \quad b_\omega = \frac{a_{\beta_-(\omega)}}{\sqrt{v_G}}.$$

It is straightforward to show that f_ω and b_ω satisfy $[f_\omega, f_{\omega'}^\dagger] = \delta(\omega - \omega')$ and $[b_\omega, b_{\omega'}^\dagger] = \delta(\omega - \omega')$. Note from eq. (18) both f_ω and b_ω are only defined for $\omega > \omega_0 - v_G\beta_0$. However, since we are assuming that the waveguide mode is only excited in a narrow band around a frequency ω_0, unless ω_0 is near $\omega_0 - v_G\beta_0$, we can extend the frequency range of definition of f_ω and b_ω from $-\infty$ to ∞ and safely assume that there will be no excitations at the fictiously introduced frequencies $(\omega < \omega_0 - v_G\beta_0)$. In terms of these operators, the total Hamiltonian can be expressed as

$$(23) \qquad H = \int_{-\infty}^\infty \omega(f_\omega^\dagger f_\omega + b_\omega^\dagger b_\omega)\mathrm{d}\omega$$

while the electric-field operators for the forward- and backward-propagating modes can be expressed as

(24a)
$$\mathbf{E}_+(\mathbf{x}) = \left(\frac{\hbar\omega_0}{2\varepsilon_0\mathcal{N}(\beta_0)v_G}\right)^{1/2} \mathbf{E}_{\beta_0}(\boldsymbol{\rho}) \exp\left[-\mathrm{i}\left(\beta_0 - \frac{\omega_0}{v_G}\right)z\right]$$
$$\times \int_{-\infty}^{\infty} f_\omega \exp\left(-\mathrm{i}\frac{\omega z}{v_G}\right)\mathrm{d}\omega + \text{h.c.},$$

(24b)
$$\mathbf{E}_-(\mathbf{x}) = \left(\frac{\hbar\omega_0}{2\varepsilon_0\mathcal{N}(-\beta_0)v_G}\right)^{1/2} \mathbf{E}_{-\beta_0}(\boldsymbol{\rho}) \exp\left[\mathrm{i}\left(\beta_0 + \frac{\omega_0}{v_G}\right)z\right]$$
$$\times \int_{-\infty}^{\infty} b_\omega \exp\left(\mathrm{i}\frac{\omega z}{v_G}\right)\mathrm{d}\omega + \text{h.c.}$$

Finally, we can introduce the spatial domain annihilation operators f_z and b_z for the forward- and backward-propagating modes via

(25)
$$f_z = \int_{-\infty}^{\infty} f_\omega \exp\left(-\mathrm{i}\frac{\omega z}{v_G}\right)\frac{\mathrm{d}\omega}{\sqrt{2\pi v_G}} \quad \text{and} \quad b_z = \int_{-\infty}^{\infty} b_\omega \exp\left(\mathrm{i}\frac{\omega z}{v_G}\right)\frac{\mathrm{d}\omega}{\sqrt{2\pi v_G}},$$

which again satisfy the commutators $[f_z, f_{z'}^\dagger] = \delta(z - z')$ and $[b_z, b_{z'}^\dagger] = \delta(z - z')$. These operators can be interpreted to be related to the creation and annihilation of an excitation at a position z in the waveguide — a notion that can be made more concrete by noting that the operators $\mathbf{E}_+(\mathbf{x} \equiv (\boldsymbol{\rho}, z))$ $[\mathbf{E}_-(\mathbf{x} \equiv (\boldsymbol{\rho}, z))]$ depend entirely upon the opertor f_z (b_z):

(26a)
$$\mathbf{E}_+(\mathbf{x}) = \left(\frac{\hbar\omega_0}{4\pi\varepsilon_0\mathcal{N}(\beta_0)v_G^2}\right)^{1/2} \mathbf{E}_{\beta_0}(\boldsymbol{\rho}) \exp\left[-\mathrm{i}\left(\beta_0 - \frac{\omega_0}{v_G}\right)z\right]f_z + \text{h.c.},$$

(26b)
$$\mathbf{E}_-(\mathbf{x}) = \left(\frac{\hbar\omega_0}{2\varepsilon_0\mathcal{N}(-\beta_0)v_G^2}\right)^{1/2} \mathbf{E}_{-\beta_0}(\boldsymbol{\rho}) \exp\left[\mathrm{i}\left(\beta_0 + \frac{\omega_0}{v_G}\right)z\right]b_z + \text{h.c.}$$

Additionally, the Hamiltonian H in eq. (23) can be expressed in terms of f_z and b_z:

(27)
$$H = \int_{-\infty}^{\infty} \omega(f_\omega^\dagger f_\omega + b_\omega^\dagger b_\omega)\mathrm{d}\omega$$
$$= \int_{-\infty}^{\infty}\int_{-\infty}^{\infty} \omega\left[f_z^\dagger f_\omega \exp\left(-\mathrm{i}\frac{\omega z}{v_G}\right) + b_z^\dagger b_\omega \exp\left(\mathrm{i}\frac{\omega z}{v_G}\right)\right]\frac{\mathrm{d}\omega\mathrm{d}z}{\sqrt{2\pi v_G}}$$
$$= \mathrm{i}v_G \int_{-\infty}^{\infty}\left(b_z^\dagger\frac{\partial b_z}{\partial z} - f_z^\dagger\frac{\partial f_z}{\partial z}\right)\mathrm{d}z.$$

While this form of the Hamiltonian might be less familiar to the reader, it can be seen that the Heisenberg equations of motion reproduce the first-order wave equations for the

operators f_z and b_z:

$$(28) \qquad \frac{\partial f_z(t)}{\partial t} + v_G \frac{\partial f_z(t)}{\partial z} = 0 \quad \text{and} \quad \frac{\partial b_z(t)}{\partial t} - v_G \frac{\partial b_z(t)}{\partial z} = 0.$$

The Hilbert space of the waveguide mode is much richer compared to the Hilbert space of a lossless cavity. For one, application of either the frequency domain or spatial domain creation operators ($f_\omega^\dagger, b_\omega^\dagger$ or $f_z^\dagger, b_z^\dagger$) to the vacuum state $|\text{vac}\rangle$ produces non normalizable states — physically, application of the frequency domain creation operator creates a "plane-wave" state which has excitations at all points along the waveguide whereas application of the spatial domain creation opertor creates a "delta-function" state which has excitations at all the supported frequencies. Constructing valid quantum states necessarily involves constructing a wave-packet out of these non-normalizable states. In the remainder of this section, we describe the notion of Fock states as well as coherent states that can exist inside a waveguide mode — for simplicity, we will restrict ourselves to states that only contain forward-propagating modes, states with backward-propagating modes components will have a similar form.

To generalize the notion of the N-photon subspaces defined in sect. **1**·1, we introduce a N-photon frequency-domain amplitude $\psi^{(N)}(\omega_1, \omega_2 \ldots \omega_N)$, the modulus square of which can be interpreted as the probability density of having N photons at frequencies $\omega_1, \omega_2 \ldots \omega_N$. The N-photon state can then be formally expressed as

$$(29) \quad \left|\Psi^{(N)}\right\rangle =$$
$$\frac{1}{\sqrt{N!}} \int_{-\infty}^{\infty} \int_{-\infty}^{\infty} \ldots \int_{-\infty}^{\infty} \psi^{(N)}(\omega_1, \omega_2 \ldots \omega_N) f_{\omega_1}^\dagger f_{\omega_2}^\dagger \ldots f_{\omega_N}^\dagger |\text{vac}\rangle \, \mathrm{d}\omega_1 \mathrm{d}\omega_2 \ldots \mathrm{d}\omega_N.$$

For the state to be normalized ($\langle \Psi^{(N)} | \Psi^{(N)} \rangle = 1$), $\psi^{(N)}(\omega_1, \omega_2 \ldots \omega_N)$ should satisfy

$$(30) \qquad \int_{-\infty}^{\infty} \int_{-\infty}^{\infty} \ldots \int_{-\infty}^{\infty} |\psi^{(N)}(\omega_1, \omega_2 \ldots \omega_N)|^2 \mathrm{d}\omega_1 \mathrm{d}\omega_2 \ldots \mathrm{d}\omega_N = 1.$$

This state can be alternatively be expressed in terms of a N-photon spatial-domain amplitude $\psi^{(N)}(z_1, z_2 \ldots z_N)$, which is related to the frequency domain amplitude via

$$(31) \qquad \psi^{(N)}(z_1, z_2 \ldots z_N) =$$
$$\int_{-\infty}^{\infty} \int_{-\infty}^{\infty} \ldots \int_{-\infty}^{\infty} \psi^{(N)}(\omega_1, \omega_2 \ldots \omega_N) \prod_{i=1}^{N} \exp\left(-\mathrm{i}\frac{\omega_i z_i}{v_G}\right) \frac{\mathrm{d}\omega_i}{\sqrt{2\pi v_G}},$$

and the N-photon state $|\Psi^{(N)}\rangle$ can be equivalently be expressed as

$$(32) \quad \left|\Psi^{(N)}\right\rangle =$$
$$\frac{1}{\sqrt{N!}} \int_{-\infty}^{\infty} \int_{-\infty}^{\infty} \ldots \int_{-\infty}^{\infty} \psi^{(N)}(z_1, z_2 \ldots z_N) f_{z_1}^\dagger f_{z_2}^\dagger \ldots f_{z_N}^\dagger |\text{vac}\rangle \, \mathrm{d}z_1 \mathrm{d}z_2 \ldots \mathrm{d}z_N.$$

The spatial-domain representation of the N-photon state is especially convenient for analyzing dyanmics of the waveguide mode, since time-evolution under the waveguide Hamiltonian (eq. (23)) is equivalent to a translation of the spatial-domain amplitude $\psi^{(N)}(z_1, z_2 \ldots z_N)$ by $v_G t$. To see this, note that the commutators for f_ω stated above imply that $[f_\omega^\dagger, H] = -\omega f_\omega^\dagger$ or equivalently $\exp(-iHt)f_\omega^\dagger \exp(iHt) = f_\omega^\dagger \exp(-i\omega t)$. This together with eq. (25) immediately implies that $\exp(-iHt)f_z^\dagger \exp(iHt) = f_{z-v_G t}$ and therefore

$$(33) \qquad \exp(-iHt)f_{z_1}^\dagger f_{z_2}^\dagger \ldots f_{z_N}^\dagger = \left[\prod_{i=1}^N \exp(-iHt)f_{z_i}^\dagger \exp(iHt) \right] \exp(-iHt)$$

$$= \left[\prod_{i=1}^N f_{z_i - v_G t}^\dagger \right] \exp(-iHt)$$

and hence

$$(34) \qquad \exp(-iHt)\left| \Psi^{(N)} \right\rangle$$

$$= \frac{1}{\sqrt{N!}} \int_{-\infty}^{\infty} \int_{-\infty}^{\infty} \ldots \int_{-\infty}^{\infty} \psi^{(N)}(z_1, z_2 \ldots z_N) \left[\prod_{i=1}^N f_{z_i - v_G t}^\dagger \right]$$

$$\times \exp(-iHt)|\text{vac}\rangle \mathrm{d}z_1 \mathrm{d}z_2 \ldots \mathrm{d}z_N$$

$$= \frac{1}{\sqrt{N!}} \int_{-\infty}^{\infty} \int_{-\infty}^{\infty} \ldots \int_{-\infty}^{\infty} \psi^{(N)}(z_1 + v_G t, z_2 + v_G t \ldots z_N$$

$$+ v_G t)f_{z_1}^\dagger f_{z_2}^\dagger \ldots f_{z_N}^\dagger |\text{vac}\rangle \mathrm{d}z_1 \mathrm{d}z_2 \ldots \mathrm{d}z_N,$$

wherein in the last step we made a change of integration variables $z_i \rightarrow z_i + v_G t$ and used the fact that $\exp(-iHt)|0\rangle = |0\rangle$ since $H|0\rangle = 0$ by definition of the vacuum state. This proves that the application of the propagator $\exp(-iHt)$ results in a translation of the position-domain amplitude by $v_G t$. This is analogous to the propagation of a classical wave down the waveguide at the group velocity of the waveguide.

Finally, the notion of a coherent state introduced in sect. **1**˙1 can be generalized to waveguides by introducing the displacement operator $\mathcal{D}[\phi(\omega)]$ defined via

$$(35) \quad \mathcal{D}\left[\phi(\omega)\right] = \exp\left[\int_{-\infty}^{\infty} (\phi(\omega)f_\omega^\dagger - \phi^*(\omega)f_\omega)\mathrm{d}\omega \right]$$

$$= \exp\left(-\frac{1}{2} \int_{-\infty}^{\infty} |\phi(\omega)|^2 \mathrm{d}\omega \right) \exp\left(\int_{-\infty}^{\infty} \phi(\omega)f_\omega^\dagger \mathrm{d}\omega \right) \exp\left(-\int_{-\infty}^{\infty} \phi^*(\omega)f_\omega \mathrm{d}\omega \right).$$

A coherent state, $|\phi(\omega)\rangle$ can then be defined by the application of this operator on the

vacuum state

$$(36) \qquad |\phi(\omega)\rangle = \mathcal{D}[\phi(\omega)]|\text{vac}\rangle$$

$$= \exp\left(-\frac{1}{2}\int_{-\infty}^{\infty}|\phi(\omega)|^2 \mathrm{d}\omega\right)\sum_{N=0}^{\infty}\frac{1}{N!}\left(\int_{-\infty}^{\infty}\phi(\omega)f_\omega^\dagger \mathrm{d}\omega\right)^N |\text{vac}\rangle.$$

Physically, $\phi(\omega)$ specifies the complex spectrum of the coherent state *i.e.* it contains information about the contribution of various frequencies to the coherent state, as well as their phase relationships. As in the case of optical cavities, these states are eigenstates of the frequency domain annihilation operator f_ω — from eq. (36), it is straightforward to show that $f_\omega|\phi(\omega)\rangle = \phi(\omega)|\phi(\omega)\rangle$. Such coherent states can be used as a fairly accurate model for pulsed light coming out of sources of classical light such as a laser.

Finally, we conclude this section by pointing out that while the model developed above was for a waveguide mode, it is a reasonable model for describing well-collimated free space modes (*e.g.* a Gaussian mode being emitted by a fiber and focused by an optical system) whose physics would otherwise be very complicated to describe exactly.

1˙3. *Model for lossy cavities*. – Section **1**˙1 introduced the quantum optical model for a lossless cavity. While this model serves as a good approximation in most cases, it is not realistic since it ignores losses (radiation and absorption) in the cavity mode. Incorporating cavity losses into our analysis is extremely important, and as we will see in the section for light matter interaction, these losses are often the limiting factor in the performance of quantum optical information processing systems.

An exact quantization of a lossy cavity with only radiation losses can be performed directly using the Maxwell's equations — a general approach to do this was first provided by Glauber [4] who considered the quantum optics of an arbitrary dielectric media. Explicit quantization of lossy Fabry-Perot cavities has been attempted by Dutra [5], who provides a method for calculating the modes of the lossy resonator. Theoretically treating absorption losses is more challenging, since the physics of the mechanism causing absorption (*e.g.* motion of electrons in solids, or coupling to phonons) is either not exactly known or very complicated. In this section, we will adopt a more phenomenological approach and assume that the losses in the cavity arise from its interaction with a continuum of harmonic oscillators [6], which we will refer to as the bath. More precisely, we will model a lossy cavity with the following Hamiltonian:

$$(37) \qquad H = \omega_c a^\dagger a + \int_{-\infty}^{\infty}\omega b_\omega^\dagger b_\omega \mathrm{d}\omega + \int_{-\infty}^{\infty}(\xi a^\dagger b_\omega + \xi^* b_\omega^\dagger a)\mathrm{d}\omega,$$

where a is the annihilation operator of the cavity mode under consideration and ω_c is its resonant frequency and b_ω is the annihilation operator corresponding to the bath mode at frequency ω. ξ is the coupling constant between the optical cavity and the bath, and would govern how "lossy" the optical cavity is. Note that while we have assumed

the cavity to only have a single mode, a similar model can be constructed for multimode cavities by coupling each cavity mode to a different bath of harmonic oscillators. Note that the relevant commuation relations satisfied by a and b_ω are: $[a, a^\dagger] = 1$, $[b_\omega, b_{\omega'}^\dagger] = \delta(\omega - \omega')$, $[a, b_\omega] = 0$ and $[a, b_\omega^\dagger] = 0$.

This model naturally captures exponential decay of the number of photons in the lossy cavity mode. This is most easily seen in the Heisenberg picture — the Heisenberg equations of motion for $a(t)$ and $b_\omega(t)$ are given by

$$(38a) \qquad \frac{\mathrm{d}a(t)}{\mathrm{d}t} = -\mathrm{i}[a(t), H(t)] = -\mathrm{i}\omega_c a(t) - \mathrm{i}\xi \int_{-\infty}^{\infty} b_\omega(t)\mathrm{d}\omega,$$

$$(38b) \qquad \frac{\mathrm{d}b_\omega(t)}{\mathrm{d}t} = -\mathrm{i}[b_\omega(t), H(t)] = -\mathrm{i}\omega b_\omega(t) - \mathrm{i}\xi^* a(t).$$

Integrating eq. (38b), we obtain

$$(39) \qquad b_\omega(t) = b_\omega(0)\exp(-\mathrm{i}\omega t) - \mathrm{i}\xi^* \int_0^t a(\tau)\exp(-\mathrm{i}\omega(t-\tau))\mathrm{d}\tau,$$

and therefore

$$(40) \qquad \int_{-\infty}^{\infty} b_\omega(t)\mathrm{d}\omega = \Phi_0(t) - \frac{\mathrm{i}\xi^*}{2}a(t),$$

wherein we have defined the operator $\Phi_0(t)$ by

$$(41) \qquad \Phi_0(t) = \int_{-\infty}^{\infty} b_\omega(0)\exp(-\mathrm{i}\omega t)\mathrm{d}\omega.$$

Note that the operator $\Phi_0(t)$ depends entirely on the state of the bath at $t = 0$, since it is defined in terms of the bath annihilation operators b_ω at $t = 0$. Substituting eq. (40) into eq. (38a), we obtain the following differential equation for $a(t)$:

$$(42) \qquad \frac{\mathrm{d}a(t)}{\mathrm{d}t} = -\mathrm{i}\omega_c a(t) - \frac{\kappa}{2}a(t) - \mathrm{i}\xi\Phi_0(t),$$

where we have introduced the decay rate $\kappa = 2\pi|\xi|^2$. Experimentally, it is typical to describe cavity losses in terms of a quality factor Q which is related to κ via $Q = \omega_c/\kappa$ — a high Q is indicative of a cavity mode with low loss. Note that the Heisenberg equation of motion resulted in the appearance of the decay term $-\kappa a(t)/2$. However, unlike its classical counterpart, a term $-\mathrm{i}\xi\Phi_0(t)$ also contributes to the dynamics of $a(t)$ — this is often called the "Langevin noise operator". It describes the impact of vaccuum fluctuations in the bath modes on the dynamics of the cavity. From a mathematical standpoint, this term is necessary for the Heisenberg equations to be consistent with a unitary evolution under the system Hamiltonian.

Using this dynamical equation, we can show that the photon number inside the cavity decays as a function of time. Consider initializing the cavity to some state $|\Psi_0\rangle$, with the bath being in the vacuum state $|0\rangle$ (*i.e.* the cavity-bath system is in the state $|\Psi(0)\rangle = |\Psi_0\rangle|0\rangle$). In the Heisenberg picture, the expectation value of the photon number at time t is given by $n(t) = \langle\Psi(t)|a^\dagger a|\Psi(t)\rangle = \langle\Psi(0)|a^\dagger(t)a(t)|\Psi(0)\rangle$, and therefore:

$$
\begin{aligned}
(43) \qquad \frac{\mathrm{d}n(t)}{\mathrm{d}t} &= \langle\Psi(0)|\frac{\mathrm{d}a^\dagger(t)}{\mathrm{d}t}a(t)|\Psi(0)\rangle + \langle\Psi(0)|a^\dagger(t)\frac{\mathrm{d}a(t)}{\mathrm{d}t}|\Psi(0)\rangle \\
&= -\kappa\langle\Psi(0)|a^\dagger(t)a(t)|\Psi(0)\rangle - 2\,\mathrm{IM}[\xi^*\langle\Psi(0)|\Phi_0^\dagger(t)a(t)|\Psi(0)\rangle] \\
&= -\kappa n(t),
\end{aligned}
$$

wherein in the last step we have used the fact that $\Phi_0(t)|0\rangle$ and $\langle 0|\Phi_0^\dagger(t) = 0$ since $b_\omega(0)|0\rangle = 0$ and $\langle 0|b_\omega^\dagger(0) = 0$. Therefore, $n(t) = n(0)\exp(-\kappa t)$, where $n(0) = \langle\Psi_0|a^\dagger a|\Psi_0\rangle$, reproducing the intuitively expected result that the number of photons in a lossy cavity exponentially decay with time.

Unlike the lossless cavity, the quantum state of a lossy cavity cannot be described by a pure state due to its interaction with the bath. Its state is more accurately captured by a density matrix $\rho(t)$, which in turn can be represented by its matrix elements $\rho_{m,n}(t)$ on the Fock state basis:

$$
(44) \qquad \rho(t) = \sum_{m,n} \rho_{m,n}(t)|m\rangle\langle n|.
$$

The time evolution of this density matrix obtained using the Lindblad master equation formalism (derived in appendix A) is given by the Lindblad master equation

$$
(45) \qquad \frac{\mathrm{d}\rho(t)}{\mathrm{d}t} = -\mathrm{i}[\omega_c a^\dagger a, \rho(t)] + \kappa a^\dagger \rho(t)a - \frac{\kappa}{2}\{\rho(t), a^\dagger a\},
$$

where $\{\cdot\}$ is the Poisson bracket ($\{A, B\} = AB + BA$). This differential equation is sufficient for completely characterizing the state of the cavity as a function of time.

2. – Light-matter interaction

In this section, we describe the fundamentals of light matter interaction — in particular, we will present a simple model for the light-matter interaction Hamiltonian, followed by an analysis of a two-level system coupling to an optical continuum. We will also describe the physics of interaction between a two-level system and an optical cavity, often called cavity quantum electrodynamics, and study the different coupling regimes that emerge in such systems.

2'1. *Interaction Hamiltonian*. – The full quantum electrodynamic Hamiltonian describing the interaction between optical modes and charges (such as electrons) is a rather complicated object — such an interaction was first described by Feynman in his seminal

work on quantum electrodynamics [7]. Adopting a microscopic approach to light-matter interaction, wherein we start from the physics of a single electron or hole interacting with optical modes, and then build up to a model of a collection of such charges (*e.g.* quantum dot) coherently interacting with optical modes, while possible, is rather complicated. An extremely good model of light-matter interaction can be obtained by treating the material system under consideration as a point dipole described by a Hermitian dipole moment operator which interacts with the electric field of the electromagnetic system.

To build up this model, consider a material system with eigenstates $|\sigma_1\rangle, |\sigma_2\rangle \ldots |\sigma_N\rangle$ — in the absence of an interaction with an optical field, these eigenstates describe possible states that the material system can perpetually be in. In the presence of interaction with an optical mode, however, there is the possibility of the system transitioning from one state to another. In general, depending on the physics of the material system, an optical mode can induce transitions between one or more pairs of states. Consider a situation where the optical mode induces a transition between a state $|e\rangle \in \{|\sigma_1\rangle, |\sigma_2\rangle \ldots |\sigma_N\rangle\}$ and a state $|g\rangle \in \{|\sigma_1\rangle, |\sigma_2\rangle \ldots |\sigma_N\rangle\}$, where we assume that the energy of $|e\rangle$ is $\hbar\omega_e$ larger than the energy of $|g\rangle$ (ω_e is often referred to as the resonant frequency of the optical transition). The Hamiltonian describing the evolution of these two states is given by

$$(46) \qquad H_{\text{matter}} = \omega_e |e\rangle \langle e| = \omega_e \sigma^\dagger \sigma,$$

where $\sigma = |g\rangle\langle e|$ is the de-excitation operator that transfers material system from the excited state $|e\rangle$ to the ground state $|g\rangle$.

The dipole-moment operator between these two transitions can then be described by three complex vectors $\boldsymbol{\mu}_{e,e}$, $\boldsymbol{\mu}_{g,g}$ and $\boldsymbol{\mu}_{e,g}$:

$$(47) \qquad \boldsymbol{\mu} = \boldsymbol{\mu}_{e,e} |e\rangle \langle e| + \boldsymbol{\mu}_{g,g} |g\rangle \langle g| + \boldsymbol{\mu}_{e,g} |e\rangle \langle g| + \boldsymbol{\mu}_{e,g}^* |g\rangle \langle e|.$$

For most systems of interest, it can be argued from the parity of $|e\rangle$ and $|g\rangle$ with respect to the dipole moment operator that $\boldsymbol{\mu}_{e,e} = \boldsymbol{\mu}_{g,g} = 0$, which simplifies eq. (47) to $\boldsymbol{\mu} = \boldsymbol{\mu}_{e,g}|e\rangle\langle g| + \boldsymbol{\mu}_{e,g}^*|g\rangle\langle e| = \boldsymbol{\mu}_{e,g}\sigma^\dagger + \boldsymbol{\mu}_{e,g}^*\sigma$. The vector $\boldsymbol{\mu}_{e,g}$ governs the strength of the dipole moment operator, and is often refered to as the "dipole moment" of the transition between the states $|e\rangle$ and $|g\rangle$.

Classically, the potential energy of interaction between a dipole moment $\boldsymbol{\mu}$ and an electric field $\mathbf{E}(\mathbf{x})$ is given by $-\boldsymbol{\mu} \cdot \mathbf{E}(\mathbf{x}_d)$, where $\mathbf{x}_d$ is the position of the dipole. It is therefore reasonable to posit that while describing this interaction in the language of quantum physics, the interaction Hamiltonian between the material system modelled as a dipole moment and an optical field with electric-field operator $\mathbf{E}(\mathbf{x}_d)$ is give by

$$(48) \qquad H_{\text{int}} = -\frac{\mathbf{E}(\mathbf{x}_d) \cdot \boldsymbol{\mu}}{\hbar}.$$

This interaction Hamiltonian provides us with a fairly general model for light-matter interaction, and is applicable to a wide variety of physical systems. To gain more insight

into the consequences of such an interaction Hamiltonian, it is useful to consider specific electromagnetic structures. For a single-mode optical cavity, using the electric-field expression in eq. (6) we obtain

$$(49) \qquad H_{\text{int}} = ga\sigma^{\dagger} + g^{*}\sigma a^{\dagger},$$

where g is the coupling strength between the cavity mode and the material system:

$$(50) \qquad g = -\left(\frac{\omega_c}{2\hbar\varepsilon_0 \mathcal{N}_c}\right)^{1/2} \boldsymbol{\mu}_{e,g} \cdot \mathbf{E}_c(\mathbf{x}_d).$$

Note that in eq. (53), we have ignored terms of the form $a\sigma$ and $a^{\dagger}\sigma^{\dagger}$ — an intuitive explanation for approximating away this terms is that they correspond to processes in which a photon is created and the atom as excited simultaneously (or its reverse), which have a high frequency contribution to the system dynamics and thus average out over the time scale of interest. This approximation is refered to as the "rotating" wave approximation [8], and is only valid in the regime in which the coupling constant g is much smaller than the frequencies ω_c and ω_e.

It is often convenient to define the mode volume V of the cavity mode, a dipole position factor $\mathcal{F}(\mathbf{x}_d)$ and a dipole orientation factor $\mathcal{O}(\mathbf{x}_d)$ via

$$(51) \qquad V = \frac{\mathcal{N}_c}{\max[\varepsilon(\mathbf{x})|\mathbf{E}(\mathbf{x})|^2]}, \qquad \mathcal{F}(\mathbf{x}_d) = \frac{|\mathbf{E}(\mathbf{x}_d)|}{\sqrt{\max[\varepsilon(\mathbf{x})|\mathbf{E}(\mathbf{x})|^2]}} \qquad \text{and}$$

$$\mathcal{O}(\mathbf{x}_d) = \frac{\boldsymbol{\mu}_{e,g} \cdot \mathbf{E}(\mathbf{x}_d)}{|\boldsymbol{\mu}_{e,g}||\mathbf{E}(\mathbf{x}_d)|},$$

in terms of which the coupling constant g can be expressed as

$$(52) \qquad g = -\left(\frac{\omega_c|\boldsymbol{\mu}_{e,g}|^2}{2\hbar\varepsilon_0}\right)^{1/2} \frac{\mathcal{F}(\mathbf{x}_d)\mathcal{O}(\mathbf{x}_d)}{\sqrt{V}}.$$

This expression for g makes clear the interplay between the different factors that affect the coupling between the material system and the cavity mode:

1) The mode volume V is a measure of how tightly confined the electromagnetic fields are inside the cavity mode — reducing this mode volume increases the coupling constant.

2) $\mathcal{F}(\mathbf{x}_d)$ is a measure of how large the cavity mode's electric field is at the location of the dipole as compared to other points in space — increasing this factor has a proportionate impact on the coupling constant.

3) $\mathcal{O}(\mathbf{x}_d)$ is a measure of the relative orientation of the dipole with respect to the cavity mode's electric field — for a large coupling constant, it is desired to orient the dipole along the cavity mode as much as possible.

Finally, the complete Hamiltonian describing the coupled light-matter system is described by

$$H = \omega_e \sigma^\dagger \sigma + \omega_c a^\dagger a + (ga\sigma^\dagger + g^* \sigma a^\dagger). \tag{53}$$

The Hamiltonian in eq. (53) is refered to as the Jaynes-Cummings Hamiltonian, and will be the subject of sect. **2**˙3.

A similar Hamiltonian can be written for the material system interacting with a continuum of optical modes, such as those of an optical waveguide. The general form of the interaction Hamiltonian in such a case under the rotating wave approximation is given by

$$H_{\text{int}} = \int_{-\infty}^{\infty} \left[\xi a_\omega \sigma^\dagger + \xi^* a_\omega^\dagger \sigma \right] \mathrm{d}\omega, \tag{54}$$

where a_ω is the annhilation operator for the mode at frequency ω and ξ is the coupling constant between the optical mode and the material system. Note that we have assumed that optical modes of all frequencies couple equally to the material system — this is termed as the "Markovian" approximation. Explicit expression for the coupling constant ξ can be obtained if the form of the optical modes are known — as an example, for a material system coupling to a forward-propagating waveguide mode, using eq. (24a), we obtain

$$\xi = -\left(\frac{\omega_e}{2\hbar\varepsilon_0 \mathcal{N}(\beta_e) v_G} \right)^{1/2} \boldsymbol{\mu}_{e,g} \cdot \mathbf{E}_{\beta_e}(\boldsymbol{\rho}), \tag{55}$$

wherein we have assumed the dipole to be located at $z = 0$, and at a position $\boldsymbol{\rho}_d$ in the transverse plane. Moreover, we have chosen ω_0 in eq. (24a) to be ω_e, since any excitation or emission of interest would be close to the resonant frequency of the optical transition. The total Hamiltonian of the coupled light-matter system is given by

$$H = \omega_e \sigma^\dagger \sigma + \int_{-\infty}^{\infty} \omega a_\omega^\dagger a_\omega \mathrm{d}\omega + \int_{-\infty}^{\infty} [\xi a_\omega \sigma^\dagger + \xi^* \sigma a_\omega^\dagger] \mathrm{d}\omega. \tag{56}$$

Finally, we note that while writing the above expressions, we have only considered one optical transition — in a number of material systems, there are multiple optical transitions. The light-matter interaction Hamiltonian in such systems can simply be expressed as a sum of interaction Hamiltonians for the different optical transitions, each of which can be formulated as described above.

2˙2. *Two-level systems interacting with an optical continuum*. – The earliest experimental investigations of light-matter interactions studied the response of material systems to free-space optical beams (*e.g.* light from lasers). Such experiments are naturally described within the framework of the material system interacting with a continuum of

optical modes. In this section, we consider such an interaction with the material system having a single optical transition (*i.e.* a two level system). We show that the interaction of a two-level system with a continuum of optical mode naturally gives rise to the phenomenon of spontaneous emission, which is an exponential decay in the excited-state probability of the system. Finally, we consider a coherently driven two-level system, *i.e.* a system that would correspond to the material system being excited with the optical field of a laser, and show that the interaction Hamiltonian described above naturally gives rise to the optical Bloch equations describing the emitter state.

Spontaneous emission: Consider a two-level system initially in its excited state, and the optical modes being in the vacuum state: $|\Psi(0)\rangle = |e\rangle|0\rangle$. At time t, the coupled system can evolve into a superposition of the two-level system being in the excited state with the optical field being in the vacuum state, and the two-level system being in the ground state with the optical field being in a single-photon state:

$$(57) \qquad |\Psi(t)\rangle = A_e(t) |e\rangle |0\rangle + \int_{-\infty}^{\infty} A_g(\omega, t) a_\omega^\dagger |g\rangle |0\rangle \, \mathrm{d}\omega,$$

where $A_e(0) = 1$ and $A_g(\omega, 0) = 0$. Using the Schrödinger equation with the Hamiltonian given in eq. (56), we obtain

$$(58a) \qquad \mathrm{i}\frac{\mathrm{d}A_e(t)}{\mathrm{d}t} = \omega_e A_e(t) + \xi \int_{-\infty}^{\infty} A_g(\omega, t)\mathrm{d}\omega,$$

$$(58b) \qquad \mathrm{i}\frac{\partial A_g(\omega, t)}{\partial t} = \omega A_g(\omega, t) + \xi^* A_e(t).$$

Equation (58b) can be integrated to obtain

$$(59) \qquad A_g(\omega, t) = -\mathrm{i}\xi^* \int_0^t A_e(\tau) \exp[-\mathrm{i}\omega(t - \tau)]\mathrm{d}\tau,$$

and therefore:

$$(60) \qquad \mathrm{i}\frac{\mathrm{d}A_e(t)}{\mathrm{d}t} = \left(\omega_e - \mathrm{i}\frac{\gamma}{2}\right)A_e(t),$$

where $\gamma = 2\pi|\xi|^2$ is the spontaneous emission decay rate of the two-level system into the optical continuum. The solution to the above equation is given by $A_e(t) = \exp(-\gamma t/2)\exp(-\mathrm{i}\omega_e t)$ — we thus see that the probability of the two-level system being in the excited state decays exponentially with time (fig. 1(a)) due to its interaction with the optical continuum. Moreover, using eq. (59), we can obtain $A_g(\omega, t)$:

$$(61) \qquad A_g(\omega, t) = -\mathrm{i}\xi^* \frac{\exp[\mathrm{i}(\omega - \omega_e)t]\exp(-\gamma t/2) - 1}{\mathrm{i}(\omega - \omega_e) - \gamma/2}.$$
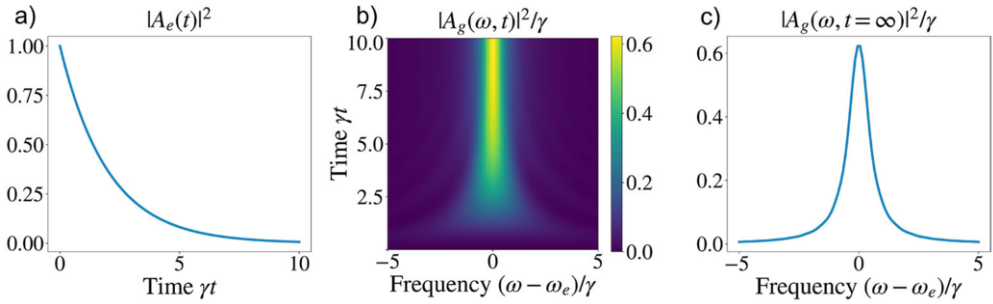
Fig. 1. – Spontaneous emission of a two-level system into a continuum of optical modes. (a) Excited-state probability as a function of time. (b) Evolution of the spectrum of the emitted single photon as a function of time during the spontaneous emission process. (c) The final Lorentizian spectrum of the emitted photon.

Figure 1(b) shows $|A_g(\omega, t)|^2/\gamma$ as a function of frequency ω and time t. Moreover, we see that as $t \to \infty$, the emitted single-photon pulse evolves into having a Lorentizian spectral lineshape (fig. 1(c)).

Coherently driven two-level systems: Next, we consider the interaction of a two-level system with a coherent state (*e.g.* from a laser source). Consider the system being prepared in an initial state $|\Psi(0)\rangle = |g\rangle|\alpha(\omega)\rangle = \mathcal{D}[\alpha(\omega)]|g\rangle|0\rangle$ where the optical mode is in a coherent state, and the two-level system in the ground state. It is more convenient to work with an equivalent state $|\Psi'(t)\rangle = \mathcal{D}^\dagger[\alpha(\omega)\exp(-\mathrm{i}\omega t)]|\Psi(t)\rangle$ which is related to the true system state $|\Psi'(t)\rangle$ via a unitary transformation (this transformation is referred to as Mollow transformation). Additionally, the equivalent state has the optical modes initially in the vacuum state: $|\Psi'(0)\rangle = |g\rangle|0\rangle$. Moreover, it can be shown that the state $|\Psi'(t)\rangle$ satisfies Schrödinger's equation with a Hamiltonian H' which is related to the light-matter interaction Hamiltonian (eq. (56)) via (refer to appendix B for a derivation of this result):

$$(62) \qquad\qquad H' = H + [\Omega(t)\sigma^\dagger + \Omega^*(t)\sigma],$$

where $\Omega(t)$ is given by:

$$(63) \qquad\qquad \Omega(t) = \xi \int \alpha(\omega)\exp(-\mathrm{i}\omega t)\mathrm{d}\omega.$$

Note that this is equivalent to using a time-dependent Hamiltonian for the system which has an additional "driving" term, $\Omega(t)\sigma^\dagger + \Omega^*(t)\sigma$, added to it which models the impact of the laser on the dynamics of the two-level system. The time-evolution of the two-level system state can now be analyzed within the master equation framework described in appendix A — the density matrix of the two-level system satisfies the following dynamical

equation:

$$(64) \qquad \frac{\mathrm{d}\rho(t)}{\mathrm{d}t} = -\mathrm{i}[\omega_e \sigma^\dagger \sigma + \Omega(t)\sigma^\dagger + \Omega^*(t)\sigma, \rho(t)] + \gamma\sigma\rho(t)\sigma^\dagger - \frac{\gamma}{2}\{\rho(t), \sigma^\dagger\sigma\}.$$

Expressing the density matrix in terms of its matrix elements, $\rho(t) = \rho_{e,e}(t)|e\rangle\langle e| + \rho_{e,g}(t)|e\rangle\langle g| + \rho_{e,g}^*|g\rangle\langle e| + (1 - \rho_{e,e}(t))|g\rangle\langle g|$, this dynamical equation can be explicitly written out as two coupled differential equations in $\rho_{e,e}(t)$ and $\rho_{e,g}(t)$:

$$(65a) \qquad \frac{\mathrm{d}\rho_{e,e}(t)}{\mathrm{d}t} = -\gamma\rho_{e,e}(t) - \mathrm{i}[\Omega(t)\rho_{e,g}^*(t) - \Omega^*(t)\rho_{e,g}(t)],$$

$$(65b) \qquad \frac{\mathrm{d}\rho_{e,g}(t)}{\mathrm{d}t} = -\mathrm{i}\omega_e\rho_{e,g}(t) - \frac{\gamma}{2}\rho_{e,g}(t) - \mathrm{i}\Omega(t)[1 - 2\rho_{e,e}(t)].$$

The above equations are often referred to as the optical Bloch equations — historically, these equations were first derived with a semi-classical model for the optical modes [9]. Such a semi-classical model, however, was unable to produce the decay terms in the optical Bloch equations, which needed to be added in phenomenologically. A quantum model of the optical modes, however, produces the decay terms naturally as a consequence of the modes existing as a continuum.

Several qualitative features of the behaviour of a two-level system with a coherent state can be deduced by solving the optical Bloch equations. Figure 2(a) shows the variation of the excited-state population $\rho_{e,e}(t)$ as a function of time t on excitation with a continuous-wave coherent state resonant with the two-level system $[\Omega(t) = \Omega_0 \exp(-\mathrm{i}\omega_e t)]$. In the limit of very small coupling between the two-level system and the optical mode ($\gamma \to 0$), we observe that the two-level system oscillates between the ground state and the excited state — this oscillations are referred to as Rabi oscillations. For $\gamma \neq 0$, we observe damped Rabi oscillations followed by the system settling to a steady state. Figure 2(b) shows the variation of the excited-state population $\rho_{e,e}(t)$ as a function of time t on excitation of the two-level system with a Gaussian pulse $\Omega(t) = \Omega_0 \exp(-t^2/\tau_p^2 - \mathrm{i}\omega_e t)$ — for a pulse longer than the life-time $1/\gamma$ of the two-level system, we observe some Rabi oscillations followed by a spontaneous emission decay of the emitter into the ground state. However, a pulse significantly shorter than the life-time $1/\gamma$ does not induce significant Rabi oscillations in the two-level system — instead, it initializes the two-level system into a superposition of the excited state and the ground state, followed by spontaneous emission of a single photon. The superposition of the excited and ground states obtained right after excitation by the pulse depends on the area under the pulse [10] — fig. 2(c) shows the dependence on the average number of emitted photons $E[n]$ as a function of the pulse area — we observe oscillations in the number of emitted photons with pulse area. This oscillations can be inuitively explained if we consider a two-level system without decay excited with a short pulse — fig. 2(c) also shows the steady-state excited-state population $\rho_{e,e}(\infty)$ obtained in such a system as a function of the pulse area. Clearly, excitation by a pulse with area π results in the two-level system being in the excited state, which in the presence of decay would result in the emission of a single photon with
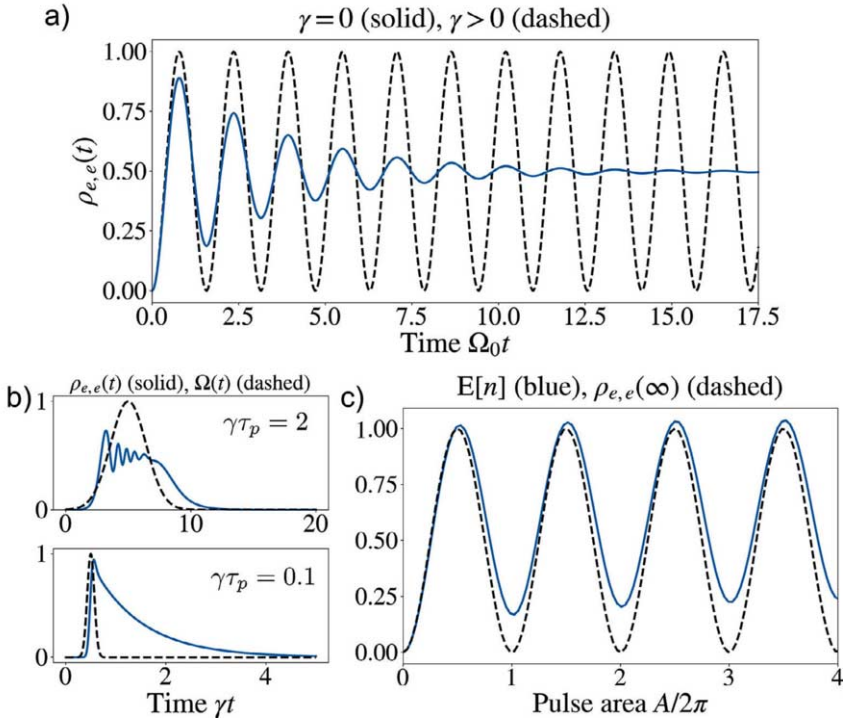
Fig. 2. – (a) Excited-state population ($\rho_{e,e}(t)$) in a two-level system resonantly driven by a continuous-wave laser: $\Omega(t) = \Omega_0 \exp(-i\omega_e t)$ in the presence and absence of decay. (b) Excited-state population ($\rho_{e,e}(t)$) in a two-level system as a function of time when resonantly driven with a Gaussian pulse $\Omega(t) = \Omega_0 \exp(-t^2/\tau_p^2 - i\omega_e t)$. (c) Average number of emitted photons $E[n]$ as well as the steady-state excited-state population $\rho_{e,e}(t \to \infty)$ for a two-level system without decay when excited with a short Gaussian pulse ($\gamma\tau_p = 0.1$) as a function of the pulse area $A = \sqrt{\pi}\Omega_0\tau_p$.

unit probability. This also forms the basis of most schemes for generating an on demand single photon using a pulsed laser. Note however, that $E[n]$ and $\rho_{e,e}(\infty)$ do not exactly coincide with each other — this is a consequence of the fact that the coupling of the two-level system to the optical modes also plays a role during the excitation process — in particular, it has been theoretically and experimentally shown that driving with a 2π pulse can induce emission of a two-photon state by the two-level system [11], as opposed to no emission as would be suggested by $\rho_{e,e}(\infty)$.

2'3. *Cavity quantum electrodynamics.* – Interaction of a two-level system with a discrete optical mode (such as the mode of an optical cavity) has significantly different features from the its interaction with a continuum of optical modes described in the previous section. In this section, we will describe the basic properties of a two-level system interacting with an optical cavity mode — the study of which is often called cavity quantum electrodynamics in quantum optics literature. We will first consider the simple case
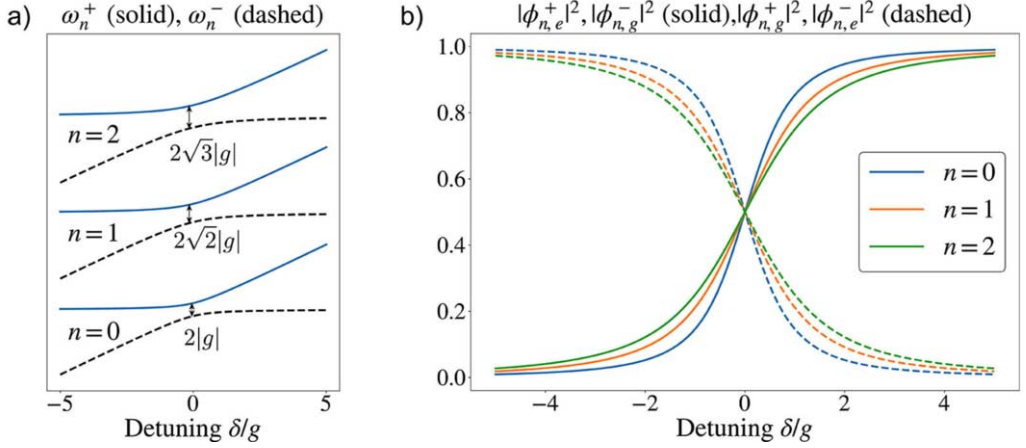
Fig. 3. – (a) Eigenfrequencies of the lossless Jaynes-Cummings system. (b) The projection of the eigenstates $|\phi_n^+\rangle$ and $|\phi_n^-\rangle$ on the subspaces with the two-level system being in the ground and excited state. In particular, $\phi_{n,e}^\pm = \langle e, n|\phi_n^\pm\rangle$ and $\phi_{n,g}^\pm = \langle g, n+1|\phi_{n+1}^\pm\rangle$.

of their being no losses in the cavity, and then analyze cavity quantum electrodynamics with a lossy cavity.

The interaction between a two-level system and a lossless cavity is described by the Hamiltonian in eq. (53). A lot of insight into the behaviour of this system can be gained from computing the eigenstates and eigenfrequencies of this Hamiltonian — this is a straightforward exercise, and the reader may verify that the eigenstates $|\phi_n^\pm\rangle$ and eigenfrequencies $\omega_n^\pm$ are given by (where $n \in \{0, 1, 2\ldots\}$):

$$(66\text{a}) \quad \omega_n^+ = (n+1)\omega_c + \delta + \Gamma_n, \; \left|\phi_n^+\right\rangle = \frac{(\delta + \Gamma_n)\,|e\rangle\,|n\rangle + g^*\sqrt{n+1}\,|g\rangle\,|n+1\rangle}{\sqrt{(\delta + \Gamma_n)^2 + (n+1)|g|^2}},$$

$$(66\text{b}) \quad \omega_n^- = (n+1)\omega_c + \delta - \Gamma_n, \; \left|\phi_n^-\right\rangle = \frac{g\sqrt{n+1}\,|e\rangle\,|n\rangle - (\delta + \Gamma_n)\,|g\rangle\,|n+1\rangle}{\sqrt{(\delta + \Gamma_n)^2 + (n+1)|g|^2}},$$

where $2\delta = \omega_e - \omega_c$ is the detuning between the two-level system and the cavity, and $\Gamma_n = \sqrt{\delta^2 + (n+1)|g|^2}$. Note that $n+1$ is the total number of excitations in the eigenstates $|\phi_n^\pm\rangle$ (*i.e.* the eigenstates either have $n+1$ photons in the cavity and the two-level system in the ground state, or n photons in the cavity and the two-level system in the excited state) — these eigensates are therefore often labelled as the $(n+1)$-excitation eigenstates. Figure 3(a) shows the eigenfrequencies as a function of the detuning δ — this dependence of the eigenfrequencies on the mismatch in resonance of the two interacting system is often referred to as an "anti-crossing". In particular, note that at $\delta = 0$ (*i.e.* both the systems oscillate at the same frequency), the eigenfrequencies are split by an amount proportional to the coupling strength $|g|$ — this splitting, called Rabi splitting, scales as $2|g|\sqrt{n+1}$ and is a direct consequence of the coupling between the

two systems. Moreover, as the detuning between the cavity and the two-level system becomes increasingly larger as compared to $|g|$, we note that the eigenfrequencies tend to $(n+1)\omega_c$ and $n\omega_c + \omega_e$ which are simply the eigenfrequencies of the uncoupled system. A similar impact of detuning on the coupling between the two systems can be observed from fig. 3(b), which shows the probability of finding the two-level system in the ground and excited state as a function of δ. It can be seen that at $\delta = 0$, it is equally likely for the two-level system to be in the ground and excited state — this corresponds to $|\phi_n^+\rangle$ and $|\phi_n^-\rangle$ being in an equal superposition of the states $|e\rangle|n\rangle$ and $|g\rangle|n+1\rangle$:

$$(67a) \qquad \left|\phi_n^+\right\rangle = \frac{|e\rangle\,|n\rangle + \exp(-\mathrm{i}\theta_g)\,|g\rangle\,|n+1\rangle}{\sqrt{2}}\,,$$

$$(67b) \qquad \left|\phi_n^-\right\rangle = \frac{\exp(\mathrm{i}\theta_g)\,|e\rangle\,|n\rangle - |g\rangle\,|n+1\rangle}{\sqrt{2}}\,,$$

where $\theta_g = \angle g$. As the detuning is increased, the eigenstates tend to $|e\rangle|n\rangle$ and $|g\rangle|n+1\rangle$, which are the uncoupled states of the cavity and the two-level system.

An immediate consequence of the anti-crossing in the eigenfrequencies of the Jaynes-Cummings system is a periodic exchange of energy between the cavity mode and the two-level atom if only one of them is initially excited. To see this, consider exciting the cavity with n photons at $t = 0$, with the emitter being in the ground state: $|\Psi(0)\rangle = |g\rangle|n\rangle$. Assuming that the cavity and the two-level system are resonant with each other, it follows from eq. (67) that

$$(68) \qquad |\Psi(0)\rangle = \frac{\exp(\mathrm{i}\theta_g)\left|\phi_{n-1}^+\right\rangle - \left|\phi_{n-1}^-\right\rangle}{\sqrt{2}}\,,$$

and since $|\phi_{n-1}^+\rangle$ and $|\phi_{n-1}^-\rangle$ are both eigenstates of the Hamiltonian,

$$(69) \qquad |\Psi(t)\rangle = \frac{\exp[\mathrm{i}(\theta_g - \omega_{n-1}^+ t)]|\phi_{n-1}^+\rangle - \exp(-\mathrm{i}\omega_{n-1}^+ t)|\phi_{n-1}^-\rangle}{\sqrt{2}}$$
$$= \cos(gt\sqrt{n})\,|g\rangle\,|n+1\rangle - \mathrm{i}\sin(gt\sqrt{n})\exp(-\mathrm{i}\theta_g)\,|e\rangle\,|n\rangle\,,$$

from which it is clear that the state of the coupled cavity two-level system oscillates between the ground and excited states with a frequency $2g\sqrt{n}$ which depends on the coupling strength between the cavity and the two-level system as well as the initial number of photons in the cavity. This oscillatory behaviour is in stark contrast with the case where the emitter is coupled to a continuum of modes (sect. **2**˙2), wherein the emitter irreversibly and exponentially decays into its ground state.

Experimentally realizable cQED systems often have losses in the cavity modes, which can have a significant impact on the properties of the system, in particular light emission from such systems. Assuming that the losses in the cavity mode are accurately captured by the model introduced in sect. **1**˙3, the spectrum of the light emitted and scattered
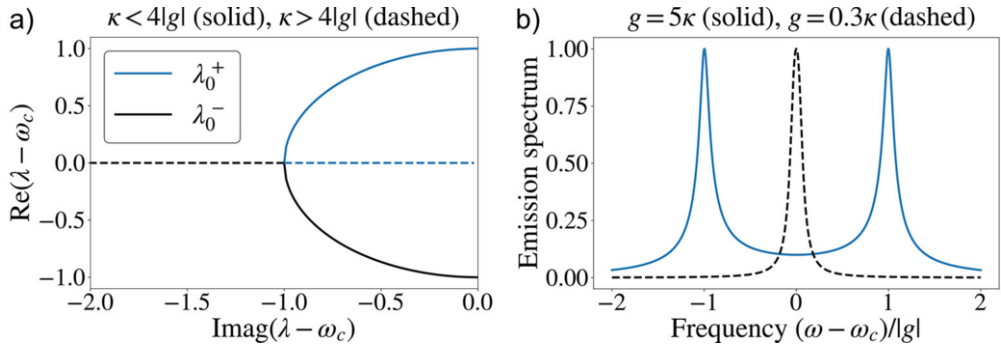
Fig. 4. – (a) Trajectory of the eigenvalues $\lambda_0^\pm$ of the effective Hamiltonian (eq. (70)) in the complex plane obtained on varying κ from 0 to ∞. (b) Emission spectrum of the Jaynes-Cummings system in the strong- and weak-coupling regimes. Refer to appendix for details on its computation.

from the system depends on the eigenstructure of a non-Hermitian effective Hamiltonian:

$$
(70) \qquad H_{\text{eff}} = H - \frac{\mathrm{i}\kappa}{2} a^\dagger a,
$$

where H is the Jaynes-Cummings Hamiltonian (eq. (53)) with a lossless cavity mode. Details of how this effective Hamiltonian comes about are beyond the scope of this paper — it is a consequence of applying the path integral formalism on calculating the propagator of the full system (*i.e.* the coupled system formed between two-level system, cavity mode and the bath), and integrating out the bath's degrees of freedom. The interested and theoretically inclined reader may refer to [12, 13] for more details. Note that since H_{eff} is non-Hermitian, its eigenvalues are complex — their real part indicates approximately the central frequencies of the peaks in the system's emission spectrum, and their imaginary part indicates the linewidth of these peaks. Note that H_{eff} has the same form as the Hamiltonian in eq. (53) with ω_c replaced by $\omega_c - \mathrm{i}\kappa/2$ — therefore, the eigenvalues $\lambda_n^\pm$ of H_{eff} are given by eq. (66) with ω_c being replaced by $\omega_c - \mathrm{i}\kappa/2$. Figure 4(a) shows the trajectory of the $\lambda_0^\pm$ in the complex plane on varying the cavity decay rate κ from 0 to ∞ and assuming the cavity and the two-level system to be resonant with each other. We note that there are two regimes of the lossy Jaynes-Cummings system — the strong coupling regime ($\kappa < 4|g|$, shown with solid lines) wherein the two eigenvalues have the same imaginary part and different real parts and the weak coupling regime ($\kappa > 4|g|$, shown in dashed lines) wherein the two eigenvalues have the same real part and different imaginary parts. Consequently, in the strong coupling regime, emission from the Jaynes-Cummings system (fig. 4(b)) has a spectrum that shows two distinct peaks (corresponding to the distinct real parts of $\lambda_0^\pm$) with the same linewidth, whereas the emission spectrum in the weak coupling regime shows only one broad peak. As noted above, for a lossless Jaynes-Cummings system, an emitter initally in the excited state would periodically exchange energy with the cavity mode as opposed to decaying

exponentially. A similar oscillation in the probability of the two-level system being in the excited state $P_e(t)$ can be observed in a lossy Jaynes-Cummings system when the coupling constant $|g|$ is much larger than the decay rate κ of the cavity (*i.e.* the system is strongly coupled) — this shown in fig. 5(a): $P_e(t)$ shows (damped) Rabi oscillations whose frequency is $\approx 2g$. When the cavity decay rate κ dominates (*i.e.* the system is weakly coupled), the two-level system decays almost exponentially to its ground state (fig. 5(a)). The decay rate of two-level system's excited state is approximately given by (refer to appendix C for a derivation):

$$(71) \qquad\qquad \gamma \approx \frac{|g|^2 \kappa}{(\omega_e - \omega_c)^2 + \kappa^2/4} \,.$$

Note that this expression indicates that it is possible to engineer the decay rate of the two-level system by engineering the cavity that it couples to. γ is maximized when the emitter is on resonance with the cavity ($\omega_e = \omega_c$) — in this case, $\gamma \approx 4|g|^2/\kappa$. Since $|g| \sim 1/\sqrt{V}$ (where V is the mode volume of the cavity as defined in eqs. (51) and (52)), and $\kappa \sim 1/Q$, where Q is the quality factor of the cavity mode, $\gamma \sim Q/V$. Therefore, coupling a two-level system to a high-Q and low-V cavity can enhance its emission — this effect is referred to as Purcell enhancement [14], and the enhancement of the decay rate of the two-level system relative to its decay rate in vacuum is often termed as Purcell factor.

Note that a lossless Jaynes-Cummings Hamiltonian has eigenfrequencies that are not equally spaced *i.e.* it has an anharmonic eigenspectrum. This anharmonicity gives rise to the phenomenon of photon blockade and photon tunnelling, which are pictorially depicted in fig. 5(b). Consider exciting a Jaynes-Cummings system (with no detuning between the cavity and the two-level system) with a coherent state — a coherent state has excitations of arbitrary numbers (eq. (36)), and thus it simultaneously tries to address all the excitation subspaces of the Jaynes-Cummings Hamiltonian. If the frequency of the coherent state is tuned to the frequency of the single-excitation eigenstates ($\omega_0^\pm = \omega_c \pm g$), then only the single-photon component of the incident coherent state is resonant with the Jaynes-Cummings system, and all the higher-photon component are off-resonance. This would result in a large transmission of the single-photon component of the incident state, and a low transmission for all other components. This is depicted in fig. 5(b) — clearly, P_1 (probability of finding a single photon in the output state) peaks near the frequency of the single-excitation eigenstates and P_2 (probability of finding two photons in the output state) is suppressed at the same frequency. This phenomena is referred to as *photon blockade*, since it blocks that transmission of all but the single-photon components of the input coherent state. In a strongly coupled Jaynes-Cummings system, photon blockade could be used for the implementation of an on-demand single-photon source.

Similarly, if we choose the frequency of the coherent state to be resonant with half the eigenfrequency of the two-excitation subspace ($\omega_1^\pm/2 = \omega_c \pm |g|/\sqrt{2}$), then a large transmission of the two-photon component of the incident coherent state is expected, along with a suppression of the single photon (and $\geq$ three-photon) component. This is referred to as *photon tunneling*, since the two photons are transmitted together, as
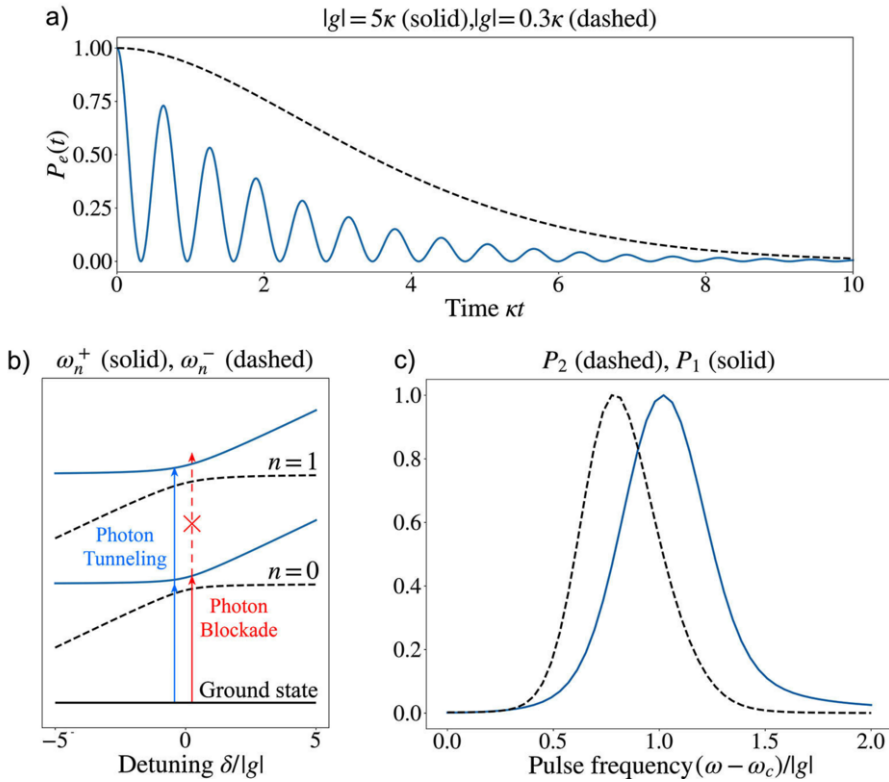
Fig. 5. – (a) Decay of energy from an excited two-level system in a lossy Jaynes-Cummings system. $P_e(t)$ is the probability that the two-level system is in excited state at time t. (b) Schematic depiction of photon blockade and photon tunneling. (c) Probability of emission of one photon (P_1) and two photons (P_2) as a function of the central frequency of an incident coherent pulse. Note that both P_1 and P_2 are respectively normalized to their maximum value.

opposed to one after the other. This is confirmed by noting that P_2 peaks near half the frequency of the two-excitation subspace, while P_1 is suppressed (fig. 5(c)). Theoretically, we would expect a similar tunneling effect in the higher photon components of the incident coherent state if the frequency of the incident coherent state is chosen appropriately — it is, however, experimentally challenging to measure and characterize $>$ two-photon states.

3. – Single-photon sources

Coupling optical modes to two-level systems, with or without a cavity, offers an excellent platform to implement sources of nonclassical light. While there is a wide variety of nonclassical light sources that are useful for different applications in quantum information processing, quantum computing and quantum metrology, perhaps the most important nonclassical light source would be a single-photon source. In this section, we
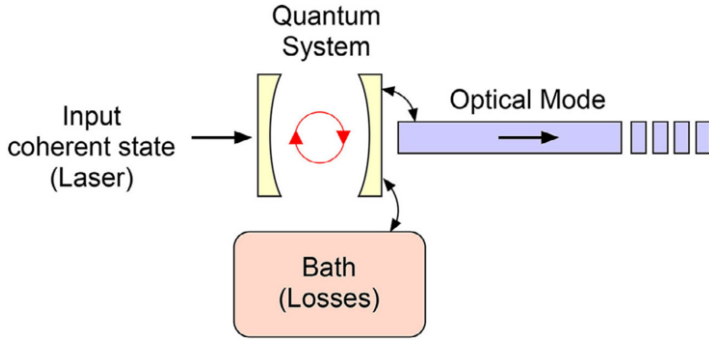
Fig. 6. – A general block diagram of a single-photon source. A quantum system (two-level system, Jaynes-Cummings system) is driven by a laser pulse and coupled to an output optical mode in which it emits photons.

will introduce the definition of a single-photon source, relevant metrics for its quality as well as the two-time correlation measurement which is a widely used experimental tool for characterizing single-photon sources.

3˙1. *Characterizing the quality of single-photon sources.* – A general block diagram of a single-photon source is shown in fig. 6 — a quantum system (*e.g.* a two-level system, or a Jaynes-Cummings system) designed to emit single photons emits light into an optical mode (*e.g.* waveguide mode or an optical-fiber mode) which then feeds the generated single photon into a quantum information processing system. In practice, the quantum system may suffer from other losses, which is modelled as another bath. An ideal single-photon source would emit the following state of light into the coupled optical mode:

$$(72) \qquad |\Psi\rangle = \int_{-\infty}^{\infty} \psi(\omega) b_\omega^\dagger \, |\text{vac}\rangle \, \mathrm{d}\omega,$$

where b_ω is the annihilation operator for frequency ω of the output optical mode, and $\psi(\omega)$ is the complex frequency-domain amplitude of the single-photon source, and would satisfy the normalization condition

$$(73) \qquad \int_{-\infty}^{\infty} |\psi(\omega)|^2 \mathrm{d}\omega = 1.$$

Practical single-photon sources, however, may not emit a single photon with unity probability. Additionally, the presence of loss mechanisms would result in the state of the optical waveguide being a mixed state. A more realistic state of a single photon in the output waveguide can be expressed as the following density matrix:

$$(74) \qquad \rho = P_0 \, |0\rangle \, \langle 0| + P_1 \rho^{(1)} + \rho^{(\chi)},$$

where P_1 is the probability of single-photon emission into the output optical mode, $P_0 = 1 - P_1$ is the probability of no photon emission. The density matrix within the single-photon subspace $\rho^{(1)}$ as well as the off-diagonal density matrix between the vacuum state and the single-photon subspace $\rho^{(\chi)}$ is defined by

$$\text{(75a)} \qquad \rho^{(1)} = \int \rho^{(1)}(\omega_1, \omega_2) b^{\dagger}_{\omega_1} |\text{vac}\rangle \langle \text{vac}| \, b_{\omega_2} \mathrm{d}\omega_1 \mathrm{d}\omega_2,$$

$$\text{(75b)} \qquad \rho^{(\chi)} = \int \left[\rho^{(\chi)}(\omega) b^{\dagger}_{\omega} |0\rangle \langle 0| \, \mathrm{d}\omega + \rho^{(\chi)*}(\omega) |0\rangle \langle 0| \, b_{\omega} \mathrm{d}\omega \right].$$

In writing these expressions, we have assumed the normalization condition that the trace of $\rho^{(1)}(\omega_1, \omega_2)$ is 1:

$$\text{(76)} \qquad \int \rho^{(1)}(\omega, \omega) \mathrm{d}\omega = 1.$$

Note that in expressing the state of the single-photon source as eq. (74), we have assumed that the source does not emit any higher number states (such as two-photon or three-photon states). If desired, emission of higher number states can be incorporated into the density matrix by adding terms corresponding to the two-photon subspace of the optical mode's Hilbert space.

Two metrics quantifying the deviation of the single-photon source (eq. (74)) from an ideal single-photon source (eq. (72)) can now be defined:

1) *Brightness*: The brightness of a single-photon source is defined as the number of "single" photons that the source emits. In terms of the density matrix, this is given by its trace within the single-photon subspace:

$$\text{(77)} \qquad n = \int \langle 0| \, a_{\omega} \rho a^{\dagger}_{\omega} |0\rangle \, \mathrm{d}\omega = P_1 \int \rho^{(1)}(\omega, \omega) \mathrm{d}\omega = P_1.$$

It is also useful to define the spectral brightness of the source as the diagonal elements of the single-photon components of the density matrix, which can be interpreted as the number of single photons emitted per unit frequency:

$$\text{(78)} \qquad n(\omega) = \langle 0| \, a_{\omega} \rho a^{\dagger}_{\omega} |0\rangle = P_1 \rho^{(1)}(\omega, \omega).$$

An ideal single-photon source would have $n = P_1 = 1$, thus exclusively emitting single photons.

2) *Trace purity*: The trace purity is a measure of how pure the quantum state is. For an ideal single-photon state (eq. (72)), the density matrix is simply an outer product of the state with itself $\rho = |\Psi\rangle\langle\Psi|$ (or equivalently, $P_0 = 0$, $P_1 = 1$, $\rho^{(\chi)}(\omega) = 0$ and $\rho^{(1)}(\omega_1, \omega_2) = \psi^*(\omega_1)\psi(\omega_2)$). Therefore, for a pure state, $\text{Tr}(\rho^2) = \text{Tr}(\rho) = 1$. For a

mixed state, it can be shown using a schmidth decomposition that $\text{Tr}(\rho^2) < 1$ [15]. Therefore, it is reasonable to define this quantity as the trace purity:

$$(79) \qquad\qquad \text{Trace purity} = \text{Tr}(\rho^2).$$

The brightness of a single-photon source can be experimentally estimated by simply measuring the number of photo-detection counts from a single-photon source. However, a direct measurement of the number of photo-detection counts cannot distinguish between the number of single photons emitted by the source, as compared to the number of two- or three-photon states emitted by the source. Additionally, measuring the trace purity of the emitted single photons also requires a more experimentally sophisticated setup in which we can interfere two identical single-photon sources with each other. The next subsection goes into the details of two-photon correlation measurement, which forms the basis of a number of experimental setups used for such characterization of single-photon sources.

3‘2. *Two-time correlation measurements*. – Consider a source emitting at $z = 0$ into an optical mode, with spatial-domain annihilation operator b_z, propagating along the z-axis. The unnormalized two-time correlation function at a detector placed at $z = L$ is defined as the following Heisenberg-picture expectation:

$$(80) \qquad G^{(2)}(t_1, t_2) = \langle b_{z=L}^\dagger(t_1) b_{z=L}^\dagger(t_2) b_{z=L}(t_1) b_{z=L}(t_2) \rangle.$$

It is often more convenient to work with a normalized version of the two-time correlation function:

$$(81) \qquad g^{(2)}(t_1, t_2) = \frac{\langle b_{z=L}^\dagger(t_1) b_{z=L}^\dagger(t_2) b_{z=L}(t_1) b_{z=L}(t_2) \rangle}{\langle b_{z=L}^\dagger(t_1) b_{z=L}(t_1) \rangle \langle b_{z=L}^\dagger(t_2) b_{z=L}(t_2) \rangle}.$$

Moreover, in experimental settings, the photodetectors being used often has a response time that is much larger than the temporal width of the light being emitted by the source. This practical limitation prohibits an exact measurement of the $g^{(2)}(t_1, t_2)$ as a function of (t_1, t_2) (or equivalently as a function of the photon arrival times), and the quantity being measured is the integrated two-time correlation function $g^{(2)}[0]$ [16]:

$$(82) \qquad g^{(2)}[0] = \frac{1}{N^2} \int_{-\infty}^{\infty} \int_{-\infty}^{\infty} G^{(2)}(t_1, t_2) \mathrm{d}t_1 \mathrm{d}t_2,$$

where N is the expectation value of the number of photons in the emitted light:

$$(83) \qquad N = \int_{-\infty}^{\infty} \langle b_{z=L}^\dagger(t) b_{z=L}(t) \rangle \mathrm{d}t.$$

Both $g^{(2)}(t_1, t_2)$ and $g^{(2)}[0]$ have remarkably different values for different states of light, making it a suitable tool for characterizing the state of light emitted by a light source:

1) If the light emitted contains at most single photons (pure or mixed), then $g^{(2)}(t_1, t_2) = g^{(2)}[0] = 0$. A small value of $g^{(2)}[0]$ is therefore often treated as an experimental signature of having a good-quality single-photon state.

2) For light emitted from an ideal coherent source (eq. (36)), $g^{(2)}(t_1, t_2) = g^{(2)}[0] = 1$ (this straightforwardly follows from the fact that the coherent state is an eigenstate of the annhilation operator).

3) For an arbitrary N photon state (eq. (29)), it can be easily be verified that

$$(84) \qquad g^{(2)}[0] = 1 - \frac{1}{N} \, .$$

Clearly, increasing the number of photons in the optical mode increases $g^{(2)}[0]$, which tends to 1 as $N \to \infty$.

Hanbury-Brown-Twiss interferometer: A popular experimental setup used for measurement of the two-time correlation function is the Hanbury-Brown-Twiss interferometer (fig. 7(a)). The output of the photon source is passed through a 50-50 beam splitter, with two separate detectors placed at the outputs of the waveguides. A correlation measurement between the two detectors would then be captured by the following two-photon correlation function:

$$(85) \qquad g^{(2)}_{\mathrm{HBT}}(t_1, t_2) = \frac{\mathrm{E}_\varphi[\langle a^\dagger_{z=L}(t_1) b^\dagger_{z=L}(t_2) b_{z=L}(t_2) a_{z=L}(t_1)\rangle]}{\mathrm{E}_\varphi[\langle a^\dagger_{z=L}(t_1) a_{z=L}(t_1)\rangle] \mathrm{E}_\varphi[\langle b^\dagger_{z=L}(t_2) b_{z=L}(t_2)\rangle]} \, ,$$

and its integrated version:

$$(86) \qquad g^{(2)}_{\mathrm{HBT}}[0] = \frac{1}{N_a N_b} \int_{-\infty}^{\infty} \int_{-\infty}^{\infty} \mathrm{E}_\varphi[\langle a^\dagger_{z=L}(t_1) c^\dagger_{z=L}(t_2) c_{z=L}(t_2) a_{z=L}(t_1)\rangle] \mathrm{d}t_1 \mathrm{d}t_2,$$

where

$$(87) \qquad N_a = \int_{-\infty}^{\infty} \mathrm{E}_\varphi[\langle a^\dagger_{z=L}(t) a_{z=L}(t)\rangle] \mathrm{d}t, \quad N_b = \int_{-\infty}^{\infty} \mathrm{E}_\varphi[\langle b^\dagger_{z=L}(t) b_{z=L}(t)\rangle] \mathrm{d}t,$$

where $\mathrm{E}_\varphi[\cdot]$ is an average over the phase φ of the beam-splitter. This averaging is necessary to include in the theoretical expressions for the two-time correlation since in a practical experiment, the phase difference between the two interferometer arms is random and changes during the course of the experiment (due to heating or other environmental effects). As is shown in appendix D, these correlation functions are identical to the correlation function defined in eqs. (81) and (82) and therefore directly inform us of the properties of the light fed as input to the interferometer. Experimentally, this correlation is measured using the start-stop scheme. Consider exciting the interferometer with a photon source — we first wait for the detector D_1 to click, followed by a click at the
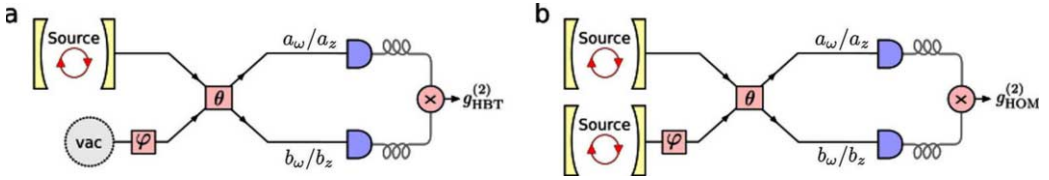
Fig. 7. – Schematic of (a) Hanbury-Brown-Twiss (HBT) interferometer and (b) Hong-Ou-Mandel (HOM) interferometer. In both setups, $\theta = \pi/4$ and φ is a random variable that models the variation in phase-difference in between the two arms in the course of the experiment.

detector D_2. The result of this experiment is a record of the time-difference τ between the two click. This experiment is repeated to obtain similar measurements for τ — a histogram of τ would then give the estimate of the probability of detecting a photon at detector D_2 conditioned on the probability of detection at D_1 which would be a measure of the following integrated two-time correlation function:

$$(88) \qquad G^{(2)}_{\text{HBT}}(\tau) = \int \text{E}_\varphi[\langle a^\dagger_{z=L}(t) b^\dagger_{z=L}(t+\tau) b_{z=L}(t+\tau) a_{z=L}(t)\rangle]\mathrm{d}t.$$

Typically, $G^{(2)}(\tau)$ tends to saturate to a finite value as $\tau \to \infty$ — at this point the two photons being measured at the two detectors are approximately uncorrelated, and hence $G^{(2)}(\tau)$ simplifies to a measure of the product of the detector efficiencies and the transmission of the HBT setup. Consequently, we could normalize the experimental measurement of $G^{(2)}(\tau)$ to its value at $\tau \to \infty$:

$$(89) \qquad g^{(2)}_{\text{HBT}}(\tau) = \frac{G^{(2)}(\tau)}{\lim_{\tau \to \infty} G^{(2)}(\tau)}.$$

Hong-Ou-Mandel interferometer: In addition to characterizing the quality of the single-photon source itself, which can be done with a $g^{(2)}$ measurement, another important aspect of the single-photon source is its indistinguishability, *i.e.* if two single-photon sources are designed and fabricated using the same process, is the emission from the two single-photon sources identical. This question can be experimentally answered by interfering the two single-photon sources using a Hong-Ou-Mandel (HOM) interferometer (fig. 7(b)), which is the same setup as the HBT interferometer, but with the two single-photon sources in its two arms. The measured correlation functions are again give by

$$(90) \qquad g^{(2)}_{\text{HOM}}(t_1, t_2) = \frac{\text{E}_\varphi[\langle a^\dagger_{z=L}(t_1) b^\dagger_{z=L}(t_2) b_{z=L}(t_2) a_{z=L}(t_1)\rangle]}{\text{E}_\varphi[\langle a^\dagger_{z=L}(t_1) a_{z=L}(t_1)\rangle]\text{E}_\varphi[\langle b^\dagger_{z=L}(t_2) b_{z=L}(t_2)\rangle]},$$

and its integrated version:

$$(91) \qquad g^{(2)}_{\text{HOM}}[0] = \frac{1}{N_a N_b} \int_{-\infty}^{\infty} \int_{-\infty}^{\infty} \text{E}_\varphi[\langle a^\dagger_{z=L}(t_1) b^\dagger_{z=L}(t_2) b_{z=L}(t_2) a_{z=L}(t_1)\rangle]\mathrm{d}t_1 \mathrm{d}t_2,$$

where

$$(92) \qquad N_a = \int_{-\infty}^{\infty} \mathrm{E}_\varphi[\langle a_{z=L}^\dagger(t)a_{z=L}(t)\rangle]\mathrm{d}t, \qquad N_b = \int_{-\infty}^{\infty} \mathrm{E}_\varphi[\langle b_{z=L}^\dagger(t)b_{z=L}(t)\rangle]\mathrm{d}t.$$

For a general single-photon source with density matrix given by eq. (74), it is straightforward to show that $g_{\mathrm{HOM}}^{(2)}[0]$ evaluates to (refer to appendix D for a derivation):

$$(93) \qquad g_{\mathrm{HOM}}^{(2)}[0] = \frac{2P_{1,a}P_{1,b}}{(P_{1,a}+P_{1,b})^2}\left[1 - \int_{-\infty}^{\infty}\int_{-\infty}^{\infty} \rho_a^{(1)*}(\omega_1,\omega_2)\rho_b^{(1)}(\omega_1,\omega_2)\mathrm{d}\omega_1\mathrm{d}\omega_2\right].$$

From this expression, it can be deduced that measurement of $g_{\mathrm{HOM}}^{(2)}[0]$ provides information about how pure the emitted single-photon states are and how well the complex spectrum of the two single photons overlap. To see this concretely, consider two limiting cases:

1) *Both sources emit pure single-photon states*: In this case, the density matrix factorizes $\rho^{(1)}(\omega_1,\omega_2) = \psi^{(1)*}(\omega_1)\psi^{(1)}(\omega_2)$:

$$(94) \qquad g_{\mathrm{HOM}}^{(2)}[0] = \frac{2P_{1,a}P_{2,a}}{(P_{1,a}+P_{2,a})^2}\left[1 - \left|\int_{-\infty}^{\infty}\psi^{(1)*}(\omega)\mathrm{d}\omega\right|^2\right],$$

from which it can clearly be seen that $g_{\mathrm{HOM}}^{(2)}[0] = 0$ indicates that the two sources have identical complex spectras. $g_{\mathrm{HOM}}^{(2)}[0]$ then provides information about how distinguishable the two single-photon sources are.

2) *Both sources are identical but not pure*: Assuming that the two photons are identical and emitted with unity probability (*i.e.* $P_1 = 1$), $g_{\mathrm{HOM}}^{(2)}[0]$ simplifies to

$$(95) \qquad g_{\mathrm{HOM}}^{(2)}[0] = \frac{1}{2}\left[1 - \int_{-\infty}^{\infty}|\rho^{(1)}(\omega_1,\omega_2)|^2\mathrm{d}\omega_1\mathrm{d}\omega_2\right] = \frac{1 - \mathrm{Tr}[\rho^2]}{2}.$$

From this expression, it is immediately obvious that the $g_{\mathrm{HOM}}^{(2)}[0]$ is a measure of trace purity $\mathrm{Tr}[\rho^2]$ — if $g_{\mathrm{HOM}}^{(2)}[0]$ is small, then the emitted photons are nearly in a pure state, else they are in a mixed state.

3$\cdot$**3.** *Solid-state implementation of single-photon sources.* – This section describes two solid-state platforms that can be used to realize the two-level systems that can interact with well defined optical modes, and behave as sources of nonclassical light. We will first discuss quantum dots, which are islands of small band-gap semiconductors trapped inside a large band-gap semiconductors, followed by color centers, which are formed by creating defects in a crystal lattice.
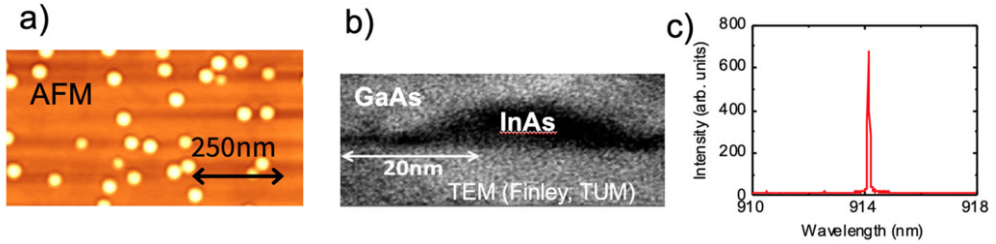
Fig. 8. – (a) An atomic-force microscope (AFM) scan of the InAs quantum dots before capping with GaAs layer. (b) Cross sectional transmission electron miscroscpe (TEM) image of a capped quantum dot. (c) A typical photoluminescence spectrum of a quantum dot, showing single, narrow emission line.

3'3.1. Quantum dots. Semiconductor quantum dots (QD) are small regions of one semiconductor embedded in a different semiconductor [17]. The most common, InAs/GaAs, QDs are inclusions of InAs in a GaAs matrix. Owing to the difference in the bandgaps of the two materials, a QD forms a potential well, which admits a handful of localized electron and hole states. The level structure of QDs can be well understood through the "particle in a finite potential well" problem. The Hamiltonian for a quantum dot can be written as: $H = H_e + H_h + H_c$, where H_e, H_h are the bound electron and hole Hamiltonians, respectively, in a potential determined by the geometrical shape and of the QD and the band-gap mismatch of the dot and its host semiconductor; H_c is the Coulomb interaction. In the case of a neutral QD, containing and electron-hole pair, H_e and H_h each have a single particle form, and H_c consists of a single term for the electron-hole Coulomb interaction. For a negatively charged QD with two electrons and one hole, electron-electron Coulomb interaction, dependent on the excitation state of each electron, needs to be considered.

Typically, QDs are several 10's of nanometers in size, as seen in fig. 8(a) and (b). Most commonly, InAs/GaAs QDs are grown by strain-driven self-assembly via molecular beam epitaxy (MBE) or metalorganic chemical vapor deposition (MOCVD). The spontaneous growth nature of QDs results in a dots randomly positioned on the substrate and varying substantially in size. Naturally, variation in the QD size results in spectral variation between different QDs.

Quantum dots are excellent single-photon sources because of their relatively short optical lifetime (0.1–1 ns); narrow optical emission, seen in fig. 8(c); and near-unity quantum efficiency, which means that the decay from the excited state to the ground state is almost always accompanied by the emission of a photon. We can observe the nonclassical nature of the light emitted by a quantum dot by measuring the second order autocorrelation function, $g^{(2)}(\tau)$, in the Hanbury Brown and Twiss configuration, discussed earlier in the paper. Experimental observation of antibunching, a signature of a nonclassical light source, is shown in fig. 9. Under pulsed excitation, perfect antibunching manifests itself as the absence of a peak at zero time delay, signifying that every pulse carries at most one photon. Experimental noise (presence of other sources of light in addition to the
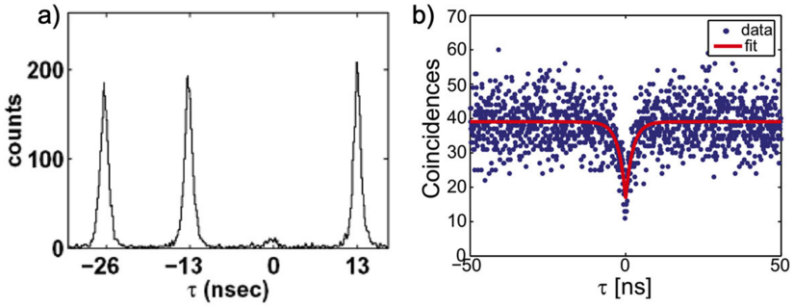
Fig. 9. – Antibunching observed in photon emission from a quantum dot that is not coupled to a cavity, for (a) pulsed excitation, (b) continuous-wave excitation [18].

QD that can be excited by the laser pulse) prevent $g^{(2)}(0)$ from reaching the levels of background noise. Under continuous-wave excitation, we see that the experimental data matches well to the theoretical prediction for $g^{(2)}(\tau)$ for a two-level system. The width of this dip corresponds to the optical lifetime of the QD in the weak-drive limit.

The large dipole moment of a QD allows it to interact strongly with light: Thus, a QD is an excellent choice for demonstrating strong coupling between a two-level system and a nanophotonic cavity. In order to reach the strong coupling regime, $g > \kappa/4 \gg \gamma$, a QD must be placed in a photonic resonator whose mode interacts strongly with the dipole moment of the QD. Since the QD is much flatter than it is wide, it has a strong in-plane dipole moment and a much weaker out-of-plane dipole moment: Thus, the QD will couple well to the TE mode of an L3 photonic crystal cavity, which has a low mode volume and
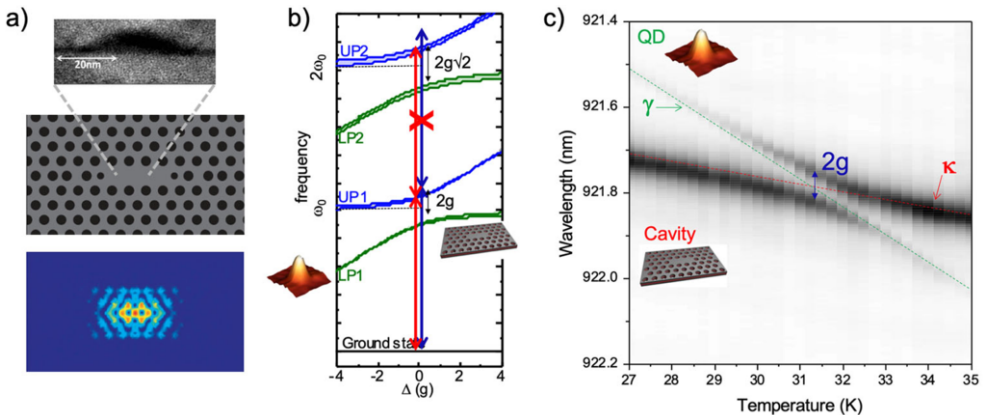
Fig. 10. – (a) The QD-cavity system: A InAs/GaAs quantum dot situated inside an L3 photonic crystal cavity. The simulated cavity mode profile is plotted. (b) The Jaynes-Cummings ladder for the QD-cavity system, showing the anharmonicity that enables photon-blocade (c) Experimentally measured strong coupling between a QD and a L3 photonic crystal cavity. A clear anti-crossing of the upper and lower polaritons is observed [19].
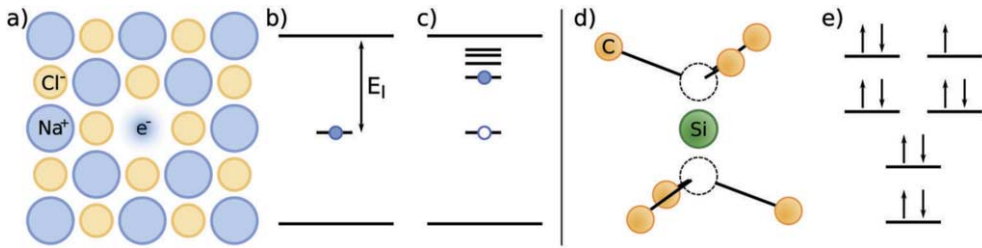
Fig. 11. – (a) Diagram of an F-center in NaCl. (b) The F-center ground state: A trapped electron. (c) The excited state: An electron-hole pair has eigenstates similar to that of a hydrogen atom with a modified effective mass and charge. (d) Diagram of a Silicon Vacancy (SiV^-) in diamond. The 10 bound valence electrons contributed by the carbon atoms and the silicon atom, as well as an additional electron acquired from the environment, form a 11-electron state, shown in (e).

a high experimentally achievable quality-factor. Experimental demonstration of strong coupling is shown in fig. 10. The tuning is achieved by sweeping the temperature of the sample, enabled by the different response of the cavity resonance and the QD frequency to temperature change. A clear anti-crossing is seen at the temperature at which the cavity and QD frequencies align.

3˙3.2. *Color centers*. Color centers — atomic point defects in crystals — have been studied for almost a century, but only recently were the particularly interesting color centers in Diamond and Silicon Carbide discovered and found to be promising for applications in single-photon sources and optically-addressable qubits. Fundamentally, the nature of state confinement in color centers is different from that of QDs. Whereas a QD can be modeled as an electron trapped in a classical, macroscopic potential, a color center rather resembles a single optically-addressable atom, well-isolated from the environment. The possibility of existence of bound states at a crystal lattice defect is made intuitive from the perspective of the Bloch theorem, which states that a periodic potential admits a continuum of propagating, nonscattering electronic states; when translational symmetry is broken, a bound state can form. However, in order for a defect to be a "color center", it must admit at least two bound states that have an allowed optical transitions between them in the visible or IR frequency. This restricts suitable candidate materials to those with a large bandgap.

The first studied color centers are single-atom defects in an ionic crystal (referred to as F-centers, for German *fabre*); An example of an F-center is a missing chlorine atom in a crystal of table salt, NaCl (fig. 11(a)–(c)). Upon removal of a sodium atom, the vacancy is filled with an electron from the environment, and the state has a binding energy of E_I. The set of bound states can be viewed as hydrogen-atom-like single electron states, where the electron is orbiting around a hole "nucleus" [20].

In order to gain an understanding of the electronic structure of more complex color centers, such as the Silicon Vacancy center in diamond (SiV^-), one can use the linear combination of atomic orbitals (LCAO) method. Each of the six carbon atoms con-
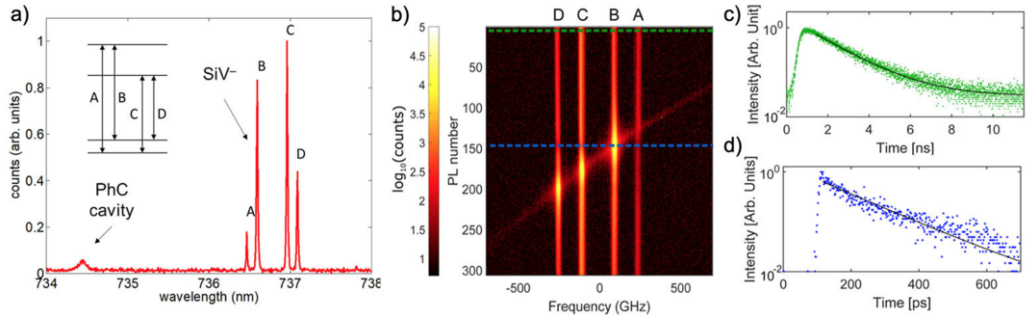
Fig. 12. – (a) Spectrum of the SiV$^-$ at 4 K, with an inset showing the level structure from which the four transitions, (denoted A, B, C and D) arise. (b) Tuning the cavity through the four transitions selectively enhances them, which can be seen as large increase in the photon emission rates. Measurement of the emitter lifetime on and off resonance is shown in (c) and (d). Lifetime reduction of 10 times is observed.

tributes one sp^3-hybridized orbital, and we assume that the interstitial Si modifies these orbitals slightly and contributes its valence electrons to them. Thus, we have six orbitals and $6 + 4 + 1$ electrons, from the C atoms, the Si atom, and the environment, respectively. This system can thus be equivalently modeled as a 1-hole system. Using group theoretical analysis based on the crystal symmetry of the defect, one can understand the color center's orbital degeneracy [21]. In the case of the SiV$^-$, the group theory analysis arrives at two nondegenerate orbitals and two pairs of degenerate orbitals, as seen in fig. 11(e).

The electronic transitions of color centers like the SiV$^-$ have a weaker dipole moment than the quantum dots discussed in previous section. Furthermore, the dipole of the SiV$^-$ (and many others) is at 45 degrees relative to that of the TE (or TM) cavity mode. As a result of these factors, strong coupling between a color center and a photonic crystal cavity has not yet been achieved. However, unlike quantum dots, color centers can have very long (millisecond) ground state spin coherence times. Making use of this new degree of freedom with which to store quantum information and to perform quantum operations does not require strong coupling of the optical transition; a large cooperativity is already sufficient for high-fidelity operation. Figure 12 shows the enhancement of a single SiV$^-$ emitter by a photonic crystal cavity, demonstrating 42-fold increase of photon detection enabled by the emitter-cavity interaction [22].

APPENDIX A.

Lindblad master equation

In this appendix, we present a derivation of the Lindblad master equation which can be used for studying the evolution of quantum systems coupling to a continuum of harmonic oscillators. The Hamiltonian for such a coupled system can be written as

the sum of the system Hamiltonian H_{sys}, the Hamiltonian of the harmonic oscillator continuum and an interaction Hamiltonian between the two:

$$(A.1) \qquad H = H_{\text{sys}} + \int_{-\infty}^{\infty} \omega a_\omega^\dagger a_\omega \mathrm{d}\omega + \int (\xi a_\omega L^\dagger + \xi^* L a_\omega^\dagger)\mathrm{d}\omega,$$

where L is the operator which describes the coupling between the system and the bath modes, and ξ is the coupling constant between them. a_ω is the annihilation operator for the bath mode at frequency ω and satisfies the commutator $[a_\omega, a_{\omega'}^\dagger] = \delta(\omega - \omega')$. Both the Hamiltonian for a lossy cavity (sect. **1**˙3), as well as the Hamiltonian describing the interaction of a continuum of optical modes with a two-level system (sect. **2**˙2) can be expressed in this form.

We consider a situation where the quantum system is initialized in the state $|\Psi_{\text{sys}}\rangle$ and the bath in the vacuum state $|0\rangle$: $|\Psi(0)\rangle = |\Psi_{\text{sys}}\rangle|0\rangle$. The state of the coupled system at time t is then given by $|\Psi(t)\rangle = \exp(-\mathrm{i}Ht)|\Psi(0)\rangle$. It is of interest to us to only calculate the dynamics of the state, which is described by a time-dependent density operator $\rho(t)$:

$$(A.2) \qquad \rho(t) = \text{Tr}_{\text{bath}}[|\Psi(t)\rangle\langle\Psi(t)|] = \text{Tr}_{\text{bath}}[\exp(-\mathrm{i}Ht)|\Psi(0)\rangle\langle\Psi(0)|\exp(\mathrm{i}Ht)].$$

To derive a dynamical equation for $\rho(t)$, we use the following simple property that it must satisfy: if Ω is an operator defined on the Hilbert space of the system, and $\bar{\Omega}(t)$ be its expectation value as a function of time, then $\bar{\Omega}(t) = \text{Tr}_{\text{sys}}[\Omega\rho(t)]$ and therefore:

$$(A.3) \qquad \frac{\mathrm{d}\bar{\Omega}(t)}{\mathrm{d}t} = \text{Tr}_{\text{sys}}\left[\Omega\frac{\mathrm{d}\rho(t)}{\mathrm{d}t}\right].$$

Alternatively, we could attempt to compute $\bar{\Omega}(t)$, and consequently its time derivative, in the Heisenberg picture. The Heisenberg equation of motion for the operator $\Omega(t)$ is given by

$$(A.4) \qquad \frac{\mathrm{d}\Omega(t)}{\mathrm{d}t} = -\mathrm{i}[\Omega(t), H_{\text{sys}}(t)] - \mathrm{i}\xi[\Omega(t), L^\dagger(t)]\Phi(t) - \mathrm{i}\xi^* \Phi^\dagger(t)[\Omega(t), L(t)],$$

where

$$(A.5) \qquad \Phi(t) = \int_{-\infty}^{\infty} a_\omega(t)\mathrm{d}\omega.$$

Note that we annotate any Heisenberg operator by writing it as a function of time (*i.e.* $\Omega(t)$ is the Heisenberg operator corresponding to the Schrödinger operator Ω) except for the density matrix which is a function of time in the Schrödinger picture. Moreover, we assume that the Heisenberg and Schrödinger picture coincide at $t = 0$ (*i.e.* $\Omega(0) = \Omega$). Similarly, the Heisenberg equation of motion for $a_\omega(t)$ is given by

$$(A.6) \qquad \frac{\mathrm{d}a_\omega(t)}{\mathrm{d}t} = -\mathrm{i}\omega a_\omega(t) - \mathrm{i}\xi^* L(t).$$

Equation (A.6) can be integrated to obtain

(A.7)
$$a_\omega(t) = a_\omega(0)\exp(-\mathrm{i}\omega t) - \mathrm{i}\xi^* \int_0^t L(\tau)\exp[-\mathrm{i}\omega(t-\tau)]\mathrm{d}\tau.$$

From which it immediately follows that

(A.8)
$$\Phi(t) = \int_{-\infty}^\infty a_\omega(t)\mathrm{d}\omega = \Phi_0(t) - \mathrm{i}\pi\xi^* L(t),$$

where

(A.9)
$$\Phi_0(t) = \int_{-\infty}^\infty a_\omega(0)\exp(-\mathrm{i}\omega t)\mathrm{d}\omega = \int_{-\infty}^\infty a_\omega \exp(-\mathrm{i}\omega t)\mathrm{d}\omega.$$

Note that since $\Phi_0(t)$ depends only on the Schrödinger picture operator a_ω, it annhilates $|0\rangle$: $\Phi_0(t)|0\rangle = 0$. Using eqs. (A.4) and (A.8), we obtain

(A.10)
$$\frac{\mathrm{d}\Omega(t)}{\mathrm{d}t} = -\mathrm{i}[\Omega(t), H_{\mathrm{sys}}(t)] - \mathrm{i}\xi[\Omega(t), L^\dagger(t)](\Phi_0(t) - \mathrm{i}\pi\xi^* L(t))$$
$$-\mathrm{i}\xi^*(\Phi_0^\dagger(t) + \mathrm{i}\pi\xi L^\dagger(t))[\Omega(t), L(t)].$$

Note that $\bar\Omega(t) = \langle\Psi(0)|\Omega(t)|\Psi(0)\rangle$ (in the Heisenberg picture, the quantum state of the system does not change). Therefore:

(A.11)
$$\frac{\mathrm{d}\bar\Omega(t)}{\mathrm{d}t} = -\mathrm{i}\,\langle\Psi(0)|\,[\Omega(t), H_{\mathrm{sys}}(t)]\,|\Psi(0)\rangle$$
$$-\pi|\xi|^2\,\langle\Psi(0)|\,[\Omega(t), L^\dagger(t)]L(t)\,|\Psi(0)\rangle + \pi|\xi|^2\,\langle\Psi(0)|\,L^\dagger(t)[\Omega(t), L(t)]\,|\Psi(0)\rangle,$$

wherein we have used the fact that $\Phi_0(t)|\Psi(0)\rangle = \Phi_0(t)|\Psi_0\rangle|0\rangle = 0$. Moreover, it is easy to see that

(A.12a)
$$\langle\Psi(0)|\,[\Omega(t), H_{\mathrm{sys}}(t)]\,|\Psi(0)\rangle =$$
$$\mathrm{Tr}[(\Omega(t)H_{\mathrm{sys}}(t) - H_{\mathrm{sys}}(t)\Omega(t))\,|\Psi(0)\rangle\,\langle\Psi(0)|] =$$
$$\mathrm{Tr}[\exp(\mathrm{i}Ht)(\Omega H_{\mathrm{sys}} - H_{\mathrm{sys}}\Omega)\exp(-\mathrm{i}Ht)\,|\Psi(0)\rangle\,\langle\Psi(0)|] =$$
$$\mathrm{Tr}[(\Omega H_{\mathrm{sys}} - H_{\mathrm{sys}}\Omega)\exp(-\mathrm{i}Ht)\,|\Psi(0)\rangle\,\langle\Psi(0)|\exp(\mathrm{i}Ht)] =$$
$$\mathrm{Tr}_{\mathrm{sys}}[(\Omega H_{\mathrm{sys}} - H_{\mathrm{sys}}\Omega)\rho_{\mathrm{sys}}(t)] =$$
$$\mathrm{Tr}_{\mathrm{sys}}[\Omega[H_{\mathrm{sys}}, \rho_{\mathrm{sys}}(t)]],$$

(A.12b)
$$\langle\Psi(0)|\,[\Omega(t), L^\dagger(t)]L(t)\,|\Psi(0)\rangle =$$
$$\mathrm{Tr}[(\Omega(t)L^\dagger(t) - L^\dagger(t)\Omega(t))L(t)\,|\Psi(0)\rangle\,\langle\Psi(0)|] =$$
$$\mathrm{Tr}[\exp(\mathrm{i}Ht)(\Omega L^\dagger - L^\dagger\Omega)L\exp(-\mathrm{i}Ht)\,|\Psi(0)\rangle\,\langle\Psi(0)|] =$$
$$\mathrm{Tr}[(\Omega L^\dagger - L^\dagger\Omega)L\exp(-\mathrm{i}Ht)\,|\Psi(0)\rangle\,\langle\Psi(0)|\exp(\mathrm{i}Ht)] =$$
$$\mathrm{Tr}_{\mathrm{sys}}[(\Omega L^\dagger - L^\dagger\Omega)L\rho_{\mathrm{sys}}(t)] =$$
$$\mathrm{Tr}_{\mathrm{sys}}[\Omega L^\dagger L\rho_{\mathrm{sys}}(t)] - \mathrm{Tr}_{\mathrm{sys}}[\Omega L\rho_{\mathrm{sys}}(t)L^\dagger],$$

(A.12c)
$$\langle\Psi(0)|\,L^\dagger(t)[\Omega(t),L(t)]\,|\Psi(0)\rangle =$$
$$\mathrm{Tr}[L^\dagger(t)(\Omega(t)L(t)-L(t)\Omega(t))\,|\Psi(0)\rangle\,\langle\Psi(0)|] =$$
$$\mathrm{Tr}[\exp(\mathrm{i}Ht)L^\dagger(\Omega L - L\Omega)\exp(-\mathrm{i}Ht)\,|\Psi(0)\rangle\,\langle\Psi(0)|] =$$
$$\mathrm{Tr}[L^\dagger(\Omega L - L\Omega)\exp(-\mathrm{i}Ht)\,|\Psi(0)\rangle\,\langle\Psi(0)|\exp(\mathrm{i}Ht)] =$$
$$\mathrm{Tr}_{\mathrm{sys}}[L^\dagger(\Omega L - L\Omega)\rho_{\mathrm{sys}}(t)] =$$
$$\mathrm{Tr}_{\mathrm{sys}}[\Omega L\rho_{\mathrm{sys}}(t)L^\dagger] - \mathrm{Tr}_{\mathrm{sys}}[\Omega L^\dagger L\rho_{\mathrm{sys}}(t)].$$

In the above calculation, we have used the fact that if A is an operator in the Hilbert space of the quantum system, then

(A.13)
$$\mathrm{Tr}[A\exp(-\mathrm{i}Ht)\,|\Psi(0)\rangle\,\langle\Psi(0)|\exp(\mathrm{i}Ht)]$$
$$= \mathrm{Tr}_{\mathrm{sys}}[A\,\mathrm{Tr}_{\mathrm{bath}}[\exp(-\mathrm{i}Ht)\,|\Psi(0)\rangle\,\langle\Psi(0)|\exp(\mathrm{i}Ht)]]$$
$$= \mathrm{Tr}_{\mathrm{sys}}[A\rho_{\mathrm{sys}}(t)].$$

Using eqs. (A.11) and (A.12), we obtain

(A.14)
$$\frac{\mathrm{d}\bar{\Omega}(t)}{\mathrm{d}t} = \mathrm{Tr}_{\mathrm{sys}}[\Omega\mathcal{L}\rho_{\mathrm{sys}}(t)],$$

where

(A.15)
$$\mathcal{L}\rho_{\mathrm{sys}}(t) = -\mathrm{i}[H_{\mathrm{sys}},\rho_{\mathrm{sys}}(t)] + \kappa L\rho_{\mathrm{sys}}(t)L^\dagger - \frac{\kappa}{2}\{\rho_{\mathrm{sys}}(t),L^\dagger L\},$$

where $\{\cdot,\cdot\}$ is the anti-commutator between two operators. Finally, since eqs. (A.3) and (A.14) hold for an arbitrary system operator Ω, it follows that $\rho_{\mathrm{sys}}(t)$ satisfies the following dynamical equation:

(A.16)
$$\frac{\mathrm{d}\rho_{\mathrm{sys}}(t)}{\mathrm{d}t} = \mathcal{L}\rho_{\mathrm{sys}}(t) = -\mathrm{i}[H_{\mathrm{sys}},\rho_{\mathrm{sys}}(t)] + \kappa L^\dagger\rho_{\mathrm{sys}}(t)L - \frac{\kappa}{2}\{\rho_{\mathrm{sys}}(t),L^\dagger L\}.$$

Equation (A.16) is the Lindblad master equation that governs the time evolution of the density matrix of the system. As a final comment, we note that the derivation provided here differs from the ones in standard quantum optics or open quantum systems text in the fact that it does not assume that the density matrix of the coupled system factorizes into the density matrix of the system and the bath at every instant of time t.

APPENDIX B.

Mollow transformation

Often, a classical laser pulse is incident on a quantum system, causing it to undergo transitions between its various levels and then re-emit the absorbed energy. The classical laser can be described as the bath coupling to the quantum system initially being in the

coherent state. For such systems, we cannot directly apply the Lindblad master equation formalism described in appendix A since it assumes the bath to be in the vacuum state. In this appendix we describe a unitary transformation on the state of the system, called the Mollow transformation, that transforms the problem to one in which the bath is in the vacuum state.

Consider a system with Hamiltonian H_S coupled to a bath described by a continuum of harmonic oscillators with mode annihilation operator a_ω. The complete system can be modeled by

$$(B.1) \qquad H = H_\mathrm{S} + \int_{-\infty}^{\infty} \omega a_\omega^\dagger a_\omega \mathrm{d}\omega + \int_{-\infty}^{\infty} \mathrm{d}\omega \left(\xi a_\omega L^\dagger + \xi^* L a_\omega^\dagger \right),$$

where ξ is the coupling constant between the bath and the quantum system, and the system coupled to the bath through the operator L. The initial state of the coherently driven system corresponds to $t = 0$

$$(B.2) \qquad |\Psi(t = 0)\rangle = \mathcal{D}[\alpha(\omega)]|\Psi_\mathrm{S}\rangle|0\rangle,$$

where $\mathcal{D}[\alpha(\omega)] = \exp(\int_{-\infty}^{\infty} (\alpha(\omega) a_\omega^\dagger - \alpha^*(\omega) a_\omega) \mathrm{d}\omega)$ is the displacement operator creating a coherent state in the waveguide. We define a transformed state $|\Psi'(t)\rangle$ via

$$(B.3) \qquad |\Psi'(t)\rangle = \mathcal{D}_t^\dagger[\alpha(\omega)]|\Psi(t)\rangle$$

where

$$(B.4) \qquad \mathcal{D}_t[\alpha(\omega)] = \exp\left[\int_{-\infty}^{\infty} \mathrm{d}\omega \left(\alpha(\omega) \exp(-\mathrm{i}\omega t) a_\omega^\dagger - \alpha^*(\omega) \exp(\mathrm{i}\omega t) a_\omega \right) \right].$$

The time evolution of the state $|\tilde{\psi}(t)\rangle$ can be computed by differentiating eq. (B.3) to obtain an effective Hamiltonian

$$(B.5) \qquad H'(t) = \mathcal{D}_t^\dagger[\alpha(\omega)] H \mathcal{D}_t[\alpha(\omega)] + \mathrm{i}\frac{\mathrm{d}}{\mathrm{d}t} \mathcal{D}_t^\dagger[\alpha(\omega)]\mathcal{D}_t[\alpha(\omega)],$$

$$\text{with} \quad \mathrm{i}\frac{\mathrm{d}}{\mathrm{d}t}|\Psi'(t)\rangle = H'(t)|\Psi'(t)\rangle.$$

We next compute the effective Hamiltonian $H'(t)$ using eq. (B.1). In particular, it follows from the identities $\mathcal{D}^\dagger[\alpha(\omega)] a_\omega \mathcal{D}[\alpha(\omega)] = a_\omega + \alpha(\omega)$ and $\mathcal{D}^\dagger[\alpha(\omega)] a_\omega^\dagger \mathcal{D}[\alpha(\omega)] = a_\omega^\dagger + \alpha^*(\omega)$ that

$$(B.6) \quad \mathcal{D}_t^\dagger[\alpha(\omega)] H \mathcal{D}_t[\alpha(\omega)] = H_S + \left(\xi \alpha(t) L^\dagger + \xi^* \alpha^*(t) L \right) + \int_{-\infty}^{\infty} \mathrm{d}\omega \omega a_\omega^\dagger a_\omega$$

$$+ \int_{-\infty}^{\infty} \mathrm{d}\omega \omega |\alpha(\omega)|^2 + \int_{-\infty}^{\infty} \mathrm{d}\omega \omega \left(a_\omega \alpha^*(\omega) \exp(\mathrm{i}\omega t) \right.$$

$$\left. + a_\omega^\dagger \alpha(\omega) \exp(-\mathrm{i}\omega t) \right) + \int_{-\infty}^{\infty} \mathrm{d}\omega \left(\xi L^\dagger a_\omega + \xi^* a_\omega^\dagger L \right),$$

where $\alpha(t) = \int_{-\infty}^{\infty} \exp(-\mathrm{i}\omega t)\alpha(\omega)\mathrm{d}\omega/\sqrt{2\pi}$.

Now, we need to compute $\mathrm{d}\mathcal{D}_t^\dagger[\alpha(\omega)]/\mathrm{d}t$ — since $\mathcal{D}_t[\alpha(\omega)]$ is the exponential of a time-dependent operator, this requires some care. Consider the problem of computing the derivative of an exponential of a time-dependent operator $A(t) = \exp(\phi(t))$, with the property that $[\phi(t), \mathrm{d}\phi(t)/\mathrm{d}t] = \zeta(t)$, with $\zeta(t)$ being a scalar. The derivative of $A(t)$ can be computed as

$$(\text{B.7}) \qquad \frac{\mathrm{d}A(t)}{\mathrm{d}t} = \lim_{\delta t \to 0} \frac{\exp(\phi(t+\delta t)) - \exp(\phi(t))}{\delta t}.$$

Using the Baker-Campbell-Hausdorff equality it follows that

$$(\text{B.8}) \qquad \exp(\phi(t+\delta t)) \approx \exp\left(\phi(t) + \delta t \frac{d\phi(t)}{dt}\right)$$

$$= \exp(\phi(t)) \exp\left(\delta t \frac{\mathrm{d}\phi(t)}{\mathrm{d}t}\right) \exp(-\delta t\, \zeta(t)/2),$$

resulting in

$$(\text{B.9}) \qquad \frac{\mathrm{d}A(t)}{\mathrm{d}t} = \exp(\phi(t))\left(\frac{\mathrm{d}\phi(t)}{\mathrm{d}t} - \frac{\zeta(t)}{2}\right).$$

Specializing this result to: $A(t) = \mathcal{D}_t^\dagger[\alpha(\omega)]$ with $\phi(t) = \int_{-\infty}^\infty \mathrm{d}\omega(\alpha^*(\omega)\exp(\mathrm{i}\omega t)a_\omega - \alpha(\omega)\exp(-\mathrm{i}\omega t)a_\omega^\dagger)$ and $\zeta(t) = 2\mathrm{i}\int_{-\infty}^\infty \mathrm{d}\omega\omega|\alpha(\omega)|^2$ then

$$(\text{B.10}) \qquad \frac{\mathrm{d}\mathcal{D}_t^\dagger[\alpha(\omega)]}{\mathrm{d}t} = \mathrm{i}\mathcal{D}_t^\dagger[\alpha(\omega)]\left(\int_{-\infty}^\infty \mathrm{d}\omega\omega\,(\alpha^*(\omega)a_\omega \exp(\mathrm{i}\omega t)\right.$$

$$\left. + \alpha(\omega)a_\omega^\dagger \exp(-\mathrm{i}\omega t)) - \int_{-\infty}^\infty \mathrm{d}\omega\omega|\alpha(\omega)|^2\right),$$

with which we obtain

$$(\text{B.11}) \qquad \frac{\mathrm{d}\mathcal{D}_t^\dagger[\alpha(\omega)]}{\mathrm{d}t}\mathcal{D}_t[\alpha(\omega)] = \mathrm{i}\int_{-\infty}^\infty \mathrm{d}\omega\omega\,(\alpha^*(\omega)a_\omega \exp(\mathrm{i}\omega t) + \alpha(\omega)a_\omega^\dagger \exp(-\mathrm{i}\omega t))$$

$$+ \int_{-\infty}^\infty \mathrm{d}\omega\omega|\alpha(\omega)|^2.$$

Putting together eqs. (B.5), (B.6) and (B.11)

$$(\text{B.12}) \qquad H'(t) = H'_\mathrm{S}(t) + \int_{-\infty}^\infty \omega a_\omega^\dagger a_\omega \mathrm{d}\omega + \int_{-\infty}^\infty \mathrm{d}\omega\left(\xi L^\dagger a_\omega + \xi^* a_\omega^\dagger L\right),$$

where

$$(\text{B.13}) \qquad H'_\mathrm{S}(t) = H_S + \left(\xi\alpha(t)L^\dagger + \xi^*\alpha^*(t)L^\dagger\right)$$

is the system Hamiltonian with an effective classical driving field added to it.

APPENDIX C.

Decay of a two-level system into a lossy cavity mode

In this appendix, we consider the problem of analyzing photon emission from a two-level system into a lossy cavity mode. We consider a Jaynes-Cummings Hamiltonian (eq. (53)), with the cavity mode coupling to a bath (continuum of harmonic oscillators (eq. (37))) — the full Hamiltonian of this system is given by

$$(C.1) \qquad H = \omega_c a^\dagger a + \omega_e \sigma^\dagger \sigma + g a \sigma^\dagger + g^* \sigma a^\dagger + \int_{-\infty}^{\infty} \omega b_\omega^\dagger b_\omega \mathrm{d}\omega + \int_{-\infty}^{\infty} [\xi b_\omega a^\dagger + \xi^* a b_\omega^\dagger] \mathrm{d}\omega.$$

where a is the annihilation operator of the cavity, σ is the de-excitation operator for the two-level system and b_ω is the annihilation operator for the bath mode at frequency ω. We initialize the two-level system in the excited state and the cavity and the bath to the vacuum state: $|\Psi(0)\rangle = |e\rangle |0\rangle |0\rangle$. The state of the coupled system at time t can be written as

$$(C.2) \qquad |\Psi(t)\rangle = A_e(t) |e\rangle |0\rangle |0\rangle + A_c(t) |g\rangle |1\rangle |0\rangle + \int_{-\infty}^{\infty} B(\omega, t) b_\omega^\dagger |g\rangle |0\rangle |0\rangle \, \mathrm{d}\omega,$$

wherein we have expressed the state as a linear combination of states where the excitation is either in the two-level system, cavity or the bath. Next, using Schrödinger's equation with the Hamiltlonian given in eq. (C.1), we obtain:

$$(C.3a) \qquad \mathrm{i}\frac{\mathrm{d}A_e(t)}{\mathrm{d}t} = \omega_e A_e(t) + g A_c(t),$$

$$(C.3b) \qquad \mathrm{i}\frac{\mathrm{d}A_c(t)}{\mathrm{d}t} = \omega_c A_c(t) + g^* A_e(t) + \xi \int_{-\infty}^{\infty} B(\omega, t) \mathrm{d}\omega,$$

$$(C.3c) \qquad \mathrm{i}\frac{\partial B(\omega, t)}{\partial t} = \omega B(\omega, t) + \xi^* A_c(t),$$

where the initial conditions are $A_e(0) = 1, A_c(0) = 0$ and $B(\omega, 0) = 0$. Integrating eq. (C.3c), we obtain

$$(C.4) \qquad B(\omega, t) = -\mathrm{i}\xi^* \int_0^t A_c(t) \exp[-\mathrm{i}\omega(t - \tau)] \mathrm{d}\tau.$$

Substituting this into eq. (C.3b), we obtain

$$(C.5) \qquad \mathrm{i}\frac{\mathrm{d}A_c(t)}{\mathrm{d}t} = \omega_c A_c(t) + g^* A_e(t) - \frac{\mathrm{i}\kappa}{2} A_c(t),$$

where $\kappa = 2\pi|\xi|^2$ is the cavity decay rate. Equations (C.3a) and (C.3b) can be solved together to obtain $A_e(t)$ as a function of time. It is most convenient to do this using the

Laplace transform technique — let $f(s)$ be the one-sided Laplace transform of a function $f(t)$:

$$(C.6) \qquad f(s) = \int_0^\infty f(t) \exp(-st)\mathrm{d}t,$$

then it immediately follows that the one-sided Laplace transform of $\mathrm{d}f(t)/\mathrm{d}t$ is $sf(s) - f(0)$. Performing a one-sided Laplace transform on eqs. (C.3a) and (C.3b), we obtain

$$(C.7a) \qquad sA_e(s) - 1 = -\mathrm{i}\omega_e A_e(s) - \mathrm{i}g A_c(s),$$

$$(C.7b) \qquad sA_c(s) = -\mathrm{i}\omega_c A_c(s) + g^* A_e(s) - \frac{\mathrm{i}\kappa}{2} A_c(s),$$

which can be solved simultaneously to obtain

$$(C.8a) \qquad A_e(s) = \frac{s + \mathrm{i}\omega_c + \kappa/2}{s^2 + \{\mathrm{i}(\omega_e + \omega_c) + \kappa/2\}s + |g|^2 - \omega_e(\omega_c - \mathrm{i}\kappa/2)} \,,$$

$$(C.8b) \qquad A_c(s) = \frac{-\mathrm{i}g^*}{s^2 + \{\mathrm{i}(\omega_e + \omega_c) + \kappa/2\}s + |g|^2 - \omega_e(\omega_c - \mathrm{i}\kappa/2)} \,.$$

We can now compute the inverse laplace transform of $A_e(s)$ to obtain $A_e(t)$:

$$(C.9) \qquad A_e(t) = \left(\frac{\lambda_0^+ - \mathrm{i}\omega_c - \kappa/2}{\lambda_0^+ - \lambda_0^-} \right) \exp(-\mathrm{i}\lambda_0^+ t) - \left(\frac{\lambda_0^- - \mathrm{i}\omega_c - \kappa/2}{\lambda_0^- - \lambda_0^+} \right) \exp(-\mathrm{i}\lambda_0^- t),$$

where $\lambda_0^\pm$ are the single-excitation eigenfrequencies of the effective Hamiltonian (eq. (70)), which are explicitly given by

$$(C.10) \qquad \lambda_0^\pm = \omega_c + \delta - \frac{\mathrm{i}\kappa}{4} \pm \left[\left(\delta - \frac{\mathrm{i}\kappa}{4} \right)^2 + |g|^2 \right]^{1/2},$$

where $2\delta = \omega_e - \omega_c$. Note that in the limit of κ going to 0, $\lambda_0^\pm$ become completely real and the solution for $A_e(t)$ no longer exponentially decays with time. Note that in the limit of $\kappa \gg |g|$, $\lambda_0^\pm$ can be approximated by

$$(C.11a) \quad \lambda_0^+ \approx \omega_c + \delta - \frac{\mathrm{i}\kappa}{4} + \left(\delta - \frac{\mathrm{i}\kappa}{4} \right) = \omega_e - \frac{\mathrm{i}\kappa}{4} \,,$$

$$(C.11b) \quad \lambda_0^- \approx \omega_c + \delta - \frac{\mathrm{i}\kappa}{4} - \left(\delta - \frac{\mathrm{i}\kappa}{4} \right) \left[1 + \frac{|g|^2}{2(\delta - \mathrm{i}\kappa/4)^2} \right] \approx \omega_c - \frac{\mathrm{i}\kappa|g|^2}{8(\delta^2 + \kappa^2/16)} \,.$$

In the limit of large κ, the imaginary part of λ_0^+ is much larger than the imaginary part of λ_0^-. Therefore, $\exp(-\mathrm{i}\lambda_0^+ t)$ would decay to zero much faster than $\exp(-\mathrm{i}\lambda_0^- t)$, and effective decay rate of the two-level system would be dominated by the imaginary part of λ_0^-. Therefore, the effective decay rate γ of the two-level system is given by

$$(C.12) \qquad \gamma \approx \frac{\kappa|g|^2}{4\delta^2 + \kappa^2/4} = \frac{\kappa|g|^2}{(\omega_e - \omega_c)^2 + \kappa^2/4} \,.$$

We can also compute the spectrum of the emitted photons using eq. (C.4): In the limit of $t \to \infty$, $A_e(t)$ and $A_c(t)$ would have completely decayed and all the energy would now be in the bath. The spectrum of the emitted photon would thus be given by

$$(\text{C.13}) \quad \lim_{t \to \infty} |B(\omega, t)|^2 = |\xi|^2 \left| \int_0^\infty A_c(\tau) \exp(\mathrm{i}\omega\tau) \right|^2 = \frac{\kappa}{2\pi} |A_c(s = -\mathrm{i}\omega)|^2$$

$$(\text{C.14}) \quad = \frac{\kappa}{2\pi} \frac{|g|^2}{|\omega^2 + \mathrm{i}\{\kappa/2 + \mathrm{i}(\omega_e - \omega_c)\}\omega + \omega_e(\omega_c - \mathrm{i}\kappa/2) - |g|^2|^2}.$$

Appendix D.

Analysis of interferometers

D'1. *Linear optical elements in loss channels.* – In this part, we describe the Hamiltonians and derive the Heisenberg equations of motion for linear optical elements that act on light propagating in an ideal loss channel. The two linear optical elements that we consider here are the phase shifter and the beam splitter — almost all, more complicated, linear optical elements can be decomposed into their cascades.

A *phase shifter* is a linear optical element that imparts a constant phase to the light propagating through it. Physical realizations of phase shifters are often as simple as just adding extra optical path lengths to the incident field, or using thermal or electro-optical effects to change the local refractive index of the loss channel. Here we focus on broadband phase shifters — phase shifters that impart the same frequency to all the frequencies propagating in the loss channel. The Hamiltonian for broadband phase shifter on a loss channel with frequency annihilation operator a_ω and spatial annihilation operator a_z is given by

$$(\text{D.1}) \quad \hat{H} = \int_{-\infty}^\infty \omega a_\omega^\dagger a_\omega \mathrm{d}\omega + v_G V a_{z=0}^\dagger a_{z=0},$$

where V is the "strength" of the phase shifter (this is related to the phase shift below) and it is assumed that the phase shifter acts at $x = 0$ on the loss channel. Note that

$$(\text{D.2}) \quad \int_{-\infty}^\infty \omega a_\omega^\dagger a_\omega \mathrm{d}\omega = \int_{-\infty}^\infty \omega a_z^\dagger a_\omega \exp\left(-\mathrm{i}\frac{\omega z}{v_G}\right) \frac{\mathrm{d}z \mathrm{d}\omega}{\sqrt{2\pi v_G}} = -\mathrm{i}v_G \int_{-\infty}^\infty a_z^\dagger \frac{\partial a_z}{\partial z} \mathrm{d}z$$

with which the phase shifter Hamiltonian can be fully expressed in terms of the position annihilation operator $a(x)$:

$$(\text{D.3}) \quad H = -\mathrm{i}v_G \int_{-\infty}^\infty a_z^\dagger \frac{\partial a_z}{\partial z} \mathrm{d}z + v_G V a_{z=0}^\dagger a_{z=0}.$$

To analyze this system, we employ the Heisenberg picture — using the commutators for the position annihilation operators allows a straightforward calculation of the equation of motion for the Heisenberg picture annihilation operator $a(t; x)$:

$$(\text{D.4}) \quad \frac{1}{v_G} \frac{\partial a_z(t)}{\partial t} + \frac{\partial a_z(t)}{\partial z} = -\mathrm{i}V a_{z=0}(t)\delta(z),$$

which we need to solve under the initial condition that $a_z(0)$ is identical to the Schrödinger picture operator a_z. Note that in the absence of the phase shifter (*i.e.* $V = 0$), this equation can be trivially solved to obtain $a_z(t) = a_{z-v_G t}$ which correspond to the wave packet in the loss channel propagating along the z-direction with velocity v_G. For $V \neq 0$, a general solution to this equation can be written as

$$
(D.5) \qquad a_z(t) = \begin{cases} a_{z-v_G t}, & \text{if } z < -v_G t, \\ S a_{z-v_G t}, & \text{if } -v_G t \leq z \leq 0, \\ a_{x-v_G t}, & \text{if } z > 0, \end{cases}
$$

where S is a scalar that captures the impact of the phase shifter on the loss channel. This form of the solution for the dynamical equations can easily be physically interpreted by noting that excitations in the loss channel propagate along the $+z$ direction at a speed v_G. Since excitations that reach a point in the region $z < -v_G t$ and $z > 0$ at time t would not have encountered the beam splitter (which is at $z = 0$), they are simply described by translating the initial operator a_z in time. Excitations that reach a point in the region $-v_G t \leq z \leq 0$ at time t would have encountered the beam splitter at $t = 0$ which performed an (unknown) linear operation described by S on the operators. To calculate S, we integrate eq. (D.4) across an infinitesmal interval around $z = 0$ to obtain

$$
(D.6) \qquad a_{z=0^+}(t) - a_{z=0^-}(t) = -\frac{\mathrm{i}V}{2}[a_{z=0^+}(t) + a_{z=0^-}(t)].
$$

Using this along with eq. (D.5), we immediately obtain

$$
(D.7) \qquad S = \frac{1 - \mathrm{i}V/2}{1 + \mathrm{i}V/2} = \exp(\mathrm{i}\varphi),
$$

where $\varphi = -2\tan^{-1}(V/2)$ is the phase-shift induced by the phase-shifter.

A *beam-splitter* is a very commonly used linear optical device that interferes with two propagating optical signals — physical realizations of a beam splitter typically used are a partially transmitting mirror for free-space optical beams, and a directional coupler for optical waveguides. While the exact dynamics of a beam splitter can be very complicated, if we assume that the bandwidth of the beam splitter is much larger than the bandwidth of the optical signals that it is interfering, it can be analyzed with a simple model, which we describe in this section. Consider two loss channels, with frequency annihilation operators a_ω, b_ω and spatial annihilation operators a_z, b_z — the Hamiltonian for a broadband beam splitter in between these two loss channels is given by

$$
(D.8) \qquad H = \int_{-\infty}^{\infty} \omega a_\omega^\dagger a_\omega \, \mathrm{d}\omega + \int_{-\infty}^{\infty} \omega b_\omega^\dagger b_\omega \, \mathrm{d}\omega + \mathrm{i}v_g \left(V^* b_{z=0}^\dagger a_{z=0} - V a_{z=0}^\dagger b_{z=0} \right),
$$

where we assume that the beam splitter couples the two loss channels at $x = 0$, and V is a dimensionless constant that governs the strength of this coupling. As was done for the phase shifter, this Hamiltonian can be expressed completely in terms of the position

annihilation operator:

(D.9)
$$H = -iv_G \left[\int_{-\infty}^{\infty} a_z^\dagger \frac{\partial a_z}{\partial z} dz + \int_{-\infty}^{\infty} b_z^\dagger \frac{\partial b_z}{\partial z} dz \right] + iv_G \left(V^* b_{z=0}^\dagger a_{z=0} - V a_{z=0}^\dagger b_{z=0} \right).$$

To analyze this system, we employ the Heisenberg picture — using the commutators for the position annihilation operators allows a straightforward calculation of the equations of motion for the Heisenberg picture annihilation operators $a_z(t)$ and $b_z(t)$:

(D.10a)
$$\frac{1}{v_G} \frac{\partial a_z(t)}{\partial t} + \frac{\partial a_z(t)}{\partial z} = -V\delta(z)b_{z=0}(t),$$

(D.10b)
$$\frac{1}{v_G} \frac{\partial b_z(t)}{\partial t} + \frac{\partial b_z(t)}{\partial z} = V^*\delta(z)a_{z=0}(t),$$

which we need to solve under the initial condition that $a_z(0)$ and $b_z(0)$ are identical to the Schrödinger picture operator a_z and b_z, respectively. Note that in the absence of the beam splitter (*i.e.* $V = 0$), these equations can be trivially solved to obtain $a_z(t) = a_{z-v_Gt}$ and $b_z(t) = b_{z-v_Gt}$ which correspond to the propagation of a wave packet down the two waveguides at velocity v_G without coupling to each other. For $V \neq 0$, a general solution to these equations can be written as

(D.11)
$$a_z(t) = \begin{cases} a_{z-v_Gt}, & \text{if } z < -v_Gt, \\ S_{a,a}a_{z-v_Gt} + S_{a,b}b_{z-v_Gt}, & \text{if } -v_Gt \leq z \leq 0, \\ a_{z-v_Gt}, & \text{if } z > 0, \end{cases}$$

(D.12)
$$b_z(t) = \begin{cases} b_{z-v_Gt}, & \text{if } z < -v_Gt, \\ S_{b,a}a_{x-v_Gt} + S_{b,b}b_{z-v_Gt}, & \text{if } -v_Gt \leq z \leq 0, \\ b_{z-v_Gt}, & \text{if } z > 0, \end{cases}$$

where $S_{i,j} \; \forall \; i,j \in \{a,b\}$ are coefficients of the scattering matrix for the beam splitter, which we still have to compute. To determine these coefficients, we integrate with respect to z eq. (D.10) across an infinitesmal region around $z = 0$ to obtain

(D.13a)
$$a_{z=0^+}(t) - a_{z=0^-}(t) = \frac{V}{2}[b_{z=0^+}(t) + b_{z=0^-}(t)],$$

(D.13b)
$$b_{z=0^+}(t) - b_{z=0^-}(t) = -\frac{V^*}{2}[a_{z=0^+}(t) + a_{z=0^-}(t)].$$

Using the expressions for $a_z(t)$ and $b_z(t)$, these equations can be translated to a set of linear equations in the scalars $S_{a,a}, S_{a,b}, S_{b,a}$ and $S_{b,b}$ which can be solved to obtain the following expression for the beam-splitter scattering matrix:

(D.14)
$$S = \begin{bmatrix} S_{a,a} & S_{a,b} \\ S_{b,a} & S_{b,b} \end{bmatrix} = \frac{1}{1+|V|^2/4} \begin{bmatrix} 1 - |V|^2/4 & V \\ -V^* & 1 - |V|^2/4 \end{bmatrix}.$$

The conventional definition of a beam splitter assumes that V is purely real, and defining θ via $\sin\theta = V/(1 + |V|^2/4)$ and $\cos\theta = (1 - |V|^2/4)/(1 + |V|^2/4)$, we obtain

$$(D.15) \qquad S = \begin{bmatrix} \cos\theta & -\sin\theta \\ \sin\theta & \cos\theta \end{bmatrix}.$$

In particular, a 50-50 beam splitter is defined as a beam splitter with $\theta = \pi/4$ — this interferes with both the input ports equally, constructively in one output arm and destructively in the other.

D˙2. *Analysis of Hanbury-Brown Twiss and Hong-Ou Mandel interferometers*. – Here, we analyze the two interferometers shown in fig. 7. Note that both the interferometers apply the same optical transformation to the input fields — in one case, one of the arms has the vacuum state as an input, whereas in the other case both arms are excited with the light source being characterized. For our analysis, we assume that the photon pulses assumed by the light have a pulse width that is much smaller than the other optical lengths involved in the setup (*e.g.* the distance between the sources or detectors from the phase shifters or beam splitters). In this case,

$$(D.16a) \qquad a_{z=L}(t) = \frac{a_{z=L-v_G t} - \exp(i\varphi) b_{z=L-v_G t}}{\sqrt{2}},$$

$$(D.16b) \qquad b_{z=L}(t) = \frac{a_{z=L-v_G t} + \exp(i\varphi) b_{z=L-v_G t}}{\sqrt{2}},$$

where we assume that $t = 0$ is the time at which both the sources emit photons and t is large enough for the light emitted by the sources to have propagated entirely to the detectors — if this is not the case, then $a_{z=L}(t)$ or $b_{z=L}(t)$ will simply annihilate the state $|\Psi\rangle$ emitted by the sources since $L - v_G t$ would lie outside the spatial region corresponding to the photon pulse. Consider now the expectation $\mathrm{E}_\varphi[\langle\Psi(0)|a_{z=L}(t_1)b_{z=L}(t_2)b^\dagger_{z=L}(t_2)a^\dagger_{z=L}(t_1)|\Psi(0)\rangle]$ — using eq. (D.16) and explicitly averaging over φ:

$$(D.17) \quad \mathrm{E}_\varphi[\langle\Psi(0)|\, a_{z=L}(t_1) b_{z=L}(t_2) b^\dagger_{z=L}(t_2) a^\dagger_{z=L}(t_1) \,|\Psi(0)\rangle] =$$

$$\frac{1}{4}\Bigg[\sum_{v\in\{a,b\}} \langle\Psi_v|\, v^\dagger_{z=L-v_G t_1} v^\dagger_{z=L-v_G t_2} v_{z=L-v_G t_1} v_{z=L-v_G t_2} \,|\Psi_v\rangle$$

$$+ \sum_{(u,v)\in\mathcal{S}} \langle\Psi_v|\, v^\dagger_{z=L-v_G t_1} v_{z=L-v_G t_1} \,|\Psi_v\rangle \langle\Psi_u|\, u^\dagger_{z=L-v_G t_2} u_{z=L-v_G t_2} \,|\Psi_u\rangle$$

$$- \sum_{(u,v)\in\mathcal{S}} \langle\Psi_v|\, v^\dagger_{z=L-v_G t_1} v_{z=L-v_G t_2} \,|\Psi_v\rangle \langle\Psi_u|\, u^\dagger_{z=L-v_G t_2} u_{z=L-v_G t_1} \,|\Psi_u\rangle \Bigg],$$

where $\mathcal{S} = \{(a,b),(b,a)\}$ and we have assumed that the two sources are not entangled with each other — note that if both the sources emit a pure state, then this would imply that the state of the composite system is $|\Psi_a\rangle|\Psi_b\rangle$ and if the sources emit a mixed state,

then the density matrix of the composite system is $\hat{\rho}_a\hat{\rho}_b$. Consequently, the expectation of a product of a_z and b_z operators (and their conjugates) can be factorized:

$$(D.18) \qquad \langle\Psi(0)|\, f_a[a_z, a_z^\dagger] f_b[b_z, b_z^\dagger]\,|\Psi(0)\rangle = \langle\Psi_a|\, f_a[a_z, a_z^\dagger]\,|\Psi_a\rangle\, \langle\Psi_b|\, f_b[b_z, b_z^\dagger]\,|\Psi_b\rangle\,.$$

Similar expressions for the expections $\mathrm{E}_\varphi(\langle\Psi(0)|a_{z=L}(t)a_{z=L}^\dagger(t)|\Psi(0)\rangle)$ and $\mathrm{E}_\varphi(\langle\Psi(0)|b_{z=L}(t)b_{z=L}^\dagger(t)|\Psi(0)\rangle)$ can be obtained by using eq. (D.16):

$$(D.19) \qquad \mathrm{E}_\varphi(\langle\Psi(0)|\, a_{z=L}^\dagger(t)a_{z=L}(t)\,|\Psi\rangle) = \mathrm{E}_\varphi[\langle\Psi|\, b_{z=L}^\dagger(t)b_{z=L}(t)\,|\Psi(0)\rangle]$$
$$= \frac{1}{2}\left[\ \sum_{v\in\{a,b\}} \langle\Psi_v|\, v_{z=L-v_Gt}^\dagger v_{z=L-v_Gt}\,|\Psi_v\rangle\ \right].$$

With the help of these relationships, we can now prove the results about the two interferometers stated in sect. **3**`2. Consider the Hanbury-Brown Twiss interferometer — since the second waveguide (labelled by $b(x)$) is in the vacuum state, it follows that

$$(D.20a) \qquad \mathrm{E}_\varphi[\langle\Psi(0)|\, a_{z=L}^\dagger(t_1)b_{z=L}^\dagger(t_2)b_{z=L}^\dagger(t_2)a_{z=L}(t_1)\,|\Psi(0)\rangle]$$
$$= \frac{1}{4}\langle\Psi_a|\, a^\dagger(L-v_Gt_1)a_{z=L-v_Gt_2}^\dagger a_{z=L-v_Gt_1}a_{z=L-v_Gt_2}\,|\Psi_a\rangle\,,$$

$$\mathrm{E}_\varphi[\langle\Psi(0)|\, a_{z=L}^\dagger(t)a_{z=L}(t)\,|\Psi(0)\rangle] = \mathrm{E}_\varphi[\langle\Psi(0)|\, b_{z=L}^\dagger(t)b_{z=L}(t)\,|\Psi(0)\rangle]$$
$$= \frac{1}{2}\langle\Psi_a|\, a_{z=L-v_Gt}^\dagger a_{z=L-v_Gt}\,|\Psi_a\rangle\,,$$

from which it immediately follows that $g_{\mathrm{HBT}}^{(2)}(t_1, t_2)$ and $g_{\mathrm{HBT}}^{(2)}[0]$ are exactly equal to $g^{(2)}(t_1, t_2)$ and $g^{(2)}[0]$.

Similarly, consider the Hong-Ou Mandel interferometer — assuming that both the sources emit a single-photon state (pure or mixed), it immediately follows that the second-order correlations in the sources vanish: $\langle\Psi_v|v_{z=L-v_Gt_1}^\dagger v_{z=L-v_Gt_2}^\dagger v_{z=L-v_Gt_1} v_{z=L-v_Gt_2}|\Psi_v\rangle = 0$ for $v\in\{a,b\}$. Using the general form for the density matrix of the light emitted by a single-photon source, the remaining expectations can be immediately evaluated:

$$(D.21) \qquad \langle\Psi_v|\, v_{z=L-v_Gt_1}^\dagger v_{z=L-v_Gt_2}\,|\Psi_v\rangle = P_{1,v}\rho_v^{(1)}(L-v_Gt_2, L-v_Gt_1) \quad \text{for } v\in\{a,b\}.$$

We can now evaluate the integrals appearing in the definition of $g_{\mathrm{HOM}}^{(2)}[0]$ — in particular note that

$$(D.22a) \qquad \int_{-\infty}^{\infty} \langle\Psi_v|\, v_{z=L-v_Gt}^\dagger v_{z=L-v_Gt}\,|\Psi_v\rangle\, \mathrm{d}t = v_G P_{1,v},$$

$$\int_{-\infty}^{\infty}\int_{-\infty}^{\infty} \langle\Psi_v|\, v_{z=L-v_Gt_1}^\dagger v_{z=L-v_Gt_2}\,|\Psi_v\rangle\, \langle\Psi_u|\, u_{z=L-v_Gt_2}^\dagger u_{z=L-v_Gt_1}\,|\Psi_u\rangle\, \mathrm{d}t_1\mathrm{d}t_2 =$$

$$v_G^2 P_{1,v}P_{1,u}\iint \rho_v^{(1)}(x_1, x_2)\rho^{(1)}(x_2, x_1)\mathrm{d}x_1\mathrm{d}x_2 =$$

$$v_G^2 P_{1,v}P_{1,u}\iint \rho_v^{(1)}(x_1, x_2)\rho_u^{(1)*}(x_1, x_2)\mathrm{d}x_1\mathrm{d}x_2,$$

With these expressions, one readily obtains

$$(\text{D.23}) \qquad g_{\text{HOM}}^{(2)}[0] = \frac{2P_{1,a}P_{1,b}}{(P_{1,a}+P_{1,b})^2}\left[1 - \int_{-\infty}^{\infty}\int_{-\infty}^{\infty}\rho_a^{(1)}(x_1,x_2)\rho_b^{(1)*}(x_1,x_2)\mathrm{d}x_1\mathrm{d}x_2\right].$$

REFERENCES

[1] Weng Cho Chew, *Waves and fields in inhomogeneous media* (IEEE Press) 1995.

[2] Leonard Mandel and Emil Wolf, *Optical coherence and quantum optics* (Cambridge University Press) 1995.

[3] Shanhui Fan, Şükrü Ekin Kocabaş and Jung-Tsung Shen, "Input-output formalism for few-photon transport in one-dimensional nanophotonic waveguides coupled to a qubit", *Phys. Rev. A*, **82** (2010) 063821.

[4] R. J. Glauber and M. Lewenstein, "Quantum optics of dielectric media" *Phys. Rev. A*, **43** (1991) 467.

[5] S. M. Dutra and G. Nienhuis, "Quantized mode of a leaky cavity" *Phys. Rev. A*, **62** (2000) 063805.

[6] Howard Carmichael, *An open systems approach to quantum optics: lectures presented at the Université Libre de Bruxelles, October 28 to November 4, 1991*, Vol. **18** (Springer Science & Business Media) 2009.

[7] Richard P. Feynman, *Quantum electrodynamics* (CRC Press) 2018.

[8] Daniel A. Steck, "Quantum and atom optics", available online at `http://steck.us/teaching` (revision 0.12.6, 23 April 2019).

[9] Pierre meystre and Murray Sargent III, *Elements of Quantum Optics* (Springer) 2017.

[10] Kevin A. Fischer, Lukas Hanschke, Malte Kremser, Jonathan J. Finley, Kai Müller and Jelena Vučković, "Pulsed rabi oscillations in quantum two-level systems: beyond the area theorem", *Quantum Sci. Technol.*, **3** (2017) 014006.

[11] Kevin A. Fischer, Lukas Hanschke, Jakob Wierzbowski, Tobias Simmet, Constantin Dory, Jonathan J. Finley, Jelena Vučković and Kai Müller, "Signatures of two-photon pulses from a quantum two-level system", *Nat. Phys.*, **13** (2017) 649.

[12] Shanshan Xu and Shanhui Fan, "Input-output formalism for few-photon transport: A systematic treatment beyond two photons", *Phys. Rev. A*, **91** (2015) 043845.

[13] Tao Shi, Darrick E. Chang and J. Ignacio Cirac, "Multiphoton-scattering theory and generalized master equations", *Phys. Rev. A*, **92** (2015) 058384.

[14] Matthew Pelton, "Modified spontaneous emission in nanophotonic structures", *Nat. Photon.*, **9** (2015) 427.

[15] Arthur Ekert and Peter L. Knight, "Entangled quantum systems and the Schmidt decomposition", *Am. J. Phys.*, **63** (1995) 415.

[16] Fischer K. A., Müller K., Lagoudakis K. G. and Vuckovic J., "Dynamical modeling of pulsed two-photon interference", *New J. Phys.*, **18** (2016) 113053.

[17] Arakawa Y. and Sakaki H., "Multidimensional quantum well laser and temperature dependence of its threshold current", *Appl. Phys. Lett.*, **40** (1982) 939.

[18] Kelley Rivoire, Sonia Buckley, Arka Majumdar, Hyochul Kim, Pierre Petroff and Jelena Vučković, "Fast quantum dot single photon source triggered at telecommunications wavelength", *Appl. Phys. Lett.*, **98** (2011) 083105.

[19] Dirk Englund, Andrei Faraon, Ilya Fushman, Nick Stoltz, Pierre Petroff and Jelena Vuckovic, "Controlling cavity reflectivity with a single quantum dot", *Nature*, **450** (2007) 857.

[20] Yong Zhang and Jianwei Wang, "Bound exciton model for an acceptor in a semiconductor", *Phys. Rev. B*, **90** (2014) 155201.

[21] Christian Hepp, *Electronic Structure of the Silicon Vacancy Color Center in Diamond*, PhD Thesis, Universität des Saarlandes, 2014.

[22] Jingyuan Linda Zhang, Shuo Sun, Michael J. Burek, Constantin Dory, Yan-Kai Tzeng, Kevin A. Fischer, Yousif Kelaita, Konstantinos G. Lagoudakis, Marina Radulaski, Zhi-Xun Shen, Nicholas A. Melosh, Steven Chu, Marko Lončar and Jelena Vučković, "Strongly cavity-enhanced spontaneous emission from silicon-vacancy centers in diamond", *Nano Lett.*, **18** (2018) 1360.

Creating quantum correlations between quantum-dot spins

M. Atatüre

Cavendish Laboratory, University of Cambridge
JJ Thomson Ave., Cambridge CB3 0HE, UK

Summary. — This paper focuses on generating nonlocal quantum correlations between electron spins in semiconductor quantum dots located far from each other. Some of the key prerequisite concepts are covered in other contributions to these proceedings and we focus on applying some of the concepts for creating correlated spins. We start by describing how nonlocal correlations can be generated between quantum systems that have no prior connection, by utilising a particular type of measurement known as quantum erasure. We will focus on self-assembled semiconductor quantum dots and contrast the observed results to other systems.

1. – Proximity and quantum correlations

Proximity is a fundamental requirement for essentially all physical phenomena involving correlations. Correlations require interactions and interactions bring forth a characteristic length scale over which they can influence the dynamics of individual physical entities. The particular nature of an interaction determines the desired length scale to build correlations. This is fundamentally the same reason why correlated systems always

---

© Società Italiana di Fisica 77

emerge beyond a critical density, as is the case for atomic or polaritonic Bose-Einstein condensation, or strongly correlated electron systems. The power of proximity holds even for only a few, countable systems. Take two isolated and independent electrons, for example. If we want the electrons to interact electrostatically, the distance between the two electrons will determine the strength of this interaction via the inverse square law. However, if we would like to correlate the spin orientations of these two electrons, we would need magnetic interaction instead, which scales inversely as the sixth power of the distance and casts an even more stringent requirement of proximity.

Now, let us assume there exists a physical mechanism, where our electrons can emit (or scatter) single photons and each emission process results in changing their spin orientation. If we detect a single photon coming from one of the electrons, we immediately learn that a spin-flip event took place with that electron. If we have prior knowledge of the spin orientation, we simply update our records and all is well in a somewhat classical world. However, if we detect a single photon without the ability to tell from which of the two electrons it originated, we end up with two coexisting possible scenarios regarding the spin orientations of our electrons. This kind of measurement is also called a quantum erasure [1]. In our situation, a quantum erasure measurement leads to a coherent superposition of two different spin orientation combinations for our electrons, which is nothing other than quantum entanglement! What is particularly worth emphasizing here is that there is no requirement for the two electrons to have interacted directly with each other.

This beautiful and powerful concept was first proposed in 1999 by Cabrillo and coauthors, using individual atoms and their optical transitions [2]. In this seminal proposal, two well-separated atoms are exposed to weak excitation that could lead to the generation of a single photon and the flip of the atomic ground state simultaneously through what is known as a lambda transition. If an atom is not excited, it does not generate a photon and the ground-state spin remains unchanged. If an atom is excited, then a single photon is generated and the ground-state spin is flipped. The excitation is weak such that the probability to emit a single photon is significantly lower than 1, so most of the time the opical excitation attempts fail, but occasionally one of the two atoms responds to the excitation and generates a single photon (and flip the ground-state spin). With much lower probability both atoms could emit a photon, in which case both ground-state spins are flipped resulting in a product state for the two atoms, as before. Hence, a measurement-based postselection of the one and only one photon emitted by the two atoms generates the nonlocal quantum correlations we discussed so far. But, there is a catch: this scheme relies crucially on not being able to distinguish the photons originating from the two atoms.

The 1999 proposal has been demonstrated experimentally with a number of physical systems [3-13] —each bringing its own strengths and weaknesses with respect to the others regarding the fidelity and the rate of entanglement generation, as well as attainable distances limited by the available coherence times. While such variations may be of secondary importance in the validation of the ever counter-intuitive quantum physics, this very process has in the meatime achieved a centre-stage role of creating quantum

networks [14]. As such, various technical challenges including photon collection efficiency and wavelength, ground-state coherence time and control fidelity, and feasably scalable architecture of many nodes need to be addressed on the road to large-scale distributed systems. This challenge alone is sufficient to motivate the years of research towards achieving high-efficiency high-quality spin-photon interfaces in solids as competitive and even adventageous alternatives to atomic systems. There are many material systems under investigation, including diamond, silicon carbide and semiconductors [15]; here we focus on self-assembled semiconductor quantum dots.

2. – Optically active semiconductor quantum dots

2˙1. *Essential properties.* – Self-assembled indium gallium arsenide (InGaAs) quantum dots (QDs), introduced in detail in other contributions to these proceedings, are grown by Molecular Beam Epitaxy (MBE) and possess many desirable attributes as a spin-photon interface system. They can host a confined spin deterministically [16] and offer atomic-like spin-selective optical transitions. The optical emission wavelength varies with the growth conditions affecting the size and shape of the QDs, but typically is centred around 950 nm with an inhomogeneous spread of around 100 nm. When using bare samples this casts the challenge of finding QDs with identical emission whavelength, but Stark tuning via electric field is used as a standard technique for spectrally overlapping multiple QD photons. The purity and the coherence properties of QD-generated photons are nearly ideal, where indistinguishability measurements via Hong-Ou-Mandel interferometry [17] consistently report beyond 95% indistinguishability in the last few years [18]. The electron (or hole) spin properties are typically less appealing for QDs: The inhomogeneous spin dephasing time, T_2^*, is typically between a few to hundred nanoseconds, while the natural dephasing time, T_2, is around a few microseconds. The limitation is caused predominantly by the presence of the QD nuclear spin noise [19]. That said, these modest timescales should nevertheless be considered in the context of all-optical ultrafast coherent control on the order of only a few picoseconds [20, 21].

2˙2. *QD spin devices.* – Confining a single spin in a QD deterministically requires electrical control via a Schottky diode structure. An n-doped GaAs layer provides the electron reservoir and a Schottky contact allows energy band tilting as a function of applied voltage. A tunnel barrier between an n-doped GaAs layer and the QD layer, and a tunnel barrier above the QD layer both prevent charge leakage while maintaining electric field. The Schottky diode structure is electrically contacted through Ohmic AuGeNi contacts to the n-doped layer and a semitransparent Ti gate ($\sim$ 6 nm) is evaporated onto the surface of the sample. The photon collection is enhanced by the growth of a distributed Bragg reflector region below the QD layer comprising alternating layers of GaAs and AlGaAs thin layers and the placement of a superhemispherical cubic zirconia solid immersion lens (SIL) on the top Schottky contact of the devices. This relatively simple construction yields on average a few million photons per second at saturation

with a photon outcoupling efficiency of 10% for QDs with an emission wavelength around 950 nm, which is sufficient to demonstrate nonlocal quantum correlations in spins.

3. – Measurement-based creation of quantum correlations

3˙1. *Entanglement concept*. – The entanglement scheme of Cabrillo *et al.* [2] relies on weak, phase-coherent excitation of two indistinguishable Λ-systems and the subsequent detection of a single photon. First step is to initialise the two QD spins to the same spin state $|{\downarrow_i}\rangle$ (with spin-1/2 ground states labelled as $|{\uparrow_i}\rangle$ and $|{\downarrow_i}\rangle$) by optical pumping. The second step is to excite the two Λ-systems from the state $|{\downarrow_i}\rangle$ to initiate a Raman scattering process with a small probability $p \ll 1$. The excitation pulse entangles the ground-state spin of each QD with an emitted Raman photon [22-24]. Combining the Raman modes from each QD on a 50:50 beam splitter erases the which-path information conveniently (so long as the photons are indistinguishable), such that the total entangled spin-photon state for the two QD devices is given by

$$
\begin{aligned}
(1) \qquad |\Psi\rangle = \;& (1-p)\,|{\downarrow_{\mathrm{QD}_1}\downarrow_{\mathrm{QD}_2}}\rangle\,|0_1 0_2\rangle \\
& + \sqrt{p(1-p)/2}\,\big(e^{i\phi_{\mathrm{QD}_1}}\,|{\uparrow_{\mathrm{QD}_1}\downarrow_{\mathrm{QD}_2}}\rangle + e^{i\phi_{\mathrm{QD}_2}}\,|{\downarrow_{\mathrm{QD}_1}\uparrow_{\mathrm{QD}_2}}\rangle\big)\,|1_1 0_2\rangle \\
& + \sqrt{p(1-p)/2}\,\big(e^{i\phi_{\mathrm{QD}_1}}\,|{\uparrow_{\mathrm{QD}_1}\downarrow_{\mathrm{QD}_2}}\rangle - e^{i\phi_{\mathrm{QD}_2}}\,|{\downarrow_{\mathrm{QD}_1}\uparrow_{\mathrm{QD}_2}}\rangle\big)\,|0_1 1_2\rangle \\
& + p/\sqrt{2}\,e^{i(\phi_{\mathrm{QD}_1}+\phi_{\mathrm{QD}_2})}\,|{\uparrow_{\mathrm{QD}_1}\uparrow_{\mathrm{QD}_2}}\rangle\,\big(|2_1 0_2\rangle - |0_1 2_2\rangle\big).
\end{aligned}
$$

Here, the indices in the photonic number states designate the beam splitter output modes (1 or 2), where the photon measurement will take place. ϕ_{QD_1} and ϕ_{QD_2} are the optical phases accumulated along the path of the interferometer going through QD 1 and QD 2, respectively, after the beam splitter transformation.

Detection of the one-photon contribution selectively in the beam splitter output projects the two QD spins into the entangled state $(|{\uparrow_{\mathrm{QD}_1}\downarrow_{\mathrm{QD}_2}}\rangle \pm e^{i\Delta\phi}\,|{\downarrow_{\mathrm{QD}_1}\uparrow_{\mathrm{QD}_2}}\rangle)/\sqrt{2}$ with the sign depending on the output port that registers the Raman photon and $\Delta\phi = \phi_{\mathrm{QD}_2} - \phi_{\mathrm{QD}_1}$. For $\Delta\phi = 0$ these states are in fact maximally entangled and correspond to two of the four Bell states $|\psi^{(\pm)}\rangle$. With a small but finite probability of p^2 both QDs emit a Raman photon and flip their spin state, which results in a two-photon state after the beam splitter (naturally exiting at the same output mode due to indistinguishability [17]), contributing to an intrinsic error in the entanglement generation of p. Consequently, an optimal value range for p is determined through a compromise between this error probability and the rate of entanglement generation, $2p(1-p)$.

3˙2. *Experimental realisation*. – Figure 1 is a basic illustration of the experimental arrangement —a faithful replica of the Cabrillo proposal. A detailed description of what we discuss below can also be found in Stockill *et al.* [13]. Two InGaAs QD devices, QD 1 and QD 2, located in separate cryostats that are 2 metres apart, provide the two
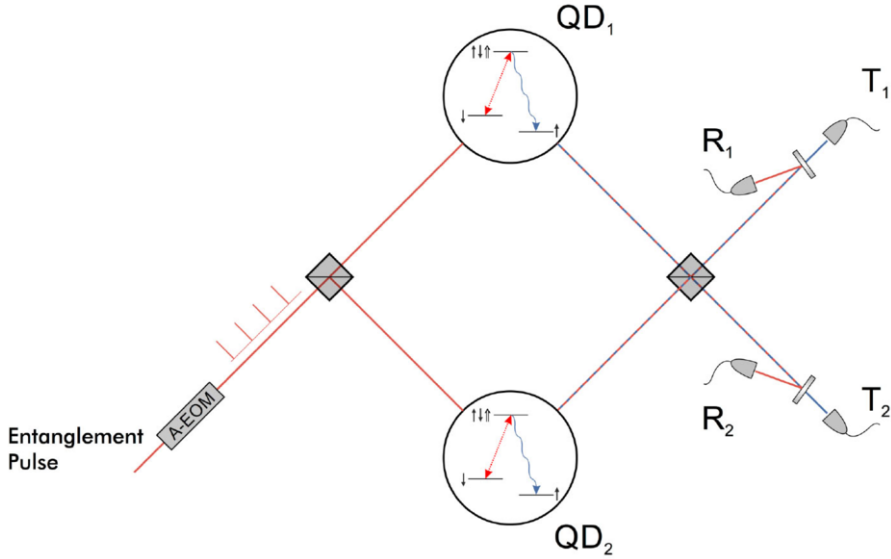
Fig. 1. – The experimental arrangement of the two QDs together with the optical paths and the output ports for detection. The first beam splitter distributes the optical excitation pulses to the two QD spins, while the second beam splitter combines the Raman photons from the QDs completing the effective Mach-Zehnder interferometer.

spins we wish to correlate. 4 T magnetic field applied perpendicular to the QD growth axis lifts the spin degeneracy of the ground and excited states of the QDs and forms the desired Λ system. The two optical transitions linking the two spin ground states to a common excited state, around 968 nm in this case, are therefore distinguishable by their frequency (25 GHz difference); the lower-energy and higher-energy transitions are denoted in red and blue, respectively. Stark tuning via electrical control further ensures that the two QDs are identical from the perspective of all relevant optical transitions. Initialisation and measurement of the spins utilise optical pulses derived from frequency-stabilized single-mode lasers using fiber-based electro-optic intensity modulators. In contrast, coherent spin rotations are achieved optically using 1 THz red-detuned pulses from a mode-locked Ti:Sa laser picked with acousto-optic modulators. An additonal far-off resonance continuous wave laser is used to measure the cumulative phase between the two optical paths in the experiment (fig. 1) and stabilise this phase to $\sim 3°$ over a DC-1.5 kHz range via a combination of electro-optic phase modulation and piezo-based compensation.

The initialisation, rotation and measurement sequence is as follows: First, both spins are optically pumped into the spin-down state. This is achieved with $\sim 97\%$ fidelity per spin. Second, a 160 ps long optical pulse drives the lower-energy transition of each QD to generate a Raman photon and flip the spin state. The exitation probability, p, is set to 7% in order to suppress the probability of both QDs being excited. The third step is
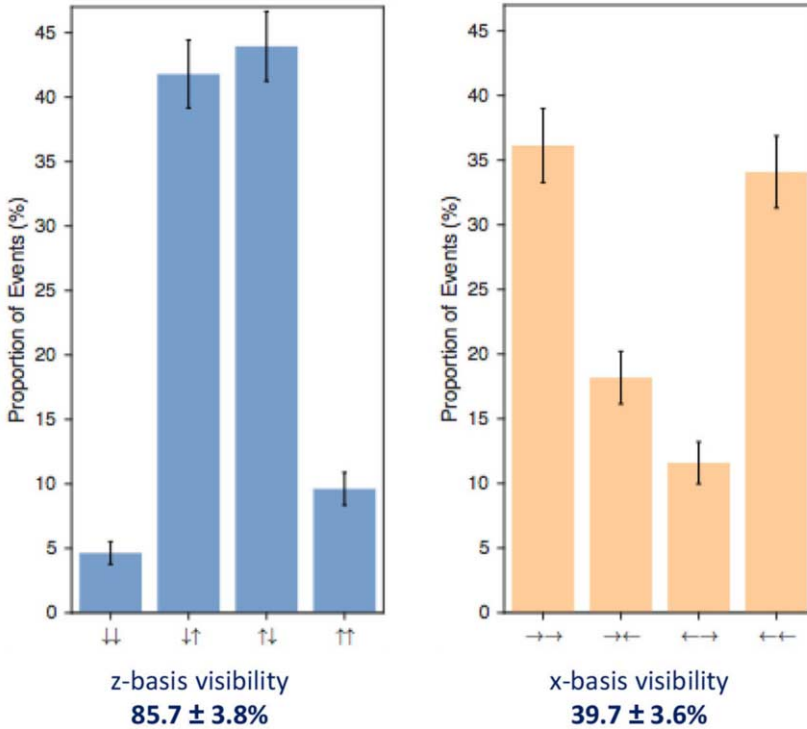
Fig. 2. – Joint spin-state reconstruction through 3-photon coincidence events. Left: Joint spin state population conditional on a single Raman photon detection event. An antisymmetric population is retrieved with a probability of $85.7 \pm 3.8\%$. The error bars represent the statistical uncertainty drawn from the 603 three-photon events that were used to reconstruct the population. Right: Spin correlations in the transverse basis for projection of $|\psi^{(+)}\rangle$ for $\Delta\phi = 0$.

to detect a single Raman photon at one of the output ports of the beam splitter. The degree of indistinguishability of the Raman photons in the two input modes as measured via the Hong-Ou-Mandel two-photon interference is $93 \pm 1\%$ in these experiments. The fourth step is to select the basis in which measurement will be conducted, obtained by applying a $1\,\mathrm{THz}$ red-detuned pulse to yield coherent rotation of the two spins. The fifth and final step in the sequence is to measure each spin individually using an $8\,\mathrm{ns}$ long optical pulse driving the higher-energy transition. The outcome is the evidence of entanglement between the spins obtained from spin correlations in different measurement bases. Following this sequence with four different iterations, we can reconstruct the population of $\{|\downarrow_{QD_1}\downarrow_{QD_2}\rangle, |\downarrow_{QD_1}\uparrow_{QD_2}\rangle, |\uparrow_{QD_1}\downarrow_{QD_2}\rangle, |\uparrow_{QD_1}\uparrow_{QD_2}\rangle\}$.

Figure 2 is a reconstruction of the projected two-spin state from the correlation of three-photon coincidence events measured along two orthogonal axes. The first measurement is the state in the population basis, parallel to the external magnetic field, measuring directly the eigenstates of the spins (left panel). The detection of a Raman

photon projects an antisymmetric spin population with a probability of $85.7 \pm 3.8\%$. The uncertainty is set by the shot noise of the 603 three-photon detection events. The presence of population in the $|\uparrow_{\mathrm{QD}_1} \uparrow_{\mathrm{QD}_2}\rangle$ state is intrinsic to the entanglement generation scheme, and follows the spin-flip probability p. Events in the $|\downarrow_{\mathrm{QD}_1} \downarrow_{\mathrm{QD}_2}\rangle$ state mainly result from imperfect spin rotation and read-out. Figure 2 (right panel) shows correlation measurements in the transverse basis. In this basis, quantum erasure imprints the interferometric phase between the Raman modes onto the nonlocal state shared between the two spins, which is tunable via the optical path length difference in the experimental arrangement. For $\Delta\phi = 0$, detecting a Raman photon in output mode 1 generates the $|\psi^{(+)}\rangle$ state, revealing a visibility of $39.5 \pm 3.8\%$. We can estimate the Bell-state fidelity from combining these two visibilities directly, which yields an average of $62.6 \pm 2.3\%$ fidelity. This value constitutes around a 5 standard deviations of the mean from that obtained from a classically described two-spin state. The measured fidelity is commensurate with cumulative error contributions, the most prominent ones being the double spin-flip rate (limiting the fidelity to 93%), the imperfect mode overlap (a further reduction of 4%), the spin-state dephasing (a visibility reduction of 13%), and the imperfect spin preparation and read-out (3% and 6%, respectively). Nevertheless, the rate at which such correlations can be generated between two QD spins is around 8 kHz, which is significantly higher than any other physical system tested through the Cabrillo scheme. This is mostly due to the very high quality of the QD photons as well as their brightness.

4. – Outlook

In this lecture we started by introducing the role of proximity for correlated systems and how we can remove it using concepts in quantum physics. We then picked one physical system, namely the semiconductor quantum dots, as one of many spin-photon interface systems, and showed how they can be used to demonstrate optically generated quantum entanglement between two confined electron spins. From the perspective of entanglement generation rate based on photon measurements, the performance of quantum dots surpasses that of all other physical systems investigated. Using current state-of-the-art light-collection strategies discussed also in this School, the entanglement rate could be improved to around 1MHz. This rate is comparable to the inverse of electron-spin coherence time. It is therefore appropriate to end this paper by pointing out that this sets an exciting benchmark for the prospect of attaining fault tolerant scalability [25].

$$* \ * \ *$$

REFERENCES

[1] Scully M. O. and Druehl K., *Phys. Rev.*, **25** (1982) 2208.
[2] Cabrillo C., Cirac J. I., Garcia-Fernandez P. and Zoller P., *Phys. Rev. A*, **59** (1999) 1025.
[3] Hensen B., Bernien H., Dreau A. E. *et al.*, *Nature*, **526** (2015) 682.
[4] Maunz P., Olmschenk S., Hayes D. *et al.*, *Phys. Rev. Lett.*, **102** (2009) 250502.
[5] Pfaff W., Hensen B., Bernien H. *et al.*, *Science*, **345** (2014) 532.
[6] Hofmann J., Krug M., Ortegel N. *et al.*, *Science*, **337** (2012) 72.
[7] Bernien H., Hensen B., Pfaff W. *et al.*, *Nature*, **497** (2013) 86.
[8] Moehring D. L., Maunz P., Olmschenk S. *et al.*, *Nature*, **449** (2007) 68.
[9] Hucul D., Inlek I. V., Vittorini G. *et al.*, *Nat. Phys.*, **11** (2014) 37.
[10] Slodicka L., Hetet G., Roeck N. *et al.*, *Phys. Rev. Lett.*, **110** (2013) 083603.
[11] Narla A., Shankar S., Hatridge M. *et al.*, *Phys. Rev. X*, **6** (2016) 031036.
[12] Delteil A., Sun Z., Gao W.-B. *et al.*, *Nat. Phys.*, **12** (2015) 218.
[13] Stockill R., Stanley M. J., Huthmacher L. *et al.*, *Phys. Rev. Lett.*, **119** (2017) 010503.
[14] Kimble H. J., *Nature*, **453** (2008) 1023.
[15] Atature M., Englund D., Vamivakas N. *et al.*, *Nat. Rev. Mat.*, **3** (2018) 38.
[16] Warburton R. J., Schflein C., Haft D. *et al.*, *Nature*, **405** (2000) 926.
[17] Hong C. K., Ou Z. Y. and Mandel L., *Phys. Rev. Lett.*, **59** (1987) 2044.
[18] Somaschi N., Giesz V., De Santis, L. *et al.*, *Nat. Photon.*, **10** (2016) 340.
[19] Urbaszek B., Marie X., Amand T. *et al.*, *Rev. Mod. Phys.*, **85** (2013) 79.
[20] Press D., Ladd T. D., Zhang B. *et al.*, *Nature*, **456** (2008) 218.
[21] Press D., de Greve K., McMahon P. L. *et al.*, *Nat. Photon.*, **4** (2010) 367.
[22] de Greve K., Yu L., McMahon P. L. *et al.*, *Nature*, **491** (2012) 421.
[23] Gao W.-B., Fallahi P., Togan E. *et al.*, *Nature*, **491** (2012) 426.
[24] Schaibley J. R., Burgers A. P., McCracken G. A. *et al.*, *Phys. Rev. Lett.*, **110** (2013) 167401.
[25] Monroe C., Raussendorf R., Ruthven A. *et al.*, *Phys. Rev. A*, **89** (2014) 022317.

Platforms for telecom entangled photon sources

E. Polino, N. Spagnolo and F. Sciarrino

Dipartimento di Fisica, Sapienza Università di Roma - P.le Aldo Moro 5, 00185 Roma, Italy

G. Corrielli, A. Crespi and R. Osellame

Istituto di Fotonica e Nanotecnologie, Consiglio Nazionale delle Ricerche (IFN-CNR)
Piazza Leonardo da Vinci 32 I-20133 Milano, Italy

Dipartimento di Fisica, Politecnico di Milano - Piazza Leonardo da Vinci 32,
I-20133 Milano, Italy

Summary. — Entanglement represents a fundamental resource for quantum technologies, including quantum communication tasks. In this context, photons are the ideal physical systems due to their capability of carrying information over long distances. Hence, it is fundamental to design reliable sources of entangled photons in the telecom wavelength regime (around $1.55\,\mu$m), where optical fiber losses are low. In this paper we review different platforms used to generate telecom entangled photon pairs, and we focus in particular on an integrated source realized by the femtosecond laser writing (FLW) technique, which allows to devise stable and compact optical circuits in glass. We show how this technique can be employed to inscribe waveguides in nonlinear crystals for generation of telecom entangled photon pairs on a chip.

1. – Introduction

Quantum resources promise to greatly enhance information tasks with respect to any classical strategy. Several applications have been identified, including quantum computation, simulation, metrology and communication [1]. Different physical systems can be exploited to implement quantum information protocols, *e.g.*: trapped and cold atoms [2-4], superconducting systems [5-7], nuclear and electronic spins [8-11] and photons [12]. The latter ones are among the most studied and attractive systems due to their high mobility and low interaction with the environment. Given these properties, photons can be employed in several quantum information processes [13, 14]. In particular quantum communication [15] is a fundamental task for future quantum networks, and photons are the best candidate for such purpose thanks to their easiness and velocity of transmission and to the long decoherence time. For long distance fiber optic quantum communication appropriate wavelengths that lie in the telecom band have to be employed to minimize losses, in particular around $1.3\,\mu$m and $1.55\,\mu$m.

Several degrees of freedom of the photon can be exploited to encode qubits and higher dimensional states, and can be divided in discrete and continuous ones. Examples of discrete degrees of freedom are: the polarization, living in a 2-dimensional space where an orthonormal basis is represented by horizontal and vertical polarizations $\{|H\rangle, |V\rangle\}$; the quantized orbital angular momentum (OAM) that lives in an unbounded Hilbert space, where an orthonormal basis is represented by optical vortices $|m\rangle$ with $m \in \mathbb{Z}$; photon number degree of freedom with basis $|n\rangle$, being $n \in \mathbb{N}$ the number of photons along a certain mode; time-bin or the path degrees of freedom, that can also be discretized in finite separated optical modes. Examples of continuous degrees of freedom are field quadratures and frequency modes. Suitable manipulation techniques of the different degrees of freedom and single-photon detection apparatuses must then be developed to employ photons in quantum information protocols. In particular, three general steps are required: *generation-preparation* of initial quantum states, *manipulation* of the states to accomplish the desired task, and *measurement* to acquire information from the system. Several techniques were then introduced in the last years to generate, manipulate and detect photons.

Generation and preparation of single photons have been demonstrated in different platforms. In particular, it is fundamental to prepare entangled photon states. Indeed entanglement is a distinctive quantum phenomenon predicted by Einstein, Podolsky and Rosen [16], which was shown to be incompatible with local causality by Bell [17]. Recent experimental realizations of Bell tests demonstrated in a nearly unambiguous way that entangled states present correlations that cannot be explained by any classical local hidden-variable theory [18-20]. Other experiments demonstrated, employing photons, entanglement in relation with another peculiar trait of quantum theory such as wave-particle duality [21-23]. Apart from its foundational importance, entanglement lies at the basis of most quantum-enhanced information protocols [1, 24-26]. Entangled photon sources can be realized by exploiting nonlinear effects in $\chi^{(2)}$ nonlinear crystals, in particular spontaneous parametric down conversion (SPDC), by exploiting four-wave mixing (FWM) processes in different platforms or by devising quantum dot platforms.

Several optical devices for each degree of freedom have been developed to manipulate photonic states. For instance the two key elements to manipulate the path degree of freedom of photons are beam splitters (BS), that combine different optical modes, and phase shifters (PS), that insert relative phase shifts between them. Through these two devices one can realize any discrete unitary operation [27]. Manipulation of the polarization degree of freedom can be performed through waveplates, birefringent materials introducing a retardation between two orthogonal polarizations. An appropriate sequence of these elements permits to implement any unitary operation on polarization qubits. Polarizing beam splitters (PBS) spatially divide orthogonal polarizations and can be used as projectors in this degree of freedom. States in the OAM degree of freedom can be generated and manipulated by different devices: spatial light modulators (SLM) [28], that can change the phase and the intensity of an optical beam in each point with a resolution given by pixels area, and q-plates (QPs) [29], inhomogeneous anisotropic materials allowing for manipulation of OAM states conditioned to the polarization states. An appropriate architecture of cascaded QPs and waveplates acting on polarization coin, can engineer arbitrary qudit states in the OAM space [30,31].

Single-photon detectors are then employed to measure the output state after manipulation. Different kind of single-photon detectors have been developed at telecom wavelengths [32,33]. Among the most used ones for $1550\,\mathrm{nm}$ there are InGaAs single-photon avalanche photodiodes (SPADs) [34-36], while higher efficiency is obtained at $1300\,\mathrm{nm}$ with Ge-on-Si SPADs [37-39]. More efficient detectors are those realized by superconducting systems [40-43] also including photon number resolution capabilities [44-46]. Some of the other platforms used for detection are those based on quantum dots [47] and up-conversion [48,49].

Besides the development of each component, future scalable and commercial quantum technologies require the realization of reliable, low-cost, standardized, versatile, compact and efficient quantum information platforms. All these requirements find a natural realization in integrated photonic circuits [50-52]. Such circuits allow for a miniaturization of processes performed in bulk apparatuses, thus reducing problems of stability and scalability. Indeed, in the last few years it has been demonstrated the capability to manipulate photons in directional couplers, to passively and actively control phase shifts, to rotate polarization, to generate and detect single photons. The final aim is then to include all building blocks for photonic quantum information in a single platform, namely: *generation & preparation - manipulation - detection* (fig. 1). Different integrated photonic platforms have been developed for quantum information processing [12,53,54] with different techniques: silica on insulator platforms [55,56], silica on silicon devices [56-58], III-V semiconductors [59-63], UV writing [64,65] and femtosecond laser writing (FLW) [66-73]. While each platform presents its own advantages and drawbacks, no unique system has been currently identified to support integration of all components in a single platform.

In this paper we will focus on the generation and preparation step in the telecom wavelength regime. To this aim, we briefly review different sources of entangled photons pairs of wavelengths at $1.55\,\mu\mathrm{m}$ both in bulk and integrated platforms. We will then focus in more details on the FLW technique, that can be used to write photonic circuits
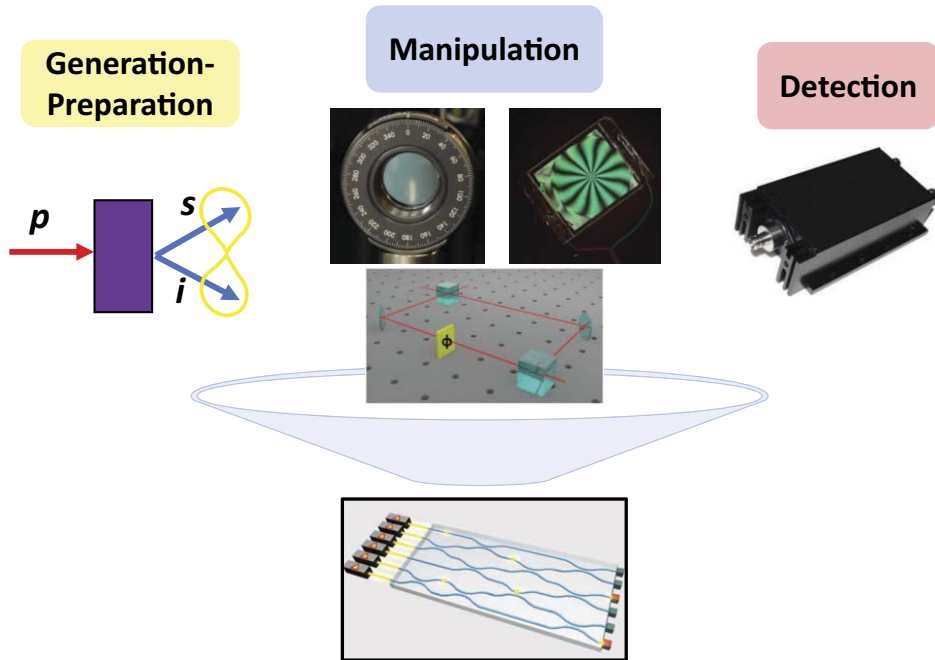
Fig. 1. – Miniaturization of quantum information processes steps in integrated photonic circuits.

for quantum information protocols in glass platforms. In particular, we will describe the adoption of such technique to implement an integrated optical source based on interfacing photonic circuits realized on different materials [74]. The implemented source is versatile and allows to switch from the generation of path-entangled to polarization-entangled photon states, thus also incorporating on the same platform optical elements for photon manipulation.

2. – Platforms for telecom entangled photons sources

In this section we briefly review different architectures for entangled photon sources in the wavelength range around $1.55\,\mu$m. The platforms most commonly employed are those based on SPDC, SFWM and quantum dots. In particular, we will focus on the SPDC process, that is at the basis of the integrated source that will be described in sect. **3**.

2˙1. *SPDC sources*. – Direct entangled photons sources based on SPDC processes in nonlinear $\chi^{(2)}$ crystals [75], were first introduced by Kwiat *et al.* [76], and now represent one of the most common architectures adopted in photonic experiments [77].

SPDC can be described through the second quantization formalism [78]. A pump photon, with the frequency ω_p and momentum $\vec{k}_p$, is annihilated during the interaction with
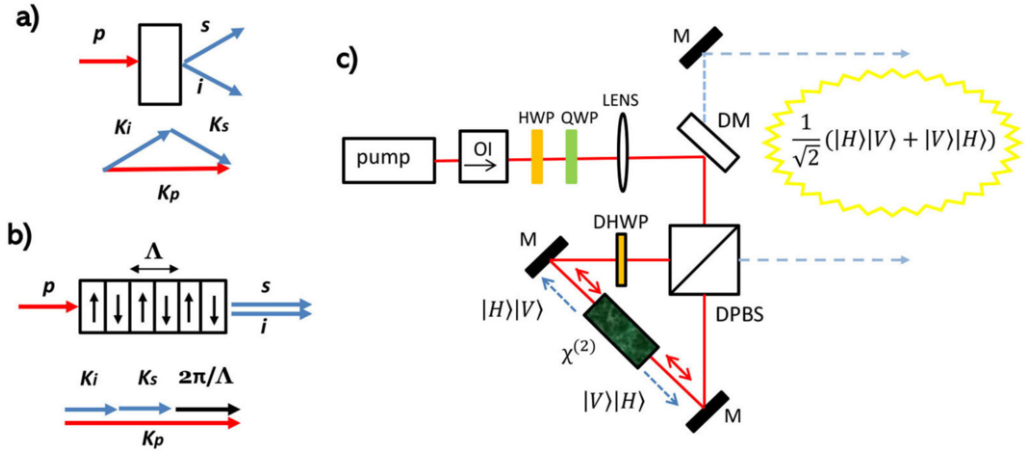
Fig. 2. – a) Non collinear SPDC generation in a $\chi^{(2)}$ crystal (up) and momentum conservation (down). b) Collinear SPDC generation in a periodically poled crystal with period of poling Λ (up) and relative momentum conservation relation (down). p = pump photon, i = idler photon, s = signal photon and k_x the momentum relative to photon x. c) Scheme of a Sagnac-based source of entangled photons in polarization degree of freedom. OI = optical isolator, HWP = half-wave plate, QWP = quarter waveplate, M = mirror, DPBS = dual polarizing beam splitter, DHWP = dual half-wave plate, DM = dichroic mirror.

the vacuum field inside the nonlinear crystal, characterized by a second-order susceptibility $\chi^{(2)}$, and generates two photons: the idler one, with frequency ω_i and momentum $\vec{k}_i$ and the signal one, with frequency ω_s and momentum $\vec{k}_s$ (fig. 2a). In this process involving three photons, two constraints have to be satisfied:

   i) energy conservation: $\omega_p = \omega_i + \omega_s$;

   ii) momentum conservation (phase-matching condition): $\vec{k}_p = \vec{k}_i + \vec{k}_s$.

Under these conditions the Hamiltonian of the process can be written as: $H = \kappa(\hat{a}_p \hat{a}_s^\dagger \hat{a}_i^\dagger + \text{c.c.})$, where $\hat{a}_x^\dagger$ is the creation operator of the photon x ($x = p, i, s$), and κ is a constant depending on $\chi^{(2)}$ and the length of the crystal. Given a coherent pump field $|\alpha\rangle_p$, the unitary operator describing the temporal evolution of the process, with an interaction time t and $\tau \equiv \kappa t$, can be written as: $U = \exp[-i\tau(\hat{a}_p \hat{a}_i^\dagger \hat{a}_s^\dagger + \text{c.c.})] = \mathbb{I} + i\gamma \hat{a}_i^\dagger \hat{a}_s^\dagger - \gamma^2(\hat{a}_i^\dagger \hat{a}_s^\dagger)^2 + \ldots$, being $\mathbb{I}$ the identity and γ^2 the probability of generating one photon pair. When a single pair is generated the state can be written as

$$(1) \qquad |\alpha\rangle_p |0\rangle_i |0\rangle_s \longrightarrow \hat{a}_p \hat{a}_i^\dagger \hat{a}_s^\dagger |\alpha\rangle_p |0\rangle_i |0\rangle_s \approx |\alpha\rangle_p |1\rangle_i |1\rangle_s.$$

The phase-matching condition can be satisfied by birefringent crystals. Different ways to fulfill the phase-matching condition are possible. In type-I phase matching the idler and signal photons share the same polarization, orthogonal with respect to the pump

polarization. Conversely, in type-II phase matching, the idler and signal photons are orthogonally polarized.

The phase-matching condition strictly limits the geometry and the classes of nonlinear crystals that can be used for photon-pair generation. In certain cases this excludes the adoption of crystals with high nonlinear coefficients for a desired generation scheme. In order to overcome such limitation it is possible to exploit a particular construction geometry of ferroelectric crystals. Through an inversion of ferroelectric polarizations it is possible to induce a periodic inversion of the sign of the crystal nonlinear coefficient, with period Λ. Then, a new phase-matching condition for photon pair generation, called *quasi–phase-matching* condition [79], holds:

$$(2) \qquad \vec{k}_p(T) = \vec{k}_s(T) + \vec{k}_i(T) + \frac{2\pi}{\Lambda(T)}\vec{z},$$

where $\Lambda(T)$ is the poling period (including its dependence on the temperature T), and $\vec{z}$ is the pump propagation direction. In this way, by appropriately choosing Λ and the operating temperature, one can reach the generation of photons at the desired wavelengths and specific phase-matching properties [80, 81]. Periodically-poled crystals enable a third phase-matching configuration different from type-I and type-II, called type-0 phase matching. In this case, the idler and the signal share the same polarization of the pump beam. For instance a collinear type-0 phase matching becomes possible, where the photons are emitted with the same polarization and spatial direction of the pump (fig. 2b).

The phase-matching condition and the energy conservation constraints generate correlations between the idler and signal photons. Such correlations can be exploited in suitable geometries to generate entangled states in different degrees of freedom. In particular one can directly generate an entangled state in polarization degree of freedom using a type-II system: by appropriately orienting the crystal optical axis with respect to the pump polarization, the two distinct emission cones (along which the idler and signal photons are generated) can be made to intersect. In this configuration, the photons emitted along these two intersections are entangled in their polarization degree of freedom [76]. Conversely when other geometries are employed, *e.g.* collinear generation, or when other phase-matching conditions are satisfied, such as type-I or type-0, it can be necessary to use interferometers with or without post-selection schemes to generate entangled states. A possible choice of nonlinear crystal for generation of polarization-entangled photons in the noncollinear scheme of [76] at telecom wavelength is beta barium borate (BBO) [82].

In the telecom range other kind of sources are also used, different from noncollinear type-II ones. In particular, a collinear geometry can be employed within interferometers to generate entangled states. One of the most used nonlinear crystals for telecom generation is periodically poled potassium titanyl phosphate (PPKTP), which can be tailored to achieve high-purity polarization-entangled states of photons that are uncorrelated in the spectral and spatial degrees of freedom [83]. The crystal nonlinearity

can be engineered by using different techniques to achieve specific generation characteristics [84, 85]. Such crystal is used in several different configurations. A particular geometry requires a type-II PPKTP generating pairs of photons along the same optical mode. The walk-off between the photons is compensated by inserting a second crystal. Finally, photons are probabilistically divided by means of a beam-splitter to obtain a polarization-entangled state in a post-selected configuration [86, 87]. Alternatively, two type-I crystals can be used to directly generate polarization-entangled states [88].

Sources based on interferometers often require an active phase-stabilization. In order to avoid such technical issue, a Sagnac interferometer can be employed to generate entangled photons from visible to telecom wavelengths [89, 90, 12]. This architecture has the advantage of not requiring active stabilization, since the geometry is intrinsically stable (fig. 2c). In such a geometry, a nonlinear crystal is placed in the centre of a Sagnac interferometer, and photons are generated with a collinear type-II phase matching. The pump beam with linear polarization at $+45°$ enters in the interferometer through a dual wavelength polarizing beam splitter (DPBS), that operates for both the wavelengths of the pump and of the generated photons. The vertically-polarized component of the pump is reflected by the DPBS, and counterclockwise propagates in the Sagnac. Before being injected in the crystal, it propagates through a dual wavelength half-wave plate (an half-wave plate for both the wavelengths at stake) that rotates the polarization to satisfy the phase-matching condition. The generated photons are splitted by the DPBS along two spatial directions ($|V\rangle|H\rangle$ contribution). Conversely the horizontally-polarized component of the pump is transmitted by the DPBS and propagates clockwise generating photons in the other direction and then producing the $|H\rangle|V\rangle$ contribution. Finally the two photons generation paths (clockwise and counterclockwise) are combined by the DPBS, generating the state

$$(3) \qquad |\Psi\rangle = \frac{1}{\sqrt{2}}(|H\rangle|V\rangle + e^{i\phi}|V\rangle|H\rangle).$$

This scheme was applied in the telecom range both with a pulsed pump beam [91-93] and with a CW pumping scheme [94, 95], obtaining high values of fidelity with a maximally entangled state. Different Sagnac-based sources were realized also in a highly nondegenerate configuration with type-I PPKTP crystals [96].

Besides Sagnac interferometer, other stable bulk interferometers can be employed for generation of polarization-entangled states. For example in [83, 20] a stable apparatus was demonstrated, composed of calcite crystals used to split and recombine two generation paths from a PPKTP crystal.

Another crystal employed for telecom entangled generation is periodically poled lithium niobate (PPLN) [97], that was used in different bulk configurations [98-102].

Photons from bulk crystals are generated in different directions. To select a specific direction, single-mode fibers are commonly adopted. Furthermore the maximum generation is limited in a small region of space inside the crystals, that is, the focal region of the pump. A different approach has been shown to allow direct generation

of photon pairs in waveguides. In this scenario, the pump is confined during all the process and the emission occurs along a single mode. Several SPDC sources in nonlinear waveguides [103] have been reported, with enhanced generation and collection efficiencies: PPLN waveguides [104-121] (also for 1310 nm generation [122, 123]), PPKTP waveguides [124], AlGaAs semiconductor waveguides [62, 125-130], periodically poled silica fibers (PPSF) that remarkably do not require a walk-off compensation [131-133], and GaAs-based semiconductor Bragg reflection waveguides (BRW) [134, 135]. PPLN waveguides were also employed in SPDC generation of three-photon polarization-entangled states [136].

Generation of entangled photons in waveguides represents a first step towards integration of sources in miniaturized circuits. This provides advantages in terms of instrinsic stability, and would allow also for generation in waveguides with consequently high brightness, coupling efficiency and fidelity of generated states. Such considerations motivate the realization of all-integrated platforms for suitable and stable sources. A recent review on integrated sources of photonic quantum states can be found in [137]. Different circuits were adopted to generate path-entangled states in chip exploiting PPLN waveguides [113, 138, 139]. First partial attempts in the direction of full integrated polarization-entangled states were done by using PPLN-based circuits [140]. However for such degree of freedom few all-in-chip sources have been realized, in which all the interferometric setup is integrated. In the next sections we will describe how this task can be accomplished by the FLW technique, that permits to generate telecom entangled photons within a tunable interferometer, embedded in an integrated circuit that includes nonlinear waveguides [74]. In table I a list of SPDC sources of entangled photon pairs with wavelengths around 1.55 μm is reported.

2˙2. *SFWM sources*. – The generation of correlated photon pairs can also be obtained through the process of spontaneous four-wave mixing (SFWM) in waveguides [141]. The $\chi^{(3)}$ nonlinearity of optical fibers enables the scattering of two pump photons of frequency $\omega_{p1} = \omega_{p2} = \omega_p$ (for simplicity we consider the case of degenerate pump photons) to generate signal (ω_s) and idler (ω_i) photons according to the energy conservation constraint: $\omega_i + \omega_s = 2\omega_p$, and the momentum conservation: $2\vec{k}_p = \vec{k}_i + \vec{k}_s$ (fig. 3a). The Hamiltonian of the SFWM interaction, assuming that the pump consists of two fields $p1$ and $p2$, can be written as: $H \sim i\hbar\chi^{(3)}\hat{a_{p1}}\hat{a_{p2}}\hat{a_s}^\dagger\hat{a_i}^\dagger$, where $\hat{a_x}^\dagger$ is the creation operator of the photon x ($x = p1, p2, i, s$). At first order, the generated two-photon state reads

$$(4) \quad |\alpha\rangle_{p1}|\alpha\rangle_{p2}|0\rangle_i|0\rangle_s \longrightarrow \hat{a_{p1}}\hat{a_{p2}}\hat{a_i}^\dagger\hat{a_s}^\dagger|\alpha\rangle_{p1}|\alpha\rangle_{p2}|0\rangle_i|0\rangle_s \approx \alpha_{p1}\alpha_{p2}|\alpha\rangle_{p1}|\alpha\rangle_{p2}|1\rangle_i|1\rangle_s.$$

SFWM can be then employed to generate polarization-entangled photons inside birefringent fibers [142], in particular fiber-Sagnac loops [143-149]. A possible scheme [146] is composed of a fiber loop in which a polarizing beam splitter (PBS) divides a linearly polarized pump at 45° (fig. 3b). The vertically polarized component of the pump is reflected by the PBS and propagates clockwise along a dispersion shifted fiber (DSF) having a zero-dispersion wavelength equal to the telecom pump wavelength. The nonlinearity of

Table I. – *Table of telecom SPDC entangled photons sources.*

References	Platforms	Generated states	$\lambda_{i,s}$ range
[82]	BBO type-II pulsed-pump	polarization entanglement	1550 nm
[83, 20]	PPKTP type-II pulsed-pumped interferometer	polarization entanglement	1552 nm
[86]	chirped PPKTP type-II CW-pumped interferometer	polarization entanglement	1490–1610 nm
[87] [95]	PPKTP type-II CW-pumped interferometer	polarization entanglement	1530–1595 nm 1540–1560 nm
[88, 98] [101]	PPKTP, PPLN type-I CW-pumped	polarization entanglement	810,1550 nm 795,1609 nm
[94]	PPKTP type-II CW-pumped Sagnac interferometer	polarization entanglement	1550 nm
[91, 92] [93]	PPKTP type-II pulsed-pump Sagnac interferometer	polarization entanglement	1584 nm 1570 nm
[96, 99]	PPKTP, PPLN type-I Sagnac interferometer	polarization entanglement	810,1550 nm
[100]	PPLN type-II pulsed-pumped	polarization entanglement	1506,1594 nm
[62] [127]	AlGaAs waveguide type-II type-0/I pulsed-pumped	polarization entanglement	1518 nm 1635 nm
[128]	AlGaAs waveguide type-II CW-pumped	polarization entanglement	1560 nm
[107] [111]	PPLN waveguides type-I pulsed-pumped in interferometer	polarization entanglement	1560 nm 1434.6,1606.5 nm
[104, 105, 112]	PPLN waveguides type-I CW-pumped in interferometer	polarization entanglement	1535–1560 nm
[114] [115] [116]	PPLN waveguides type-II CW-pumped	polarization entanglement	1559.8 nm 1551,1571 nm 1540.2 nm
[109] [110]	PPLN waveguides type-0 pulsed-pumped in interferometer	polarization entanglement	1542,1562 nm 1538.8,1558.66 nm
[117] [119, 106]	PPLN waveguides type-0 CW-pumped in interferometer	polarization entanglement	1560.5 nm 1546,1574 nm

Table I. – *Continued.*

References	Platforms	Generated states	$\lambda_{i,s}$ range
[124]	PPKTP waveguides type-II pulsed-pumped in interferometer	polarization entanglement	1540 nm
[120]	PPLN waveguides type-I CW-pumped in interferometer	path entanglement	1551.7,1548.5 nm
[131-133]	PPSF type-II	polarization entanglement	1500–1620 nm
[134] [135]	BRW type-II CW-pumped	polarization entanglement	1537,1575 nm 1550 nm
[138] [139]	PPLN CW pumped pulsed-pumped integrated chip	path entanglement	1560 nm 1519.4 nm
[140]	PPLN type-II CW-pumped partially integrated	polarization entanglement	1554.44 nm
[113]	PPLN type-0 pulsed-pumped integrated chip	path entanglement	1560 nm
[74]	PPLN type-0 CW-pumped all integrated FLW chip	path/polarization entanglement	1560 nm

the fiber enables the SFWM process in which two pump photons annihilate to generate idler and signal photons with vertical polarization: $|V\rangle|V\rangle$. Conversely the horizontally polarized component of the pump propagates counterclockwise along the same fiber generating a contribution $|H\rangle|H\rangle$. The two possible generation paths recombine in the PBS and exit along the same output port. After suppressing the pump through a filter F and separating the idler and signal photons through an arrayed waveguide grating (AWG), the final state reads

$$(5) \qquad |\Psi\rangle = \frac{1}{\sqrt{2}}(|H\rangle|H\rangle + e^{i\phi}|V\rangle|V\rangle),$$

being ϕ a relative phase shift that can be modulated by acting on the polarization of the pump beam.

SFWM (time-energy/polarization) entangled pairs sources can be realized through integrated silicon waveguides [150-164] or AlGaAs waveguides [165]. SFWM generation in waveguides, possibly enhanced by using a ring resonator architecture, is at the basis of photon sources for Si-based photonic integrated circuits. Such circuits, that can be realized in silica-on-silicon and silicon-on-insulator platforms, permit the realization of
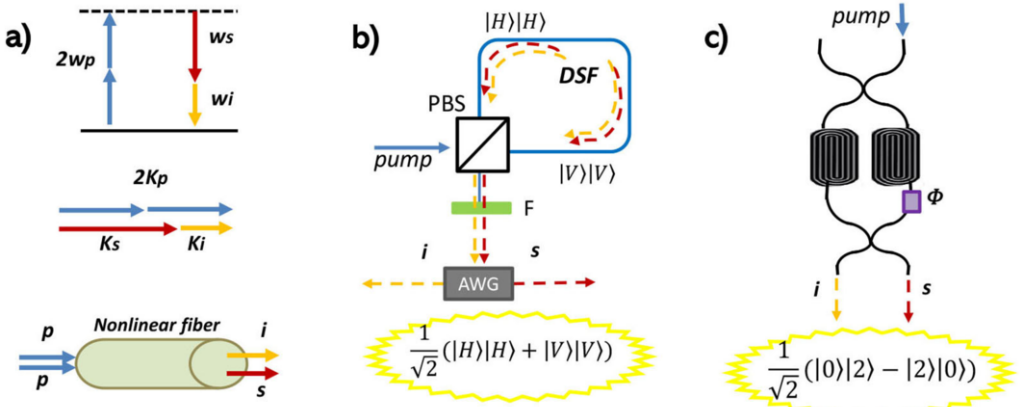
Fig. 3. – a) Energy diagram (up), momentum conservation (middle) of SFWM generation in a nonlinear fiber for degenerate pump photons. p = pump photon, i = idler photon, s = signal photon, w_x and k_x the frequency and momentum relative to photon x = p, i, s. b) Scheme of SFWM polarization-entangled photons generation in a fiber Sagnac loop. DSF = dispersion shifted fiber, AWG = arrayed waveguide grating, F = pump filter, PBS = polarizing beam splitter. c) Scheme of a FWM source of path-entangled photon pairs, in a silicon-on-insulator device. The final state is obtained in the degenerate generation in which the phase shift ϕ between the arms of the interferometer is set to zero.

integrated quantum photonics thanks to the properties of Si-based waveguides [55-58]. The high refractive index contrast of the waveguides allows high field confinement, thus leading to reduced circuit size. Furthermore, such platforms present large nonlinearities exploitable for entangled photons generation, and are compatible with different standard electronics elements, and fast optical modulators. However, the possibility of supporting the propagation of polarization-entangled states is currently prevented by birefringence. For this reason, the main degree of freedom manipulated for quantum processes within this platform is given by the optical path. It is then crucial to include sources of path-entangled photon sources integrated in these devices. This aim can be accomplished by exploiting SFWM [166-168]. A scheme for the generation of two-photons path-entangled states [166] exploits the silicon-on-insulator integrated circuit represented in fig. 3c. The pump beam enters along a waveguide and is equally split by a first directional coupler. For each of the two paths, the pump beam enters in a spiralled waveguide where signal (s) and idler (i) photons are generated by SFWM. The two parallel generations are combined in a second coupler leading to the generation of an output state of the form

$$
(6) \qquad |\Psi\rangle = \cos\phi \left[\frac{1}{\sqrt{2}} (|1_s 1_i\rangle_A |0_s 0_i\rangle_B - |0_s 0_i\rangle_A |1_s 1_i\rangle_B) \right]
$$
$$
+ \sin\phi \left[\frac{1}{\sqrt{2}} (|1_s 0_i\rangle_A |0_s 1_i\rangle_B + |0_s 1_i\rangle_A |1_s 0_i\rangle_B) \right],
$$

where A and B are the two paths, and ϕ is a relative phase shift that can be tuned

by means of a thermal phase shifter. For the case of degenerate generated photons and $\phi = 0$, the maximally entangled state is obtained: $|\Psi\rangle = \frac{1}{\sqrt{2}}(|2\rangle|0\rangle - |0\rangle|2\rangle)$ (fig. 3c). Note that a two-colour pump is necessary for degenerate generation, otherwise the pump cannot be divided from the generated photons. Such platforms can be also exploited to generate multidimensional entangled states [169].

2˙**3.** *Other sources*. – SPDC and FWM are nondeterministic processes that cannot be exploited to realize on demand sources. In order to achieve deterministic single-photon sources different platforms have been proposed. In particular, quantum dots are becoming a fundamental tool to generate single photons on demand [170-175]. They can also be employed to generate entangled pairs at telecom wavelength, in both windows around 1300 nm [176] and 1550 nm [177], by using InGaAs-based quantum dots.

3. – Femtosecond Laser Writing Technique for integrated source of telecom entangled states

Here we will briefly describe the FLW technique and its capability to design circuits that permit to generate and manipulate photons in both path and polarization degrees of freedom. Then, we will show how such technique enables the realization of a modular and reconfigurable path and polarization-entangled photon source in an integrated device [74].

3˙1. *FLW technique*. – Femtosecond laser waveguide writing is a fabrication technique that has been recently employed to design integrated quantum photonics platforms [68-73, 178-181]. Femtosecond laser writing exploits strong laser pulses (in the femtosecond regime), with energy lower than the energy gap of the substrate material. The laser is focused inside the material substrate to induce a localized permanent modification of the refractive index by non-linear absorption processes [68, 178, 182-187]. Moving the substrate with respect to the laser focus, waveguides and complex photonic circuits can be written at constant velocity with micrometric precision (fig. 4). Two writing configurations can be adopted [179]. The longitudinal one, in which the substrate is translated along the direction of the focused laser beam, has spatial range limitations due to the working distances of the employed optics. Conversely, the transverse writing configuration, in which the translation is perpendicular to the laser propagation direction, leads to asymmetric waveguide cross sections (higher birefringence). This latter drawback can be overcome by multiscan approaches. The features of the written waveguides depend on different parameters such as wavelength and energy pulse of the laser, pulse duration and the focus numerical aperture. FLW offers several advantages compared to other microfabrication techniques such as lithographic technologies. The production cost is relatively low and the fabrication process is fast (above 40 mm/s), without the need of clean rooms. Circuits within the substrates can be written in the 3D space, allowing for the realization of complex geometries [188-197]. In parallel, losses are relatively low: propagation losses can reach values near 0.1–0.3 dB/cm while coupling losses $\sim 27\%$ [198]. Laser-written waveguides in glasses can show a low birefringence and can be realized with circular cross section, then they are polarization insensitive [199]. Hence, these waveguide
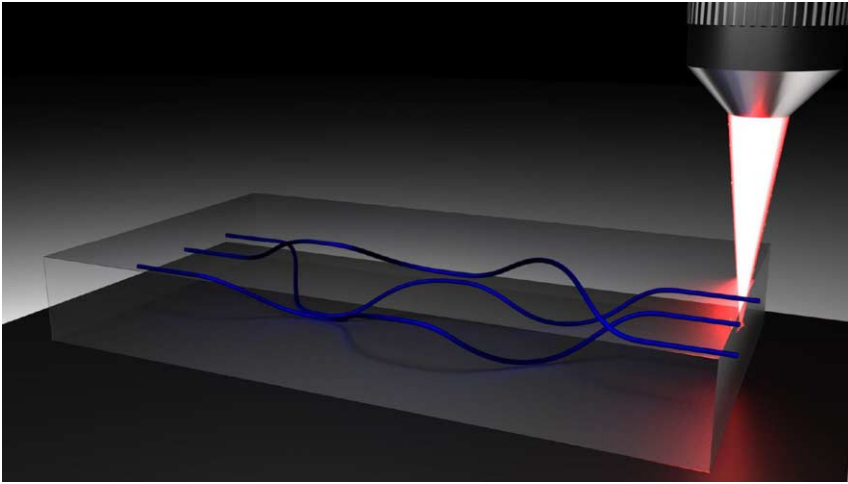
Fig. 4. – Femtosecond laser writing on a glass via a transverse geometry.

support propagation of polarization qubits [200]. Different transparent materials, such as glasses, crystals and polymers can be processed for the realization of FLW circuits.

Through the geometry of the waveguides, the path degree of freedom of the photons can be manipulated. Appropriately chosen sequences of two-dimensional beam splitters and phase shifters allow for the implementation of any arbitrary discrete unitary in the path degree of freedom [27]. It is then crucial to obtain capability of implementing these two key elements with high precision. Beam splitters can be realized through directional couplers (DCs). In the lossless assumption, a directional coupler can be expressed by the unitary matrix

$$(7) \qquad U_{dr} = \begin{pmatrix} \sqrt{T} & i\sqrt{1-T} \\ i\sqrt{1-T} & \sqrt{T} \end{pmatrix},$$

where T is the coupler transmittivity. Such operation is achieved by means of the evanescent fields coupling mechanism between two adjacent waveguides, which allows the transfer of electromagnetic field amplitude from one waveguide to another. The two key fabrication parameters of a directional coupler that permit to control the transmittivity T are the interaction length, L and the distance d between the two waveguides (fig. 5a), according to

$$(8) \qquad T \approx \sin^2(KL),$$

where K is a coupling coefficient that decreases exponentially with the distance d.

A static phase shifter can be achieved by implementing a delay in one waveguide
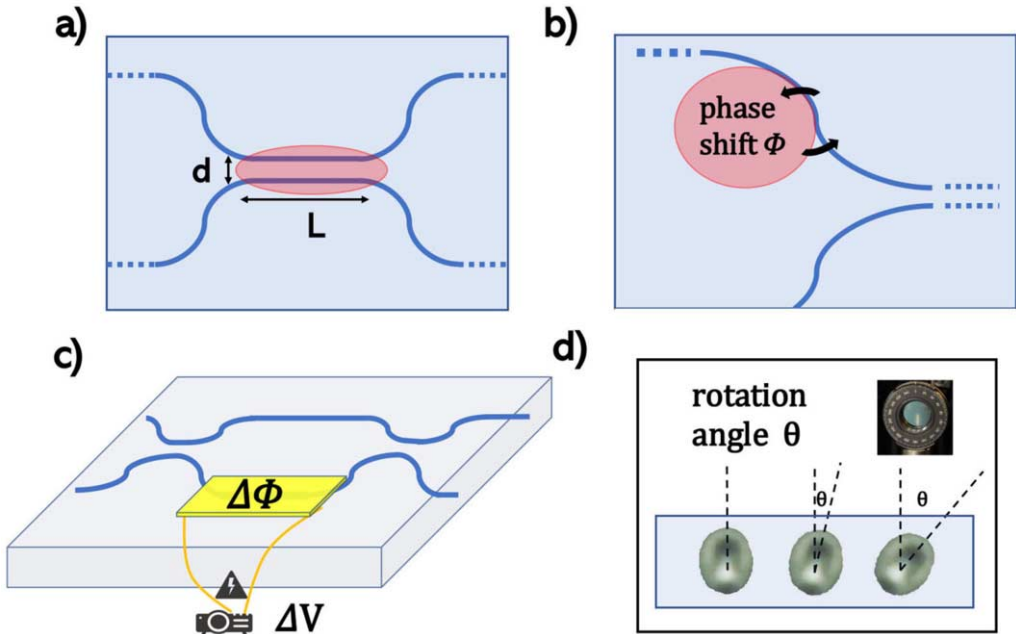
Fig. 5. – a) Scheme of a directional coupler, whose transmittivity depends on the length (L) and distance (d) of interaction between the coupled waveguides. By appropriately controlling the geometry, polarization independent beam-splitters or polarizing beam-splitters can be implemented. b) Static phase shift (ϕ) can be controlled by appropriately bending one of the waveguide. c) Tunable phase shifts can be obtained through thin gold thermoresistors upon the waveguide: applying a voltage ΔV, the dissipated heat changes locally the waveguide index of refraction. d) Cross sections of the waveguides at different rotations of angle θ.

compared to another. It can be written as the unitary transformation

$$(9) \qquad U_{ps} = \begin{pmatrix} 1 & 0 \\ 0 & e^{i\phi} \end{pmatrix},$$

where ϕ is the relative phase shift. In an integrated device this is obtained by bending the waveguide and hence stretching the optical path (fig. 5b). This method introduces a static phase shift defined at the fabrication stage, that cannot be changed during the circuit operation. FLW allows also to design circuits with reconfiguration capabilities, allowing to change the phase shifts by means of thermal shifters [201,202]. These devices induce a local change of the refractive index in an arbitrary point of the chip by exploiting thermo-optics effects. Such operation can be performed by means of resistive heaters, constituted by thin gold films (~ 50 nm) deposited on the chip in the proximity of the waveguides. The resistor pattern is defined by laser ablation, obtained by focusing on the sample surface a femtosecond laser beam. By applying a voltage ΔV over the resistor, heat is dissipated into the bulk of the chip changing locally the waveguide index of refraction,

thus resulting in a phase modification. Given the dissipated power $P_{diss} = \Delta V^2/R$ on the ohmic resistor R, the phase shift $\Delta\phi$ induced on the waveguide can be expressed by

$$(10) \qquad\qquad\qquad\qquad \Delta\phi \approx \alpha P_{diss},$$

being α a coefficient dependent on the geometric, thermal and optical properties of the substrate material. Then, through phase shifters and directional couplers, arbitrary linear optical interferometers can be realized to obtain full control of the path degree of freedom.

Moreover, the potential of the FLW technique allows to design integrated optical elements for manipulation of the polarization degree of freedom. In order to employ polarization states inside the circuits, two requirements are necessary: i) directional couplers whose splitting ratio is polarization independent that can be implemented by FLW, and ii) optical elements that allow for the manipulation of the polarization. In this degree of freedom, the two key optical elements are waveplates and polarizing beam splitter. Such devices can be realized by the FLW technique [203-207]. In [204,205] directional couplers were implemented with splitting ratio that can be regulated indipendently for horizontal and vertical polarizations, enabling the integration of polarizing beam splitters. In [203] integrated waveplates with arbitrarily rotated birefringence axis were realized. This is obtained by modifying the writing laser beam angle with respect to the substrate. In such a way the fabricated waveguide will have a tilted cross-section and hence tilted birefringence axis, acting as a rotated waveplate.

FLW has been used for a broad range of quantum information applications. Integrated circuits were used to perform: quantum gates [205, 208, 209, 189, 190], quantum walks and simulation processes [210-213], generation of path-polarization hyper-entangled and cluster states [214], boson sampling experiments [215-218] quantum contextuality test [219], quantum multiphase estimation [220], sensing application [221], photon indistinguishability test [222], quantum single-photon storage [223], state transfer of entangled qubits [224], microfluidics in fused silica [225].

3.2. *FLW for fully integrated source of telecom entangled states.* – We describe here how FLW can be exploited to implement an all-in-chip source able to generate path- or polarization-entangled states at telecom wavelength with a modular approach [74]. Such fully integrated source relies on the hybrid assembly of three circuits written on different materials through the FLW technique. The three cascaded integrated devices implement the entangled source and the third device can be changed to switch between polarization- and path-entangled output states.

The first circuit is written in aluminum-borosilicate glass and includes a reconfigurable and balanced directional coupler at 780 nm wavelength. The laser pulses, employed for the writing process, have duration of about 300 fs, wavelength $\lambda_{pulses} = 1030$ nm, 1 MHz repetition rate and 220 nJ pulse energy. The coupler, inscribed 25 µm below the chip surface, is used for single-mode manipulation of the continuous-wave pump at 780.31 nm with waveguides having a $1/e^2$ mode size of $8\times9\,\mu m^2$ at that wavelength. The first device

(D1) is covered by a 50 nm gold layer, required for a thermo-optic resistor (75 ohm) able to implement a phase shift ϕ from 0 to 2π with a dissipated power up to about 0.4 W. Such phase shift will be the relative phase in the generated polarization-entangled state and will be the control of the amount of entanglement in the case of path entangled state.

The pump, equally divided by the first device, is coupled with $\sim 75\%$ of efficiency to the second 18 mm-long chip (D2), containing the nonlinear waveguides written in a PPLN substrate. The crystal is z-cut and has a poling period $\Lambda = 19.5\,\mu$m, satisfying a degenerate type-0 phase-matching condition at room temperature with a pump wavelength $\lambda_p = 780.31$ nm, corresponding to idler and signal wavelengths of $\lambda_{i,s} = 1560.62$ nm. The two inscribed waveguides have a single-mode size of $12 \times 12\,\mu$m^2 for 780 nm and $18 \times 16\,\mu$m^2 for 1550 nm wavelength. Waveguides were fabricated by exploiting a multiscan technique [226]. The waveguides have a very similar nonlinear properties since the measured overlap between their second-harmonic generations was above 99%. The power of SPDC emission from a waveguide pumped with an input power P_p, can be expressed as [227]

$$(11) \qquad P_{\text{SPDC}} \propto \omega_i \int \left| \frac{\sinh(l\sqrt{(\omega_i/\omega_s)\kappa^2 P_p - \Delta^2})}{l\sqrt{(\omega_i/\omega_s)\kappa^2 P_p - \Delta^2}} \right|^2 \, d\omega_s,$$

where l is the length of interaction, κ the nonlinear coupling coefficient and Δ is the phase mismatch.

The telecom photon pair generated by SPDC processes along the nonlinear waveguides are coupled to the third device with an efficiency of $\sim 80\%$. The third chip is necessary for the entangled state generation and can be chosen between two different devices (D3a and D3b) depending on the desired output state. For the path-entangled state D3a has to be adopted. The latter is composed of a balanced directional coupler at 1560 nm that recombines the two possible generation paths from the PPLN device. The waveguides are written at $170\,\mu$m depth with respect to the glass surface, through laser pulses of 370 nJ pulse energy. The mode profile is near circular with a $1/e^2$ diameter of $15.5\,\mu$m. Propagation losses of this device are approximately 0.3 dB/cm. To generate a polarization-entangled state, the 37 mm $\times$ 12 mm device D3b has to replace D3a. Such circuit contains two integrated half-wave plates, with optical axis tilted, respectively, by $22.5°$ and $-22.5°$, implemented through the technique discussed in [203], and achieving a polarization rotation efficiency $> 98\%$. Then, a balanced polarization-insensitive directional coupler at 1560 nm [228] recombines two possible generation paths.

Let us now discuss the generation process in more detail. We consider the case in which a pump photon generates a photon pair. The pump is injected along the mode 2 of D1 propagating through the directional coupler and the phase shifter. The state at the output of D1 reads

$$(12) \qquad |\Psi\rangle_{\text{in}} = |0\rangle_1 |\alpha\rangle_2 \xrightarrow{\text{D1}} |\alpha/\sqrt{2}\rangle_1 |e^{\imath\phi}\alpha/\sqrt{2}\rangle_2,$$

where state $|\beta\rangle_i$ stands for a coherent state along the mode $i = 1, 2$. Then, the pump

enters in D2 and generates, through type-0 SPDC, a pair of degenerate telecom photons:

$$(13) \qquad |\alpha/\sqrt{2}\rangle_1 |e^{\iota\phi}\alpha/\sqrt{2}\rangle_2 \xrightarrow{\text{D2}} \frac{1}{\sqrt{2}} \left(|0\rangle_1 |2\rangle_2 + e^{i\phi}|2\rangle_1 |0\rangle_2 \right),$$

where $|k\rangle_i$ stands for k photons in mode $i = 1, 2$.

Finally the two possible generation paths are combined in the directional couplers of D3a or D3b. In the case of D3a the final state $|\Psi(\phi)\rangle^a_{fin}$ is a path entangled state:

$$(14) \qquad |\Psi(\phi)\rangle^a_{\text{fin}} = \cos(\phi/2) \left[\frac{1}{\sqrt{2}} \left(|0\rangle_1 |2\rangle_2 + |2\rangle_1 |0\rangle_2 \right) \right] + \sin(\phi/2) \, |1\rangle_1 |1\rangle_2.$$

The degree of entanglement can be modified by tuning the phase shift ϕ, through a change in the voltage applied on the thermoresistor. For $\phi = 0$ we obtain the maximally entangled NOON state: $|\Psi(0)\rangle^a_{\text{fin}} = \frac{1}{\sqrt{2}}(|0\rangle_1 |2\rangle_2 + |2\rangle_1 |0\rangle_2)$, while for $\phi = \pi$ the state will be separable: $|\Psi(\pi)\rangle^a_{\text{fin}} = |1\rangle_1 |1\rangle_2$.

The generation can be switched from path- to polarization-entanglement by substituting D3a with D3b. In this case, photons along path 1 will be rotated by the half-wave plate to a diagonal state, $|+\rangle \equiv \frac{1}{\sqrt{2}}(|H\rangle + |V\rangle)$, while photons along path 2 will be rotated by the half-wave plate to an antidiagonal state $|-\rangle \equiv \frac{1}{\sqrt{2}}(|H\rangle - |V\rangle)$. By post-selecting to those cases in which one photon exits from each output port of D3b, the final state $|\Psi(\phi)\rangle^b_{\text{fin}}$ will be

$$(15) \qquad |\Psi(\phi)\rangle^b_{\text{fin}} = \frac{1}{\sqrt{2}} \left(|+\rangle_1 |+\rangle_2 + e^{i\phi}|-\rangle_1 |-\rangle_2 \right),$$

that is, a maximally entangled state in the polarization degree of freedom.

The experimental setup used in [74] to generate and analyze the generated states is shown in fig. 6. A single-mode fiber array at 780 nm injects the pump beam, a CW Ti:Sapphire laser, in input port 1 of D1. After the third chip, the generated photons from the two output modes are collected in a second single-mode fiber array at 1560 nm and are separated from the residual pump beam by long-pass filters with an extinction ratio of 102 dB at 780 nm. The photons are detected by recording two-fold coincidences between two single-photon detectors placed at the output. The first one operates in free running mode and triggers the other in external gating mode (in this configuration, both detectors reach an efficiency of 25%).

Let us first discuss the measurements on the path-entangled state (D3a inserted). In this case there are two possible measurement configurations (fig. 6a): i) measurements of the contribution $|1\rangle_1 |1\rangle_2$ for which the two outputs are directly connected to the detectors, ii) measurements on the contribution $|0\rangle_1 |2\rangle_2$, obtained by injecting the output 2 into a fiber beam splitter (FBS), whose two outputs are set to the detectors. The measurements of the two contributions are performed separately. Given the state in (14), the detection probability of the contribution $|1\rangle_1 |1\rangle_2$ varies as $\sin^2(\phi/2)$ with respect to the phase shift ϕ, while the probability of the contribution $|2\rangle_1 |0\rangle_2$ changes as $\cos^2(\phi/2)$. The measured
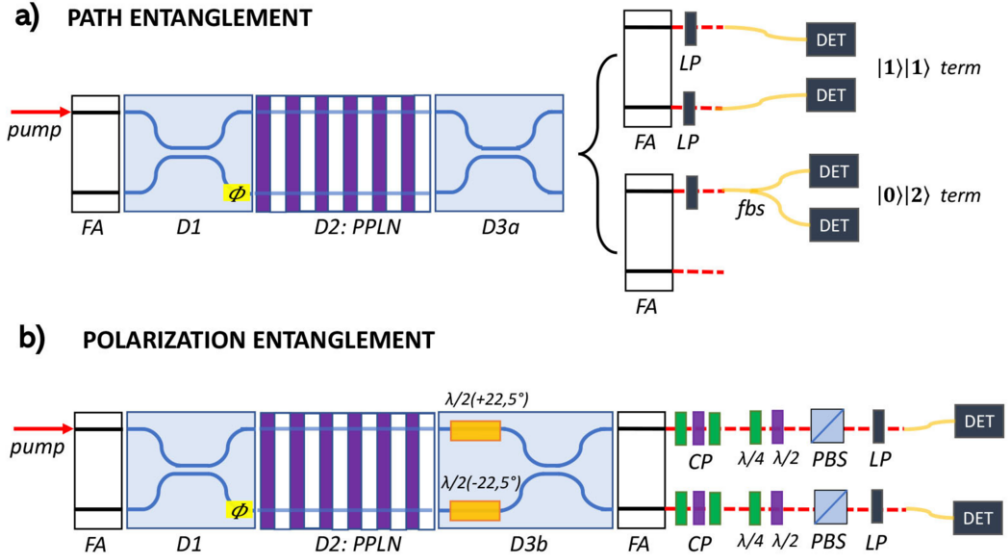
Fig. 6. – a) Scheme of the source of path entangled state. Two measurement configurations are used to measure, respectively, the $|1\rangle_1|1\rangle_2$ (up) and $|0\rangle_1|2\rangle_2$ (down) generated terms. b) Scheme of the source of path entangled state. FA = fiber array, D1 = first device composed of balanced directional coupler at 780 nm and tunable phase shift ϕ, D2 = PPLN chip, D3a = balanced directional coupler 1560 nm, fbs = fiber beam splitter, $\lambda/2$ = half-wave plate, $\lambda/4$ = quarter-wave plate, D3b = device composed of half-wave plates and directional coupler at 1560 nm, CP = polarization control, PBS = polarizing beam splitter, LP = long pass filter, DET = single photon detector.

fringe patterns are shown in fig. 7a, and the corresponding fringes visibilities, are reported in table II. The obtained results demonstrate the high quality of the generated state.

On the other hand, the measurements on the polarization-entangled state are performed by a polarization stage and a detector for each output mode (fig. 6b). The output state in (15) is rotated, by means of compensation waveplates, to the state

$$(16) \qquad |\Psi(\phi)\rangle_{\text{fin}}^{b'} = \frac{1}{\sqrt{2}} \left(|H\rangle_1|H\rangle_2 + e^{i\phi}|V\rangle_1|V\rangle_2 \right).$$

Such state presents sinusoidal fringes as a function of ϕ when measured in the diagonal basis $|+/-\rangle$, while being constant in the $|H/V\rangle$ basis (fig. 7b). The obtained visibilities are reported in table II and demonstrate the quality of the generated state.

Finally we set to $\phi = \pi$ the phase shift in state (16), thus generating the Bell state: $|\Phi^-\rangle = \frac{1}{\sqrt{2}}(|H\rangle_1|H\rangle_2 - |V\rangle_1|V\rangle_2)$. To fully verify the generated state, a quantum state tomography [229] has been performed. The measured fidelity of the generated density matrix ρ_{exp} with respect to the ideal Bell state ρ_{ϕ^-} was: $\mathcal{F}(\rho_{\text{exp}}, \rho_{\phi^-}) = \text{Tr}[(\sqrt{\rho_{\text{exp}}}\rho_{\phi^-}\sqrt{\rho_{\text{exp}}})^{1/2}]^2 = 0.929 \pm 0.011$. For such a state the purity was $\Psi = \text{Tr}[\rho_{\text{exp}}^2] =$
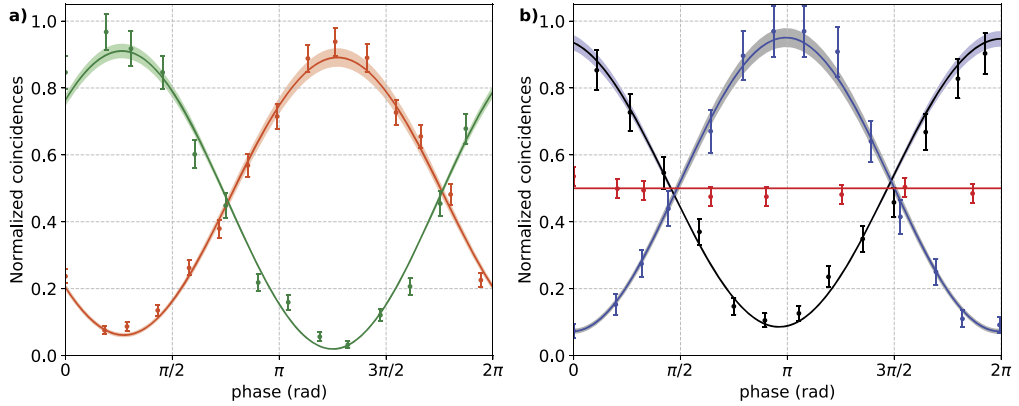
Fig. 7. – a) Measured fringe patterns for path-entangled state as a function of phase shift ϕ, tuned by changing the applied voltage on thermo-resistor in D1. Green: $|0\rangle_1|2\rangle_2$ contribution. Orange: $|1\rangle_1|1\rangle_2$ contribution. b) Measured fringe patterns for polarization-entangled state as a function of phase shift ϕ, tuned by changing the applied voltage on thermo-resistor in D1. Black: $|+\rangle_1|+\rangle_2$ contribution. Blue: $|+\rangle_1|-\rangle_2$ contribution. Red: $|H\rangle_1|H\rangle_2$ contribution. In all plots, shaded regions are 1-σ confidence intervals on the fit parameters. Error bars are due to the Poissonian statistics of the measured coincidences.

0.908 ± 0.018, and the concurrence was $C = 0.905 \pm 0.022$. Furthermore another measure of entanglement is performed through the quantity [230]: $S \equiv \sum_{i=X,Y,Z} |\langle \sigma_i \otimes \sigma_i \rangle|$, where σ_i $(i = x, y, z)$ represent the Pauli matrices. For all separable states this inequality holds: $S \leq 1$, thus representing an entanglement witness on the state [24]. We measured a value $S_{\mathrm{exp}} = 2.782 \pm 0.015$ (by subtracting for accidental coincidences). The separable limit is violated by ~ 118 standard deviations, thus demonstrating the presence of polarization entanglement in the generated state.

4. – Conclusions

Reliable generation of entangled photons at telecom wavelength is a crucial requirement in the context of quantum communication and for future quantum networks. Dif-

TABLE II. – *Table of the fringes visibilities for both the path- and polarization-entangled states and for different measurement configurations. V^{raw} are the experimental visibilities obtained from raw data, while V are obtained by subtracting for accidental coincidences.*

	$|0\rangle_1|2\rangle_2$	$|1\rangle_1|1\rangle_2$	$|+\rangle_1|-\rangle_2$	$|+\rangle_1|+\rangle_2$
V	0.980 ± 0.004	0.970 ± 0.004	0.929 ± 0.017	0.957 ± 0.015
V^{raw}	0.935 ± 0.003	0.877 ± 0.004	0.834 ± 0.018	0.858 ± 0.019

ferent platforms have been developed to accomplish such task. A promising approach employs integrated photonics circuits for stable, scalable and efficient implementation of quantum information protocols. In particular FLW enabled the realization of a broad range of photonic components including photon sources.

Recently a fully integrated source able to generate telecom photons in both the polarization and path degrees of freedom was implemented by using the FLW technique. This kind of platform promises to be a building block for future all-in-chip quantum processes that will include on-chip sources, manipulation and detection [231-235]. Minimizing the losses and maximizing stability and efficiency, fully integrated circuits can be employed to accomplish several tasks that cannot be tackled with a bulk optics approach. A near term goal is represented quantum-enhanced multiphase estimation experiments [236, 237, 220]. In this context, dynamical reconfigurability of the devices will permit to implement adaptive estimation protocols that generalize single-parameter approaches [238, 239]. This would also require the development of integrated sources at wavelengths different from $1.55\,\mu m$, for applications in quantum sensing on biological systems [221]. The integration of photon sources can also be a fundamental step to improve boson sampling experiments in systems of progressively increasing size [215-218, 240-250]. Finally, integrated sources can also become a significant tool for future satellite-based quantum network [251-255].

$$* * *$$

REFERENCES

[1] Nielsen M. A. and Chuang I. L., *Quantum Computation and Quantum Information* (Cambridge University Press) 2010.
[2] Morsch O. and Oberthaler M., *Rev. Mod. Phys.*, **78** (2006) 179.
[3] Cirac J. I. and Zoller P., *Phys. Rev. Lett.*, **74** (1995) 4091.
[4] Schaetz T., *J. Phys. B: At. Mol. Opt. Phys.*, **50** (2017) 102001.
[5] Clarke J. and Frank K. W., *Nature*, **453** (2008) 1031.
[6] Nakamura Y., Pashkin Yu. A. and Tsai J. S., *Nature*, **398** (1999) 6730.
[7] Wendin G., *Rep. Prog. Phys.*, **80** (2017) 106001.
[8] Kane B., *Nature*, **393** (1998) 133.
[9] Cory D. G., Fahmy A. F. and Havel T. F., *Proc. Natl. Acad. Sci. U.S.A.*, **94** (1997) 1634.
[10] Hanson R., Kouwenhoven L. P., Petta J. R., Tarucha S. and Vandersypen L. M. K., *Rev. Mod. Phys.*, **79** (2007) 1217.
[11] Imamoglu A., Awschalom D. D., Burkard G., DiVincenzo D. P., Loss D., Sherwin M. and Small A., *Phys. Rev. Lett.*, **83** (1999) 4204.
[12] Flamini F., Spagnolo N. and Sciarrino F., *Rep. Prog. Phys.*, **82** (2019) 016001.
[13] Dowling J. P. and Milburn G. J., *Trans. R. Soc. London, Ser. A*, **361** (2003) 1655.

[14] O'Brien J. L., Furusawa A. and Vučković J., *Nat. Photon.*, **3** (2009) 687.

[15] Gisin N. and Thew R., *Nat. Photon.*, **1** (2007) 165.

[16] Einstein A., Podolsky B. and Rosen N., *Phys. Rev.*, **47** (1935) 10.

[17] Bell J. S., *Phys. Rev. Lett.*, **1** (1964) 3.

[18] Hensen B. *et al.*, *Nature*, **526** (2015) 682.

[19] Giustina M. *et al.*, *Phys. Rev. Lett.*, **115** (2015) 250401.

[20] Shalm L. K. *et al.*, *Phys. Rev. Lett.*, **115** (2015) 250402.

[21] Rab A. S., Polino E., Man Z.-X., An N. B., Xia Y.-J., Spagnolo N., Lo Franco R. and Sciarrino F., *Nat. Commun.*, **8** (2017) 915.

[22] Kaiser F., Coudreau T., Milman P., Ostrowsky D. B. and Tanzilli S., *Science*, **338** (2012) 1226755.

[23] Peruzzo A., Shadbolt P. J., Brunner N., Popescu S. and O'Brien J. L., *Science*, **338** (2012) 1226719.

[24] Horodecki R., Horodecki P., Horodecki M. and Horodecki K., *Rev. Mod. Phys.*, **81** (2009) 865.

[25] Brunner N., Cavalcanti D., Pironio S., V. Scarani V. and Wehner S., *Rev. Mod. Phys.*, **86** (2014) 419.

[26] Adesso G., Bromley T. R. and Cianciaruso M., *J. Phys. A Math. Theor.*, **49** (2016) 473001.

[27] Reck M., Zeilinger A., Bernstein H. J. and Bertani P., *Phys. Rev. Lett.*, **73** (1994) 58.

[28] Gruneisen M. T., Miller W. A., Dymale R. C. and Sweiti A. M., *Appl. Opt.*, **47** (2008) 4.

[29] Marrucci L., Manzo C. and Paparo D., *Phys. Rev. Lett.*, **96** (2006) 163905.

[30] Giordani T., Polino E., Emiliani S., Suprano A., Innocenti L., Majury H., Marrucci L., Paternostro M., Ferraro A., Spagnolo N. and Sciarrino F., *Phys. Rev. Lett.*, **122** (2019) 020503.

[31] Innocenti L., Majury H., Giordani T., Spagnolo N., Sciarrino F., Paternostro M. and Ferraro A., *Phys. Rev. A*, **96** (2017) 062326.

[32] Hadfield R. H., *Nat. Photon.*, **3** (2009) 696.

[33] Eisaman M. D., Fan J., Migdall A. and Polyakov S. V., *Rev. Sci. Instrum.*, **82** (2011) 071101.

[34] Hiskett P. A., Buller G. S., Loudon A. Y., Smith J. M., Gontijo I., Walker A. C., Townsend P. D. and Robertson M. J., *Appl. Opt.*, **39** (2010) 6818.

[35] Zhang J., Itzler M. A., Zbinden H. and Pan J. W., *Light Sci. Appl.*, **4** (2015) e286.

[36] Comandar L. C., Fröhlich B., Dynes J. F., Sharpe A. W., Lucamarini M., Yuan Z. L., Penty R. V. and Shields A. J., *J. Appl. Phys.*, **117** (2015) 083109.

[37] Warburton R. E., Intermite G., Myronov M., Allred P., Leadley D. R., Gallacher K., Paul D. J., Pilgrim N. J., Lever L. J. M., Ikonic Z., Kelsall R. W., Huante-Cerón E., Knights A. P. and Buller G. S., *IEEE Trans. Electr. Dev.*, **60** (2013) 3807.

[38] Martinez N. J. D., Gehl M., Derose C. T., Starbuck A. L., Pomerene A. T., Lentine A. L., Trotter D. C. and Davids P. S., *Opt. Express*, **25** (2017) 16130.

[39] Peacock A., Verhoeve P., Rando N., Dordrecht A., Taylor B. G., Erd C., Perryman M. A. C., Venn R., Howlett J., Goldie D. J., Lumley J. and Wallis M., *Nature*, **381** (1996) 135.

[40] Goltsman G. N., Okunev O., Chulkova G., Lipatov A., Semenov A., Smirnov K., Voronov B. and Dzardanov A., *Appl. Phys. Lett.*, **79** (2001) 705.

[41] Rosfjord K. M., Yang J. K. W., Dauler E. A., Kerman A. J., V. Anant, Voronov B. M., Goltsman G. N. and Berggren K. K., *Opt. Express*, **14** (2006) 527.

[42] Natarajan C. M., Tanner M. G. and Hadfield R. H., *Supercond. Sci. Technol.*, **25** (2012) 063001.

[43] Marsili F., Verma V. B., Stern J. A., Harrington S., Lita A. E., Gerrits T., Vayshenker I., Baek B., Shaw M. D., Mirin R. P. and Nam S. W., *Nat. Photon.*, **7** (2013) 210.

[44] Rosenberg D., Lita A. E., Miller A. J., Nam S. W., *Phys. Rev. A*, **71** (2005) 061803.

[45] Divochiy A., Marsili F., Bitauld D., Gaggero A., Leoni R., Mattioli F., Korneev A., Seleznev V., Kaurova N., Minaeva O., Goltsman G., Lagoudakis K. G., Benkhaoul M., Lévy F. and Fiore A., *Nat. Photon.*, **2** (2008) 302.

[46] Gerrits T., Thomas-Peter N., Gates J. C., Lita A. E., Metcalf B. J., Calkins B., Tomlin N. A., Fox A. E., Lamas Linares A., Spring J. B., Langford N. K., Mirin R. P., Smith P. G. R., Walmsley I. A. and Nam S. W., *Phys. Rev. A*, **84** (2011) 060301.

[47] Li H. W., Kardynał B. E., See P., Shields A. J., Simmonds P., Beere H. E. and Ritchie D. A., *Appl. Phys. Lett.*, **91** (2007) 073516.

[48] Vandevender A. P. and Kwiat P. G., *J. Mod. Opt.*, **51** (2004) 1433.

[49] Zheng M. Y., Shentu G. L., Ma F., Zhou F., Zhang H. T., Dai Y. Q., Xie X., Zhang Q. and Pan J. W., *Rev. Sci. Instrum.*, **87** (2016) 093115.

[50] Tanzilli S., Martin A., Kaiser F., De Micheli M., Alibart O. and Ostrowsky D. B., *Rev. Sci. Instrum.*, **6** (2012) 115.

[51] Orieux A. and Diamanti E., *J. Opt.*, **18** (2016) 083002.

[52] Carolan J., Harrold C., Sparrow C., Martin-Lopez E., Russell N. J., Silverstone J. W., Shadbolt P. J., Matsuda N., Oguma M., Itoh M., Marshall G. D., Thompson M. G., Matthews J. C. F., Hashimoto T., O'Brien J. L. and Laing A., *Science*, **349** (2015) 711.

[53] Bogdanov S., Shalaginov M. Y., Boltasseva A. and Shalaev V. M., *Opt. Mat. Express*, **7** (2017) 111.

[54] Tanzilli S., Martin A., Kaiser F., De Micheli M. P., O. Alibart O. and Ostrowsky D. B., *Laser Photon. Rev.*, **6** (2012) 115.

[55] Vivien L. and Pavesi L., *Handbook of Silicon Photonics* (CRC Press) 2013.

[56] Silverstone J. W., Bonneau D., O'Brien J. L. and Thompson M. G., *IEEE J. Sel. Top. Quantum Electron.*, **22** (2016) 6700113.

[57] Politi A., Cryan M. J., Rarity J. G., Yu S. and O'Brien J. L., *Science*, **320** (2008) 1155441.

[58] Politi A., Matthews J., Thompson M. G. and O'Brien J. L., *IEEE J. Sel. Top. Quantum Electron.*, **15** (2009) 1673.

[59] Wang J., Santamato A., Jiang P., Bonneau D., Engin E., Silverstone J. W., Lermer M., Beetz J., Kamp M., Hofling S., Tanner M. G., Natarajan C. M., Hadfield R. H., Dorenbos S. N., Zwiller V., O'Brien J. L. and Thompson M. G., *Opt. Commun.*, **327** (2014) 49.

[60] Xiong C., Pernice W., Ryu K. K., Schuck C., Fong K. Y., Palacios T. and Tang H. X., *Opt. Express*, **19** (2011) 10462.

[61] Abellan C., Amaya W., Domenech D., Muñoz P., Capmany J., Longhi S., Mitchell M. W. and Pruneri V., *Optica*, **3** (2016) 989.

[62] Orieux A., Eckstein A., Lemaître A., Filloux P., Favero I., Leo G., Coudreau T., Keller A., Milman P. and Ducci S., *Phys. Rev. Lett.*, **110** (2013) 160502.

[63] Dietrich C. P., Fiore A., Thompson M. G., Kamp M. and Hofling S., *Phys. Rev. Lett.*, **10** (2016) 870.

[64] Smith B. J., Kundys D., Thomas-Peter N., Smith P. G. R. and Walmsley I. A., *Opt. Express*, **17** (2009) 13516.

[65] Kundys D. O., Gates J. C., Dasgupta S., Gawith C. B. E. and Smith P. G. R., *IEEE Photon. Technol. Lett.*, **21** (2009) 947.

[66] Davis K. M., Miura, K., Sugimoto N. and Hirao K., *Opt. Lett.*, **21** (1996) 1729.

[67] Gattass R. R. and Mazur E., *Nat. Photon.*, **2** (2008) 229.

[68] Della Valle G., Osellame R. and Laporta P., *J. Opt. A*, **11** (2009) 013001.

[69] Meany T., Gräfe M., Heilmann R., Perez-Leija A., Gross S., Steel M. J., Withford M. J. and Szameit A., *Laser Photon. Rev.*, **9** (2015) 363.

[70] Osellame R., Taccheo S., Marangoni M., Ramponi R., Laporta P., Polli D., De Silvestri S. and Cerullo G., *J. Opt. Soc. Am. B*, **20** (2003) 1559.

[71] Ams M., Marshall G. D., Spence D. J. and Withford M. J., *Opt. Express*, **13** (2005) 5676.

[72] Eaton S. M., Chen W., Zhang L., Zhang H., Iyer R., Aitchison J. S. and Herman P. R., *IEEE Photon. Technol. Lett.*, **18** (2006) 2174.

[73] Szameit A. and Nolte S., *J. Opt. B: Mol. Opt. Phys.*, **43** (2010) 163001.

[74] Atzeni S., Rab A. S., Corrielli G., Polino E., Valeri M., Mataloni P., Spagnolo N., Crespi A., Sciarrino F. and Osellame R., *Optica*, **5** (2018) 3.

[75] Boyd R. W., *Nonlinear Optics* (Academic Press, Boston) 1992.

[76] Kwiat P., Mattle K., Weinfurter H. and Zeilinger A., *Phys. Rev. Lett.*, **75** (1995) 4337.

[77] Zhong H.-S., Li Y., Li W., Peng L. C., Su Z. E., Hu Y., He Y. M., Ding X., Zhang W., Li H., Zhang L., Wang Z., You L., Wang X.-L., Jiang X., Li L., Chen Y. A., Liu N. L., Lu C.-Y. and Pan J.-W., *Phys. Rev. Lett.*, **121** (2018) 250505.

[78] De Martini F. and Sciarrino F., *Prog. Quantum Electron.*, **29** (2005) 165.

[79] Armstrong J. A., N Bloembergen N., Ducuing J. and Pershan P. S., *Phys. Rev.*, **127** (1962) 1918.

[80] Hum D. S. and Fejer M. M., *C. R. Phys.*, **8** (2007) 180.

[81] Chen J., Pearlman J. A., Ling A., Fan J. and Migdall A. L., *Opt. Express*, **17** (2009) 6727.

[82] Noh T.-G., Kim H. and Zyung T., *Appl. Phys. Lett.*, **90** (2007) 011116.

[83] Evans P. G., Bennink R. S., Grice W. P., Humble T. S. and Schaake J., *Appl. Phys. Lett.*, **105** (2010) 253601.

[84] Graffitti F., Kundys D., Reid D. T., A. M. Brańczyk and Fedrizzi A., *Quantum Sci. Technol.*, **2** (2017) 035001.

[85] Graffitti F., Barrow P., Proietti M., Kundys D. and Fedrizzi A., *Optica*, **5** (2018) 514.

[86] Fraine A., Minaeva O., Simon D., Egorov R. and Sergienko A., *Opt. Lett.*, **37** (2012) 1910.

[87] Zhou Z. Y., Jiang Y. K., Ding D. S. and Shi B. S., *J. Mod. Opt.*, **60** (2013) 1910.

[88] Pelton M., Marsden P., Ljunggren D., Tengner M., Karlsson A., Fragemann A., Canalias C. and Laurell F., *Opt. Express*, **12** (2004) 3573.

[89] Kim T., Fiorentino M. and Wong F. N. C., *Phys. Rev. A*, **73** (2006) 012316.

[90] Fedrizzi A., Herbst T., Poppe A., Jennewein T. and Zeilinger A., *Opt. Express*, **15** (2007) 15377.

[91] Jin R. B., Shimizu R., Wakui K., Fujiwara M., Yamashita T., Miki S., Terai H., Wang Z. and Sasaki M., *Opt. Express*, **22** (2014) 11498.

[92] Jin R. B., Takeoka M., Takagi U., Shimizu R. and Sasaki M., *Opt. Express*, **5** (2015) 9333.

[93] Weston M. M., Chrzanowski H. M., Wollmann S., Boston A., Ho J., Shalm L. K., Verma V. B., Allman M. S., Nam S. W., Patel R. B., Slussarenko S. and Pryde G. J., *Opt. Express*, **24** (2016) 10869.

[94] Li Y., Zhou Z. Y., Ding D. S. and Shi B. S., *Opt. Express*, **22** (2015) 28792.

[95] Shimizu R. and Edamatsu K., *Opt. Express*, **17** (2009) 16385.

[96] Hentschel M., Hübel H., Poppe A. and Zeilinger A., *Opt. Express*, **17** (2009) 23153.

[97] Alibart O., D'Auria V., De Micheli M., Doutre F., Kaiser F., Labonté L., Lunghi T., Picholle E. and Tanzilli S., *J. Opt.*, **18** (2016) 104001.

[98] Hübel H., Vanner M. R., Lederer T., Blauensteiner B., Lorünser T., Poppe A. and Zeilinger A., *Opt. Express*, **16** (2008) 9701.

[99] Sauge S., Swillo M., Tengner M. and Karlsson A., *Opt. Express*, **16** (2008) 9701.

[100] Ueno W., Kaneda F., Suzuki H., Nagano S., Syouji A., Shimizu R., Suizu and Edamatsu K., *Opt. Express*, **20** (2012) 5517.

[101] König F., Mason E. J., Wong F. N. C. and Albota M. A., *Phys. Rev. A*, **71** (2005) 033805.

[102] Bruno N., Cruzeiro E. Z., Martin A. and Thew R. T., *Opt. Commun.*, **327** (2014) 3.

[103] Tanzilli J. S., De Riedmatten H., Tittel W., Zbinden H., Baldi P., De Micheli M., Ostrowsky D. B. and Gisin N., *Electron. Lett.*, **37** (2001) 26.

[104] Yoshizawa A. and Tsuchida H., *Appl. Phys. Lett.*, **85** (2004) 2457.

[105] Yoshizawa A., Kaji R. and Tsuchida H., *Electron. Lett.*, **39** (2003) 621.

[106] Odate S., Yoshizawa A. and Tsuchida H., *Electron. Lett.*, **43** (2007) 1376.

[107] Takesue H., Inoue K., Tadanaga O., Nishida Y. and Asobe M., *Opt. Lett.*, **30** (2005) 293.

[108] Halder M., Beveratos A., Thew R. T., Jorel C., Zbinden H. and Gisin N., *New J. Phys.*, **10** (2008) 023027.

[109] Lim C., Yoshizawa A., Tsuchida H. and Kikuchi K., *Opt. Express*, **16** (2008) 12460.

[110] Arahira S., Namekata N., Kishimoto T., Yaegashi H. and Inoue S., *Opt. Express*, **19** (2011) 16032.

[111] Jiang Y. K. and Tomita A., *J. Phys. B: At. Mol. Opt. Phys.*, **40** (2007) 437.

[112] Kawashima J., Fujimura M. and Suhara T., *IEEE Photon. Technol. Lett.*, **21** (2009) 566.

[113] Vergyris P., Meany T., Lunghi T., Sauder G., Downes J., Steel M. J., Withford M. J., Alibart O. and Tanzilli S., *Sci. Rep.*, **6** (2016) 35975.

[114] Suhara T., Okabe H. and Fujimura M., *IEEE Photon. Technol. Lett.*, **19** (2007) 1093.

[115] Herrmann H., Yang X., Thomas A., Poppe A., Sohler W. and Silberhorn C., *Opt. Express*, **21** (2013) 27981.

[116] Kaiser F., Issautier A., Ngah L. A., Danila O., Herrmann H., Sohler W., Martin A. and Tanzilli S., *New J. Phys.*, **14** (2012) 085015.

[117] Kaiser F., Ngah L. A., Issautier A., Delord T., Aktas D., D'Auria V., DeMicheli M. P., Kastberg A., Labonté L., Alibart O., Martin A. and Tanzilli S., *Opt. Commun.*, **327** (2014) 7.

[118] Meany T., Ngah L. A., Collins M. J., Clark A. S., Williams R. J., Eggleton B. J., Steel M., Withford M. J., Alibart O. and Tanzilli S., *Laser Photon. Rev.*, **8** (2014) L42.

[119] Vergyris P., Kaiser F., Gouzien E., Sauder G., Lunghi T. and Tanzilli S., *Quantum Sci. Technol.*, **2** (2017) 024007.

[120] Schaeff C., Polster R., Lapkiewicz R., Fickler R., Ramelow S. and Zeilinger A., *Opt. Express*, **20** (2012) 16145.

[121] Pomarico E., Sanguinetti B., Gisin, N., Thew R., Zbinden H., Schreiber G., Thomas A. and Sohler W., *New J. Phys.*, **11** (2009) 113042.

[122] Martin A., Cristofori V., Aboussouan P., Herrmann H., Sohler W., Ostrowsky D.B., Alibart O. and Tanzilli S., *Opt. Express*, **17** (2009) 1033.

[123] Martin A., Issautier A., Herrmann H., Sohler W., Ostrowsky D. B., Alibart O. and Tanzilli S., *New J. Phys.*, **12** (2010) 1033.

[124] Meyer-Scott E., Prasannan N., Eigner C., Quiring V., Donohue J.M., Barkhofen S. and Silberhorn C., *Opt. Express*, **26** (2018) 32475.

[125] Lanco L., Ducci S., Likforman J.-P., Marcadet X., van Houwelingen J. A. W., Zbinden H., Leo G. and Berger V., *Phys. Rev. Lett.*, **97** (2006) 173901.

[126] Caillet X., Orieux A., Lemaître A., Filloux P., Favero I., Leo G. and Ducci S., *Opt. Express*, **18** (2010) 9967.

[127] Kang D., Kim M., He H. and Helmy A. S., *Phys. Rev. A*, **92** (2015) 13821.

[128] Autebert C., Trapateau J., Orieux A., Lemaître A., Gomez-Carbonell C., Diamanti E., Zaquine I. and Ducci S., *Quantum Sci. Technol.*, **1** (2016) 01LT02.

[129] Sarrafi P., Zhu E. Y., Holmes B. M., Hutchings D. C., Aitchison S. and Qian L., *Opt. Lett.*, **39** (2014) 5188.

[130] Autebert C., Bruno N., Martin A., Lemaitre A., Gomez-Carbonelli C., Favero I., Leo G., Zbinden H. and Ducci S., *Optica*, **3** (2016) 143.

[131] Zhu E. Y., Tang Z., Qian L., Helt L. G., Liscidini M., Sipe J., Corbari C., Canagasabey A., Ibsen M. and Kazansky P. G., *Phys. Rev. Lett.*, **108** (2012) 213902.

[132] Zhu E. Y., Tang Z., Qian L., Helt L. G., Liscidini M., Sipe J., Corbari C., Canagasabey A., Ibsen M. and Kazansky P. G., *Opt. Lett.*, **38** (2013) 4397.

[133] Chen C., Zhu E. Y., Riazi A., Gladyshev A. V., Corbari C., Ibsen M., Kazansky P. G. and Qian L., *Opt. Express*, **25** (2017) 22667.

[134] Horn R. T., Kolenderski P., Kang D., Abolghasem P., Scarcella C., Della Frera A., Tosi A., Helt L. G., Zhukovsky S. V., J. E. Sipe J. E., Weihs G., Helmy A. S. and Jennewei T., *Sci. Rep.*, **25** (2013) 2314.

[135] Vallés A., Hendrych M., Svozilík J., Machulka R., Abolghasem P., Kang D., Bijlani B. J., Helmy A. S. and Torres J. P., *Opt. Express*, **21** (2013) 10841.

[136] Hamel D. R., Shalm L. K., Hubel H., Miller A. J., Marsili F., Verma V. B., Mirin R. P., Nam S. W., Resch K. J. and Jennewein T., *Nat. Photon.*, **8** (2014) 801.

[137] Caspani L., Xiong C., Eggleton B. J., Bajoni D., Liscidini M., Galli M., Morandotti R. and Moss D., *Light Sci. Appl.*, **6** (2017) e17100.

[138] Jin H., Liu F. M., Xu P., Xia J. L., Zhong M. L., Yuan Y., Zhou J. W., Gong Y. X., Wang W. and Zhu S. N., *Phys. Rev. Lett.*, **113** (2014) 103601.

[139] Kruse R., Sansoni L., Brauner S., Ricken R., Hamilton C. S., Jex I. and Silberhorn C., *Phys. Rev. A*, **92** (2015) 053841.

[140] Sansoni L., Luo K. H., Eigner C., Ricken R., Quiring V., Herrmann v. and Silberhorn C., *npj Quantum Inf.*, **3** (2017) 22667.

[141] Fiorentino M., Voss P. L., Li X., Sharping J. E., Barbosa G. A. and Kumar P., *IEEE Photon. Technol. Lett.*, **14** (2002) 983.

[142] Chen J., Lee K. F., Liang C. and Kumar P., *Opt. Lett.*, **31** (2006) 2798.

[143] Li X., Voss P. L., Sharping J. E. and Kumar P., *Phys. Rev. Lett.*, **94** (2005) 053601.

[144] Li X., Liang C., Lee K. F., Chen J., Voss P. L. and Kumar P., *Phys. Rev. A*, **73** (2006) 052301.

[145] Liang C., Lee K. F., Levin T., Chen J. and Kumar P., *Opt. Express*, **14** (2006) 6941.

[146] Takesue H. and Inoue K., *Phys. Rev. A*, **70** (2004) 031802(R).

[147] Lee K. F., Chen J., Liang C., Li X., Voss P. L. and Kumar P., *Opt. Lett.*, **31** (2006) 1905.

[148] Medic M., Altepeter J. B., Hall M. A., Patel M. and Kumar P., *Opt. Lett.*, **35** (2010) 802.

[149] Takesue H., Harada K. I., Fukuda H., Tsuchizawa T., T. Watanabe, Yamada K., Tokura Y. and Itabashi S. I., *J. Nanosci. Nanotechnol.*, **10** (2010) 1814.

[150] Harada K. I., Takesue H., Fukuda H., Tsuchizawa T., Watanabe T., Yamada K., Tokura Y. and Itabashi S. I., *Opt. Express*, **16** (2008) 20368.

[151] Sharping J. E., Lee K. F., Foster M. A., Turner A. C., Schmidt B. S., Lipson M., Gaeta A. L. and Kumar P., *Opt. Express*, **14** (2006) 12388.

[152] Takesue H., Tokura Y., Fukuda H., Tsuchizawa T., Watanabe T., Yamada K. and Itabashi S., *Appl. Phys. Lett.*, **91** (2007) 201108.

[153] Li Y.-H., Zhou Z.-Y., Feng L.-T., Fang W.-T., Liu S.-l., Liu S.-K., Wang K., Ren X.-F., Ding D.-S, Xu L.-X. and Shi B.-S., *Appl. Phys. Lett.*, **7** (2017) 064005.

[154] Zhang M., Feng L. T., Zhou Z. Y., Chen Y., Wu H., Li M., Guo G. P., Guo G. C., Dai D. X. and Ren X. F., *preprint* (2018) arXiv:1803.01641.

[155] Takesue, Fukuda H., Tsuchizawa T., Watanabe T., Yamada K., Tokura Y. and Itabashi S., *Opt. Express*, **16** (2008) 5721.

[156] Olislager L., Safioui J., Clemmen S., Huy K. P., Bogaerts W., Baets R., Emplit P. and Massar S., *Opt. Express*, **38** (2013) 1960.

[157] Matsuda N., Le Jeannic H., Fukuda H., Tsuchizawa T., Munro W. J., Shimizu K., Yamada K., Tokura Y. and Takesue H., *Sci. Rep.*, **2** (2012) 817.

[158] Lv N., Zhang W., Guo Y., Zhou Q., Huang Y. and Peng J., *Opt. Lett.*, **38** (2013) 2873.

[159] Harris N. C., Grassani D., Simbula A., Pant M., Galli M., Baehr-Jones T., Hochberg M., Englund D., Bajoni D. and Galland C., *Phys. Rev. X*, **4** (2014) 041047.

[160] Fang W. T., Li Y. H., Zhou Z. Y., Xu L. X., Guo G. C. and Shi B. S., *Opt. Express*, **26** (2018) 12912.

[161] Suo J., Dong S., Zhang W., Huang Y. and Peng J., *Opt. Express*, **23** (2015) 3985.

[162] Grassani D., Azzini S., Liscidini M., Galli M., Strain M. J., Sorel M., Sipe J. E. and Bajoni D., *Optica*, **2** (2015) 88.

[163] Rogers S., Mulkey D., Lu X., Jiang W. C. and Lin Q., *ACS Photon.*, **3** (2016) 1754.

[164] Clemmen S., Huy K. P., Bogaerts W., Baets R. G., Emplit P. and Massar S., *Opt. Express*, **17** (2009) 16558.

[165] Kultavewuti P., Zhu E. Y., Xing X., Qian L., Pusino V., Sorel M. and Aitchison J. S., *Sci. Rep.*, **7** (2017) 5785.

[166] Silverstone J. W., Bonneau D., Ohira K., Suzuki N., Yoshida H., Iizuka N., Ezaki M., Natarajan C. M., Tanner M. G., Hadfield R. H., Zwiller V., Marshall G. D., Rarity J. G., O'Brien J. L. and Thompson M. G., *Nat. Photon.*, **8** (2013) 104.

[167] Silverstone J. W., Santagati R., Bonneau D., Strain M. J., Sorel M., O'Brien J. L. and Thompson M. G., *Nat. Commun.*, **6** (2015) 7948.

[168] Wang J., Bonneau, D., Villa M., Silverstone J. W., Santagati R., Miki S., Yamashita T., Mikio Fujiwara, Sasaki M., Terai H., Tanner M. G., Natarajan C. M., Hadfield R. H., O'Brien J. L. and Thompson M. G., *Optica*, **3** (2016) 407.

[169] Wang J., Paesani S., Ding Y., Santagati R., Skrzypczyk P., Salavrakos A., Tura J., Augusiak R., Mancinska L., Bacco D., Bonneau D., Silverstone J. W., Gong Q., Acín A., Rottwitt K., Oxenløwe L. K., O'Brien J. L., Laing A. and Thompson M. G., *Science*, **6** (2018) 6386.

[170] Benson O., Santori C., Pelton M. and Yamamoto Y., *Phys. Rev. Lett.*, **84** (2000) 2513.

[171] Michler P., Kiraz A., Becher C., Schoenfeld W. V., Petroff P. M., Zhang L., Hu E. and Imamoglu A., *Science*, **290** (2000) 2282.

[172] Akopian N., Lindner N., Poem E., Berlatzky Y., Avron J., Gershoni D., Gerardot B. and Petroff P., *Phys. Rev. Lett.*, **96** (2006) 130501.

[173] Huber D., Reindl M., Huo Y., Huang H., Wildmann J. S., Schmidt O. G., Rastelli A. and Trotta R., *Nat. Commun.*, **8** (2017) 15506.

[174] Jöns K. D., Schweickert L., Versteegh M. A. M., Dalacu D., Poole P. J., Gulinatti A., Giudice A., Zwiller V. and Reimer M. E., *Sci. Rep.*, **7** (2017) 1700.

[175] Shields A. J., *Nat. Photon.*, **1** (2007) 215.

[176] Ward M. B., Dean M. C., Stevenson R. M., Bennett A. J., Ellis D. J. P., Cooper K., Farrer I., Nicoll C. A., Ritchie D. A. and Shields A. J., *Nat. Commun.*, **5** (2014) 3316.

[177] Olbrich F., Höschele J., Müller M., Kettler J., Portalupi S. L., Paul M., Jetter M. and Michler P., *Appl. Phys. Lett.*, **111** (2017) 133106.

[178] Davis K. M., Miura K., Sugimoto N. and Hirao K., *Opt. Lett.*, **21** (1996) 1729.

[179] Gattass R. R. and Mazur E., *Nat. Photon.*, **2** (2008) 219.

[180] Minoshima k., Kowalevicz A. M., Ippen E. P. and Fujimoto J. G., *Nat. Photon.*, **10** (2002) 645.

[181] Booth M. J. and Salter P. S., *Quantum Sensing and Nano Electronics and Photonics XVI, SPIE Proceedings*, **10926** (2019) 109261Y.

[182] Streltsov A. M. and Borrelli N. F., *J. Opt. Soc. Am. B*, **19** (2002) 2496.

[183] Streltsov A. M. and Borrelli N. F., *Opt. Lett.*, **26** (2001) 42.

[184] Bricchi E., Klappauf B. G. and Kazansky P. G., *Opt. Lett.*, **29** (2004) 119.

[185] Bhardwaj V. R., Corkum P. B., Rayner D. M., Hnatovsky C., Simova E. and Taylor R. S., *Opt. Lett.*, **29** (2004) 1312.

[186] Fernandes L. A., Grenier J. R., Herman P. R., Aitchison J. S. and Marques P.V.S., *Opt. Express*, **20** (2012) 24103.

[187] Chen F. and Aldana J. R. V., *Laser & Photonics Rev.*, **8** (2014) 251.

[188] Nolte S., Will M., Burghoff J. and Tuennermann A., *Appl. Phys. A*, **77** (2003) 109.

[189] Crespi A., Osellame R., Ramponi R., Bentivegna M., Flamini F., Spagnolo N., Viggianiello N., Innocenti L., Mataloni P. and Sciarrino F., *Nat. Commun.*, **7** (2016) 10469.

[190] Flamini F., Viggianiello N., Bentivegna M., Spagnolo N., Mataloni P., Crespi A., Ramponi R., Osellame R. and Sciarrino F., *Interdiscip. Inf. Sci.*, **23** (2017) 115.

[191] Chaboyer Z., Meany T., Helt L. G., Withford M. J. and Steel M. J., *Sci. Rep.*, **5** (2015) 9601.

[192] Spagnolo N., Vitelli C., Aparo L., Mataloni P., Sciarrino F., Crespi A., Ramponi R. and Osellame R., *Nat. Commun.*, **4** (2013) 1606.

[193] Arriola A., Gross S., Jovanovic N., Charles N., Tuthill P. G., Olaizola S. M., Fuerbach A. and Withford M. J., *Nat. Commun.*, **21** (2013) 2978.

[194] Gross S., Riesen N., Love J. D. and Withford M. J., *Nat. Commun.*, **8** (2014) L81.

[195] Gross S. and Withford M. J., *Nanophotonics*, **4** (2015) 332.

[196] Kowalevicz A. M., Sharma V., Ippen E. P., Fujimoto J. G. and Minoshima K., *Opt. Lett.*, **30** (2005) 1060.

[197] Flamini F., Viggianiello N., Giordani T., Bentivegna M., Spagnolo N., Crespi A., Corrielli G., Roberto Osellame R., Martin-Delgado M. A. and Sciarrino F., *J. Opt.*, **20** (2018) 074001.

[198] Heilmann R., Greganti C., Gräfe M., Nolte S., Walther P. and Szameit A., *Appl. Opt.*, **57** (2018) 377.

[199] Rojas-Rojas S., Morales-Inostroza L., Naether U., Xavier G. B., Nolte S., Szameit A., Vicencio R. A. Lima G. and Delgado A., *Phys. Rev. A*, **90** (2014) 063823.

[200] Crespi A., Ramponi R., Osellame R., Sansoni R., Bongioanni I., Sciarrino F., Vallone G. and Mataloni P., *Phys. Rev. Lett.*, **105** (2010) 200503.

[201] Flamini F., Magrini L., Rab A.S., Spagnolo N., D'Ambrosio V., Mataloni P., Sciarrino F., Zandrini T., Crespi A., Ramponi R. and Osellame R., *Light Sci. Appl.*, **4** (2015) e354.

[202] Dyakonov I., Pogorelov I., Bobrov I., Kalinkin A., Dyakonov P., Evlashin S., Straupe S. and Kulik S., *Phys. Rev. Appl.*, **10** (2018) 044048.

[203] Corrielli G., Crespi A., Geremia R., Ramponi R., Sansoni L., Santinelli A., Mataloni P., Sciarrino F. and Osellame R., *Nat. Commun.*, **5** (2014) 4249.

[204] Fernandes L. A., Grenier J. R., Herman P. R., Aitchison J. S. and Marques P. V., *Opt. Express*, **19** (2011) 11992.

[205] Crespi A., Ramponi R., Osellame R., Sansoni R., Bongioanni I., Sciarrino F., Vallone G. and Mataloni P., *Nat. Commun.*, **2** (2011) 566.

[206] Heilmann R., Gräfe M., Nolte S. and Szameit A., *Sci. Rep.*, **4** (2014) 4118.

[207] Wang C. Y., Gao J. and Jin X. M., *Opt. Lett.*, **44** (2019) 102.

[208] Viggianiello N., Flamini F., Innocenti L., Cozzolino D., Bentivegna M., Spagnolo N., Crespi A., Brod D. J., Galvão E. F., Osellame R. and Sciarrino F., *New. J. Phys.*, **20** (2018) 033017.

[209] Weimann S., Perez-Leija A., Lebugle M., Keil R., Tichy M., Gräfe M., Heilmann R., Nolte S., Moya-Cessa H., Weihs G., Christodoulides D. N. and Szameit A., *Nat. Commun.*, **7** (2016) 11027.

[210] Owens J. O., Broome M. A., Biggerstaff D. N., Goggin M. E., Fedrizzi A., Linjordet T., Ams M., Marshall G. D., Twamley J. and White A. G., *New J. Phys.*, **13** (2011) 075003.

[211] Sansoni L., Sciarrino F., Vallone G., Mataloni P., Crespi A., Ramponi R. and Osellame R., *Phys. Rev. Lett.*, **108** (2012) 010502.

[212] Crespi A., Osellame R., Ramponi R., Giovannetti V., Fazio R., Sansoni L., De Nicola F., Sciarrino F. and Mataloni P., *Nat. Commun.*, **7** (2013) 322.

[213] Pitsios I., Banchi L., Rab, A. S., Bentivegna M., Caprara D., Crespi A., Spagnolo N., Bose S., Mataloni P., Osellame R. and Sciarrino F., *Nat. Commun.*, **8** (2017) 1569.

[214] Ciampini M. A., Orieux A., Paesani S., Sciarrino F., Corrielli G., Crespi A., Ramponi R., Osellame R. and Mataloni P., *Light Sci. Appl.*, **5** (2016) e16064.

[215] Tillmann M., Dakić B., Heilmann R., Nolte S., Szameit A. and Walther P., *Nat. Photon.*, **7** (2013) 540.

[216] Crespi A., Osellame R., Ramponi R., Brod D. J., Galvão E. F., Spagnolo N., Vitelli C., Maiorino E., Mataloni P. and Sciarrino F., *Nat. Photon.*, **7** (2013) 545.

[217] Spagnolo N., Vitelli C., Bentivegna M., Brod D. J., Crespi A., Flamini F., Giacomini S., Milani G., Ramponi R., Mataloni P., Galvão E. F., Osellame R. and Sciarrino F., *Nat. Photon.*, **8** (2014) 615.

[218] Bentivegna M., Spagnolo N., Vitelli C., Flamini F., Viggianiello N., Latmiral L., Mataloni P., Brod D. J., Galvão E.F,, Crespi A., Ramponi R., Osellame R. and Fabio Sciarrino, *Science Adv.*, **1** (2015) e1400255.

[219] Crespi A., Bentivegna M., Pitsios I., Rusca D., Poderini D., Carvacho G., D'Ambrosio V., Cabello A., Sciarrino F. and Osellame R., *ACS Photon.*, **4** (2017) 2807.

[220] Polino E., Riva M., Valeri M., Silvestri R., Corrielli G., Crespi A., Spagnolo N., Osellame R. and Sciarrino F., *Optica*, **6** (2019) 288.

[221] Crespi A., Lobino M., Matthews J. C. F., Politi A., Neal C. R., Ramponi R., Osellame R. and O'Brien J. L., *Appl. Phys. Lett.*, **100** (2012) 233704.

[222] Viggianiello N., Flamini F., Bentivegna M., Spagnolo N., Crespi A., Brod D. J., Galvão E. F., Osellame R. and Sciarrino F., *Sci. Bull.*, **63** (2018) 1470.

[223] Seri A., Corrielli G., Lago-Rivera D., Lenhard A., de Riedmatten H., Osellame R. and Mazzera M., *Optica*, **5** (2018) 934.

[224] Chapman R. J., Santandrea M., Huang Z., Corrielli G., Crespi A., Yung M. H., Osellame R. and Peruzzo A., *Nat. Commun.*, **7** (2016) 11339.

[225] Osellame R., Hoekstra H. J. W. M., Cerullo G. and Pollnau M., *Laser Photon. Rev.*, **5** (2011) 442.

[226] Osellame R., Lobino M., Chiodo N., Marangoni M., Cerullo G., Ramponi R., Bookey H. T., Thomson R. R., Psaila N. D. and Kar A. K., *Appl. Phys. Lett.*, **90** (2007) 241107.

[227] Suhara T. and Kintaka H., *IEEE Quantum Electron.*, **41** (2005) 1203.

[228] Corrielli G., Atzeni S., Piacentini S., Pitsios I., Crespi A. and Osellame R., *Opt. Express*, **26** (2018) 15101.

[229] James D. F. V., Kwiat P. G., Munro W. J. and White A.G., *Phys. Rev. A*, **64** (2001) 052312.

[230] Eisenberg H., Khoury G., Durkin G., Simon C. and Bouwmeester D., *Phys. Rev. Lett.*, **93** (2004) 193901.

[231] Pernice W. H. P., Schuck C., Minaeva O., Li M., Goltsman G. N., Sergienko A. V. and Tang H. X., *Nat. Commun.*, **3** (2012) 1325.

[232] Najafi F., Mower J., Harris N. C., Bellei F., Dane A., Lee C., Hu X., Kharel P., Marsili F., Assefa S., Berggren K. K. and Englund D., *Nat. Commun.*, **6** (2015) 5873.

[233] Sahin D., Gaggero A., Zhou Z., Jahanmirinejad S., Mattioli F., Leoni R., Beetz J., Lermer M., Kamp M., Höfling S. and Fiore A., *Appl. Phys. Lett.*, **103** (2013) 111116.

[234] Calkins B., Mennea P. L., Lita A. E., Metcalf B. J., Kolthammer W. S., Lamas-Linares A., Spring J. B., Humphreys P. C., Mirin R. P., Gates J. C., Smith P. G. R., Walmsley I. A., Gerrits T. and Nam S. W., *Opt. Express*, **21** (2013) 22657.

[235] Korneev A., Goltsman G. G. and Pernice W., *Laser Focus World*, **51** (2015) 47.

[236] Humphreys P. C., Barbieri M., Datta A. and Walmsley I. A., *Sci. Rep.*, **111** (2013) 070403.

[237] Ciampini M. A., Spagnolo N., Vitelli C., Pezzè L., Smerzi A. and Sciarrino F., *Sci. Rep.*, **6** (2016) 28881.

[238] Hentschel A. and Sanders B. C., *Phys. Rev. Appl.*, **104** (2010) 063603.

[239] Lumino A., Polino E., Rab A. S., Milani G., Spagnolo N., Wiebe N. and Sciarrino F., *Phys. Rev. Appl.*, **10** (2018) 044033.

[240] Aaronson S. and Arkhipov A., *Proceedings of the 43rd Annual ACM Symposium on Theory of Computing* (ACM) 2011, p. 333.

[241] Spring J. B., Metcalf B. J., Humphreys P. C., Kolthammer W. S., Jin X. M., Barbieri M., Datta A., Thomas-Peter N., Langford N. K., Kundys D., Gates J. C., Smith B. J., Smith P. G. R. and Walmsley I. A., *Science*, **339** (2013) 798.

[242] Broome M. A., Fedrizzi A., Rahimi-Keshari S., Dove J., Aaronson S., Ralph T. C. and White A. G., *Science*, **339** (2013) 794.

[243] Spagnolo N., Vitelli C., Sansoni L., Maiorino E., Mataloni P., Sciarrino F., Brod D. J., Galvão E. F., Crespi A., Ramponi R. and Osellame R., *Phys. Rev. Lett.*, **111** (2013) 130503.

[244] Carolan J., Meinecke J. D. A., Shadbolt P. J., Russell N. J., Ismail N., Worhoff K., Rudolph T., Thompson M. G., O'Brien J. L., Matthews J. C. F. and Laing A., *Nat. Photon.*, **8** (2014) 621.

[245] Lund A. P., Laing A., Rahimi-Keshari S., Rudolph T., O'Brien J. L. and Ralph T. C., *Phys. Rev. Lett.*, **113** (2014) 100502.

[246] Carolan J., Harrold C., Sparrow C., Martin-Lopez E., Russell N. J., Silverstone J. W., J. Shadbolt P., Matsuda N., Oguma M., Itoh M., Marshall G. D., Thompson M. G., Matthews J. C. F., Hashimoto T., O'Brien J. L. and Laing A., *Science*, **349** (2014) 711.

[247] Loredo J. C., Broome M. A., Hilaire P., Gazzano O., Sagnes I., Lemaitre A., Almeida M. P., Senellart P. and White A. G., *Phys. Rev. Lett.*, **118** (2017) 130503.

[248] He Y., Ding X., Su Z.-E., Huang H.-L., Qin J., Wang C., Unsleber S., Chen C., Wang H., He Y.-M., Wang X.-L., Zhang W.-J., Chen S.-J., Schneider C., Kamp M., You L.-X., Wang Z., Hofling S., Lu C.-Y. and Pan J.-W., *Phys. Rev. Lett.*, **118** (2017) 190501.

[249] Wang H., He Y., Li Y.-H., Su Z.-E., Li B., Huang H.-L., Ding X., Chen M.-C., Liu C., Qin J., Li J.-P., He Y.-M., Schneider C., Kamp M., Peng C.-Z., Hofling S., Lu C.-Y. and Pan J.-W., *Nat. Photon.*, **11** (2017) 361.

[250] Wang H., Li W., Jiang X., He Y.-M., Li Y.-H., Ding X., Chen M.-C., Qin J., Peng C.-Z., Schneider C., Kamp M., Zhang W.-J., Li H., You L.-X., Wang Z., Dowling J.P., Hofling S., Lu C.-Y. and Pan J.-W., *Nat. Photon.*, **120** (2018) 230502.

[251] Aspelmeyer M., Jennewein T., Pfennigbauer M., Leeb W. R. and Zeilinger A., *IEEE J. Sel. Top. Quantum Electron.*, **9** (2003) 1541.

[252] Vallone G., Bacco D., Dequal D., Gaiarin S., Luceri V., Bianco G. and Villoresi P., *Phys. Rev. Lett.*, **115** (2015) 040502.

[253] Yin J. *et al.*, *Science*, **356** (2017) 1140.

[254] Oi D. K. L., Ling A., Vallone G., Villoresi P., Greenland S., Kerr E., Macdonald M., Weinfurter H., Kuiper H., Charbon E. and Ursin R., *EPJ Quantum Technol.*, **4** (2017) 6.

[255] Liao S. K. *et al.*, *Phys. Rev. Lett.*, **120** (2018) 030501.

Quantum optics with single spins

Lee C. Bassett

Quantum Engineering Laboratory, Department of Electrical & Systems Engineering
University of Pennsylvania - Philadelphia, PA, USA

Summary. — Defects in solids are in many ways analogous to trapped atoms or molecules. They can serve as long-lived quantum memories and efficient light-matter interfaces. As such, they are leading building blocks for long-distance quantum networks and distributed quantum computers. This paper describes the quantum-mechanical coupling between atom-like spin states and light, using the diamond nitrogen-vacancy (NV) center as a paradigm. We present an overview of the NV center's electronic structure, derive a general picture of coherent light-matter interactions, and describe several methods that can be used to achieve all-optical initialization, quantum-coherent control, and readout of solid-state spins. These techniques can be readily generalized to other defect systems, and they serve as the basis for advanced protocols at the heart of many emerging quantum technologies.

1. – Introduction

Solid-state spins are among the most versatile platforms for quantum science and technology. Select semiconductor defects — exemplified by the nitrogen-vacancy (NV) center in diamond — exhibit spin coherence at room-temperature and intrinsic optical spin-readout mechanisms that underly their remarkable capabilities as room-temperature qubits and quantum sensors. When used in this way, quantum-coherent control is performed using microwaves that couple resonantly to the qubit's electron spin Hamiltonian.

Optical pumping and fluorescence are used for spin initialization and readout, respectively, but these processes rely on dissipation through nonradiative and vibronic transitions that involve coupling to phonons in the crystal and are therefore incoherent. When the crystal is cooled down, however, the optical transitions between different orbital states become coherent, and they can be manipulated using resonant optical fields just as the spin is controlled with microwaves. Moreover, spin-orbit coupling mediates interactions between optical fields and spins, enabling all-optical (*i.e.*, microwave free) spin control, robust spin initialization and readout, and various schemes for generating spin-photon entanglement.

In this paper based on lectures from the 2018 Enrico Fermi Summer School on *Nanoscale Quantum Optics*, we introduce a general picture for coherent light-matter interactions based on coherent, dispersive interactions with spin-selective optical transitions based on the Jaynes-Cummings Hamiltonian for quantum electrodynamics. The paper is organized as follows. In sect. **2**, we introduce the spin and optical fine structure of the NV center, including the role of various perturbations. Subsequently, in sect. **3** we summarize key concepts of quantum optics including the Jaynes-Cummings Hamiltonian, and show how coherent, dispersive, light-matter interactions give rise to the optical Stark effect and the Faraday effect, which can be used respectively to control and measure NV-center spin states. In sect. **4** we generalize the treatment to include more complex dynamics exhibited by an optical Λ configuration, including coherent population trapping and stimulated Raman transitions, and in sect. **5** we describe an alternate, non-dispersive technique to probe and control quantum dynamics using ultrafast optical pulses. Section **6** summarizes the paper and highlights future directions for the application of these techniques to address other spin-qubit platforms, and to enable more advanced schemes for quantum control within quantum networks. Much of the material is adapted from Buckley *et al.* [1], Yale *et al.* [2], and Bassett *et al.* [3], and more information regarding the experiments and models can be found in those references.

2. – Electronic structure of the diamond nitrogen-vacancy center

The NV center in diamond has been an object of fascination since the 1950s as one of the predominant color centers in diamond, and the focus of intense study in quantum information science since the turn of the 21st century [4]. Its popularity and importance in quantum science stem from several key characteristics, including long spin coherence of the triplet ground state, which persists to room temperature and above, and efficient, stable, visible photoluminescence (PL) that can be used to measure the spin state populations. The latter property stems from the NV center's specific electronic level structure, which at room temperature takes the effective form shown in fig. 1(a). The spin-triplet ground state and optically excited state — which is responsible for the visible PL — is connected to manifold of intermediate singlet states through an inter-system crossing (ISC). The nonradiative ISC is mediated by phonons and the spin-orbit interaction, and the rates in both the upper and lower branches depend on the triplet spin projection. In particular, the upper ISC transition from the triplet excited
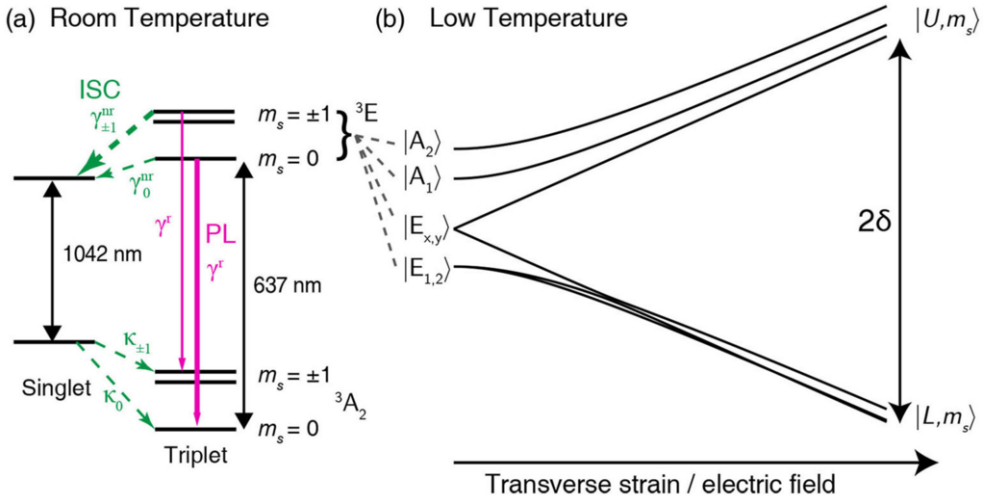
Fig. 1. – Electronic structure of the diamond NV center. (a) At room temperature, rapid phonon transitions within the orbitals of the ^3E excited state lead to an effective spin-triplet with spin-dependent non-radiate decay channels, $\gamma_{m_s}^{\mathrm{nr}}$, through the ISC as shown. These dynamics produce the NV center's spin-dependent PL. (b) At low temperature, the orbital fine structure within ^3E is resolved. The unperturbed spin-orbit states evolve into two separated orbital branches as a function of the transverse strain or dc Stark shift, δ. Eigenstates in (b) are calculated according to eq. (2) for $B = 0\,\mathrm{G}$ and $\alpha_s = 0$.

state occurs predominantly for the $m_s = \pm 1$ spin sublevels (labeled according to the S_z projection, where z is along the defect's symmetry axis). These intrinsic, spin-dependent optical dynamics provide the mechanisms for optical spin initialization and PL-based spin readout that are used in a majority of NV-center applications, especially at room temperature [5].

While the $^3A_2$ ground state is an orbital singlet, the ^3E excited state is an orbital doublet. At room temperature, rapid phonon-mediated transitions between the orbital branches result in an effective spin-triplet Hamiltonian as shown in fig. 1(a). At temperatures below $\approx 20\,\mathrm{K}$, however, phonon-induced transitions are suppressed, and the fine structure associated with the full six-dimensional excited-state Hamiltonian emerges in the optical transitions, as shown in fig. 1(b) [6,7]. At these temperatures, and in pure diamond samples, the zero-phonon-line (ZPL) transitions become spectrally narrow, in some cases approaching the lifetime limit, such that coherent Rabi oscillations can be observed between the ground- and excited-state orbitals [8].

2˙1. *The electronic Hamiltonian*. – The form of the NV center's electronic Hamiltonian can be derived and understood using group theory [9,10]. The ground-state Hamiltonian is given by

$$(1) \qquad H_{\mathrm{gs}} = D_{\mathrm{gs}} \left(S_z^2 - \frac{2}{3} \right) + g_{\mathrm{gs}} \mu_{\mathrm{B}} \mathbf{S} \cdot \mathbf{B},$$

where D_{gs} is the reduced matrix element (RME) for the axial spin-spin interaction, and the second term describes the Zeeman interaction in terms of the Landé g-factor, g_{gs}, Bohr magneton μ_{B}, electron spin operator **S** (where $S^2 = 1$, $S_{\pm} = S_x \pm iS_y$), and magnetic field **B**. We generally set $h = 1$ such that terms in the Hamiltonian can be written in either energy or frequency units. Similarly, the excited-state Hamiltonian can be written as a sum of terms due to intrinsic (spin-orbit, spin-spin) interactions and extrinsic (magnetic, strain/electric) fields,

$$(2) \qquad\qquad H_{\text{es}} = H_{\text{so}} + H_{\text{ss}} + H_{\text{Z}} + H_L + H_{\text{s}}.$$

Below we give explicit matrix expressions for these terms in the product basis $|\varepsilon, m_s\rangle \in \{(|X\rangle, |Y\rangle) \otimes (|-1\rangle, |0\rangle, |+1\rangle)\}$, where $(|X\rangle, |Y\rangle)$ are E-symmetry orbital states transforming like the vectors (x, y) in the NV-center coordinate system. The spin sublevels $|m_s\rangle$ are eigenstates of the S_z operator, whereas the orbital part of the Hamiltonian can be written in terms of the Pauli matrices σ_i^{es} ($i = x, y, z$) and $\sigma_{\pm}^{\text{es}} = \sigma_z^{\text{es}} \pm i\sigma_x^{\text{es}}$, which operate on the two-dimensional orbital excited-state degree of freedom, $i.e.$, $\sigma_z^{\text{es}}|X\rangle = |X\rangle$ and $\sigma_z^{\text{es}}|Y\rangle = -|Y\rangle$. Note that $\sigma_{\pm}^{\text{es}}$ are not the standard raising and lowering operators.

The only spin-orbit coupling allowed by symmetry is the axial one ($i.e.$, proportional to S_z [10]), with RME λ. In the product basis, this takes the form

$$(3) \qquad H_{\text{so}} = -\lambda \sigma_y^{\text{es}} S_z = \begin{pmatrix} 0 & 0 & 0 & -i\lambda & 0 & 0 \\ 0 & 0 & 0 & 0 & 0 & 0 \\ 0 & 0 & 0 & 0 & 0 & i\lambda \\ i\lambda & 0 & 0 & 0 & 0 & 0 \\ 0 & 0 & 0 & 0 & 0 & 0 \\ 0 & 0 & -i\lambda & 0 & 0 & 0 \end{pmatrix}.$$

The spin-spin interaction has three symmetry-allowed RMEs, corresponding to one axial (D_{es}) and two transverse couplings (Δ_1, Δ_2). This takes the form

$$(4) \quad H_{\text{ss}} = D_{\text{es}}\left(S_z^2 - \frac{2}{3}\right) - \frac{\Delta_1}{4}\left(S_+^2 \sigma_-^{\text{es}} + S_-^2 \sigma_+^{\text{es}}\right) + \frac{\Delta_2}{2\sqrt{2}}\left(\{S_+, S_z\}\sigma_+^{\text{es}} + \{S_-, S_z\}\sigma_-^{\text{es}}\right)$$

$$= \begin{pmatrix} D_{\text{es}}/3 & -\Delta_2/2 & -\Delta_1/2 & 0 & i\Delta_2/2 & -i\Delta_1/2 \\ -\Delta_2/2 & -2D_{\text{es}}/3 & \Delta_2/2 & -i\Delta_2/2 & 0 & -i\Delta_2/2 \\ -\Delta_1/2 & \Delta_2/2 & D_{\text{es}}/3 & i\Delta_1/2 & i\Delta_2/2 & 0 \\ 0 & i\Delta_2/2 & -i\Delta_1/2 & D_{\text{es}}/3 & \Delta_2/2 & \Delta_1/2 \\ -i\Delta_2/2 & 0 & -i\Delta_2/2 & \Delta_2/2 & -2D_{\text{es}}/3 & -\Delta_2/2 \\ i\Delta_1/2 & i\Delta_2/2 & 0 & \Delta_1/2 & -\Delta_2/2 & D_{\text{es}}/3 \end{pmatrix}.$$

Here, $\{A, B\} \equiv AB + BA$ denotes the anticommutator.

The Zeeman (H_Z), diamagnetic (H_L) and strain/dc-Stark (H_s) perturbations affect only the spin or orbital degrees of freedom individually. The E symmetry of the excited state allows different effective g-factors ($g_{es}^{\parallel}, g_{es}^{\perp}$) for axial and transverse components of the Zeeman interaction, such that

$$
(5) \qquad H_Z = g_{es}^{\perp}\mu_B(B_x S_x + B_y S_y) + g_{es}^{\parallel}\mu_B B_z S_z
$$

$$
= I_2 \otimes \mu_B \begin{pmatrix} -g_{es}^{\parallel}B_z & g_{es}^{\perp}(B_x + iB_y) & 0 \\ g_{es}^{\perp}(B_x - iB_y) & 0 & g_{es}^{\perp}(B_x + iB_y) \\ 0 & g_{es}^{\perp}(B_x - iB_y) & g_{es}^{\parallel}B_z \end{pmatrix}.
$$

Similarly, the axial diamagnetic shift is given by the orbital operator

$$
(6) \qquad H_L = \mu_B L_z B_z \sigma_y^{es} = \mu_B L_z B_z \begin{pmatrix} 0 & -i \\ i & 0 \end{pmatrix} \otimes I_3,
$$

where $L_z\mu_B$ is the z component of the orbital magnetic moment. Symmetry implies that transverse diamagnetic components are zero. The orbital magnetic moment is known to be relatively small from measurements of circular dichroism [11, 12], with a value $L_z = 0.05$ that corresponds to a frequency shift of only $L_z\mu_B B/h \approx 50\,\mathrm{MHz}$ at $B = 100\,\mathrm{G}$. This value is comparable to typical optical linewidths and smaller than most other terms in the Hamiltonian, hence the diamagnetic shift is often ignored for measurements performed at relatively low magnetic fields.

Finally, the perturbation due to transverse strain or electric fields is given by

$$
(7) \qquad H_s = -\delta_x \sigma_z^{es} + \delta_y \sigma_x^{es} = \delta \begin{pmatrix} -\cos(\alpha_s) & \sin(\alpha_s) \\ \sin(\alpha_s) & \cos(\alpha_s) \end{pmatrix} \otimes I_3,
$$

where $\delta_x = \delta\cos(\alpha_s)$ and $\delta_y = \delta\sin(\alpha_s)$ are the strain (or dc Stark) perturbation components in crystallographic x- and y-directions with units of energy, where the total transverse perturbation has an effective angle α_s (note the total energy splitting between the orbital branches is 2δ).

2·2. *Low- and high-strain regimes.* – An arbitrary crystal strain tensor can be decomposed into components that transform according to the C_{3v} irreducible representations A_1 (transforming like the vector z), and E (with components $\{E_x, E_y\}$ that transform like the vectors $\{x, y\}$, respectively). Similarly, the dc Stark perturbation due to electric fields applied along z transform like A_1 whereas transverse fields transform like E. Since the perturbations affect the excited-state Hamiltonian in exactly the same way, the dc Stark effect can be used to compensate an uncontrolled local strain [13]. Whereas transverse strain/Stark fields shift the orbital energies and eigenstates according to eq. (7),

the longitudinal perturbation is proportional to the orbital identity operator, amounting to an overall shift of the optical transition frequency between the ground and excited state, but no variations of the eigenstates within the excited-state manifold. The longitudinal shift can be important when multiple NV centers need to be tuned to interact with indistinguishable photons [14], however for control of individual defects it is generally possible to compensate this shift by tuning the laser, so this term is neglected here.

Near $\delta = 0$, it is convenient to use the spin-orbit basis in which the Hamiltonian is nearly diagonal [10,9], aside from the small spin-spin coupling Δ_2. The spin-orbit basis states can be written as follows in terms of the product basis:

$$(8a) \qquad |A_1\rangle = -\frac{i}{2}(|X,-1\rangle + |X,+1\rangle + i\,|Y,-1\rangle - i\,|Y,+1\rangle),$$

$$(8b) \qquad |A_2\rangle = \frac{1}{2}(|X,-1\rangle - |X,+1\rangle + i\,|Y,-1\rangle + i\,|Y,+1\rangle),$$

$$(8c) \qquad |E_1\rangle \equiv |E_{\pm,x}\rangle = -\frac{i}{2}(|X,-1\rangle + |X,+1\rangle - i\,|Y,-1\rangle + i\,|Y,+1\rangle),$$

$$(8d) \qquad |E_2\rangle \equiv |E_{\pm,y}\rangle = -\frac{1}{2}(|X,-1\rangle - |X,+1\rangle - i\,|Y,-1\rangle - i\,|Y,+1\rangle),$$

$$(8e) \qquad |E_x\rangle \equiv |E_{0,x}\rangle = -\,|Y,0\rangle,$$

$$(8f) \qquad |E_y\rangle \equiv |E_{0,y}\rangle = |X,0\rangle.$$

In this basis, the states are labeled according to the symmetry of the tensor product of spin and orbital states, which can be obtained from tables of group-theoretic coupling coefficients [15]. For example, the state $|A_1\rangle$ transforms like the irreducible representation A_1. The arrangement of these levels at zero strain and zero magnetic field is shown in fig. 1(b). It is important to work in this low-strain regime for some applications. For example, spin-orbit optical selection rules that link particular spin states with circular polarization states are present when $|A_1\rangle$ and $|A_2\rangle$ are excited-state eigenstates, and these selection rules can be used to generate spin-photon entanglement [16] or to map photon states onto spin states [17].

On the other hand, when the transverse strain/Stark perturbation is large, the excited-state manifold splits into two orbital branches, each with (spin-independent) linear polarization optical selection rules for transitions to the ground state. This situation occurs when the strain splitting, 2δ, dominates over the other coupling terms between the orbital branches, the most important being the spin-orbit parameter $\lambda = 5.33\,\text{GHz}$ [3]. Since strain splittings observed for NV centers in high-quality bulk diamond typically range between 5–50 GHz, this is often the natural situation for experiments, and it can be useful when one wishes to isolate the role of a single orbital branch.

Below, we use the Schrieffer-Wolff transformation to derive approximate expressions for the Hamiltonian in each orbital branch in this regime. Rotating the basis in orbital space by the angle α_s enclosed by the crystallographic x-axis and the direction of the

transverse perturbation, we rewrite the Hamiltonian in the form

$$
(9) \qquad \tilde{H} = e^{-i\alpha_s \sigma_y^{\text{es}}} H_{\text{es}} e^{i\alpha_s \sigma_y^{\text{es}}} = g\mu_B B S_z - \lambda \sigma_y^{\text{es}} S_z - \delta \sigma_z^{\text{es}}
$$

$$
+ D_{\text{es}} \left(S_z^2 - \frac{2}{3} \right) - \frac{\Delta_1}{4} \left(e^{-i\alpha_s} S_+^2 \sigma_-^{\text{es}} + e^{i\alpha_s} S_-^2 \sigma_+^{\text{es}} \right)
$$

$$
+ \frac{\Delta_2}{2\sqrt{2}} \left(e^{i\alpha_s} \{S_+, S_z\} \sigma_+^{\text{es}} + e^{-i\alpha_s} \{S_-, S_z\} \sigma_-^{\text{es}} \right),
$$

where the strain term is block diagonal. Note that in this expression we have assumed that the magnetic field is applied along z, and we ignore the orbital diagmagnetic shift. In this basis, the states are labeled $|\varepsilon, m_s\rangle$, where $\varepsilon \in \{L, U\}$ are the lower-energy and higher-energy states, respectively, and $m_s \in \{-1, 0, +1\}$.

Provided that $2\delta > \lambda$, we can treat the inter-branch coupling as a perturbation, dividing the Hamiltonian into

$$
(10) \qquad \qquad \tilde{H} = H_0 + V,
$$

with the inter-branch coupling term

$$
(11) \quad V =
$$

$$
\left[-\lambda S_z + \frac{i\Delta_1}{4} \left(e^{-i\alpha_s} S_+^2 - e^{i\alpha_s} S_-^2 \right) + \frac{i\Delta_2}{2\sqrt{2}} \left(e^{i\alpha_s} \{S_+, S_z\} - e^{-i\alpha_s} \{S_-, S_z\} \right) \right] \sigma_y^{\text{es}}.
$$

Starting from this model, we apply quasi-degenerate perturbation theory in the form of a Schrieffer-Wolff transformation

$$
(12) \qquad H_{\text{eff}} = e^G \tilde{H} e^{-G} = \tilde{H} + \left[G, \tilde{H} \right] + \frac{1}{2} \left[G, \left[G, \tilde{H} \right] \right] + O(G^3)
$$

$$
= H_0 + V + [G, H_0] + [G, V] + \frac{1}{2} [G, [G, H_0]] + \cdots,
$$

where the generator G is defined such that $G^\dagger = -G$ in order to eliminate the couplings between the two strain-split branches in lowest order. The condition for this to work is $[G, H_0] = -V$, because it implies a transformed effective Hamiltonian

$$
(13) \qquad \qquad H_{\text{eff}} = H_0 + \frac{1}{2}[G, V],
$$

which is second order in the couplings λ, Δ_1, and Δ_2. This effective Hamiltonian is block-diagonal, *i.e.*, it can be split up into a lower and upper branch component, each containing the contributions due to virtual transitions *via* the other branch up to linear order in the couplings.

The effective Hamiltonian takes the general form

$$(14) \qquad H_{\text{eff}} = D_{\text{es}}\left(S_z^2 - \frac{2}{3}\right) + g\mu_B B S_z - \delta\sigma_z^{\text{es}} + \begin{pmatrix} H_L & 0 \\ 0 & H_U \end{pmatrix}.$$

Within the lengthy expressions for H_L and H_U, we assume the strain splitting 2δ is the dominant energy scale, and expand to lowest order in $1/\delta$ to obtain

$$(15) \qquad H_L \simeq$$
$$\begin{pmatrix} -\dfrac{\lambda^2}{2\delta} - \dfrac{\Delta_1^2}{8\delta} & -\dfrac{1}{8}e^{-2i\alpha_s}\Delta_2 f_+(\alpha_s) & \dfrac{1}{2}e^{-i\alpha_s}\Delta_1\left(\dfrac{\lambda}{\delta}-1\right) \\ -\dfrac{1}{8}e^{2i\alpha_s}\Delta_2 f_+(\alpha_s)^* & 0 & \dfrac{1}{8}e^{-2i\alpha_s}\Delta_2 f_+(\alpha_s) \\ \dfrac{1}{2}e^{i\alpha_s}\Delta_1\left(\dfrac{\lambda}{\delta}-1\right) & \dfrac{1}{8}e^{2i\alpha_s}\Delta_2 f_+(\alpha_s)^* & -\dfrac{\lambda^2}{2\delta} - \dfrac{\Delta_1^2}{8\delta} \end{pmatrix} + O\left(\dfrac{1}{\delta^2}\right),$$

for the lower branch and

$$(16) \qquad H_U \simeq$$
$$\begin{pmatrix} \dfrac{\lambda^2}{2\delta} + \dfrac{\Delta_1^2}{8\delta} & \dfrac{1}{8}e^{-2i\alpha_s}\Delta_2 f_-(\alpha_s) & \dfrac{1}{2}e^{-i\alpha_s}\Delta_1\left(\dfrac{\lambda}{\delta}+1\right) \\ \dfrac{1}{8}e^{2i\alpha_s}\Delta_2 f_-(\alpha_s)^* & 0 & -\dfrac{1}{8}e^{-2i\alpha_s}\Delta_2 f_-(\alpha_s) \\ \dfrac{1}{2}e^{i\alpha_s}\Delta_1\left(\dfrac{\lambda}{\delta}+1\right) & -\dfrac{1}{8}e^{2i\alpha_s}\Delta_2 f_-(\alpha_s)^* & \dfrac{\lambda^2}{2\delta} + \dfrac{\Delta_1^2}{8\delta} \end{pmatrix} + O\left(\dfrac{1}{\delta^2}\right)$$

for the upper branch. Here, we have introduced the expression $f_\pm(\alpha_s) = \frac{\Delta_1}{\delta} + 2e^{3i\alpha_s}(2\pm\frac{\lambda}{\delta})$, which leads to an oscillation with the strain angle α_s of the splitting between the $S_z = 0$ and $S_z = \pm 1$ states at their respective crossing points. The diagonal elements in eqs. (15) and (16) are the spin-orbit and spin-spin induced level repulsions between the two branches, while the off-diagonal elements are second-order spin-flip terms.

3. – Coherent light-matter coupling

Experiments that probe spin-light coherence [1, 18], and related protocols for all-optical coherent control [2, 3] of NV-center spins draw on a rich history in quantum optics and atomic physics. For general background in this subject, we refer the reader to excellent textbooks such as those by Gerry and Knight [19] or Cohen-Tannoudji and Guéry-Odelin [20]. In this section, we give a brief introduction to the concept of coherent coupling between a light field and atomic transitions, using the Jaynes-Cummings Hamiltonian to derive expressions for the optical (ac) Stark effect and the Faraday effect. This derivation naturally captures the correspondence between these two effects, which

both result from the polariton energy shifts due to the interactions between the light field and atomic transitions. We discuss how the concept was applied by Buckley *et al.* [1] to demonstrate dispersive optical measurements of the spin state and all-optical coherent spin rotations.

3.1. *The Jaynes-Cummings Hamiltonian.* – The Jaynes-Cummings Hamiltonian describes the interaction between light and matter in the rotating wave approximation (see, *e.g.*, Chapter 4 of Gerry and Knight [19] for a full derivation). It is typically used in the context of cavity quantum electrodynamics to describe coherent coupling of an atom-like system to the optical field in a cavity, however it can be applied more generally even when cavities are not involved. For example, in the experiments by Buckley *et al.* [1] and Yale *et al.* [2], the "cavity" is defined by the duration of a laser pulse, τ, which is assumed to propagate in a single spatial mode that we can treat as a coherent state of light with a well-defined electric-field amplitude and phase. We assume that the turn-on and turn-off of this pulse is smooth, such that the interaction with the NV center is adiabatic. We also neglect spontaneous emission and other forms of decoherence such as spectral hopping and laser noise. A treatment of these effects can be found in ref. [1].

Our starting point is the dipole interaction Hamiltonian

$$H_{\text{int}} = \sqrt{F_{\text{DW}}}\vec{\mu} \cdot \vec{E}, \tag{17}$$

where $\vec{\mu}$ is the NV-center electric dipole, $\vec{E}$ is the local electric field, and $F_{\text{DW}} = 0.04 \pm 0.01$ is the Debye-Waller factor, which empirically accounts for the reduced resonant coupling between NV-center ground and excited states due to displacement of the nuclear coordinates during optical transitions [21]. The dipole magnitude is directly related to the NV center's spontaneous decay rate $\gamma^r = 1/13\,\text{ns}^{-1}$ [22] through

$$|\vec{\mu}|^2 = \frac{3\pi\varepsilon_0\hbar^4 c^3\gamma^r}{E_{\text{ph}}^3 n_{\text{D}}}, \tag{18}$$

where $E_{\text{ph}} = 1.945\,\text{eV}$ is the photon energy and $n_{\text{D}} = 2.4$ is the refractive index of diamond. The amplitude of the electric field can be expressed in terms of the total number of photons n in the pulse and the effective equal-intensity optical mode area at the NV-center A_{eff} through the classical irradiance

$$I = \frac{c n_{\text{D}}\varepsilon_0}{2}|\vec{E}_0|^2 = \frac{n E_{\text{ph}}}{\tau A_{\text{eff}}}, \tag{19}$$

such that

$$|\vec{E}_0| = \sqrt{\frac{2n E_{\text{ph}}}{n_{\text{D}}\varepsilon_0 A_{\text{eff}} c\tau}}. \tag{20}$$

By introducing the operators $\hat{\vec{E}} = |\vec{E}_0|(\hat{a}^\dagger + \hat{a})$ and $\hat{\vec{\mu}} = |\vec{\mu}|(\hat{\sigma}_+ + \hat{\sigma}_-)$ for the electric field and optical dipole, respectively, we cast H_{int} into the form

$$
(21) \qquad \hat{H}_{\text{int}} \simeq \frac{\hbar\Omega_0}{2} \left(\hat{a}^\dagger \hat{\sigma}_- + \hat{a}\hat{\sigma}_+ \right),
$$

where $\hat{a}^\dagger$ ($\hat{a}$) and $\hat{\sigma}_+$ ($\hat{\sigma}_-$) are creation (annihilation) operators for optical photons and atomic excitations, respectively. If the atomic ground and excited states are $|g\rangle$ and $|e\rangle$, then $\hat{\sigma}_+ = |e\rangle\langle g|$ and $\hat{\sigma}_- = |g\rangle\langle e|$. Here we neglect energy-nonconserving terms $\hat{a}\hat{\sigma}_-$ and $\hat{a}^\dagger\hat{\sigma}_+$ in the rotating wave approximation. The quantity Ω_0 is the on-resonance optical Rabi frequency, given by

$$
(22) \qquad \Omega_0 = \frac{\sqrt{F_{\text{DW}}}|\vec{\mu}||\vec{E}_0|\cos(\theta)}{\hbar},
$$

where θ is the angle between the optical dipole and the light's linear polarization axis. With the addition of the non-interacting Hamiltonian for the spin and light fields, given by

$$
(23) \qquad \hat{H}_0 = E_{\text{ph}} \left(\hat{a}^\dagger \hat{a} + \frac{1}{2} \right) + E_j \frac{\hat{\sigma}_z^{(j)}}{2},
$$

where E_j is the transition energy for the spin state with $m_s = j$ and $\hat{\sigma}_z^{(j)} = |e_j\rangle\langle e_j| - |g_j\rangle\langle g_j|$ describes the NV-center orbital excitation, we obtain the Jaynes-Cummings Hamiltonian describing the light-matter system when the spin is in state j,

$$
(24) \qquad \hat{H}_{\text{JC}}^{(j)} = \hat{H}_0^{(j)} + \hat{H}_{\text{int}}^{(j)}
$$

$$
(25) \qquad = E_{\text{ph}}\hat{a}^\dagger\hat{a} + E_j \frac{\hat{\sigma}_z^{(j)}}{2} + \frac{\hbar\Omega_0}{2} \left(\hat{a}\hat{\sigma}_+^{(j)} + \hat{a}^\dagger\hat{\sigma}_-^{(j)} \right),
$$

where we have set the optical zero-field energy to zero for simplicity.

The Hamiltonian $\hat{H}_{\text{JC}}$ is naturally expressed in the basis of non-interacting polariton states

$$
(26) \qquad \begin{cases} \left|\psi_0^{(n,j)}\right\rangle = |g_j\rangle \otimes |n+1\rangle, \\ \left|\psi_1^{(n,j)}\right\rangle = |e_j\rangle \otimes |n\rangle, \end{cases}
$$

where $|g_j\rangle$ ($|e_j\rangle$) are the bare ground (excited) states of the NV-center orbital transition for $m_s = j$, and $|n\rangle$ is a photon-number Fock state of the electromagnetic field. By diagonalizing $\hat{H}_{\text{JC}}$ in this basis, we obtain the eigenenergies

$$
(27) \qquad E_\pm(n, \Delta_j) = E_{\text{ph}} \left(n + \frac{1}{2} \right) \pm \frac{\hbar}{2}\sqrt{\Delta_j^2 + \Omega_0^2(n)},
$$
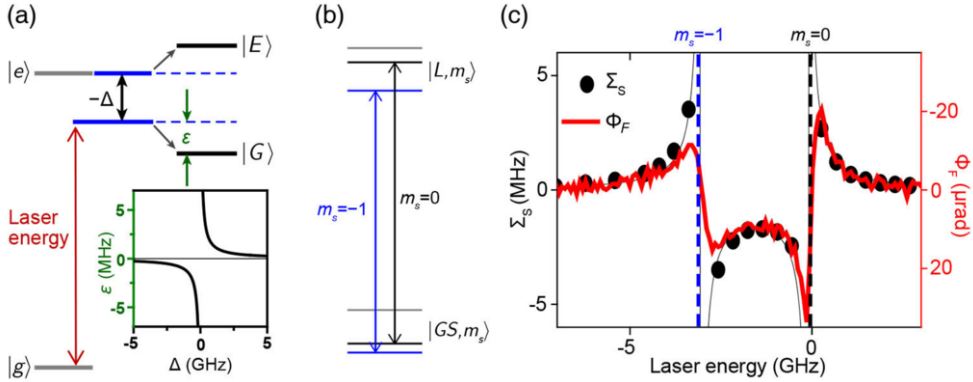
Fig. 2. – Light-matter coupling in the diamond NV center. (a) The interaction between an atomic transition with ground and excited states $\{|g\rangle, |e\rangle\}$ and a near-resonant laser field is described by the Jaynes Cummings Hamiltonian in terms of polariton states $\{|G\rangle, |E\rangle\}$ with an energy shift ε. (b) Energy-resolved transitions for different spin sublevels in the NV center's optical fine structure produce spin-dependent interactions, which manifest (c) as optical Stark rotations with frequency Σ_S and a Faraday phase shift, Φ_F as a function of laser energy. Panels (a) and (c) are adapted from ref. [1] and reprinted with permission from AAAS.

where $\Delta_j = (E_{\mathrm{ph}} - E_j)/\hbar$ is the detuning of the laser from the unshifted NV-center transition frequency and the n-dependence of Ω_0 (implicit through $|\vec{E}_0|$ in eq. (22)) is shown explicitly. These eigenenergies take the form of an anticrossing about $\Delta_j = 0$.

Since the atom is initially in the ground state and we assume that the onset of the light field is adiabatic, the occupied state during the pulse will be the polariton eigenstate having maximum overlap with $|\psi_0\rangle$, which has energy $E_g = E_\pm$ for $\Delta_j \gtrless 0$. The observed energy shift of this "$|g_j\rangle$-like" state relative to its non-interacting energy

$$(28) \qquad E_{g0} = E_{\mathrm{ph}}(n+1) - \frac{E_j}{2}$$

is therefore given by

$$(29) \qquad \varepsilon_g(n, \Delta_j) = E_g - E_{g0} = \frac{\hbar \Delta_j}{2} \left[\sqrt{1 + \frac{\Omega_0^2}{\Delta_j^2}} - 1 \right],$$

and is plotted in fig. 2(a). This energy shift, present for the duration of the laser pulse, adds a net phase to the polariton given by

$$(30) \qquad \Phi(n, \Delta_j) = \frac{\tau \varepsilon_g}{\hbar}$$

which in the far-detuned limit $|\Delta_j| \gg \Omega_0$ reduces to

$$\Phi(n, \Delta_j) \simeq \frac{\tau \Omega_0^2}{4\Delta_j} = D \frac{n}{\Delta_j} \,, \tag{31}$$

where

$$D = \frac{|\mu|^2 F_{\text{DW}} E_{\text{ph}} \cos^2(\theta)}{2\hbar^2 c n_{\text{D}} \varepsilon_0 A_{\text{eff}}} \,. \tag{32}$$

In typical experiments using a high-NA free-space objective to focus on a single NV center through a planar, (100)-oriented, diamond surface, $D/2\pi \approx 10\,\text{kHz}$, so the accumulated phase per photon is only $D/\Delta_j \approx 10^{-5}\,\text{rad}$ for typical detunings in the GHz range. Nonetheless, an optical pulse with power $\approx 1\,\mu\text{W}$ and duration $\approx 1\,\mu\text{s}$ contains $\approx 10^6$ photons, so we can still obtain an observable signal from the total accumulated phase.

3ˈ2. *The Faraday and optical Stark effects.* – In order to obtain expressions for the Faraday and optical Stark effects using this model, we need to resolve the resulting polariton state into its spin and optical components. For that purpose, we calculate the reduced density matrices

$$\begin{cases} \hat{\rho}_{\text{light}} = \text{Tr}_{\text{spin}}(\hat{\rho}), \\ \hat{\rho}_{\text{spin}} = \text{Tr}_{\text{light}}(\hat{\rho}), \end{cases} \tag{33}$$

in terms of the full density matrix $\hat{\rho}$ for polariton states, which we derive below. Whereas the polariton states are naturally written in terms of the Fock basis of photon number states, the laser field is best described by an optical coherent state, $|\alpha\rangle$, defined by

$$\hat{a}|\alpha\rangle = \alpha|\alpha\rangle. \tag{34}$$

The coherent state can be expanded in the Fock basis using the relation

$$|\alpha\rangle = e^{-\frac{|\alpha|^2}{2}} \sum_n \frac{\alpha^n}{\sqrt{n!}} |n\rangle, \tag{35}$$

which describes a Poisson distribution of Fock states, characterized by mean photon number $\langle n \rangle = |\alpha|^2$ and with uncertainty $\Delta n = |\alpha| = \sqrt{\langle n \rangle}$. An initial polariton state described by

$$|\Psi_0\rangle = \left(\sum_j \beta_j |g_j\rangle \right) \otimes |\alpha\rangle \tag{36}$$

therefore evolves to the state

$$(37) \qquad |\Psi\rangle = \sum_j \beta_j \, e^{-\frac{|\alpha|^2}{2}} \sum_n \frac{\alpha^n}{\sqrt{n!}} \, e^{i\Phi(n,\Delta_j)} \, |g_j\rangle \otimes |n\rangle$$

after an interaction involving n photons. Using eq. (31) in the limit $|\Delta_j| \gg \Omega_0$ we recast this as

$$(38) \qquad |\Psi\rangle = \sum_j \beta_j \, e^{-\frac{|\alpha|^2}{2}} \sum_n \frac{\left(\alpha e^{i\phi_j}\right)^n}{\sqrt{n!}} \, |g_j\rangle \otimes |n\rangle$$

$$(39) \qquad = \sum_j \beta_j \, |g_j\rangle \otimes \left|\alpha e^{i\phi_j}\right\rangle,$$

where $\phi_j = D/\Delta_j$ is the phase per photon accumulated by the state $|g_j\rangle \otimes |\alpha\rangle$. The full density matrix of the resulting spin-light system is then given by $\rho = |\Psi\rangle\langle\Psi|$.

We first consider the Faraday effect, which describes the observable properties of the laser light following the interaction. The reduced density matrix for the optical field is readily evaluated as

$$(40) \qquad \hat{\rho}_{\text{light}} = \sum_k \langle g_k| \, \hat{\rho} \, |g_k\rangle$$

$$(41) \qquad = \sum_j |\beta_j|^2 \left|\alpha e^{i\phi_j}\right\rangle \left\langle \alpha e^{i\phi_j}\right|.$$

Thus the optical field is in the state $|\alpha e^{i\phi_j}\rangle$ with a probability $|\beta_j|^2$ equal to the initial occupation probability of the spin state $|g_j\rangle$. The observable quantity in this case is the sinusoidal phase of the electric field, which for a coherent state $\alpha = |\alpha|e^{i\gamma}$ has an expectation value given by

$$(42) \qquad \langle \hat{E}(\vec{x}, t)\rangle_\alpha = -\sqrt{2}\mathcal{E}_0 |\alpha| \vec{u}(\vec{x}) \sin(\omega t - \gamma),$$

where $\vec{u}(\vec{x})$ describes the spatial mode and $\mathcal{E}_0$ is the vacuum electric field [19]. The complex phase of the coherent state $|\alpha\rangle$ is therefore reflected as the phase of the electric field. In the experiment by Buckley *et al.* [1], only one linear polarization of light is coupled to the transition j. Its phase is shifted relative to the non-interacting polarization state by an amount ϕ_j, which rotates the linear polarization angle of the transmitted light. Figure 3 shows a schematic of the experimental setup.

The experiment is performed in the intermediate-strain regime ($2\delta \approx 17\,\text{GHz}$) where the excited-state orbitals are energetically separated and can be individually addressed. The approximate level structure of the ground state and lower-branch excited state is shown in fig. 2(b); a relatively large axial magnetic field of $B_z = 1920\,\text{G}$ ensures that the $\hat{S}_z$ eigenstates are a good spin basis for the excited state, however the spin-spin and spin-orbit interactions shift the energies relative to the ground state as shown by eq. (15).
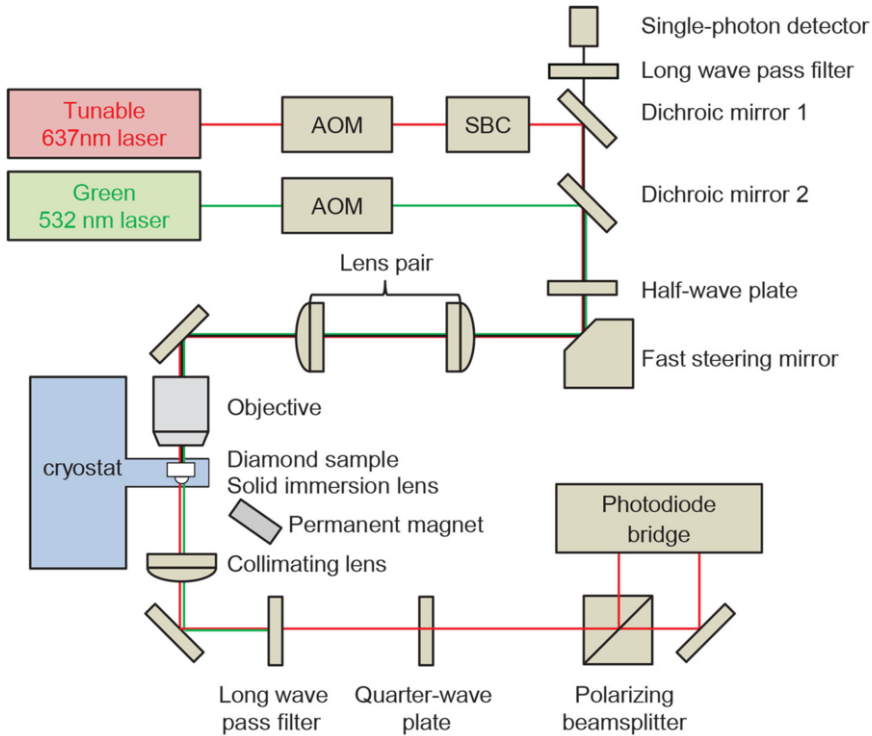
Fig. 3. – Measurement setup. Schematic of the experimental setup used to measure Faraday and optical Stark effects. A tunable laser near the NV-center ZPL at 637 nm provides the coherent optical pulses. A second laser at 532 nm is used to initialize the NV-center spin and charge state. [AOM: Acousto-optic modulator; SBC: Soleil-Babinet compensator]. Adapted from ref. [1] and reprinted with permission from AAAS.

Thus, the optical resonance for different spin sublevels occur at different frequencies, with the $m_s = -1$ transition roughly 3 GHz lower in frequency than the $m_s = 0$ transition.

We define the Faraday phase Φ_F as the difference in phase between the $m_s = 0$ and $m_s = -1$ spin states, given by

$$(43) \qquad \Phi_\mathrm{F} = \phi_0 - \phi_{-1} = D\left(\frac{1}{\Delta_0} - \frac{1}{\Delta_{-1}}\right) = -D\frac{\omega_s}{\Delta_0 \Delta_{-1}},$$

where $\omega_s = (E_{-1} - E_0)/\hbar$ is the frequency spacing between the resonances.

Similarly, the reduced density matrix for the spin is given by

$$(44) \qquad \hat{\rho}_\mathrm{spin} = \langle\alpha|\,\hat{\rho}\,|\alpha\rangle$$

$$(45) \qquad = \sum_{j,k} \beta_k^* \beta_j \exp\left[-|\alpha|^2\left(2 - e^{i\phi_j} - e^{-i\phi_k}\right)\right] |g_j\rangle\langle g_k|,$$

where we have used the identity

$$(46) \qquad \langle \alpha \mid \alpha' \rangle = \exp\left[-\frac{1}{2} \left(|\alpha|^2 + |\alpha'|^2 - 2\alpha^* \alpha' \right) \right].$$

Since $\phi_j \ll 1$, we can approximate

$$(47) \qquad \hat{\rho}_{\text{spin}} \simeq \sum_{j,k} \beta_k^* \beta_j \, e^{i \langle n \rangle (\phi_j - \phi_k)} |g_j\rangle \langle g_k|,$$

from which we identify the effective spin states

$$(48) \qquad |\text{spin}\rangle = \sum_j \beta_j \, e^{i \langle n \rangle \phi_j} |g_j\rangle = \sum_j \beta_j \, e^{i \frac{\tau \Omega_0^2}{4 \Delta_j}},$$

such that $\hat{\rho}_{\text{spin}} = |\text{spin}\rangle\langle\text{spin}|$. Physically, this shows that the spin states acquire relative phases due to their different detunings from the light field, producing an effective spin rotation. In the experiment [1], this relative optical-Stark-effect phase is directly proportional to the corresponding Faraday-effect phase through the photon number:

$$(49) \qquad \Phi_{\text{OSE}} = n \Phi_{\text{F}}.$$

The optical field in the experiment consists of two polarization modes, each with photon number n, of which only one is coupled to the NV-center optical transitions, so the total laser power is given by $P_{\text{L}} = 2n E_{\text{ph}} / \tau$, and the corresponding optical Stark frequency shift is

$$(50) \qquad \Sigma_{\text{S}} = \frac{\Phi_{\text{OSE}}}{2\pi\tau} = \frac{P_{\text{L}}}{4\pi E_{\text{ph}}} \Phi_{\text{F}}.$$

This proportionality in the far-detuned regime allows the two measurements to be shown together on the same graph as in fig. 2(c).

Although the expressions above were derived assuming the limit of large detuning ($|\Delta_j| \gg \Omega_0$), the full expressions across the absorption resonance are known from other arguments. The Faraday effect results from the real part of the frequency-dependent refractive index of the atomic transition near an absorption resonance. As a consequence of the Kramers-Kronig relation between the refractive index's real and imaginary parts, the full Faraday effect lineshape is known to be an odd Lorentzian of the form

$$(51) \qquad \phi_j = \frac{\mathcal{F}_j \Delta_j}{\Delta_j^2 + \Gamma_j^2},$$

where Γ_j is the width of absorption resonance j and $\mathcal{F}_j$ is the Faraday amplitude. By comparing this expression with eq. (43) in the far-detuned limit we see that the constant

D takes the place of the Faraday amplitude $\mathcal{F}$. Likewise, the shift in the Larmor precession rate due to the optical Stark effect is a direct consequence of the polariton energy shift of eq. (29), and so is given across all detunings by

$$(52) \qquad S_j = \frac{\Delta_j}{4\pi} \left[\sqrt{1 + \frac{\Omega_0^2}{\Delta_j^2}} - 1 \right].$$

In comparing measurements to these expressions, we can extract experimental values for $\mathcal{F}_j$, Γ_j, and Ω_0 for the appropriate transitions. For the data in fig. 2(c) from ref. [1], we obtain $\mathcal{F}_0 = 2\pi \times 6.9\,\mu\text{rad} \cdot \text{GHz}$, $\Gamma_0 = 2\pi \times 140\,\text{MHz}$, $\mathcal{F}_{-1} = 2\pi \times 7.6\,\mu\text{rad} \cdot \text{GHz}$, $\Gamma_{-1} = 2\pi \times 300\,\text{MHz}$ and $\Omega_0 = 2\pi \times 70\,\text{MHz}$. The asymmetry in the curve mainly results from the different absorption widths for the $m_s = 0$ and $m_s = -1$ transitions.

3˙3. *Discussion and implications.* – The preceding derivation illustrates how coherent light-matter interactions give rise to observable spin-dependent optical phase shifts (the Faraday effect) and coherent, optical-power-dependent spin rotations (the optical Stark effect). In principle, the Faraday effect provides a means to measure the spin state nondestructively, *i.e.*, without exciting the optical transition and re-initializing the state. This is possible since the absorption resonance has a Lorentzian lineshape, varying as $1/\Delta^2$ for large Δ, whereas the Faraday phase shift is an odd Lorentzian, varying as $1/|\Delta|$. Nondestructive measurements are important for certain applications in quantum information processing, and similar dispersive measurements are used extensively in the circuit quantum electrodynamics paradigm of superconducting qubits [23]. In practice, the Faraday phase shifts on the order of 10^{-5} rad are too small to allow high-fidelity, nondestructive measurements of individual NV centers without an optical cavity to amplify the interaction. Although it remains a challenge to fabricate nanophotonic optical cavities containing NV centers while maintaining stable optical transitions, such a platform has recently been achieved for silicon-vacancy (SiV) centers in diamond [24], where dispersive interactions analogous to those we have discussed above can also serve to mediate interactions between two SiV spins within the same cavity [25].

The optical Stark effect, meanwhile, provides a means to perform operations on a spin qubit using light rather than microwaves, which can allow addressing of individual qubits within optical networks. With enhanced interactions from an optical cavity, the optical Stark effect can provide a means for generating spin-photon entanglement or quantum operations between remote spins. Whereas the spin rotations that result from the optical Stark shifts in a level structure like fig. 2(b) generate precession about the qubit's polar axis, variations in the energy level structure and experimental design can enable rotations about arbitrary axes on the Bloch sphere, in addition to general protocols for qubit readout and initialization [2], as we discuss in the next section.
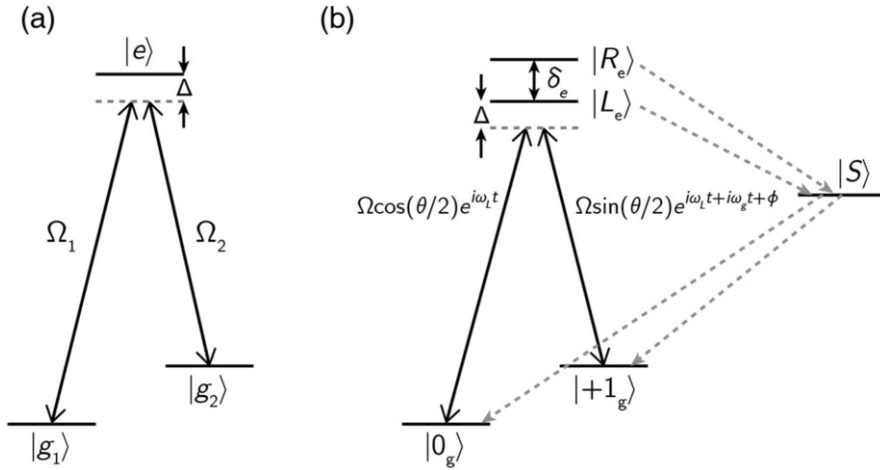
Fig. 4. – Physics of Λ configurations. (a) Three levels arranged in a Λ configuration. (b) Realization of a Λ system for the NV center from an excited-state avoided level crossing.

4. – All-optical coherent spin control

In the previous section, the optical Stark effect — viewed as the spin-like component of the coherent polariton dynamics as in eq. (44) — manifests as a relative energy shift between spin sublevels, with no change in the spin eigenstates. This is analogous to the application of a magnetic field along the defect's symmetry axis. When treating two of the triplet spin sublevels as a qubit, this amounts to a light-induced rotation about the z-axis in the Bloch sphere. In order to achieve arbitrary unitary operations on a qubit, however, rotations about two noncollinear axes are required. One can therefore ask if it is possible to realize optical Stark effects that perturb the ground-state Hamiltonian in more complex ways, $e.g.$, to generate an effective magnetic field pointing along x or y. Indeed, this is possible if one can engineer the electronic structure and optical transition diagram to enable light-induced mixing of the spin eigenstates.

Such mixing occurs naturally in a level configuration known as a lambda (Λ) system, where two lower-energy states (the qubit manifold) couple coherently to a single excited state, as shown in fig. 4(a). Lambda configurations occur in a variety of quantum systems including atoms [26, 27], trapped ions [28], quantum dots [29], and superconducting qubits [30]. As we will show below, the concept of optical Stark rotations as applied to a Λ system can be extended to realize arbitrary qubit operations; in this context they are known as stimulated Raman transitions. Furthermore, the Λ configuration is the basis for many well-known effects in quantum optics, including coherent population trapping (CPT) [26], electromagnetic-induced transparency [31], slow light [32], atomic clocks [33], and spin-photon entanglement [18].

4˙1. *Dark states and coherent population trapping.* – The essential feature of a Λ system is the appearance of "dark resonances" that occur when two light fields coherently drive both transitions to the excited state. When the light fields are tuned such that their frequency difference exactly matches the resonance frequency of the ground-state sublevels, the atom is no longer pumped to the excited state and therefore becomes dark. This phenomenon can be simply understood from the following argument [20]. If the atom is initially in a superposition of ground states,

$$|\psi(t=0)\rangle = c_1 |g_1\rangle + c_2 |g_2\rangle, \tag{53}$$

and it interacts with two laser fields characterized by instantaneous Rabi frequencies (here assumed to be complex quantities),

$$\Omega_i = \frac{\vec{\mu}_i \cdot \vec{E}_i}{\hbar}, \tag{54}$$

then the amplitude for a transition to occur from state $|g_i\rangle$ to the excited state, $|e\rangle$, is proportional to the product $c_i \Omega_i$. If a ground-state superposition $|\psi\rangle$ exists such that

$$c_1 \Omega_1 + c_2 \Omega_2 = 0, \tag{55}$$

then the amplitudes for the transitions from both ground states interfere destructively, and the atom cannot be excited. This is called a *dark state*. Since both the probability amplitudes c_i and the electric field amplitudes $\vec{E}_i$ are functions of time, the atom is not guaranteed to stay in a dark state indefinitely; however, it is straightforward to show that the condition of eq. (55) is maintained continuously if

$$\varepsilon_2 - \varepsilon_1 = \hbar(\omega_1 - \omega_2), \tag{56}$$

where ε_i and ω_i are the ground-state energies and laser frequencies, respectively, *i.e.*, if the detuning of the two light fields matches the ground-state energy splitting.

The existence of a persistent dark state results in the phenomena of CPT and electromagnetic-induced transparency. Starting from an arbitrary ground-state configuration and subject to light fields satisfying eq. (56), the atom is transiently excited and relaxes until it is trapped in the dark state and no longer interacts with the optical fields. One can think of this dissipative process as a generalization of traditional optical pumping, *i.e.*, where only one arm of the Λ system is driven. Intuitively, if only transition 1 is driven, the system will quickly relax into a steady state with $|g_2\rangle$ fully populated, uncoupled to the optical field. This scenario is a special case of eq. (55) with $\Omega_2 = 0$, where the dark state is $|D\rangle = |g_2\rangle$. In fact, a dark state satisfying eq. (55) is guaranteed to exist for any values of Ω_i, and there will always be a corresponding *bright state*, $|B\rangle$, that is orthogonal to $|D\rangle$ and couples maximally to the optical field. Thus, by choosing the amplitude and phases of the optical fields that define Ω_i, one can initialize the system into an arbitrary superposition of qubit ground states.

While the CPT process is necessarily dissipative (*i.e.*, non-unitary), coherent evolution in the ground state can be achieved using dispersive interactions in analogy with the optical Stark effect. When the optical fields satisfying eq. (56) are simultaneously detuned from the resonance condition with $|e\rangle$ as shown in fig. 4(a), the resulting light shift occurs only for the state $|B\rangle$ and not $|D\rangle$. In the qubit manifold, this manifests as a light-induced rotation about the axis pointing from $|D\rangle$ to $|B\rangle$ in the Bloch sphere. The axis can be chosen arbitrarily, including configurations on the equator when $|\Omega_1| = |\Omega_2|$ that result in complete population transfer between the qubit eigenstates. The effect in this context is usually known as stimulated Raman transitions (SRTs), drawing inspiration from an alternative picture of the process in terms of virtual transitions through the excited state. However, it is important to understand that SRTs are a dispersive effect that do not involve absorption. Again, whereas CPT varies with $1/\Delta^2$, where Δ is the detuning from the optical resonance(s), the effective Rabi frequency of SRTs scales with $1/\Delta$, so it can be substantial even when absorption is negligible.

On a practical note, it is important to recognize that the condition to have a dark state can only be sustained if the two optical fields have a deterministic phase relationship. If the fields are derived from different lasers, they must be frequency and phase stabilized to a suitable reference. Alternatively, if the required frequency difference occurs in the radiofrequency or microwave spectrum, the two fields can be derived from a single laser using an optical modulator to generate frequency sidebands. This is often the easiest approach, and it is the one adopted by ref. [2].

4‧2. *Forming a Λ system from the NV center*. – NV centers in diamond have long been known to exhibit electromagnetic-induced transparency and CPT [34,11,35,36], evidence that Λ configurations can be realized under certain conditions. At zero strain and zero magnetic field, the spin-orbit eigenstates $|A_1\rangle$ and $|A_2\rangle$ are equal superpositions of the $m_s = \pm 1$ spin eigenstates, $|\pm 1_g\rangle$, with circular-polarization optical selection rules that facilitate the generation of spin-photon entanglement [18] and CPT in the $\{|+1_g\rangle, |-1_g\rangle\}$ ground-state subspace [16]. However, it is often more convenient to work with a ground-state qubit defined in a manifold including the $m_s = 0$ sublevel, $|0_g\rangle$, since this state is naturally prepared by off-resonant optical pumping, and at low temperature it features optical cycling transitions that facilitate robust, high-fidelity readout [37].

As is apparent from the spin-spin terms in the excited-state Hamiltonian, eq. (4), and the approximate spin-triplet representations in the high-strain regime, eqs. (15) and (16), the excited-state $m_s = 0$ states are weakly admixed with $m_s = \pm 1$ by the spin-spin parameter Δ_2. However, this parameter is rather small ($\Delta_2 = 150\,\mathrm{MHz}$ [3]), so the mixing only becomes apparent near an avoided level crossing, when the $m_s = 0$ sublevel becomes nearly degenerate with $m_s = +1$ or $m_s = -1$. Such a situation is depicted in fig. 4(b), where the applied magnetic field is tuned such that a crossing occurs between the $m_s = +1$ and $m_s = 0$ spin sublevels of the lower orbital branch, $\{|+1_e\rangle, |0_e\rangle\}$. (This particular crossing can only occur when the strain is relatively small, since for large transverse perturbations the $|+1_e\rangle$ state is higher in energy than $|0_e\rangle$ even when $B = 0$; see fig. 1(b).) At the closest approach, the anticrossing levels are separated by an energy

$\delta_e \approx \Delta_2$, and the eigenstates become

$$(57a) \qquad\qquad |R_e\rangle = \frac{1}{\sqrt{2}}(|0_e\rangle + |+1_e\rangle),$$

$$(57b) \qquad\qquad |L_e\rangle = -\frac{1}{\sqrt{2}}(|0_e\rangle - |+1_e\rangle).$$

Either of these states can serve as the upper state of a Λ system connecting the $\{|+1_e\rangle, |0_e\rangle\}$ qubit states.

Yale *et al.* [2] explored this situation by tuning to an excited-state avoided level crossing as shown in fig. 4(b) and modulating a tunable laser near 637 nm using an electro-optic phase modulator in order to generate sidebands separated by the ground-state resonance frequency, ω_{gs}. This also allows for control of the relative phase between the two optical fields and their relative amplitude through the power and phase of the microwave signal applied to the modulator. These parameters determine the azimuthal (ϕ) and polar (θ) angles of the dark state formed in the ground-state Bloch sphere.

4˙3. *All-optical initialization, control, and readout.* – To describe the dynamics of the NV-center spin under optical excitation as shown in fig. 4(b), we construct a model including five energy levels: two out of the three ground-state levels $|0_g\rangle$, $|+1_g\rangle$, the two mixed excited states $|L_e\rangle$ and $|R_e\rangle$, as well as the intermediate singlet $|S\rangle$, which plays a role in mediating unintentional ISC transitions that cause dissipation. The Hamiltonian, in the rotating frame, for the subspace spanned by these five basis states can be expressed as

$$(58) \quad H = \begin{pmatrix} \Delta_L & 0 & \Omega\cos(\theta/2) & \Omega\cos(\theta/2) & 0 \\ 0 & \Delta_L & \Omega\sin(\theta/2)e^{i\phi} & -\Omega\sin(\theta/2)e^{i\phi} & 0 \\ \Omega\cos(\theta/2) & \Omega\sin(\theta/2)e^{-i\phi} & 0 & 0 & 0 \\ \Omega\cos(\theta/2) & -\Omega\sin(\theta/2)e^{-i\phi} & 0 & -\delta_e & 0 \\ 0 & 0 & 0 & 0 & \epsilon_S \end{pmatrix},$$

where the ordering of the states is $\{|+1_g\rangle, |0_g\rangle, |R_e\rangle, |L_e\rangle, |S\rangle\}$, Δ_L is the detuning of the laser frequency (ω_L) from resonance to the $|R_e\rangle$ Λ system, δ_e is the separation of the excited state levels, Ω is the optical Rabi frequency, ϕ is the relative phase between the two coherent light fields, and $\tan(\theta/2)$ is the relative amplitude between the driving fields.

The time evolution of the system includes both coherent and dissipative processes. These can be captured using the Lindblad master equation,

$$(59) \qquad \dot{\rho} = i\,[\rho, H] + \sum_{\alpha, \alpha'} \Gamma_{\alpha\alpha'} \left(\sigma_{\alpha'\alpha}\rho\sigma_{\alpha\alpha'} - \frac{1}{2}\sigma_{\alpha\alpha}\rho - \frac{1}{2}\rho\sigma_{\alpha\alpha} \right) \equiv W\rho.$$

The first term describes unitary evolution of the density matrix due to the Hamiltonian of eq. (58), whereas the second term captures dissipative processes, with the Lindblad operators $\sigma_{\alpha\alpha} = |\alpha\rangle\langle\alpha| = \sigma_{\alpha'\alpha}^{\dagger}\sigma_{\alpha'\alpha}$ and $\sigma_{\alpha'\alpha} = \sigma_{\alpha\alpha'}^{\dagger} = |\alpha'\rangle\langle\alpha|$. For $n = 5$ levels, the density matrix ρ is a Hermitian 5×5 matrix and can be described by $n^2 = 25$ real parameters ($n^2 - 1 = 24$ including the normalization condition $\text{Tr}(\rho) = 1$). The superoperator W can thus be viewed as a 25×25 matrix with rank 24.

The Lindblad operators describe incoherent, spontaneous transitions between states. We denote the decay rate from the excited states ($E = L_e, R_e$) to the ground states ($G = 0, 1$) with $\Gamma = \Gamma_{E,G_g}$, the rate for ISC from the excited states to the singlet $\Gamma_i = \Gamma_{E,S}$, and the inverse ISC rate from $|S\rangle$ to one of the ground-state levels as $\Gamma_i' = \Gamma_{S,G_g}$. The spin relaxation rate in the ground state is $\Gamma_1 = 1/T_1$. At $T \approx 10\,\text{K}$, the thermal frequency $k_B T/h \approx 200\,\text{GHz}$ exceeds the relevant NV level splittings $\approx 1\,\text{GHz}$ by orders of magnitude, and therefore $\Gamma_{+1_g,0_g} = \Gamma_{0_g,+1_g} = \Gamma_1/2$. Pure dephasing between the two ground-state levels is approximated by adding a term $\gamma = 1/T_2 = \Gamma_{0_g,0_g}$. All other rates are set to zero.

The state of the system after optical excitation during time t is obtained by integrating eq. (59),

$$(60) \qquad \rho(t) = e^{Wt}\rho(0),$$

where the initial state, $\rho(0)$, is typically one of the ground states. Equation (60) admits simple analytical solutions only for special cases, so in general we simulate the dynamics numerically. Depending on the parameters, this model can describe both CPT and SRT. In the idealized case $\Gamma_1 = \gamma = \Gamma_i = 0$, and with only one of the excited levels included, the system reduces to the three-level Λ system of fig. 4(a), and the stationary state $\bar{\rho}$ in the long-time limit $t \gg 1/\Gamma$ obtained from $\dot{\rho} = 0$ as the null space of W is the dark state:

$$(61) \qquad |D\rangle = \cos(\theta/2)|0_g\rangle - \exp(\mp i\phi)\sin(\theta/2)|+1_g\rangle,$$

where the upper (lower) sign holds for the single excited state level being $E = R\ (E = L)$.

With realistic parameters, the evolution is not so simple, since the ISC and spin decoherence tend to disspate the system away from the ideal dark state. Furthermore, we notice from eq. (61) that the dark states corresponding to the different excited states $|L_e\rangle$ and $|R_e\rangle$ have opposite phases. When these states lie on the equator ($\theta = 0$), they are orthogonal, such that the dark states from one Λ system is actually the bright state from the other. Since the separation between these states is small ($\delta_e/h \sim 180\,\text{MHz}$ in ref. [2]), there exists a tradeoff between the speed of the operations, set by the laser power, and the competition between these two orthogonal Λ systems, which becomes more prevalent as the laser power increases.

In any case, the time-dynamics of the Bloch vector representing the qubit density matrix can be obtained from

$$(62) \qquad \mathbf{b}(t) = \text{Tr}\left(\boldsymbol{\sigma}\rho(t)\right),$$
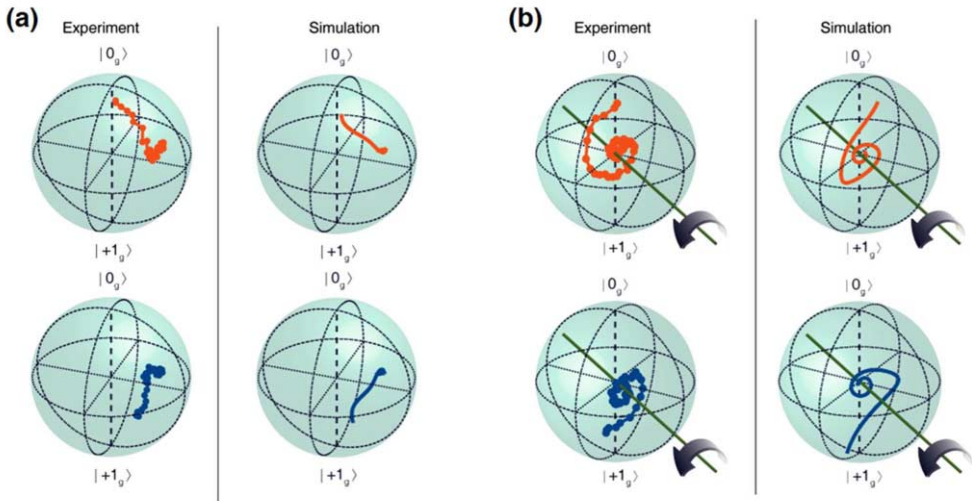
Fig. 5. – All-optical control *via* coherent dark states. Experiments (points) and simulations (curves) of quantum dynamics in the NV-center ground state driven by optical pulses designed to achieve CPT (a) and SRT (b). Orange (top) and blue (bottom) trajectories correspond to situations where the initial state is $|0_g\rangle$ or $|+1_g\rangle$, respectively. Adapted from ref. [2] and reprinted with permission from the National Academy of Sciences.

where the components of $\boldsymbol{\sigma}$ are the Pauli matrices in the ground-state subspace,

$$(63) \qquad \sigma_{\mathrm{x}} = |+1_g\rangle\langle 0_g| + |0_g\rangle\langle +1_g|,$$

$$(64) \qquad \sigma_{\mathrm{y}} = i(|+1_g\rangle\langle 0_g| - |0_g\rangle\langle +1_g|),$$

$$(65) \qquad \sigma_{\mathrm{z}} = |0_g\rangle\langle 0_g| - |+1_g\rangle\langle +1_g|.$$

The fidelity of an operation can be calculated by comparing the final density matrix to a target state, *e.g.* for initialization *via* CPT in the dark state $|D\rangle$,

$$(66) \qquad F(t) = \langle D|\rho(t)|D\rangle.$$

Figure 5 shows examples of experimental CPT and SRT trajectories from Yale *et al.* [2] alongside simulations performed using this model. The measurements (points) are acquired by performing Bayesian quantum state tomography to reconstruct the state vector from experiments where the NV-center spin is repeatedly initialized, subjected to a particular optical pulse, and then measured in one of three orthogonal bases. In addition to arbitrary-basis initialization and coherent control *via* CPT and SRT, respectively, Yale *et al.* [2] also demonstrated how the intrinsic fluorescence contrast between the bright and dark state can be used to perform projective readout of the spin state in an arbitrary basis. It is thus possible to perform full quantum operations, for example Rabi, Ramsey,

or Hahn-echo spin coherence measurements, using light fields alone. Crucially, these methods do not rely on the NV center's intrinsic level structure and spin-dependent ISC dynamics; they can be adapted to any system where a Λ configuration can be realized through tuning of external electric or magnetic fields. Indeed, the methods have recently been adapted to study the quantum properties of spin defects that do not exhibit an ISC, for example the negatively-charged SiV in diamond [38, 39] and transition-metal impurities in silicon carbide [40].

5. – Ultrafast control

The versatile concepts of light-matter coupling presented in sects. **3** and **4** underlie many applications in quantum optics and quantum information science. In particular, dispersive effects such as the Faraday phase shift, the optical Stark shift, and stimulated Raman transitions provide a means to perform coherent quantum operations on individual spins and to generate quantum correlations between light and matter. However, practical limitations mean they are not always the most efficient method to control solid-state defects. Although the technique is all-optical in the sense that only light fields interact with the spin, generation of the requisite phase-locked optical fields demands stable, tunable laser sources, optical modulators, and corresponding microwave equipment. Moreover, the CPT and SRT trajectories shown in fig. 5 exhibit several drawbacks of this technique as applied to the NV center specifically. The CPT trajectories do not terminate on the surface of the Bloch sphere, indicating a partially mixed initialized state, and the SRT trajectories rapidly spiral inwards towards a totally mixed state at the Bloch-sphere center. These nonidealities result from various experimental factors such as laser noise and spectral drift of the NV-center optical resonances, and from intrinsic properties of the NV center. One key limitation is the small spin-spin coupling parameter, $\Delta_2/h \approx 150\,\text{MHz}$, responsible for the excited-state anticrossing that forms a pair of Λ systems for the $\{|0\rangle, |+1\rangle\}$ spin sublevels as in fig. 4(b). Since the bright state from one Λ system is the dark state for the other, competing dynamics between the two Λ systems limit the fidelity of CPT initialization and add decoherence to SRT operations. This dual-Λ configuration also limits the effective speed of SRT operations (*i.e.* the ground-state Rabi frequency, Ω_g) such that $\hbar\Omega_g \ll \Delta_2$. For the NV center, the practical limit is $\Omega_g/2\pi \approx 10\,\text{MHz}$, whereas traditional microwave control of the ground state can facilitate high-fidelity operations at Rabi frequencies approaching $1\,\text{GHz}$ [41].

5˙1. *Quantum control with ultrafast optical pulses.* – In this section, we introduce an alternate approach to achieving all-optical quantum control using ultrafast optical pulses that mitigates some of these limitations [3]. This approach abandons the dispersive approximation of negligible optical excitation; rather, we directly leverage dynamics generated by the excited-state Hamiltonian to achieve desired unitary operations on the spin. Figure 6(a) shows the NV center's orbital structure in the intermediate-to-high strain regime. As described in sect. **2**˙2, transverse strain splits the excited state into two orbital manifolds, each of which are connected to the ground state *via* orthogonal,
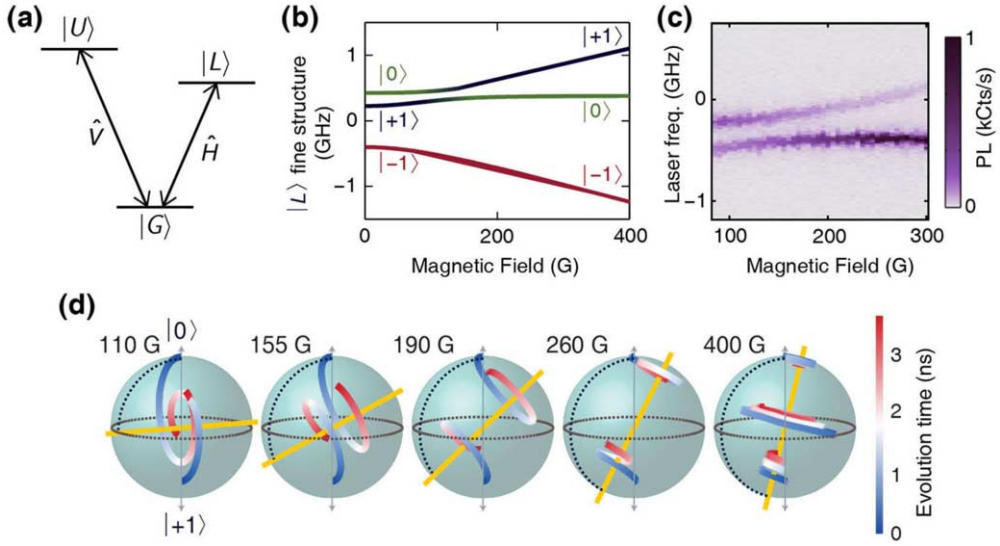
Fig. 6. – Coherent spin control with ultrafast pulses. (a) Orbital structure of the NV center at intermediate-to-high transverse strain. (b) Fine structure as a function of axial magnetic field in the $|L\rangle$ orbital branch when $\delta = 6.7\,\mathrm{GHz}$. (c) PL excitation spectroscopy as a function of axial magnetic field, showing the level anticrossing between $|L,0\rangle$ and $|L,+1\rangle$ around $B = 110\,\mathrm{G}$. (d) Trajectories of the ground-state spin qubit as a function evolution time between two optical pulses, for different settings of the magnetic field. Adapted from ref. [3] and reprinted with permission from the AAAS.

linear-polarization selection rules. Whereas previously we considered optical pulses derived from a continuous-wave laser with durations measured in nanoseconds, which can resolve the NV center's gigahertz-scale fine structure, an optical pulse with duration $\lesssim 1\,\mathrm{ps}$ has a bandwidth $\gtrsim 1\,\mathrm{THz}$, much larger than the spin-dependent frequency splittings of the ground and excited states. Such pulses operate on the orbital degrees of freedom only, effectively altering the orbital population instantaneously from the point of view of the spin dynamics.

The orbital Hamiltonian with $h = 1$ in the $\{|G\rangle, |X\rangle, |Y\rangle\}$ basis with a strain δ in direction α_S is given by

$$
(67) \qquad \mathbf{H_{orb}} = \begin{pmatrix} 0 & 0 & 0 \\ 0 & f_0 - \dfrac{\delta}{2}\cos(\alpha_S) & \dfrac{\delta}{2}\sin(\alpha_S) \\ 0 & \dfrac{\delta}{2}\sin(\alpha_S) & f_0 + \dfrac{\delta}{2}\cos(\alpha_S) \end{pmatrix},
$$

where $f_0 = c/\lambda$ is the optical transition frequency. Each pulse corresponds to a unitary operation on the orbital states, with parameters determined by the pulse intensity, shape,

and polarization. We parameterize the electric field of the optical pulses by

$$
\mathcal{E}(\alpha_E, \beta_E) = \begin{pmatrix} \cos(\alpha_E)\cos(\beta_E) - i\sin(\alpha_E)\sin(\beta_E) \\ \sin(\alpha_E)\cos(\beta_E) + i\cos(\alpha_E)\sin(\beta_E) \end{pmatrix},
$$

(68)

where α_E is the angle of the linearly-polarized component (major axis) in the NV center's (x, y)-plane, and $\beta_E \in [-\frac{\pi}{4}, \frac{\pi}{4}]$ defines the ellipticity, such that $\beta_E = 0$ and $\beta_E = \pm\frac{\pi}{4}$ correspond to linearly and circularly polarized light, respectively. Using the dipole matrix elements $\langle X|\hat{y}|G\rangle = -\langle Y|\hat{x}|G\rangle$ (other combinations vanish), we find that a pulse of polarization $\mathcal{E}(\alpha_E, \beta_E)$ couples $|G\rangle$ to the orbital state

$$
|E\rangle = \begin{pmatrix} 0 \\ -\mathcal{E}_y \\ \mathcal{E}_x \end{pmatrix},
$$

(69)

leaving the orthogonal ES basis state,

$$
|E'\rangle = \begin{pmatrix} 0 \\ \mathcal{E}_x^* \\ \mathcal{E}_y^* \end{pmatrix},
$$

(70)

unaffected.

In the experiments by Bassett *et al.* [3], pairs of pulses were derived from a single seed laser using beamsplitters and a delay line, so they were nominally identical. In this case, we can treat the pulses as instantaneous unitary operators parameterized by a rotation angle, θ, and with a relative phase, ϕ:

$$
U_{\text{FP1}} = |E'\rangle\langle E'| + \cos\left(\frac{\theta}{2}\right)(|E\rangle\langle E| + |G\rangle\langle G|)
$$

(71a)

$$
+ \sin\left(\frac{\theta}{2}\right)(|E\rangle\langle G| - |G\rangle\langle E|),
$$

$$
U_{\text{FP2}} = |E'\rangle\langle E'| + \cos\left(\frac{\theta}{2}\right)(|E\rangle\langle E| + |G\rangle\langle G|)
$$

(71b)

$$
+ \sin\left(\frac{\theta}{2}\right)(e^{i\phi}|E\rangle\langle G| - e^{-i\phi}|G\rangle\langle E|).
$$

Between the pulses, the system freely evolves according to the system Hamiltonian. The evolution can include both unitary and dissipative processes, *e.g.*, following a Lindblad master equation similar to eq. (59).

Even though the pulses only act on the orbital degrees of freedom directly, spin-orbit interactions in the excited state naturally induce spin dynamics during the free evolution period. Depending on the pulse parameters, this scheme can be adapted to probe both orbital and spin dynamics on timescales spanning femtoseconds to nanoseconds, and to realize deterministic control over the spin. For example, a pair of phase-locked

optical pulses can be designed to perform a generalized Ramsey sequence on the three-dimensional orbital Hamiltonian, where the first pulse generates a coherent superposition of ground and excited states that proceeds to evolve, and the second pulse projects the resulting state onto the measurement basis of excited states (which emit PL) and the ground state (which is dark). This scheme can be adapted to probe orbital coherence between the ground state and excited states or (by tuning the polarization to excite a superposition of $|L\rangle$ and $|U\rangle$) coherence within the excited-state manifold. Alternatively, by setting $\theta = \pi$, the optical pulses can be designed to achieve full population transfer from $|G\rangle$ to a desired excited state orbital, and *vice versa*. From the point of view of the spin, this manifests as an instantaneous change in the Hamiltonian. For a pair of such pulses that populates and subsequently depopulates the excited state after a time, t, the excited-state evolution generates a deterministic unitary operation on the spin.

5·2. *Applications*. – This novel approach to generating coherent spin rotations by utilizing free evolution in the excited state has several applications. As a time-domain spectroscopy technique, measurements of the spin dynamics that result from pairs of optical pulses provide the means to map an arbitrary excited-state Hamiltonian. The technique is termed *time-domain quantum tomography* (TDQT). In contrast to frequency-domain spectroscopies which typically yield only the Hamiltonian eigenvalues, TDQT yields both the eigenvalues and eigenvectors, from which it is possible to construct the full Hamiltonian matrix. TDQT also provides time-domain information about various non-unitary, dissipative processes. Bassett *et al.* applied the TDQT technique to extract the spin-orbit and spin-spin parameters of the NV center's excited state Hamiltonian, and to study the role of decoherence due to spontaneous photon emission, spectral diffusion, phonon-mediated orbital relaxation, hyperfine-induced spin dephasing, and the state-selective ISC transitions.

As a quantum control technique, the pulse timings can be chosen to achieve a desired unitary quantum operation on the ground-state spin. If we are interested in the evolution within a qubit subspace (and assuming we can effectively isolate the evolution to that subspace within the excited state), we can view the effect of a pair of such pulses as a temporary change in the effective magnetic field. With appropriate control over the pulse timings and excited-state Hamiltonian, this all-optical, and microwave-free technique can be applied to generate rotations for the ground-state spin qubit.

Consider for example the situation of the double-Λ configuration of fig. 4(b) that is formed near an excited-state anticrossing of the $|L, 0\rangle$ and $|L, +1\rangle$ eigenstates. By tuning the polarization of the optical pulses following eq. (69) such that the optically-coupled excited state is $|E\rangle = |L\rangle$, we can isolate most of the unitary dynamics to the four-dimensional subspace spanned by $\{|G, 0\rangle, |G, +1\rangle\}$ and $\{|L, 0\rangle, |L, +1\rangle\}$. To model this, we start from a diagonal ground-state Hamiltonian

$$(72) \qquad H_{\text{gs}} = \frac{\omega_{\text{gs}}}{2} s_z,$$

describing precession of the effective spin-1/2 qubit about the z-axis due to the effective

external magnetic field with frequency ω_{gs}. Here, s_z is a spin-1/2 Pauli-z operator acting on the $\{|G,0\rangle, |G,+1\rangle\}$ spin subspace. Similarly, the effective excited-state qubit Hamiltonian describes a precession about an axis tilted by an angle η relative to the ground state, and with a different frequency ω_{es},

$$(73) \qquad H_{\mathrm{es}} = \frac{\omega_{\mathrm{es}}}{2}\left(\sin\eta\, s_x + \cos\eta\, s_z\right) = \frac{\omega_{\mathrm{es}}}{2} s_z'.$$

Here we have set the complex phase of the off-diagonal matrix element to zero, since in experiments this phase is convolved with the constant but unspecified relative timing between the optical pulses and the microwaves used to address the ground-state spin.

The full four-dimensional Hamiltonian of this effective model is

$$(74) \qquad H = \begin{pmatrix} H_{\mathrm{gs}} & 0 \\ 0 & H_{\mathrm{es}} + \omega_{\mathrm{opt}}I \end{pmatrix} = \frac{1}{2}\left(1 - \sigma_z\right)H_{\mathrm{gs}} + \frac{1}{2}\left(1 + \sigma_z\right)\left(H_{\mathrm{es}} + \omega_{\mathrm{opt}}I\right),$$

where ω_{opt} is the optical frequency difference between $|G\rangle$ and $|L\rangle$, and σ_z is a Pauli operator for the orbital GS-ES degree of freedom, i.e., $\sigma_z|GS\rangle = -|GS\rangle$ and $\sigma_z|ES\rangle = |ES\rangle$. The action of a resonant ultrafast pulse with polarization $\hat{H}$ (see fig. 6) is described by the unitary operator of eq. (71), which reduces to

$$(75) \qquad U_{\mathrm{FP}}(\theta, \phi) = \cos\left(\frac{\theta}{2}\right) - i\sin\left(\frac{\theta}{2}\right)\left(\cos(\phi)\sigma_x + \sin(\phi)\sigma_y\right),$$

corresponding to a coherent rotation in the $\{|G\rangle, |L\rangle\}$ orbital basis by an angle θ about an axis defined by $|G\rangle + e^{-i\phi}|L\rangle$ (i.e., an equatorial axis in the orbital Bloch sphere).

The excited-state Hamiltonian parameters η and ω_{es} can be tuned by the external magnetic, electric, and strain fields. The effective expression, eq. (15), for the $|L\rangle$-branch Hamiltonian is useful for identifying regimes in which unwanted mixing with other spin and orbital states are minimized. Figure 6(b) shows the fine structure of $|L\rangle$ as a function of B_z corresponding to the strain configuration ($\delta/h = 6.7\,\mathrm{GHz}$, $\alpha_s = -0.08\,\mathrm{rad}$) from ref. [3]. The configuration is similar to the one we considered in sect. **4**, where an avoided level crossing occurs between $|L,0\rangle$ and $|L,+1\rangle$ around $B_z = 110\,\mathrm{G}$. The existence of such an anticrossing is confirmed using standard photoluminescence excitation spectroscopy as in fig. 6(c). However, frequency-domain spectroscopy only provides information about the energy eigenvalues, not the eigenstates.

According to the Hamiltonian, the excited-state spin eigenstates are fully hybridized at the center of the anticrossing; hence the effective precession axis in the excited state is orthogonal to that of the ground state, lying in the equatorial plane of the qubit Bloch sphere. At other field values, the precession axis is tilted by an angle η that approaches zero far from the level anticrossing. These eigenstates are directly revealed by TDQT measurements of the spin evolution between two ultrafast optical pulses, as shown in fig. 6(d). The figures show trajectories that begin from an initialized state in either $|0\rangle$ or $|+1\rangle$ (and, at $B = 400\,\mathrm{G}$, from a spin superposition state). The trajectories are

fits to the raw TDQT data using an analytical model that captures both unitary and dissipative dynamics [3].

At the center of the anticrossing where $\eta = \pi/2$, a full π-pulse on the spin qubit can be achieved using a single pair of optical pulses. For sequences of multiple single-qubit operations, the relative phase between pulses is deterministically set by the pulse timings. In this way, universal quantum operations on the spin can be achieved using pairs of identical optical pulses. Furthermore, whereas the dispersive SRT technique is limited in this configuration to a Rabi frequency $\Omega_g \lesssim 10\,\text{MHz} \ll \Delta_2$, direct evolution in the excited state occurs at the bare coupling rate, $\Omega_g \sim \omega_e s \sim \Delta_2$. In the data of fig. 6(d), $\Omega_g = 260\,\text{MHz}$, corresponding to a π rotation in only $1.9\,\text{ns}$, which approaches the fastest operation times demonstrated for NV centers using microwaves [41].

6. – Conclusions and future directions

The purpose of this paper is to provide an introduction to quantum optics in the context of solid-state spins like the diamond NV center. However, the methods and techniques we describe only scratch the surface of quantum optics and its potential applications for quantum information science. For example, the CPT and SRT techniques described in sect. **4** have been applied to realize alternate forms of robust quantum control employing geometric phases [42-44]. Whereas we focused on the diamond NV center, the techniques are general and are now routinely applied to other quantum systems including quantum dots [45] and other defect systems [38, 39, 46, 40, 47, 48]. As the number of materials platforms and applications for spin-based quantum technologies expands [49, 50], the importance of these techniques will only continue to grow.

* * *

REFERENCES

[1] BUCKLEY B. B., FUCHS G. D., BASSETT L. C. and AWSCHALOM D. D., *Science*, **330** (2010) 1212.
[2] YALE C. G., BUCKLEY B. B., CHRISTLE D. J., BURKARD G., HEREMANS F. J., BASSETT L. C. and AWSCHALOM D. D., *Proc. Natl. Acad. Sci. U.S.A.*, **110** (2013) 7595.
[3] BASSETT L. C., HEREMANS F. J., CHRISTLE D. J., YALE C. G., BURKARD G., BUCKLEY B. B. and AWSCHALOM D. D., *Science*, **345** (2014) 1333.

[4] Doherty M. W., Manson N. B., Delaney P., Jelezko F., Wrachtrup J. and Hollenberg L. C., *Phys. Rep.*, **528** (2013) 1.

[5] Hopper D. A., Shulevitz H. J. and Bassett L. C., *Micromachines*, **9** (2018) 437.

[6] Fu K.-M. C., Santori C., Barclay P. E., Rogers L. J., Manson N. B. and Beausoleil R. G., *Phys. Rev. Lett.*, **103** (2009) 256404.

[7] Batalov A., Jacques V., Kaiser F., Siyushev P., Neumann P., Rogers L. J., McMurtrie R. L., Manson N. B., Jelezko F. and Wrachtrup J., *Phys. Rev. Lett.*, **102** (2009) 195506.

[8] Robledo L., Bernien H., van Weperen I. and Hanson R., *Phys. Rev. Lett.*, **105** (2010) 177403.

[9] Maze J. R., Gali A., Togan E., Chu Y., Trifonov A., Kaxiras E. and Lukin M. D., *New J. Phys.*, **13** (2011) 025025.

[10] Doherty M. W., Manson N. B., Delaney P. and Hollenberg L. C. L., *New J. Phys.*, **13** (2011) 025019.

[11] Reddy N., Manson N. and Krausz E., *J. Lumin.*, **38** (1987) 46.

[12] Rogers L. J., McMurtrie R. L., Sellars M. J. and Manson N. B., *New J. Phys.*, **11** (2009) 063007.

[13] Bassett L. C., Heremans F. J., Yale C. G., Buckley B. B. and Awschalom D. D., *Phys. Rev. Lett.*, **107** (2011) 266403.

[14] Bernien H., Hensen B., Pfaff W., Koolstra G., Blok M. S., Robledo L., Taminiau T. H., Markham M., Twitchen D. J., Childress L. and Hanson R., *Nature*, **497** (2013) 86.

[15] Koster G. F., Dimmock J. O., Wheeler R. G. and Statz H., *Properties of the thirty-two point groups* (MIT Press) 1963.

[16] Togan E., Chu Y., Imamoglu A. and Lukin M. D., *Nature*, **478** (2011) 497.

[17] Yang S., Wang Y., Rao D. D. B., Hien Tran T., Momenzadeh A. S., MarkhamM. J. T., Wang P., Yang W., Stöhr R., Neumann P., Kosaka H. and Wrachtrup J., *Nat. Photon.*, **10** (2016) 507.

[18] Togan E., Chu Y., Trifonov A. S., Jiang L., Maze J., Childress L., Dutt M. V. G., Sorensen A. S., Hemmer P. R., Zibrov A. S. and Lukin M. D., *Nature*, **466** (2010) 730.

[19] Gerry C. C. and Knight P. L., *Introductory Quantum Optics* (Cambridge University Press, Cambridge) 2005.

[20] Cohen-Tannoudji C. and Guéry-Odelin D., *Advances in atomic physics: An overview*, in *Annals of the Academy of Medicine* (World Scientific, Singapore) 2011.

[21] Davies G., *J. Phys. C: Solid State Phys.*, **7** (1974) 3797.

[22] Collins A. T., Thomaz M. F. and Jorge M. I. B., *J. Phys. C: Solid State Phys.*, **16** (1983) 2177.

[23] Blais A., Huang R.-S., Wallraff A., Girvin S. M. and Schoelkopf R. J., *Phys. Rev. A*, **69** (2004) 062320.

[24] Sipahigil A., Evans R. E., Sukachev D. D., Burek M. J., Borregaard J., Bhaskar M. K., Nguyen C. T., Pacheco J. L., Atikian H. A., Meuwly C., Camacho R. M., Jelezko F., Bielejec E., Park H., Lončar M. and Lukin M. D., *Science*, **354** (2016) 847.

[25] Evans R. E., Bhaskar M. K., Sukachev D. D., Nguyen C. T., Sipahigil A., Burek M. J., Machielse B., Zhang G. H., Zibrov A. S., Bielejec E., Park H., Lončar M. and Lukin M. D., *Science*, **362** (2018) 662.

[26] Alzetta G., Gozzini A., Moi L. and Orriols G., *Nuovo Cimento B*, **36** (1976) 5.

[27] Gray H. R., Whitley R. M. and Stroud C. R., *Opt. Lett.*, **3** (1978) 218.

[28] Wineland D., Monroe C., Itano W., King B., Leibfried D., Meekhof D., Myatt C. and Wood C., *Fortsch. Phys.*, **46** (1999) 363.

[29] Xu X., Sun B., Berman P. R., Steel D. G., Bracker A. S., Gammon D. and Sham L. J., *Nat. Phys.*, **4** (2008) 692.

[30] Kelly W. R., Dutton Z., Schlafer J., Mookerji B., Ohki T. A., Kline J. S. and Pappas D. P., *Phys. Rev. Lett.*, **104** (2010) 163601.

[31] Boller K.-J., Imamoğlu A. and Harris S. E., *Phys. Rev. Lett.*, **66** (1991) 2593.

[32] Budker D., Kimball D. F., Rochester S. M. and Yashchuk V. V., *Phys. Rev. Lett.*, **83** (1999) 1767.

[33] Vanier J., *Appl. Phys. B*, **81** (2005) 421.

[34] Harley R. T., Henderson M. J. and Macfarlane R. M., *J. Phys. C: Solid State Phys.*, **17** (1984) L233.

[35] Hemmer P. R., Turukhin A. V., Shahriar M. S. and Musser J. A., *Opt. Lett.*, **26** (2001) 361.

[36] Santori C., Tamarat P., Neumann P., Wrachtrup J., Fattal D., Beausoleil R. G., Rabeau J., Olivero P., Greentree A. D., Prawer S., Jelezko F. and Hemmer P., *Phys. Rev. Lett.*, **97** (2006) 247401.

[37] Robledo L., Childress L., Bernien H., Hensen B., Alkemade P. F. A. and Hanson R., *Nature*, **477** (2011) 574.

[38] Rogers L. J., Jahnke K. D., Metsch M. H., Sipahigil A., Binder J. M., Teraji T., Sumiya H., Isoya J., Lukin M. D., Hemmer P. and Jelezko F., *Phys. Rev. Lett.*, **113** (2014) 263602.

[39] Pingault B., Becker J. N., Schulte C. H. H., Arend C., Hepp C., Godde T., Tartakovskii A. I., Markham M., Becher C. and Atatüre M., *Phys. Rev. Lett.*, **113** (2014) 263601.

[40] Koehl W. F., Diler B., Whiteley S. J., Bourassa A., Son N. T., Janzén E. and Awschalom D. D., *Phys. Rev. B*, **95** (2017) 035207.

[41] Fuchs G. D., Dobrovitski V. V., Toyli D. M., Heremans F. J. and Awschalom D. D., *Science*, **326** (2009) 1520.

[42] Yale C. G., Heremans F. J., Zhou B. B., Auer A., Burkard G. and Awschalom D. D., *Nat. Photon.*, **10** (2016) 184.

[43] Zhou B. B., Baksic A., Ribeiro H., Yale C. G., Heremans F. J., Jerger P. C., Auer A., Burkard G., Clerk A. A. and Awschalom D. D., *Nat. Phys.*, **13** (2017) 330.

[44] Zhou B. B., Jerger P. C., Shkolnikov V. O., Heremans F. J., Burkard G. and Awschalom D. D., *Phys. Rev. Lett.*, **119** (2017) 140503.

[45] Greve K. D., Press D., McMahon P. L. and Yamamoto Y., *Rep. Progr. Phys.*, **76** (2013) 092501.

[46] Becker J. N., Görlitz J., Arend C., Markham M. and Becher C., *Nat. Commun.*, **7** (2016) 13512.

[47] Becker J. N., Pingault B., Gross D., Gündoğan M., Kukharchyk N., Markham M., Edmonds A., Atatüre M., Bushev P. and Becher C., *Phys. Rev. Lett.*, **120** (2018) 053603.

[48] Christle D. J., Klimov P. V., de las Casas C. F., Szász K., Ivády V., Jokubavicius V., Ul Hassan J., Syväjärvi M., Koehl W. F., Ohshima T., Son N. T., Janzén E., Gali A. and Awschalom D. D., *Phys. Rev. X*, **7** (2017) 021046.

[49] Atatüre M., Englund D., Vamivakas N., Lee S.-Y. and Wrachtrup J., *Nat. Rev. Mater.*, **3** (2018) 38.

[50] Awschalom D. D., Hanson R., Wrachtrup J. and Zhou B. B., *Nat. Photon.*, **12** (2018) 516.

Nanoscale sensing and quantum coherence

FRIEDEMANN REINHARD

Walter Schottky Institut and Physik-Department, Technische Universität München
München, Germany

Summary. — Small solid-state qubits, most prominently single spins in solids, can be remarkable sensors for various physical quantities ranging from magnetic fields to temperature. They package the performance of their bulk semiconductor counterparts into a nanoscale device, sometimes as small as a single atom. This review is a minimalist introduction into this concept. It gives a brief summary of quantum coherence, Ramsey spectroscopy and a derivation of the "standard quantum limit" of the sensitivity that a single-qubit sensor can reach. It goes on to discuss the surprising improvement that dynamical decoupling has brought about and concludes with an outlook to the major frontiers of the field.

1. – Introduction

The history of quantum mechanics is a history of repeated underestimation. When it emerged in the early 20th century, its strange consequences were discovered only in theory, and illustrated by a series of speculative "Gedankenexperiment"s. Observing them in reality —on single photons, single atoms and single spins— seemed like an impossible mission.

When it became reality half a century later, the experimental effort of these low-energy experiments rivaled their early counterparts in high-energy physics. Operating a

set of even few qubits involved a lab densely packed with electronics, optics and vacuum setups, and a team of skilled students that would spend their days aligning dye lasers and chasing leaks —an effort comparable to a lab-scale accelerator in the 1930s. Skepticism remained whether these setups would ever make the way out of the lab into the real world.

Today, this is a realistic prospect, which is largely owing to some decisive progress of the 2000s and 2010s: the discovery of several qubits that can be implemented in the solid state, in real devices interfaced with the classical world, partly even at room temperature and ambient conditions. With this tool at hand, the attention of the scientific world is increasingly shifting to a very different question: "what to do with it?" rather than "how to do it?".

The situation is remarkably similar to the early days of the laser, which was admired as "a solution looking for a problem". This problem, at least a major one, turned out to be sensing. The perfectly monochromatic light of a laser lent itself to measurements of tiny displacements in interferometers, precise spectroscopy of molecules and, since it enabled diffraction-limited focusing, readout of compact discs. It is a tempting idea that perfectly monochromatic matter —which qubits essentially are— will find similar applications. Their narrow spectral lines could respond to tiny shifts imprinted by external fields, making them attractive sensors for various quantities. In those applications where size and effort do not matter, this development has already taken place. Atomic clocks —which can be regarded a quantum sensor for frequency and phase— have become the state of the art for timekeeping and have transformed our life by enabling satellite navigation. Finding similar applications for the younger solid-state qubits remains an exciting challenge. One obvious window of opportunity is sensing at the nanoscale. Solid-state qubits are the smallest sensors that have ever been conceived —as small as a single atom. Since such a tool has not existed until a decade ago, the mere smallness of nanoscale sensors will open unchartered territory for applications, even in the case that their sensitivity cannot be pushed beyond competing large-scale technology.

2. – Single molecules and spins as scanning probes

When scanning probe microscopy was invented in the 1980s, it quickly became clear that it would become a generic tool, not limited to tunneling microscopy on conductive surfaces. This insight sparked the development of the atomic force microscope [1], and subsequent proposals to use it as a novel detector for magnetic fields [2, 3] and magnetic-resonance microscopy on small ensembles of spins [4]. At roughly the same time, optical detection of single fluorescent molecules became widely available. This catalyzed the development of numerous novel techniques in biology, ranging from fast DNA sequencing [5] to superresolution microscopy [6-8], and led to a strong interest in nanoscale optics. Scanning near-field microscopy was developed, a technique to image optical properties with 10 nm-scale resolution by a subwavelength aperture formed by the tip of a pulled glas fiber [9]. Using a single fluorescent molecule or color center as a scanning probe in this technique became both a realistic vision and an attractive goal. It

would push near-field microscopy to its ultimate resolution limit, enabling the study of energy transfer between single molecules, single plasmons and other nano-emitters. This technique has been proposed [10] and demonstrated [11], but failed to find widespread adoption because molecules would photobleach too fast to enable reliable imaging and color centers would reside too deep in their host crystal for photonic coupling.

Some visionaries were not scared away by these problems and proposed an even more ambitious extension: to use a fluorophore with a stable electron spin, whose state could be optically "read out" by fluorescence [12]. Some fluorophores of this kind were known to exist, most prominently organic molecules with a metastable triplet state. Optically detected magnetic resonance had already been demonstrated in these systems on the level of single stationary molecules in pioneering work in the 1990s [13, 14]. If successful, a scanning probe microscope with such a sensor promised to transform near-field microscopy into a magnetic resonance microscopy technique. Spins in the sample coupling to the sensor spin would cause spin flips that could be read out by fluorescence. The whole arsenal of multidimensional magnetic resonance could be used to infer the location of spins in the sample, potentially with atomic resolution. On a lower technical level, shifts of the sensor spin resonance could be used to measure and image electric fields (via a Stark shift) and magnetic fields (via a Zeeman shift).

It was around 2008 that this idea suddenly became a realistic prospect, when several groups put forward proposals and demonstrations indicating that NV (Nitrogen-Vacancy) defects in nanodiamonds could provide a photostable fluorescent nanoprobe with an optically readable electron spin [15-18]. These properties had already been established in the 80s [19] and, on the level of single spins, in the 90s [20]. We will not present them in detail here, since this review will focus on spin sensing and is agnostic with respect to the exact spin employed an the way its readout is implemented. Suffice it to say that spin readout of the NV center is possible, because its fluorescence is slightly spin dependent (fig. 1b). It is roughly 30% more intense if the center is prepared in its lowest spin state $|0\rangle$, because fluorescence competes with a strong non-radiative pathway when the center is prepared in a higher spin state $|1\rangle$. Due to some lucky incidents, this nonradiative path has a preference to decay into the lower spin state $|0\rangle$, so that optical excitation not only reads out the spin, but also initializes it into a known state ($|0\rangle$). Finally, the energies of these spins states are shifted by magnetic fields, experiencing a field-dependent Zeeman-shift $\Delta\omega = \gamma B$, where $\gamma/2\pi \approx 30\,\mathrm{MHz/mT} = 3\,\mathrm{MHz/G}$ denotes the gyromagnetic ratio. Similar shifts exist for other physical quantities, but we will, without loss of generality, focus on magnetic field sensing in the following.

These properties are the basis for the simplest sensing experiment —measuring magnetic fields by spectroscopy of the Zeeman shift (fig. 1c). Here, the sensor spin state is continuously probed by a continous-wave laser and excited by a microwave at a tuneable frequency ω. For most frequencies, the microwave will not be resonant with the spin transition, so that the laser pumps the spin state into the bright state $|0\rangle$, causing a high level of fluorescence. When the microwave is tuned into resonance (so that $\omega = \omega_0 + \gamma B$), it will excite the center into the dark state $|1\rangle$, which becomes visible as a dip in fluorescence. By this combined microwave-optical spectroscopy, the Zeeman shift can be
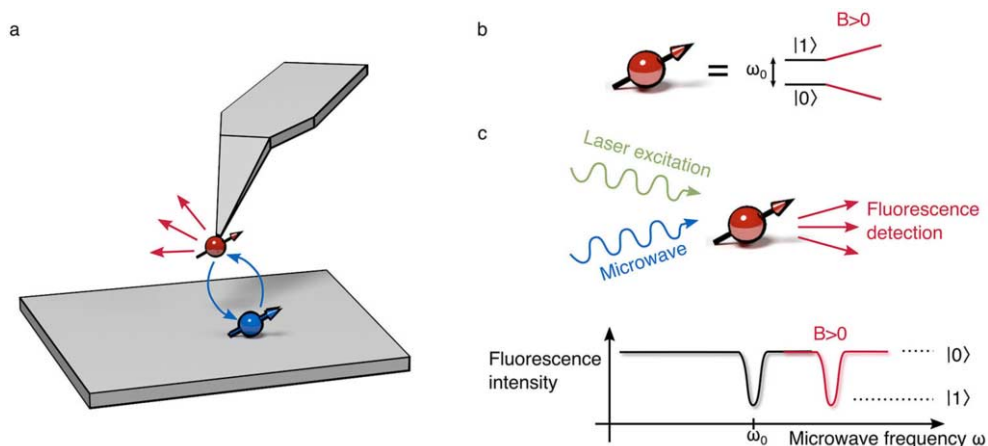
Fig. 1. – Single spins as scanning probes. a) An optically readable electron spin at the tip of a scanning probe microscope provides a sensor to image single electron and nuclear spins in samples, as well as magnetic fields. b+c) magnetic-field sensing by resonant spectroscopy. b) The energy levels of an electron spin are shifted in a magnetic field by the Zeeman effect. c) Measurement of the Zeeman shift by optically detected magnetic resonance (ODMR) spectroscopy. Laser illumination pumps the spin into a specific state $|0\rangle$. A tuneable microwave switches the spin into a less fluorescent state $|1\rangle$ if it is resonant with the Zeeman-shifted spin transition.

measured with reasonable precision, from which the magnetic field at the center can be infered. These experiments reach a typical precision in the μT range, roughly 1% of the Earth's magnetic field. While this is inferior to most existing semiconductor sensors, it is measured by the smallest sensor that can possibly be conceived, consisting of little more than a single atom.

Single NV centers can be attached to the tip of a scanning probe microscope, either by packaging them in nanodiamonds that can be glued to a commercial tip [17], or by sculpting all-diamond AFM tips with a single center embedded at their apex [21]. Repeating the Zeeman spectroscopy experiment at every pixel of a scan, magnetic fields can be imaged with higher resolution than the 10 nm-scale state of the art achieved by magnetic-force microscopy. As an additional benefit, the stray field of the NV spin does not exert backaction on soft-magnetic samples. These advantages have made spin-based scanning probe magnetometry a fertile field of research, and highlight results include images of moving domain walls [22, 23], antiferromagnets [24], Skyrmions [25, 26], hard disk write heads [27] and superconducting vortices [28, 29].

3. – Sensing by quantum coherence —reaching the fundamental limit of sensitivity

3'1. *Quantum coherence as a sensor*. – The continous-wave protocol of fig. 1 has a number of technical problems. Laser and microwave power need to be carefully tuned to ensure that the microwave excitation performs exactly one full spin-flip between two
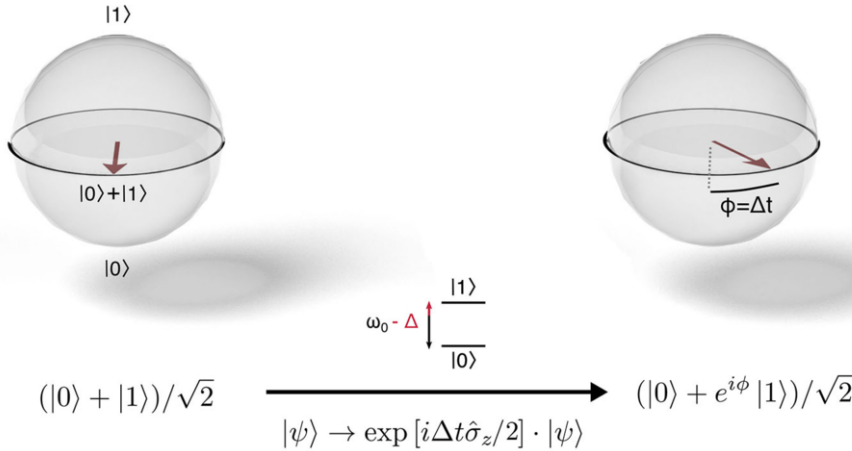
Fig. 2. – Quantum phase as a sensor for level shifts. The phase ϕ of a coherent superposition $(|0\rangle + e^{i\phi} |1\rangle)$ grows as $\phi = \Delta t$ under a spectral shift Δ.

fluorescence events. Furthermore, the spectral resolution depends on microwave power, since a high-power pulse can excite spins even if its frequency is slightly off-resonant.

It is for these reasons that most experiments today are performed using pulsed protocols, inspired by atomic clocks [30] and quantum logic. The key idea, presented in fig. 2, is to employ the quantum-mechanical phase ϕ of a coherent superposition $(|0\rangle + e^{i\phi} |1\rangle)/\sqrt{2}$ as a sensor. To see why this phase is sensitive to a small spectral shift $\Delta = \gamma B$, we consider a qubit evolving under the Hamiltonian

$$\hat{H} = \frac{\hbar}{2}(\omega_0 - \Delta)\hat{\sigma}_z \stackrel{\text{rot. frame}}{=} -\frac{\hbar}{2}\Delta\hat{\sigma}_z.$$

Here we have applied a transformation into a rotating frame, essentially a renormalization of the qubit energy, to remove the static energy ω_0. The time evolution under this Hamiltonian is

$$(2) \qquad |\psi(t)\rangle = \exp\left[-\frac{it}{\hbar}\hat{H}\right] |\psi(t=0)\rangle$$

$$(3) \qquad = \exp\left[i\frac{\Delta t}{2}\hat{\sigma}_z\right] |\psi(t=0)\rangle$$

$$(4) \qquad \stackrel{|\psi(t=0)\rangle=(|0\rangle+|1\rangle)/\sqrt{2}}{=} (|0\rangle + e^{i\Delta t} |1\rangle)/\sqrt{2}$$

up to an insignificant global phase $e^{-i\Delta t/2}$. For a nonzero detuning Δ, the phase ϕ grows over time. Since this evolution occurs in the absence of any manipulation and readout pulses, it is insensitive to experimental fluctuations in laser and microwave power.

It is instructive to consider this evolution on the "Bloch sphere" (fig. 2). This sphere is a map from $SU(2)$ (spin states) to the unit sphere in $\mathbb{R}^3$. $|0\rangle$ and $|1\rangle$ are mapped to

Fig. 3. – Rabi oscillations. A spin driven by a resonant microwave oscillates between states $|0\rangle$ and $|1\rangle$ by alternating phases of absorption and stimulated emission. A pulsed microwave drive can be applied for a full spin flip ("π-pulse") or can be stopped half-way ("$\pi/2$-pulse"), leaving the spin in a coherent superposition $(|0\rangle + |1\rangle)/\sqrt{2}$.
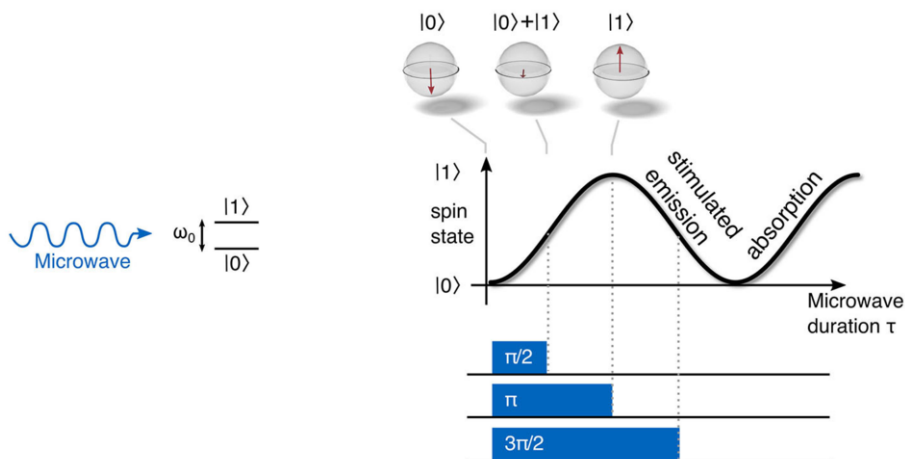
its south and nord poles, respectively. Coherent superpositions $(|0\rangle + e^{i\phi}|1\rangle)/\sqrt{2}$ reside on the equator, with ϕ translating into their geographical longitude. In this picture the time evolution of eq. (2) is a rotation of the spin along the equator. Since this rotation revolves with angular velocity Δ, it is very much reminiscent of the movement of the needle in a classical instrument.

3˙2. *Creating and reading out quantum coherence —the Ramsey protocol*. – In contrast to a classical needle, the quantum-mechanical phase ϕ is invisible. Therefore, the protocol of fig. 2 needs to be supplemented by two additional steps, one to prepare a coherent superposition and one to convert the phase into a measurable quantity such as the spin state itself (fig. 4). Both steps are implemented by microwave pulses, specifically "$\pi/2$" pulses of carefully tuned length.

The key idea behind these pulses can be understood by considering the evolution of a spin that is driven by a resonant microwave (fig. 3). A spin starting in state $|0\rangle$ will absorb a photon from the microwave, flipping from $|0\rangle$ to $|1\rangle$. Somewhat counterintuitively, a spin starting from $|1\rangle$ will flip back from $|1\rangle$ to $|0\rangle$, emitting a microwave photon by stimulated emission. Under continuous driving, these processes will alternate, so that the spin rotates back and forth between $|0\rangle$ and $|1\rangle$, a process known as Rabi oscillation. This rotation revolves at an angular frequency Ω, referred to as Rabi frequency, which is set by the power of the microwave drive. The effect of a microwave pulse depends on its duration. It can be set to perform half of an oscillation, flipping the spin from $|0\rangle$ to $|1\rangle$. Such a pulse is referred to as a π pulse, since its duration τ is chosen such that $\Omega\tau = \pi$. Crucially however, the Rabi oscillation can also be stopped "half-way" between $|0\rangle$ and $|1\rangle$, leaving the spin in the coherent superposition $(|0\rangle + |1\rangle)/\sqrt{2}$. Since the duration of

such a pulse is twice shorter (such that $\Omega\tau = \pi/2$), it is referred to as a $\pi/2$ pulse.

In a more rigorous manner, these effects can be derived from the Hamiltonian of atom-light interaction

$$\hat{H} = \frac{\hbar}{2}(\omega_0 - \Delta)\hat{\sigma}_z + \hbar\Omega\cos(\omega_0 t)\hat{\sigma}_y,$$

$$\stackrel{\text{rot. frame}}{=} -\frac{\hbar}{2}\Delta\hat{\sigma}_z + \frac{\hbar\Omega}{2}(1 + e^{-2i\omega_0 t})\hat{\sigma}_y,$$

$$\stackrel{\text{rot. wave approx.}}{\approx} -\frac{\hbar}{2}\Delta\hat{\sigma}_z + \frac{\hbar\Omega}{2}\hat{\sigma}_y.$$

Here the transformation into a rotating frame with frequency ω_0 (step 1) not only renormalizes the qubit energy, it also introduces an oscillatory factor $e^{-i\omega_0 t}$ to all terms coupling states $|0\rangle$ and $|1\rangle$, in particular $\hat{\sigma}_y = i|0\rangle\langle 1| + H.C.$ In this process the two components $\cos(\omega_0 t) = (e^{i\omega_0 t} + e^{-i\omega_0 t})/2$ of the cosine are transformed into a constant term (1) and a rapidly oscillating term $(e^{2i\omega_0 t})$. This latter term can be neglected in a "rotating frame approximation" as long as $\Omega, \Delta \ll \omega_0$.

In this description, a microwave drive is equivalent to a rotation of the spin around the axis y of the Bloch sphere, induced by the term proportional to $\hat{\sigma}_y$. Typically, the drive is so strong that $\Omega \gg \Delta$, so that the term in $\hat{\sigma}_z$ can be neglected whenever the drive is applied. In these conditions, π and $\pi/2$ pulses correspond to the propagators

$$\hat{\pi} = \exp\left[-i\frac{\Omega\tau_\pi}{2}\hat{\sigma}_y\right],$$

$$\frac{\hat{\pi}}{2} = \exp\left[-i\frac{\Omega\tau_{\pi/2}}{2}\hat{\sigma}_y\right],$$

with

$$\hat{\pi}|0\rangle = \frac{\hat{\pi}}{2} \cdot \frac{\hat{\pi}}{2} \cdot |0\rangle = \frac{\hat{\pi}}{2} \cdot (|0\rangle + |1\rangle)/\sqrt{2} = |1\rangle.$$

With these ingredients we can understand the most fundamental quantum sensing protocol, the Ramsey sequence (fig. 4). An initial $\pi/2$ pulse prepares the spin into the coherent superposition $(|0\rangle + |1\rangle)/\sqrt{2}$. It is subsequently subjected to free evolution under a spectral shift Δ for some waiting time τ, picking up a phase $\phi = \Delta t$. A second $\pi/2$ pulse converts this phase to a population inversion of the spin state by transforming the state from $(|0\rangle + e^{i\phi}|1\rangle)/\sqrt{2}$ to $i\sin\frac{\phi}{2}|0\rangle + \cos\frac{\phi}{2}|1\rangle$. This population inversion is measurable, since it affects the probability $|\langle 1|\psi\rangle|^2$ of finding the spin in state $|1\rangle$ at the end of the sequence. This probability is an oscillatory function of ϕ

$$|\langle 1|\psi\rangle|^2 = \cos^2\left(\frac{\phi}{2}\right) = \frac{1}{2}(1 + \cos\phi).$$
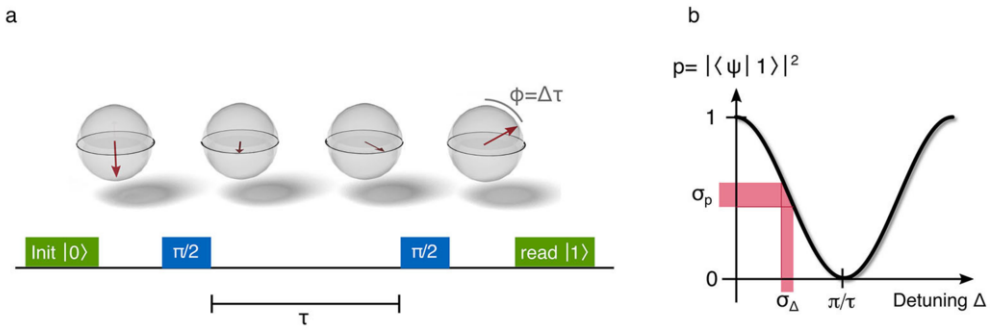
Fig. 4. – The Ramsey protocol. a) An initial $\pi/2$-pulse prepares a coherent superposition, which undergoes free evolution to pick up a phase $\phi = \Delta\tau$. This phase is converted into spin population by a second $\pi/2$-pulse. b) Sensitivity of Ramsey spectroscopy. For a fixed evolution time τ, the spin state is an oscillatory function of the shift Δ. Its state can be measured with uncertainty σ_p, which translates into an uncertainty σ_Δ on the measurement of Δ.

If there is no precession during the free evolution τ, the two $\pi/2$ pulses will add up to a π pulse, leaving the spin in state $|1\rangle$ at the end of the sequence. Precession during τ will be translated into a rotation between states $|0\rangle$ and $|1\rangle$.

Experimentally, ϕ can be varied both by varying τ and by varying Δ. In both cases, the measurement result will trace an oscillatory function, referred to as Ramsey fringes in the time and frequency domain, respectively. For sensing applications, the latter implementation is more relevant. Here, the oscillating spin signal at the end of the experiment provides a ruler for spectral shifts Δ, similar to the fringes of an optical interferometer providing a ruler for displacement.

Since quantum sensing experiments typically aim at detecting very small signals, the fringes are hardly ever recorded in their entirety. Instead, the sensor is operated at a fixed detuning Δ_0, chosen such that the spin signal $p = |\langle 1 | \psi \rangle|^2$ is maximally sensitive to small fluctuations in Δ. This is typically the slope of a Ramsey fringe, and operation at this point can be ensured by applying a fixed detuning of $\Delta_0 = \pi/(2\tau)$ to the microwave drive.

The precision of such a sensing experiment is limited by the precision of spin readout. The measurement of $p = |\langle 1 | \psi \rangle|^2$ will always have some experimental uncertainty σ_p, which translates into an uncertainty σ_Δ on the measurement of Δ by Gauss' law of error propagation.

$$\sigma_\Delta = -\sigma_p \cdot \left.\frac{\mathrm{d}\Delta}{\mathrm{d}p}\right|_{\text{steepest slope}} = \sigma_p \cdot \frac{2}{\tau} .$$

If all technical fluctuations are eliminated, the fundamental limit of σ_p is set by quantum projection noise. A single measurement of p cannot access a floating point value between 0 and 1. Instead, spin readout will project the spin into either $|0\rangle$ or $|1\rangle$, providing one

quantized bit of information ($p_{\text{measured}} = 0$ or $p_{\text{measured}} = 1$). Since we are operating at the slope, where $p \approx 0.5$, this measurement is always wrong, with an error of

$$\sigma_p = \sqrt{\langle p^2_{\text{measured}} \rangle - \langle p_{\text{measured}} \rangle^2} = \sqrt{1/2 - 1/4} = 1/2,$$

$\langle \cdot \rangle$ denoting the expectation value. As we average the results of M repeated measurements on N sensors operating in parallel, this error diminishes according to

$$\sigma_p = \frac{1}{2\sqrt{MN}}$$

so that the sensor achieves a precision of

$$\sigma_\Delta = \frac{1}{\tau\sqrt{MN}} \,.$$

This result could have been obtained by common sense: a single measurement of duration τ is able to measure a frequency with a Fourier-limited resolution $1/\tau$, and averaging the result over $M \cdot N$ uncorrelated measurements will boost precision by a factor of $1/\sqrt{MN}$.

For simplicity, we have assumed single-shot readout, $i.e.$ that the spin state can be measured in a single experimental repetition. In experiments, this is frequently impossible, for instance because of low detection efficiency of photodetectors or because the readout signal differs by less than 100% between states $|0\rangle$ and $|1\rangle$. In this case, the number of repetitions M has to be replaced by M/M_0, where M_0 denotes the number of measurements required to measure the spin state once.

3˙**3.** *Decoherence and the fundamental limit to sensitivity.* – The above expression for σ_Δ is not yet a useful figure of merit for sensor performance, because σ_Δ can always be boosted to infinite precision by averaging over a larger number of measurements N or by increasing the slope of the fringes by increasing τ. Obviously, there are practical limits to both of these tricks that need to be taken into account by a reasonable figure of merit. In practice this is achieved by comparing sensor performance in terms of "sensitivity", a corrected figure of merit which we will derive in the following paragraphs.

Regarding averaging, it is important to note that this concept can be applied to any sensor. A statement like "an NV qubit can measure fields with nT precision" is useless (although we have made it above), since even a simple compass could in principle be pushed to this level by averaging its signal over a long time. To discount for this effect, sensor sensitivity is normalized to acquisition time. Since M measurements will take a time $T = M \cdot \tau$, spectral resolution scales as $\sigma_\Delta = 1/(\sqrt{\tau NT})$, and the precision in sensing a magnetic field is

$$(5) \qquad \sigma_B = \frac{\sigma_\Delta}{\gamma} = \frac{1}{\gamma\sqrt{\tau NT}} = \eta_B \frac{1}{\sqrt{T}} \,.$$

Here, the *sensitivity* $\eta_B = 1/(\gamma\sqrt{\tau N})$ provides a figure of merit that discounts for averaging. A sensor that can reach a higher precision in a given amount of averaging time is rated a better sensor, quantified by a lower value of sensitivity. Similar formulas can be established for other quantities $(E, T, \ldots)$ that can be measured by spectroscopy of some suitable spectral shift. The units of these figures are

$$[\eta_B] = \frac{\mathrm{T}}{\sqrt{\mathrm{Hz}}}\,, \qquad [\eta_E] = \frac{\mathrm{V/cm}}{\sqrt{\mathrm{Hz}}}\,, \qquad [\eta_T] = \frac{\mathrm{K}}{\sqrt{\mathrm{Hz}}}\,, \qquad \ldots\,.$$

The slightly un-intuitive unit $1/\sqrt{\mathrm{Hz}}$ is omnipresent whenever sensitivities are involved. It is best understood as "sensor precision obtained after 1 second of averaging".

Still, sensitivity as defined in eq. (5) is not a meaningful figure of merit, since it can be pushed to arbitrary limits by increasing τ. The fundamental limit to this parameter is set by a quantum-mechanical effect known as decoherence, which limits τ to values less than the qubit's "coherence time" T_2^*. Decoherence refers to the fact that a quantum superposition $(|0\rangle + e^{i\phi}|1\rangle)/\sqrt{2}$ does not persist forever. It is a fragile state, which decays into a "classical mixture", where the qubit is in state $|0\rangle$ or $|1\rangle$ with 50/50 probability. This state is different from the coherent superposition that the qubit started from, where the spin in a way lives simultaneously in both $|0\rangle$ and $|1\rangle$. The difference can be quantified by the density matrix

$$\hat{\rho} = \sum_i p_i |\psi_i\rangle \langle\psi_i|\,,$$

where p_i denotes the (classical) probability of the qubit to be prepared in a quantum state ψ_i chosen from some set of states indexed by i. The density matrix $\hat{\rho}$ can capture the difference between "simultaneously $|0\rangle$ and $|1\rangle$" and "either $|0\rangle$ or $|1\rangle$ with 50/50 probability", since

$$\hat{\rho}\left[(|0\rangle + e^{i\phi}|1\rangle)/\sqrt{2}\right] = \frac{1}{2}\begin{pmatrix} 1 & e^{i\phi} \\ e^{-i\phi} & 1 \end{pmatrix},$$

$$\hat{\rho}_{50/50} = \frac{1}{2}(|0\rangle\langle0| + |1\rangle\langle1|) = \frac{1}{2}\begin{pmatrix} 1 & 0 \\ 0 & 1 \end{pmatrix}.$$

We see that quantum coherence is quantified by the off-diagonal elements of $\hat{\rho}$. To see why quantum states have a tendency to decay from a coherent state into classical mixtures, we consider a qubit that has some intrinsic uncertainty σ_Δ on its transition frequency Δ (fig. 5b). This uncertainty could arise from a fluctuating magnetic background field, for instance the stray field from nuclear spins in the carbon lattice in the case of an NV center. We assume the background field to take a random value in each experimental repetition, so that the detuning Δ is normally distributed with a probability density

$$p(\Delta) = \frac{1}{\sqrt{2\pi\sigma_\Delta^2}} e^{-\frac{(\Delta - \Delta_0)^2}{2\sigma_\Delta^2}}\,.$$
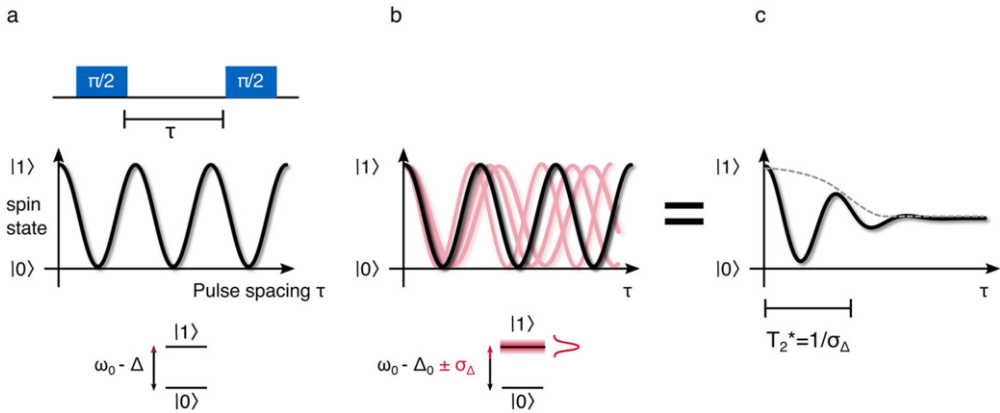
Fig. 5. – Decoherence. A random static background shift σ_Δ blurs the Ramsey fringes, inducing a decay of spin contrast over a timescale $T_2^* = 1/\sigma_\Delta$.

Each random value of Δ will lead to a different state $(|0\rangle + e^{i\Delta\tau} |1\rangle)$ at the end of the free evolution, so that the spin state before the second $\pi/2$ pulse is described as the statistical mixture

$$(6) \quad \hat{\rho} = \int \mathrm{d}\Delta\, p(\Delta) \begin{pmatrix} 1 & e^{i\Delta\tau} \\ e^{-i\Delta\tau} & 1 \end{pmatrix} \overset{\text{Gaussian integral}}{=} \begin{pmatrix} 1 & e^{-\frac{1}{2}\sigma_\Delta^2\tau^2} e^{i\Delta_0\tau} \\ e^{-\frac{1}{2}\sigma_\Delta^2\tau^2} e^{-i\Delta_0\tau} & 1 \end{pmatrix}.$$

The off-diagonal elements of this state decay as $e^{-\frac{1}{2}\sigma_\Delta^2\tau^2}$ for increasing evolution time τ, with a time constant

$$1/\sigma_\Delta := T_2^*.$$

Since it is the off-diagonal terms that are converted into spin population by the second $\pi/2$ pulse, this decay manifests itself as a decay of the time-domain Ramsey fringes over a timescale of T_2^* (fig. 5c). This result can also be derived from a more classical argument: a randomly varying detuning Δ will lead to randomly varying frequencies of the time-domain Ramsey oscillations (fig. 5b). For small evolution times τ, this does not have a visible effect, since the spin will roughly end in the same peak or valley in any experimental repetition. For large evolution times, the measurement result is increasingly randomized, with the spin ending randomly in a peak or a valley depending on the exact value of Δ in a specific experimental repetition. Averaging over all these results can only lead to one result: $p = 0.5$, zero spin contrast, no fringes.

Once decoherence is considered, the choice of τ in a sensing experiment is subject to a compromise. Too short values will lower sensitivity, because the frequency-domain fringes become less steep. Too long values will lower sensitivity, because decoherence reduces fringe contrast and, concomittantly, their slope. An educated guess suggests that the

optimum choice is $\tau \approx T_2^*$, long enough to build up a steep slope, but sufficiently short to avoid death from decoherence. This guess is correct, as can be verified by an explicit minimization of the sensitivity as a function of τ. With this choice, the sensitivity of a quantum sensor reads

$$(1) \qquad\qquad \eta_B = \frac{1}{\gamma\sqrt{NT_2^*}},$$

which is known as the "standard quantum limit". This relation is so fundamental that it is referred to as "eq. (1)" by some researchers in the field [31] and in this review.

We conclude this section by a discussion of some of its more subtle implications

- It is a frequent misconception that a stronger coupling to the environment γ will automatically yield a sensor with a better sensitivity, suggested by the fact that γ appears in the denominator of eq. (1). The fallacy is that a stronger coupling to the environment also impacts $T_2^* = \sigma_\Delta^{-1}$ by increasing the frequency noise σ_Δ. A famous example of this subtlety is the use of entangled states of multiple qubits such as $(|00\rangle + e^{i\phi}|11\rangle)/\sqrt{2}$. These have long been believed to result in better sensitivity than a sensor built from independent qubits. Since their total magnetic moment grows linearly with N, an entangled sensor employing a single effective spin of N entangled qubits would at first sight achieve a sensitivity of $1/(\gamma N\sqrt{T_2^*})$, a factor of $\sqrt{N}$ better than eq. (1) [32-34]. Unfortunately, stronger coupling also increases the impact of background noise, so that increased decoherence shrinks T_2^* by a factor of N, spoiling the improvement [35, 36].

- While we frequently speak of T_2^* as an intrinsic constant of a specific qubit, we should think of it just as much as a constant of a qubit's environment, quantifying the level of intrinsic background noise. As a specific example, NV centers have orders of magnitude higher coherence times than quantum dots, and we might easily think of them as "better" qubits. Yet, both are based on the same quantum entity, a single electron spin, and the difference merely results from the fact that nuclear spins are a lot less abundant in diamond than in typical quantum dot materials like GaAs. As a consequence, the relation might turn upside down if quantum dots could be engineered in diamond, and the search for new spin qubits could result in disappointment if it is focused on the wrong materials. Most importantly, both qubits could become equally bad sensors when they have to be operated close to a sample with high intrinsic noise.

4. – Sensing by dynamical decoupling —the hidden revolution

Despite its fundamental nature, eq. (1) can be broken. The key idea here is that T_2^* can be extended to longer timescales if a tool is found to suppress buildup of a random phase $\sigma_\Delta\tau$ in the presence of a random spectral shift σ_Δ. Such a tool is provided by quantum control protocols, more complicated manipulations of the spin than a mere creation and
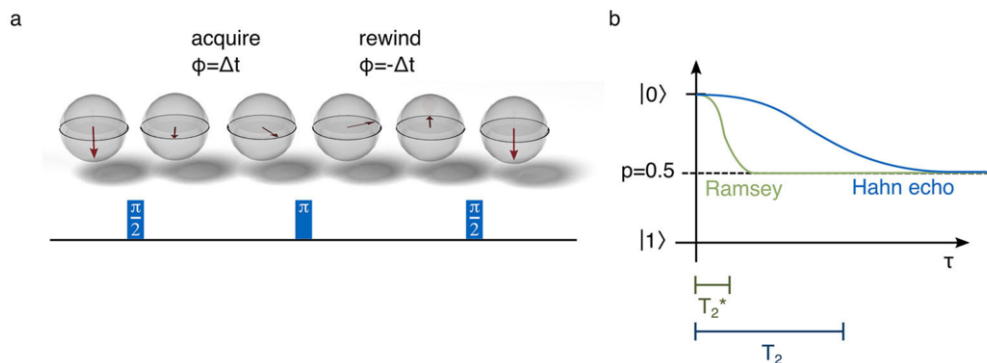
Fig. 6. – Hahn echo. a) A π-pulse in the middle of the free evolution time mirrors the spin to the back side of the equator, so that a phase acquired from a static shift Δ is exactly rewound in the second half of the sequence. b) Coherence persists for a longer time T_2 under the Hahn echo sequence.

detection of coherence. The first protocol of this kind, known as "spin echo" or "Hahn echo", was developed by Erwin Hahn in 1950 [37]. It is presented in fig. 6. It differs from standard Ramsey spectroscopy by an additional π-pulse, introduced in the middle of the free evolution time. This pulse mirrors the spin state to the other side of the equator, so that a phase built up by a constant detuning Δ in the first half of evolution is exactly rewound in the second half. By this mechanism, the effect of a constant Δ is canceled and decoherence is suppressed, so that τ can be chosen much longer than T_2^*. In practice there is a new limit to τ, referred to as T_2, arising from the fact that Δ is never purely static and that the spin phase remains sensitive to fluctuations that vary over the timescale of the Hahn echo sequence. This timescale is situated between T_2^* and T_1, the spin-flip lifetime of an incoherent spin state like $|1\rangle$.

At first sight the Hahn echo protocol appears to be useless for sensing, since it cancels a constant detuning Δ. While this mitigates decoherence, it comes at the price of cancelling a static signal, too. It turns out, however, that a qubit subjected to a Hahn echo sequence remains sensitive to signals oscillating at a nonzero frequency and that this sensitivity can actually be tuned to specific signal frequencies in a very selective manner [38-45]. The key idea, referred to as "quantum lock-in detection" or "dynamical decoupling" is presented in fig. 7a. We consider a qubit that is exposed to an oscillating signal at a frequency ν. This signal could not be detected in a Ramsey sequence, since positive and negative half-cycles would imprint opposite phases on the spin and cancel over the free evolution time. We can, however, effectively rectify the signal by applying periodic π pulses to the spin, whose spacing τ is synchronized to the signal by the choice $2\tau = \nu^{-1}$. Since each pulse induces a flip of the sensor spin, it effectively inverts the sign of the signal in the flipping reference frame of the sensor. The effect of this scheme is similar to classical lock-in-detection, where the signal would be inverted by a mixer or a similar device. Signals at a frequency $1/(2\tau)$ are rectified to DC (zero frequency) while
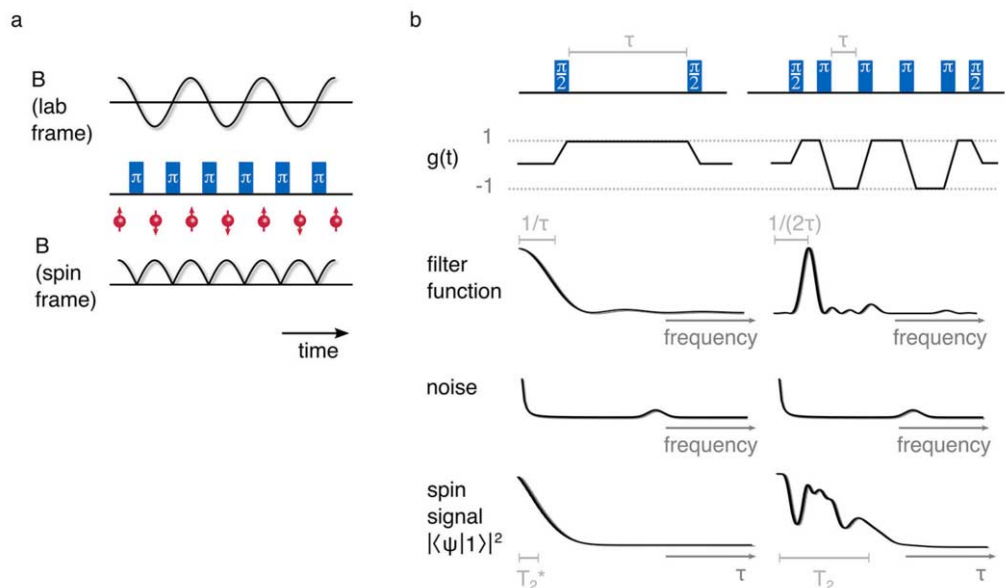
Fig. 7. – Dynamical decoupling. a) A train of π-pulses acts as a lock-in grating, effectively inverting the sign of the signal in the flipping reference frame of the sensor spin. b) The spectral sensitivity of a spin under dynamical decoupling is modeled by a "filter function", the Fourier transform of a time-domain sensitivity function $g(t)$. For a τ-periodic grating (right), the filter function is peaked at a frequency $1/(2\tau)$, so that the spin coherence decay traces an inverted copy of the noise spectrum, turning the spin into a spectrum analyzer.

static shifts will be converted to some nonzero frequency so that their effect cancels over time.

To employ this scheme in a sensing sequence, the lock-in grating of periodic π-pulses is embedded into two $\pi/2$-pulses to create and read a quantum phase (fig. 7b). The π-pulse grating tunes sensitivity to a specific frequency, which simultaneously suppresses decoherence from static shifts and sensitizes the quantum phase to specific AC signals. With dynamical decoupling, a qubit becomes a quantum spectrum analyzer. Ramsey spectroscopy and Hahn echo can be regarded the two simplest incarnations of this concept, tuning sensitivity to DC and $1/(2\tau)$, respectively, but a whole multitude of novel experiments can be conceived by playing with the placement of π pulses.

The spectral sensitivity of an arbitrary decoupling sequence can be computed by a formalism known as the "sensitivity function" or "filter function" [38, 46]. In this formalism the phase that a qubit picks up over a dynamical decoupling sequence is written as

$$\phi = \int \mathrm{d}t\, g(t)\Delta(t)$$

where $g(t)$ is a sensitivity function, modeling the effective inversion of the signal by the π pulses. It can be constructed from a few simple rules. The initial $\pi/2$ pulse initializes g with $g(t) = 1$, since it creates a coherent superposition whose phase is sensitive to Δ. g changes sign with every π-pulse to model the effective inversion of the signal in the flipping frame of the spin. Finally, $g(t) = 0$ before and after the initial and final $\pi/2$-pulses, since there is no quantum coherence beyond these points. In an alternative interpretation, g can be understood as the "Platonic ideal" of a signal that will impart a maximum phase ϕ on the qubit.

In the most general case, a signal does not have a constant intensity and phase, so that the quantum phase ϕ is a random variable with a variance $\langle \phi^2 \rangle$. The spin signal $|\langle \psi | 1 \rangle|^2$ at the end of the sequence can be computed from (6)

$$| \langle \psi | 1 \rangle |^2 = \frac{1}{2} \left(1 + e^{-\langle \phi^2 \rangle / 2} \right).$$

In the absence of a signal ($\langle \phi^2 \rangle = 0$) coherence will be preserved, so that the final $\pi/2$-pulse flips the spin into $|1\rangle$. A nonzero signal will induce decoherence ($\langle \phi^2 \rangle > 0$), reducing the spin signal. We now rewrite eq. (3), expressing the g and Δ involved by their Fourier coefficients g_n, Δ_n

$$\phi = \int_0^T \mathrm{d}t \, g(t) \Delta(t),$$

$$\overset{f(t) = \frac{1}{T} \sum_{-\infty}^{\infty} f_n e^{i 2\pi n t / T}}{=} \frac{1}{T^2} \sum_{n,n'} g_n \Delta_{n'} \int_0^T \mathrm{d}t \, e^{i 2\pi n t / T} e^{i 2\pi n' t / T},$$

$$\overset{\int \ldots = T \delta_n^{n'}}{=} \frac{1}{T} \sum_n g_n \Delta_{-n}.$$

Here, T denotes the full length of the free evolution from the initial to the final $\pi/2$ pulse. The variance $\langle \phi^2 \rangle$ becomes thus

$$\langle \phi^2 \rangle = \frac{1}{T^2} \left\langle \sum_{n,n'} g_n^* \Delta_{-n}^* g_{n'} \Delta_{-n'} \right\rangle,$$

$$\overset{\langle \Delta_n \Delta_{n'}^* \rangle = 0}{=} \frac{1}{T^2} \sum_n |g_n|^2 |\Delta_n|^2,$$

$$= \sum_n S_g(\nu_n) S_\Delta(\nu_n).$$

Here, the relation $\langle \Delta_n \Delta_{n'}^* \rangle = 0$ holds, since different Fourier components of noise are uncorrelated. $S_f(\nu_n) = |f_n|^2 / T$ denotes the power spectral density of a quantity f. This final relation underlines the above statement that a dynamical decoupling sequence sensitizes a qubit to noise at specific frequencies, described by the Fourier transform $S_g(\nu_n)$ of the sensitivity function $g(t)$.

Table I. – *Sensitivity of magnetic-field sensors. Grey shaded numbers denote extrapolations from published values. Numbers differ from the shot noise limit of eq. (1) because the efficiency of spin readout is not unity in most experiments. SQUID: Superconducting Quantum Inferference Device.*

	Single NV	Single NV (^{12}C)	NV ensemble	NV ensemble theory	Smartphone Hall sensor	SQUID
N	1	1	10^{11} $(100\,\mu\text{m})^3$	10^{16} $(1\,\text{cm}^3)$		
T_2^*	$1\,\mu\text{s}$	$228\,\mu\text{s}$	$30\,\mu\text{s}$	–		
T_2	$300\,\mu\text{s}$	$2\,\text{ms}$	$50\,\mu\text{s}$	$300\,\mu\text{s}$		
η_{DC}	$1\,\mu\text{T}/\sqrt{\text{Hz}}$	$20\,\text{nT}/\sqrt{\text{Hz}}$	$1\,\text{pT}/\sqrt{\text{Hz}}$	–	$30\,\text{nT}/\sqrt{\text{Hz}}$	$1\,\text{fT}/\sqrt{\text{Hz}}$
η_{AC}	$20\,\text{nT}/\sqrt{\text{Hz}}$	$4\,\text{nT}/\sqrt{\text{Hz}}$	$1\,\text{pT}/\sqrt{\text{Hz}}$	$250\,\text{aT}/\sqrt{\text{Hz}}$		$20\,\text{aT}/\sqrt{\text{Hz}}$
Refs.	[15]	[47, 48]	[49-51]	[15]	[52]	[53, 54]

Some practical examples of this concept are presented in fig. 7b. Ramsey spectroscopy (left) has a constantly positive sensitivity function in the time domain, resulting in a filter function with DC sensitivity in the frequency domain. It is insensitive to signals with a frequency $\nu \gg \tau^{-1}$, which average to zero over the free evolution. Accordingly, the frequency-domain filter function is a lowpass filter with bandwidth $1/\tau$. Since noise is mostly stronger at low frequencies, the spin signal decays on a fast timescale T_2^* under Ramsey spectroscopy.

Under dynamical decoupling (specifically: the Carr-Purcell-Meiboom-Gill sequence, right), the time-domain sensitivity function periodically alternates between $+1$ and -1. The Fourier transform of this signal is peaked at a frequency $1/(2\tau)$, and vanishes at DC, modeling the fact that some AC signals are rectified while DC signals are suppressed as discussed above. The sequence can be used as a quantum spectrum analyzer by varying τ. This will displace the peak of maximum sensitivity across a wide range of frequencies. The spin signal traces an inverted copy of the noise spectrum, with strong decoherence occuring whenever the sensitivity peak coincides with a peak of noise. Since the sequence equally supresses decoherence from DC background fields, coherence time under CPMG rises to T_2. By virtue of this second aspect, the sensitivity for detection of AC signals is higher than the sensitivity obtained in a Ramsey sequence, and eq. (1) is modified to

$$\eta_B = \frac{1}{\gamma\sqrt{T_2 N}}\,.$$

The effect of dynamical decoupling can be profound (table I). For NV centers, T_2 can be four orders of magnitude longer than T_2^* (10 ms [55] rather than $1\,\mu$s), so that sensitivity improves by two orders of magnitude whenever dynamical decoupling can be

employed. Moreover, the ability to perform spectroscopy of a time-dependent magnetic signal is a powerful benefit.

Arguably the most prominent example for the power of dynamical decoupling is the detection of magnetic resonance signals from nanoscale samples, first achieved in 2013 [56, 57]. Here, a single stationary NV center, embedded few nanometers beneath the surface of a bulk diamond, is employed as a quantum spectrometer to detect magnetic noise from samples on the diamond surface. This magnetic noise is mostly dominated by stochastic fluctuations of nuclear spins, peaked at the characteristic Larmor frequency of the molecules on the surface. Dynamical decoupling has pushed the sensitivity of a single NV center into a range where detection of this spin noise is possible. Both nuclear spins [58] and electron spin signals [59] have been detected from single biomolecules. The door seems open to transform magnetic resonance spectroscopy, previously limited to mm-scale samples or complicated low-temperature setups [60], into a single-molecule technique.

5. – Outlook —prospects and hopes after one decade

Despite the impressive progress over the past decade, the achievements of nanoscale sensing by spin qubits have covered only a fraction of its full potential. Several important goals remain open and great further breakthroughs are likely to emerge:

- *Scanning probe magnetometry* is still mostly based on measurements of strong DC fields, using the Ramsey sequence or resonant spectroscopy. Dynamical decoupling is hardly ever employed, so that orders of magnitude in sensitivity remain to be harvested. The reason for this surprising fact is that spin coherence is strongly degraded in nanodiamonds and nanofabricated diamond tips. Clearly, this problem is not fundamental, and will be overcome by improved fabrication, more robust color centers or novel concepts for scanning probe positioning [61]. With better sensitivity, novel samples will shift into reach. Likely targets are scanning-probe imaging of nuclear spins —so far limited to some proof-of-principle experiments in "best-case" conditions [62, 63], imaging of current patterns in solid-state samples [64], or spectroscopy of magnetic fluctuations as a tabletop complement to neutron scattering experiments in materials science [65, 66].

- *Single-molecule magnetic resonance* is so far limited to a mere spectroscopy technique and suffers from very slow data acquisition. Much of the power of its bulk counterpart derives from imaging, most evident in the beautiful images provided by clinical scanners. Translating this technique to a three-dimensional imaging method for single molecules is technically challenging, but seems to be doable in the years to come. Improved strategies for signal acquisition like Fourier processing [67-69] and single-shot readout will be crucial to keep acquisition times at a manageable level.

- *Sensing using spins in nanoparticles* has led to proof-of-principle measurements of temperature inside living cells [70, 71]. Progress is being made towards monitoring

of chemical reactions [72, 73]. Also, fluorescent defect centers in nanoparticles have been used for superresolution microscopy [74, 75]. This application does not make use of any spin properties and merely exploits the fact that the fluorescence of color centers is photostable. All of these techniques have not found widespread adoptance yet, presumably because directed attachment to specific parts of a cell is difficult, owing to the complex surface chemistry of nanoparticles.

- While much work has been done using single spins as detectors for nanoscale signals, all techniques discussed in this review can be scaled to *sensing on the micron-scale*, using ensembles of spins as slightly larger detectors with better sensitivity. This line of research has led to magnetic microscopy of inclusions in meteorites [76] and bacteria [77] and, very recently, to NMR spectroscopy on μm-scale samples [78]. We might soon see commercial magnetic microscopes and microfluidic NMR detectors. With these detectors, magnetic resonance microscopy could ultimately bridge all length scales between atomic resolution and the mm-scale resolution of clinical scanners.

- Finally, the progress of the past decades can be seen as a success of quantum control. In a first wave, manipulation of quantum states has been achieved in very clean artificial systems like trapped ions or ultracold atoms in vacuum. In a second wave, these achievements were extended to some selected solid-state systems. A logical third challenge could be control of *arbitrary spins in arbitrary samples.* Indeed, many streams of work are directed towards this goal. NV centers cannot only be used to detect nuclear spins, but also to prepare them in a specific state by polarisation exchange. This could lead to a novel way for nuclear hyperpolarisation of arbitrary samples, a direction of research that is even starting to be pursued by industry. If nanoscale magnetic resonance could be pushed down to the level of single nuclei, solid-state phases could be studied in real materials with atomic resolution, providing a third way between top-down studies on bulk samples and bottom-up replication of matter in ultracold atoms. Dynamical decoupling as a generic tool to tailor the spectral properties of materials could become the key to translate quantum effects like slow light to a much wider range of materials [79].

REFERENCES

[1] BINNIG G., QUATE C. F. and GERBER CH., "Atomic Force Microscope," *Phys. Rev. Lett.*, **56** (1986) 930.
[2] SÁENZ J. J., GARCÍA N., GRÜTTER P., MEYER E., HEINZELMANN H., WIESENDANGER R., ROSENTHALER L., HIDBER H. R. and GÜNTHERODT H.-J., "Observation of magnetic forces by the atomic force microscope," *J. Appl. Phys.*, **62** (1987) 4293.
[3] MARTIN Y. and WICKRAMASINGHE H. K., "Magnetic imaging by "force microscopy" with 1000 Å resolution," *Appl. Phys. Lett.*, **50** (1987) 1455.
[4] ZÜGER O. and RUGAR D., "First images from a magnetic resonance force microscope," *Appl. Phys. Lett.*, **63** (1993) 2496.

[5] Shendure Jay and Ji Hanlee, "Next-generation DNA sequencing," *Nat. Biotechnol.*, **26** (2008) 1135.

[6] Hell Stefan W. and Wichmann Jan, "Breaking the diffraction resolution limit by stimulated emission: stimulated-emission-depletion fluorescence microscopy," *Optics Lett.*, **19** (1994) 780.

[7] Betzig Eric, Patterson George H., Sougrat Rachid, Lindwasser O. Wolf, Olenych Scott, Bonifacino Juan S., Davidson Michael W., Lippincott-Schwartz Jennifer and Hess Harald F., "Imaging Intracellular Fluorescent Proteins at Nanometer Resolution," *Science*, **313** (2006) 1642.

[8] Rust Michael J., Bates Mark and Zhuang Xiaowei, "Sub-diffraction-limit imaging by stochastic optical reconstruction microscopy (STORM)," *Nat. Methods*, **3** (2006) 793.

[9] Betzig Eric and Chichester Robert J., "Single Molecules Observed by Near-Field Scanning Optical Microscopy," *Science*, **262** (1993) 1422.

[10] Sekatskii S. K. and Letokhov V. S., "Single fluorescence centers on the tips of crystal needles: First observation and prospects for application in scanning one-atom fluorescence microscopy," *Appl. Phys. B*, **63** (1996) 525.

[11] Michaelis J., Hettich C., Mlynek J. and Sandoghdar V., "Optical microscopy using a single-molecule light source," *Nature*, **405** (2000) 325.

[12] Chernobrod Boris M. and Berman Gennady P., "Spin microscope based on optically detected magnetic resonance," *J. Appl. Phys.*, **97** (2005) 014903.

[13] Wrachtrup J., von Borczyskowski C., Bernard J., Orritt M. and Brown R., "Optical detection of magnetic resonance in a single molecule," *Nature*, **363** (1993) 244.

[14] Köhler J., Disselhorst J. a. J. M., Donckers M. C. J. M., Groenen E. J. J., Schmidt J. and Moerner W. E., "Magnetic resonance of a single molecular spin," *Nature*, **363** (1993) 242.

[15] Taylor J. M., Cappellaro P., Childress L., Jiang L., Budker D., Hemmer P. R., Yacoby A., Walsworth R. and Lukin M. D., "High-sensitivity diamond magnetometer with nanoscale resolution," *Nat. Phys.*, **4** (2008) 810.

[16] Degen Christian, "Nanoscale magnetometry: Microscopy with single spins," *Nat. Nano*, **3** (2008) 643.

[17] Balasubramanian Gopalakrishnan, Chan I. Y., Kolesov Roman, Al-Hmoud Mohannad, Tisler Julia, Shin Chang, Kim Changdong, Wojcik Aleksander, Hemmer Philip R., Krueger Anke, Hanke Tobias, Leitenstorfer Alfred, Bratschitsch Rudolf, Jelezko Fedor and Wrachtrup Jorg, "Nanoscale imaging magnetometry with diamond spins under ambient conditions," *Nature*, **455** (2008) 648.

[18] Maze J. R., Stanwix P. L., Hodges J. S., Hong S., Taylor J. M., Cappellaro P., Jiang L., Gurudev M. V., Togan E., Zibrov A. S., Yacoby A., Walsworth R. L. and Lukin M. D., "Nanoscale magnetic sensing with an individual electronic spin in diamond," *Nature*, **455** (2008) 644.

[19] van Oort E., Manson N. B. and Glasbeek M., "Optically detected spin coherence of the diamond N-V centre in its triplet ground state," *J. Phys. C: Solid State Phys.*, **21** (1988) 4385.

[20] Gruber A., Dräbenstedt A., Tietz C., Fleury L., Wrachtrup J. and von Borczyskowski C., "Scanning Confocal Optical Microscopy and Magnetic Resonance on Single Defect Centers," *Science*, **276** (1997) 2012.

[21] Maletinsky Patrick, Hong S., Grinolds M. S., Hausmann Birgit, Lukin M. D., Walsworth R. L., Loncar M. and Yacoby A., "A robust scanning diamond sensor for nanoscale imaging with single nitrogen-vacancy centres," *Nat. Nano*, **7** (2012) 320.

[22] TETIENNE J.-P., HINGANT T., KIM J.-V., HERRERA DIEZ L., ADAM J.-P., GARCIA K., ROCH J.-F., ROHART S., THIAVILLE A., RAVELOSONA D. and JACQUES V., "Nanoscale imaging and control of domain-wall hopping with a nitrogen-vacancy center microscope," *Science*, **344** (2014) 1366.

[23] TETIENNE J.-P., HINGANT T., MARTÍNEZ L. J., ROHART S., THIAVILLE A., HERRERA DIEZ L., GARCIA K., ADAM J.-P., KIM J.-V., ROCH J.-F., MIRON I. M., GAUDIN G., VILA L., OCKER B., RAVELOSONA D. and JACQUES V., "The nature of domain walls in ultrathin ferromagnets revealed by scanning nanomagnetometry," *Nat. Commun.*, **6** (2015) 6733.

[24] GROSS I., AKHTAR W., GARCIA V., MARTÍNEZ L. J., CHOUAIEB S., GARCIA K., CARRÉTÉRO C., BARTHÉLÉMY A., APPEL P., MALETINSKY P., KIM J.-V., CHAULEAU J. Y., JAOUEN N., VIRET M., BIBES M., FUSIL S. and JACQUES V., "Real-space imaging of non-collinear antiferromagnetic order with a single-spin magnetometer," *Nature*, **549** (2017) 252.

[25] DOVZHENKO Y., CASOLA F., SCHLOTTER S., ZHOU T. X., BÜTTNER F., WALSWORTH R. L., BEACH G. S. D. and YACOBY A., "Magnetostatic twists in room-temperature skyrmions explored by nitrogen-vacancy center spin texture reconstruction," *Nat. Commun.*, **9** (2018) 2712.

[26] YU GUOQIANG, JENKINS ALEC, MA XIN, RAZAVI SEYED ARMIN, HE CONGLI, YIN GEN, SHAO QIMING, HE QING LIN, WU HAO, LI WENJING, JIANG WANJUN, HAN XIUFENG, LI XIAOQIN, JAYICH ANIA CLAIRE BLESZYNSKI, AMIRI PEDRAM KHALILI and WANG KANG L., "Room-Temperature Skyrmions in an Antiferromagnet-Based Heterostructure," *Nano Lett.*, **18** (2018) 980.

[27] JAKOBI INGMAR, NEUMANN PHILIPP, WANG YA, BHAKTAVATSALA RAO DASARI DURGA, EL HALLAK FADI, ASIF BASHIR MUHAMMAD, MARKHAM MATTHEW, EDMONDS ANDREW, TWITCHEN DANIEL and WRACHTRUP JÖRG, "Measuring broadband magnetic fields on the nanoscale using a hybrid quantum register," *Nat. Nanotechnol.*, **12** (2017) 67.

[28] THIEL LUCAS, ROHNER DOMINIK, GANZHORN MARC, APPEL PATRICK, NEU ELKE, MÜLLER BENEDIKT, KLEINER REINHOLD, KOELLE DIETER and MALETINSKY PATRICK, "Quantitative nanoscale vortex-imaging using a cryogenic quantum magnetometer," arXiv:1511.02873, 2015.

[29] PELLICCIONE MATTHEW, JENKINS ALEC, OVARTCHAIYAPONG PREETI, REETZ CHRISTOPHER, EMMANUELIDU EVE, NI NI and JAYICH ANIA C. BLESZYNSKI, "Scanned probe imaging of nanoscale magnetism at cryogenic temperatures with a single-spin quantum sensor," arXiv:1510.02780 [cond-mat].

[30] RAMSEY NORMAN F., "A Molecular Beam Resonance Method with Separated Oscillating Fields," *Phys. Rev.*, **78** (1950) 695.

[31] BUDKER DMITRY and ROMALIS MICHAEL, "Optical magnetometry," *Nat. Phys.*, **3** (2007) 227.

[32] WINELAND D. J., BOLLINGER J. J., ITANO W. M., MOORE F. L. and HEINZEN D. J., "Spin squeezing and reduced quantum noise in spectroscopy," *Phys. Rev. A*, **46** (1992) R6797.

[33] WINELAND D. J., BOLLINGER J. J., ITANO W. M. and HEINZEN D. J., "Squeezed atomic states and projection noise in spectroscopy," *Phys. Rev. A*, **50** (1994) 67.

[34] GIOVANNETTI VITTORIO, LLOYD SETH and MACCONE LORENZO, "Quantum-Enhanced Measurements: Beating the Standard Quantum Limit," *Science*, **306** (2004) 1330.

[35] HUELGA S. F., MACCHIAVELLO C., PELLIZZARI T., EKERT A. K., PLENIO M. B. and CIRAC J. I., "Improvement of Frequency Standards with Quantum Entanglement," *Phys. Rev. Lett.*, **79** (1997) 3865.

[36] Giovannetti Vittorio, Lloyd Seth and Maccone Lorenzo, "Advances in quantum metrology," *Nat. Photon.*, **5** (2011) 222.

[37] Hahn E. L., "Spin Echoes," *Phys. Rev.*, **80** (1950) 580.

[38] Álvarez Gonzalo A. and Suter Dieter, "Measuring the Spectrum of Colored Noise by Dynamical Decoupling," *Phys. Rev. Lett.*, **107** (2011) 230501.

[39] de Lange G., Ristè D., Dobrovitski V. V. and Hanson R., "Single-Spin Magnetometry with Multipulse Sensing Sequences," *Phys. Rev. Lett.*, **106** (2011) 080802.

[40] Kotler Shlomi, Akerman Nitzan, Glickman Yinnon, Keselman Anna and Ozeri Roee, "Single-ion quantum lock-in amplifier," *Nature*, **473** (2011) 61.

[41] de Lange G., Wang Z. H., Ristè D., Dobrovitski V. V. and Hanson R., "Universal Dynamical Decoupling of a Single Solid-State Spin from a Spin Bath," *Science*, **330** (2010) 60.

[42] Du Jiangfeng, Rong Xing, Zhao Nan, Wang Ya, Yang Jiahui and Liu R. B., "Preserving electron spin coherence in solids by optimal dynamical decoupling," *Nature*, **461** (2009) 1265.

[43] Biercuk Michael J., Uys Hermann, Van Devender Aaron P., Shiga Nobuyasu, Itano Wayne M. and Bollinger John J., "Optimized dynamical decoupling in a model quantum memory," *Nature*, **458** (2009) 996.

[44] Viola Lorenza and Lloyd Seth, "Dynamical suppression of decoherence in two-state quantum systems," *Phys. Rev. A*, **58** (1998) 2733.

[45] Uhrig Götz S., "Keeping a Quantum Bit Alive by Optimized π-Pulse Sequences," *Phys. Rev. Lett.*, **98** (2007) 100504.

[46] Cywinski Lukasz, Lutchyn Roman M., Nave Cody P. and Das Sarma S., "How to enhance dephasing time in superconducting qubits," *Phys. Rev. B*, **77** (2008) 174509.

[47] Zhao Nan, Honert Jan, Schmid Bernhard, Klas Michael, Isoya Junichi, Markham Matthew, Twitchen Daniel, Jelezko Fedor, Liu Ren-Bao, Fedder Helmut and Wrachtrup Jörg, "Sensing single remote nuclear spins," *Nat. Nanotechnol.*, **7** (2012) 657.

[48] Balasubramanian Gopalakrishnan, Neumann Philipp, Twitchen Daniel, Markham Matthew, Kolesov Roman, Mizuochi Norikazu, Isoya Junichi, Achard Jocelyn, Beck Johannes, Tissler Julia, Jacques Vincent, . Hemmer Philip R., Jelezko Fedor and Wrachtrup Jörg, "Ultralong spin coherence time in isotopically engineered diamond," *Nat. Mater.*, **8** (2009) 383.

[49] Wolf Thomas, Neumann Philipp, Nakamura Kazuo, Sumiya Hitoshi, Ohshima Takeshi, Isoya Junichi and Wrachtrup Jörg, "Subpicotesla Diamond Magnetometry," *Phys. Rev. X*, **5** (2015) 041001.

[50] Bauch Erik, Hart Connor A., Schloss Jennifer M., Turner Matthew J., Barry John F., Kehayias Pauli, Singh Swati and Walsworth Ronald L., "Ultralong Dephasing Times in Solid-State Spin Ensembles via Quantum Control," arXiv:1801.03793 [quant-ph].

[51] Clevenson Hannah, Trusheim Matthew E., Schroder Tim, Teale Carson, Braje Danielle and Englund Dirk, "Broadband Magnetometry and Temperature Sensing with a Light Trapping Diamond Waveguide," arXiv:1406.5235 [cond-mat, physics:physics, physics:quant-ph].

[52] AKM8975 Datasheet, 2010.

[53] Kominis I. K., Kornack T. W., Allred J. C. and Romalis M. V., "A subfemtotesla multichannel atomic magnetometer," *Nature*, **422** (2003) 596.

[54] Simmonds M. B., Fertig W. and Giffard R., "Performance of a resonant input SQUID amplifier system," *IEEE Trans. Magn.*, **15** (1979) 478.

[55] Farfurnik Demitry, Jarmola Andrey, Pham Linh M., Wang Zhi-Hui, Dobrovitski Viatcheslav V., Walsworth Ronald L., Budker Dmitry and Bar-Gill Nir, "Optimizing a Dynamical Decoupling Protocol for Solid-State Electronic Spin Ensembles in Diamond," *Phys. Rev. B*, **92** (2015) 060301.

[56] Mamin H. J., Kim M., Sherwood M. H., Rettner C. T., Ohno K., Awschalom D. D. and Rugar D., "Nanoscale Nuclear Magnetic Resonance with a Nitrogen-Vacancy Spin Sensor," *Science*, **339** (2013) 557.

[57] Staudacher T., Shi F., Pezzagna S., Meijer J., Du J., Meriles C. A., Reinhard F. and Wrachtrup J., "Nuclear Magnetic Resonance Spectroscopy on a (5-Nanometer) 3 Sample Volume," *Science*, **339** (2013) 561.

[58] Lovchinsky I., Sushkov A. O., Urbach E., de Leon N. P., Choi S., De Greve K., Evans R., Gertner R., Bersin E., Müller C., McGuinness L., Jelezko F., Walsworth R. L., Park H. and Lukin M. D., "Nuclear magnetic resonance detection and spectroscopy of single proteins using quantum logic," *Science*, **351** (2016) 836.

[59] Shi Fazhan, Zhang Qi, Wang Pengfei, Sun Hongbin, Wang Jiarong, Rong Xing, Chen Ming, Ju Chenyong, Reinhard Friedemann, Chen Hongwei, Wrachtrup Jörg, Wang Junfeng and Du Jiangfeng, "Single-protein spin resonance spectroscopy under ambient conditions," *Science*, **347** (2015) 1135.

[60] Degen C. L., Poggio M., Mamin H. J., Rettner C. T. and Rugar D., "Nanoscale magnetic resonance imaging," *Proc. Natl. Acad. Sci. U.S.A.*, **106** (2009) 1313.

[61] Ernst Stefan, Irber Dominik M., Waeber Andreas M., Braunbeck Georg and Reinhard Friedemann, "A Planar Scanning Probe Microscope," arXiv:1805.03199 [physics].

[62] Rugar D., Mamin H. J., Sherwood M. H., Kim M., Rettner C. T., Ohno K. and Awschalom D. D, "Proton magnetic resonance imaging using a nitrogen-vacancy spin sensor," *Nat. Nanotechnol.*, **10** (2015) 120.

[63] Häberle T., Schmid-Lorch D., Reinhard F. and Wrachtrup J., "Nanoscale nuclear magnetic imaging with chemical contrast," *Nat. Nanotechnol.*, **10** (2015) 125.

[64] Chang K., Eichler A., Rhensius J., Lorenzelli L. and Degen C. L., "Nanoscale Imaging of Current Density with a Single-Spin Magnetometer," *Nano Lett.*, **17** (2017) 2367.

[65] Kolkowitz S., Safira A., High A. A., Devlin R. C., Choi S., Unterreithmeier Q. P., Patterson D., Zibrov A. S., Manucharyan V. E., Park H. and Lukin M. D., "Probing Johnson noise and ballistic transport in normal metals with a single-spin qubit," *Science*, **347** (2015) 1129.

[66] Ariyaratne Amila, Bluvstein Dolev, Myers Bryan A. and Jayich Ania C. Bleszynski, "Nanoscale electrical conductivity imaging using a nitrogen-vacancy center in diamond," *Nat. Commun.*, **9** (2018) 2406.

[67] Boss J. M., Cujia K. S., Zopes J. and Degen C. L., "Quantum sensing with arbitrary frequency resolution," *Science*, **356** (2017) 837.

[68] Schmitt Simon, Gefen Tuvia, Stürner Felix M., Unden Thomas, Wolff Gerhard, Müller Christoph, Scheuer Jochen, Naydenov Boris, Markham Matthew, Pezzagna Sebastien, Meijer Jan, Schwarz Ilai, Plenio Martin, Retzker Alex, McGuinness Liam P. and Jelezko Fedor, "Submillihertz magnetic spectroscopy performed with a nanoscale quantum sensor," *Science*, **356** (2017) 832.

[69] Arai K., Belthangady C., Zhang H., Bar-Gill N., De Vience S. J., Cappellaro P., Yacoby A. and Walsworth R. L., "Fourier magnetic imaging with nanoscale resolution and compressed sensing speed-up using electronic spins in diamond," *Nat. Nanotechnol.*, **10** (2015) 859.

[70] Kucsko G., Maurer P. C., Yao N. Y., Kubo M., Noh H. J., Lo P. K., Park H. and Lukin M. D., "Nanometre-scale thermometry in a living cell," *Nature*, **500** (2013) 54.

[71] Alkahtani Masfer, Jiang Linkun, Brick Robert, Hemmer Philip and Scully Marlan, "Nanometer-scale luminescent thermometry in bovine embryos," *Optics Lett.*, **42** (2017) 4812.

[72] Rendler Torsten, Neburkova Jitka, Zemek Ondrej, Kotek Jan, Zappe Andrea, Chu Zhiqin, Cigler Petr and Wrachtrup Jörg, "Optical imaging of localized chemical events using programmable diamond quantum nanosensors," *Nat. Commun.*, **8** (2017) 14701.

[73] Zhang Ting, Liu Gang-Qin, Leong Weng-Hang, Liu Chu-Feng, Kwok Man-Hin, Ngai To, Liu Ren-Bao and Li Quan, "Hybrid nanodiamond quantum sensors enabled by volume phase transitions of hydrogels," *Nat. Commun.*, **9** (2018) 3188.

[74] Rittweger Eva, Young Han Kyu, Irvine Scott E., Eggeling Christian and Hell Stefan W., "STED microscopy reveals crystal colour centres with nanometric resolution," *Nat. Photon.*, **3** (2009) 144.

[75] Pfender Matthias, Aslam Nabeel, Waldherr Gerald, Neumann Philipp and Wrachtrup Jörg, "Single-spin stochastic optical reconstruction microscopy," *Proc. Natl. Acad. Sci. U.S.A.*, **111** (2014) 14669.

[76] Fu Roger R., Weiss Benjamin P., Lima Eduardo A., Harrison Richard J., Bai Xue-Ning, Desch Steven J., Ebel Denton S., Suavet Clément, Wang Huapei, Glenn David, Sage David Le, Kasama Takeshi, Walsworth Ronald L. and Kuan Aaron T., "Solar nebula magnetic fields recorded in the Semarkona meteorite," *Science*, **346** (2014) 1089.

[77] Le Sage D., Arai K., Glenn D. R., DeVience S. J., Pham L. M., Rahn-Lee L., Lukin M. D., Yacoby A., Komeili A. and Walsworth R. L., "Optical magnetic imaging of living cells," *Nature*, **496** (2013) 486.

[78] Glenn David R., Bucher Dominik B., Lee Junghyun, Lukin Mikhail D., Park Hongkun and Walsworth Ronald L., "High-resolution magnetic resonance spectroscopy using a solid-state spin sensor," *Nature*, **555** (2018) 351.

[79] Joas T., Waeber A. M., Braunbeck G. and Reinhard F., "Quantum sensing of weak radio-frequency signals by pulsed Mollow absorption spectroscopy," *Nat. Commun.*, **8** (2017) 964.

This page intentionally left blank

Many-body physics and quantum simulations with strongly interacting photons

Jirawat Tangpanitanon

Centre for Quantum Technologies, National University of Singapore
3 Science Drive 2, 117543 Singapore

Dimitris G. Angelakis

Centre for Quantum Technologies, National University of Singapore
3 Science Drive 2, 117543 Singapore

School of Electrical and Computer Engineering, Technical University of Crete
Chania, 73100 Greece

Summary. — Simulating quantum many-body systems on a classical computer generally requires a computational cost that grows exponentially with the number of particles. This computational complexity has been the main obstacle to understanding various fundamental emergent phenomena in condensed matters such as high-T_c superconductivity and the fractional quantum-Hall effect. The difficulty arises because even the simplest models that are proposed to capture those phenomena cannot be simulated on a classical computer. Recognizing this problem in 1981, Richard Feynman envisioned a quantum simulator, an entirely new type of machine that exploits quantum superposition and operates by individually manipulating its constituting quantum particles and their interactions. Recent advances in various experimental platforms from cold atoms in optical lattices, trapped ions, to solid-state systems have brought the idea of Feynman to the realm of reality. Among those, interacting photons in superconducting circuits has been one of the promising platforms thanks to their local controllability and long coherence times. Early theoretical proposals have shown possibilities to realize quantum many-body phenomena of light using coupled cavity arrays such as Mott to superfluid transitions and fractional quantum Hall states. State-of-the-art experiments include realization of interacting chiral edge states and stroboscopic signatures of localization of interacting photons in a three-site and a nine-site superconducting circuit, respectively. Interacting photons also serve as a natural platform to simulate driven-dissipative quantum many-body phenomena. A 72-site superconducting circuit has also recently been fabricated to study a dissipative phase transition of light.

169

1. – Introduction

Quantum simulation is an emerging interdisciplinary field in physics [1-3]. It aims to develop a new type of devices that exploit quantum coherence to answer questions about models that describe complex quantum phenomena that are beyond the reach of a classical computer. Experimental progress in the past 30 years have made it possible to control and manipulate individual quantum systems including trapped ions [4], cold atoms in optical lattices [5], nuclear magnetic resonance (NMR) [6], interacting photons [7], quantum dots [8], superconducting circuits [9], and nitrogen-vacancy centers [10]. These new exciting developments transit quantum simulation from a theoretical proposal to the realm of reality.

Below, we first discuss the concept of simulation on a classical computer, its limitation, and motivation of quantum simulation. We then review various experimental platforms for quantum simulation. We conclude the section by giving an overview of the lecture which will be focused on interacting photons in superconducting circuits for quantum simulation of both in- and out-of-equilibrium quantum many-body systems.

1‘1. *Computer simulation.* – Imitating a complex real-world process or system by simulating relevant models on a classical computer has been an essential technique for the development of science and technology. To simulate something, one needs first to develop a model that describes the characteristics and behavior of such system [11]. By changing variables of the model in the simulator, one can make predictions about the behavior of the real complex system. In many cases, these predictions can be used to reduce a high cost of performing several trial-and-error experiments on the real system. For example, the drug design process can be drastically speed up by appropriately modeling molecular systems [12]. An airplane wing can be designed by simulating relevant drag forces via fluid dynamics models [13].

In some cases, simulation is useful when it is difficult or not possible to perform experiments on a real system. For example, the climate system can be predicted by solving differential equations that represent essential factors of climate and their interactions including atmosphere, oceans, land surface, and ice [14]. We note that the act of simulation itself, *i.e.*, imitating real-world processes or systems, is not necessarily done on a classical computer. For example, simulating a weightless in the outer space can be done by aerobatic maneuvers on the Earth that undergo a parabolic motion [15].

1‘2. *Quantum simulation.* – Despite the tremendous success of computer simulation over the past 70 years from the nuclear detonation process in the Manhattan Project in World War II [16] to forecasting of prices on financial markets [17], there remains a large class of systems that are too complex to be simulated by any conceivable classical computer. In physics, this usually involves simulating systems that are non-linear or chaotic due to their non-integrability. In quantum mechanics, although the Schrödinger equation is a linear equation, simulating it generally requires a computational cost that grows exponential with the number of particles. For example, to describe a wavefunction of N spin-1/2 particles, one needs to store 2^N complex coefficients. Also, one needs

to perform linear algebra to such vectors in order to evaluate physical observables that describe the dynamics or even the ground state of the system. This task can be impossible when N is as small as 50 which requires several petabytes of classical memories [18,19]. This number is far less than the number of electrons in real materials which are of the order of 10^{23}. This computational complexity is the main obstacle to understanding various fundamental emergent phenomena such as high-T_c superconductivity [20] and the fractional quantum-Hall effect [21].

Recognizing this problem, in 1981 Richard Feynman envisioned an idea of a quantum simulator, a machine that exploits quantum parallelism and operates by individually manipulating its constituting quantum particles and their interactions [22]. Predictions are made by performing appropriate measurements on those particles. Feynman proposed to quantize both space and time to allow such simulator to be universal, *i.e.*, that can be programmed to simulate any quantum systems. The idea was later extended by Seth Lloyd in 1996 [23], who proved that by evolving in small time steps, or trotterization, such simulator could simulate the dynamics of any local quantum many-body Hamiltonian with the time scale that grows only polynomially with the number of particles.

Such universal or a "digital" quantum simulator, however, requires full control over quantum many-body systems and may still be a long time ahead. Alternatively, one may aim at a less ambitious goal of an "analog" quantum simulator. The idea is to use reasonably well-controlled quantum systems to simulate only certain classes of quantum systems which are, nevertheless, interesting and cannot be simulated on a classical computer. Building the latter may be less prone to errors because it does not require trotterization. Also, phases of matter are typically robust against local perturbation. Nevertheless, as pointed out in ref. [2], a functioning quantum simulator should i) be able to mimic a simple model, or a family of simple models, ii) simulate models that are of some relevance for applications, iii) simulate models that are computationally hard for classical computers, and iv) allow for broad control of the parameters of the simulated model. Also, a quantum simulator should allow for validation, for example, by benchmarking against a classical computer in the regimes where numerical or analytical techniques exist or against different quantum simulators, ideally implemented in different platforms which are subjected to different noises.

It might be hard, if not impossible, to prove that a given system cannot be efficiently simulated with a classical computer. Many quantum many-body systems can be simulated on a classical computer with approximate numerical methods such as artificial neural networks [24], tensor networks [25], dynamical mean-field theory, density matrix renormalization group (DMRG) theory [26], density functional theory [27] and quantum Monte Carlo [28]. However, they are known to be limited to certain classes of problems. For example, DMRG is appreciable only to gapped systems in one dimension. Quantum Monte Carlo does not work with fermionic statistics or frustrated models, due to the sign problem. Mean-field theory only works when the correlation between sites is weak and often fails in one dimension.

With this in mind, the models that benefited most from a quantum simulator are expected to be the ones that involve a large amount of entanglements such as zero-

temperature ground states of many-body Hamiltonians near the phase transition, non-equilibrium dynamics of driven or quenched systems, and dissipative dynamics of open systems. A quantum simulator can, for example, rule out or validate candidate models such as the Femi-Hubbard model for describing high-temperature superconductivity [29], check the eigenstate thermalization hypothesis with various quantum many-body systems [30], and compute accurate calculations of molecular properties for quantum chemistry [31, 32].

1˙3. *Platforms for quantum simulation.*

1˙3.1. Cold neutral atoms in optical lattices. Ultracold atoms in optical lattices represent one of the most versatile platforms for quantum simulation [5, 33, 34]. Optical lattices are formed by interfering laser beams in different directions to create a controllable standing-wave pattern that mimics the crystal lattice of a solid. Atoms can be trapped in the optical lattice due to an effective periodic potential landscape induced by laser beams via a dipole moment of the atoms. Ultracold atoms in optical lattices were first used to simulate the celebrated Mott to the superfluid phase transition in the Bose-Hubbard model [35]. Subsequent work has shown quantum gas microscopes which enable fluorescence detection of atoms in single sites [36], quantum magnetism [37], possibilities to create artificial gauge fields by lattice shaking or by laser-induced tunneling [38], and realization of the Fermi-Hubbard model [39-42]. The Bose-Einstein condensation to Bardeen-Cooper-Schrieffer crossover was also observed in the continuum limit [43]. Recently, cold atoms in optical lattices were recently used to study the breakdown of the thermodynamics description of interacting boson gas in two-dimensional disordered lattices [44]. Predicting a thermalized to a many-body localized phase transition in such a system is currently not possible with a classical computer due to the lack of efficient numerical techniques. A quantum simulator with 51 cold atoms trapped using optical tweezers has also been realized to observe different ordering in quantum Ising model [45].

1˙3.2. Trapped ions. Another approach for atom-based quantum simulators is the use of trapped atomic ions held in linear radio-frequency traps [46, 47]. Here ion crystals are formed by balancing the Coulomb repulsion between ions and trap confinement force, allowing them to be accurately controlled and manipulated. A wide range of models has been simulated in trapped ion systems from spin models [48, 49], to dynamical phase transitions [50] and discrete time crystal [50]. High controllability in trapped ions also makes it a promising platform for quantum computing [51, 52]. The number of ions in a quantum simulator varies by a large factor depending on their controllability. For example, in 2012 a few hundreds of trapped ions with no local control were used to realize the quantum Ising model [53], while a fully-programmable quantum simulator was only recently realized with five atoms in 2016 [54]. This controllability is also a crucial factor for building a scalable quantum simulator in addition to the number of constituting atoms. Building a scalable quantum processor with high controllability and long coherent time over a few hundred qubits and defining relevant real-world applications are near-term challenges faced by all quantum technologies platforms [55].

1˙3.3. Solid-state systems. There are also platforms for quantum simulation that are based on solid-state systems. For example, nitrogen-vacancy centers in diamond have been recently used to observe signatures of discrete time crystal [45]. Donor spins in silicon have been used together with Nuclear Magnetic Resonance technique to demonstrate quantum gates between two qubits [6]. A programmable quantum processor consisting of two single-electron-spin qubits in a silicon/silicon germanium (Si/SiGe) double quantum dot has been illustrated [56]. The Fermi-Hubbard model has also been simulated using a quantum dot array in a GaAs/AlGaAs heterostructure semiconductor [8].

1˙3.4. Interacting photons. In parallel to the above progress, a new type of quantum simulators based on photons and hybrid light-matter excitations, known as polaritons, has been slowly emerging [57,58], inspired by advances in the field of quantum nonlinear optics and cavity quantum electrodynamics (QED) in the last two decades [7]. Pioneer theoretical works have shown possibilities to realize strongly correlated states of lights in coupled resonator arrays (CRAs) and to observe the Mott to the superfluid phase transition of light [59-61]. Subsequent works extend the results to a family of many-body phenomena including an artificial field for the fractional quantum Hall effect [62-64], effective spin models [65-68], and topological transport of quantum states [69]. Signatures of localization of interacting photons in a quasi-periodic potential have recently been observed with a nine-site superconducting circuit by directly measuring statistics of eigenenergies and spreading of energy eigenstates [70]. This platform will be the main focus of this lecture.

Complementarily with cold atoms, interacting photons provide a natural setting for simulating open quantum systems because light-matter systems dissipate to the environment and because they can be driven by external fields. The coupling to the environment is usually weak, and the bath is memoryless. Consequently, the system may reach a dynamically-stable steady state that depends on the symmetries of the system [71]. Early theoretical works have shown that such steady states manifest various quantum many-body phases [72-77] and can exhibit dissipative phase transitions (DPT) [78,79]. A 72-site nonlinear superconducting circuit has recently been fabricated to study DPT with light [80].

Perhaps, the most promising platform for realizing interacting photons is superconducting circuits where conventional optical and electron-beam lithography is used, allowing CRAs to be designed with great flexibility and high controllability [9]. The circuit is made superconducting by cooling to few milli-kelvins using a dilution refrigerator. Photonic modes can be realized from the co-planar transmission line or an LC circuit which effectively acts as a Fabry-Perot microwave cavity [81]. An "artificial" two-level atom can be made from the use of Josephson junctions [82]. Both strong coupling [83] and ultra-strong coupling [84] between an artificial atom and transmission line have also been reported. Non-linear coupled resonator arrays up to 19 sites have been implemented using superconducting circuits [70,85,86].

We note that there is also active research in the field of exciton polaritons in semiconductor materials, realizing quantum fluid of light [87]. However, the interaction strength
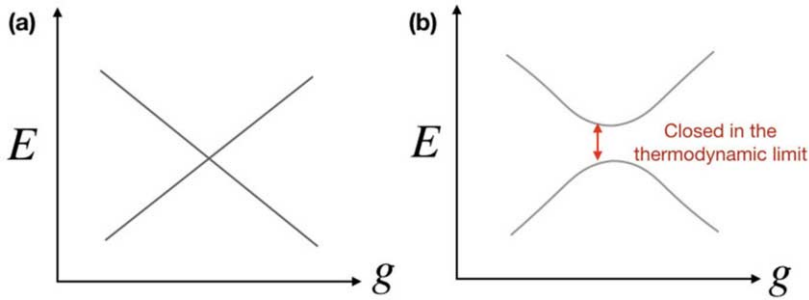
Fig. 1. – Two types of non-analyticity at a quantum phase transition. Eigenenergies of $\hat{H} = \hat{H}_1 + g\hat{H}_2$ as a function of g in the case of (a) $[\hat{H}_1, \hat{H}_2] = 0$ and (b) $[\hat{H}_1, \hat{H}_2] \neq 0$.

of such a system is typically weak at a few-photon level. Nevertheless, there are possibilities to enhance such interaction, for example, by resonantly coupling a pair of cavity polaritons to a biexciton state [88]. Experiments in this platform have led to realization of exotic phases of matter such as non-equilibrium Bose-Einstein condensation [89, 90] and non-equilibrium polariton superfluidity [91, 92].

1.3.5. *Conclusions.* In this section, we have discussed several platforms for quantum simulators. Next, we will discuss the basic concept of quantum phase transition with a specific example of the Mott to the superfluid phase transition in the Bose-Hubbard model. We then discuss the basic concepts in light-matter interaction, including field quantization in a cavity QED, the Jaynes-Cummings model, and photon blockade. We then review the early proposal for Mott to superfluid transitions of light, state-of-the-art experiments, and various works on both equilibrium and driven-dissipative many-body phases of light in CRAs. Lastly, we discuss circuit quantization and recent experimental progress in achieving interacting photons in superconducting circuits.

2. – Quantum phase transitions

Identifying phases of matter is one of the main goals in condensed matter and material science. During a phase transition, specific properties of the material change abruptly as a result of the change of some external parameters. In classical physics, these parameters could be, for example, temperature, pressure, electric or magnetic fields. Classical phase transitions are driven by thermal fluctuations and cease to exist at zero temperature. Quantum phase transitions (QPTs), on the other hand, exist at zero temperature and are driven by quantum fluctuations [93]. Although, strictly speaking, absolute zero temperature is not physically realizable, signatures of QPTs can be observed when the energy scale of the thermal fluctuation $k_B T$ is much smaller than that of the quantum fluctuations $\hbar\omega$, where ω is a typical frequency of the quantum oscillation.

To concretize the above description of QPT, let us consider a Hamiltonian of the form

$$\hat{H} = \hat{H}_1 + g\hat{H}_2,$$

where g is a dimensionless parameter. The QTP deals with the non-analytic dependence of the ground-state energy,

$$E(g) = \langle G|\hat{H}|G\rangle,$$

as the parameter g changes. Here $|G\rangle$ is the ground state of the system, *i.e.*, $\hat{H}|G\rangle = E(g)|G\rangle$. In the case of $[\hat{H}_1, \hat{H}_2] = 0$, non-analyticity can happen due to crossing of eigenvalues, see fig. 1. In the case of $[\hat{H}_1, \hat{H}_2] \neq 0$, non-analyticity can happen due to the closing of the energy gap between the ground state and the first excited state which happens in the thermodynamic limit. The latter is more common and has a closer analogy to classical phase transitions, while the former often occurs in conjunction with the latter. The QPT is usually accompanied by an abrupt change in the correlations in the ground state.

2`1. *Example: the Mott-to-superfluid phase transition.* – The Fermi-Hubbard model was originally proposed in 1963 by Hubbard [94] to approximately describe a conducting to an insulating QPT of electrons in solids. Its bosonic version was proposed in the same year by Gersch and Knollman [95] and was named the Bose-Hubbard model. The phase diagram of the latter was first calculated in 1989 [96] and the corresponding QPT was realized in cold atoms in optical lattices in [35]. Specifically, the Bose-Hubbard (BH) model describes the system of N bosonic particles moving on a lattice consisting of L lattice sites,

$$(1) \qquad \hat{H}_{\mathrm{BH}} = -J \sum_{\langle i,j \rangle} \hat{a}_i^\dagger \hat{a}_j - \mu \sum_{i=0}^{L-1} \hat{n}_j + \frac{U}{2} \sum_{i=0}^{L-1} \hat{n}_j(\hat{n}_j - 1),$$

where $\hat{a}_j$ ($\hat{a}_j^\dagger$) is a bosonic annihilation (creation) operator at site j, $\hat{n}_j = \hat{a}_j^\dagger \hat{a}_j$ is the number operator at site j, $\langle \ldots \rangle$ denotes the sum over nearest-neighbour, J is the hopping strength between site i and j, μ is the chemical potential, and U is the on-site interaction. The first term in eq. (1) describes kinetic energy of particles, the second term determines the number of particles in the ground state, and the last term describes interaction between particles.

To understand different phases exhibited by the BH model, let us first consider the limit $J = 0$. In this case, $\hat{H}_{\mathrm{BH}}$ reduces to the sum of on-site Hamiltonians, *i.e.*, $\hat{H}_{\mathrm{BH}} = \sum_j \hat{h}_j$, where $\hat{h}_j = -\mu\hat{n}_j + \frac{U}{2}\hat{n}_j(\hat{n}_j - 1)$. Hence, the ground state takes the form of a product state $|G\rangle = \prod_j |n\rangle_j$, where $|n\rangle_j$ is an n-particle Fock state at site j, *i.e.*, $\hat{n}_j|n\rangle_j = n|n\rangle_j$. The corresponding ground state energy is $E(n) = L[-\mu n + \frac{U}{2}n(n-1)]$. As shown in fig. 2-b, there are different level crossing between states with different integer fillings n for $\mu = nU$. The ground state has an energy gap, hence they should be stable
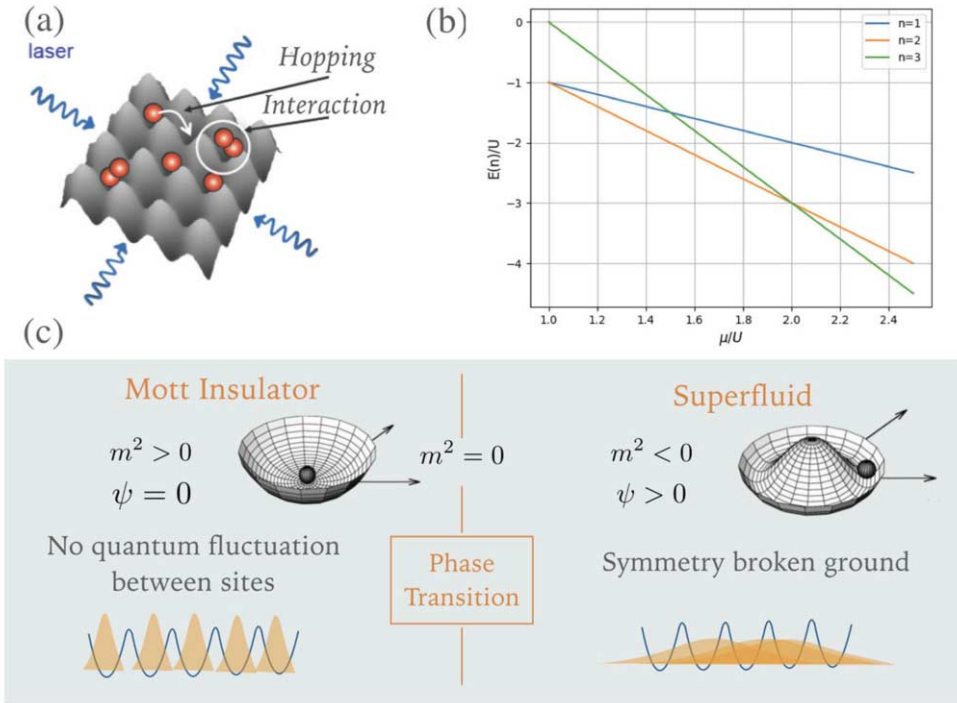
Fig. 2. – The Bose-Hubbard model. (a) A sketch of cold atoms in optical lattices realizing the Bose-Hubbard model. (b) The mean-field energy as a function of μ/U for three different numbers of particles $n = 1, 2, 3$. The mean-field energy landscape in the Mott and the superfluid phase are shown in (b) and (c), respectively.

against small changes in the Hamiltonian such as small tunneling. This integer-filling ground states are known as Mott insulating states.

Another phase can be revealed by considering the limit $U = 0$, where the Hamiltonian is reduced to the tight-binding model $\hat{H}_{\text{tight binding}} = -J \sum_{\langle i,j \rangle} \hat{a}_i^\dagger \hat{a}_j - \mu \sum_j \hat{n}_j$. The Hamiltonian can be diagonalized by applying the quantum Fourier transform $\hat{a}_k = \frac{1}{\sqrt{L}} \sum^{ikj} \hat{a}_j$. The Hamiltonian is then casted into the form $\hat{H}_{\text{tight binding}} = \sum_k \omega_k \hat{a}_k^\dagger \hat{a}_k$, where ω_k is a constant depending on μ and k. For example, for a one-dimensional periodic lattice, we have $\omega_k = -\mu - 2J \cos(k)$. For $\mu, J > 0$, the ground state is then $|G\rangle = (\hat{a}_{k=0}^\dagger)^N |000 \ldots\rangle$ which is a product state in the momentum space, not in the position space as in the Mott. This state is known as the superfluid state.

2˙**2.** *The mean-field phase diagram.* – Now let us consider an approximate method to calculate the many-body phases for the full range of J/U. The key idea is to decompose $\hat{a}_j = \psi + \delta \hat{a}_j$, where $\delta \hat{a}_j$ is the fluctuation from the mean value $\psi \equiv \langle \hat{a}_j \rangle$. The mean-field approximation proceeds by dropping the second-order terms in $\delta \hat{a}_j$ in the Hamiltonian, assuming that correlations between sites can be ignored. This approximation becomes

exact in infinite dimensions, but often fails in one-dimension. To see how this leads to the sum of approximated on-site Hamiltonians, let us write the hopping term as

$$
\begin{aligned}
\hat{a}_i^\dagger \hat{a}_j + \text{H.c.} &= (\psi^* + \delta\hat{a}_i^\dagger)(\psi + \delta\hat{a}_j) + \text{H.c.} \\
&= \psi^*\psi + \delta\hat{a}_i^\dagger\psi + \psi^*\delta\hat{a}_j + \delta\hat{a}_i\delta\hat{a}_j + \text{H.c.} \\
&\approx \psi^*\psi + \delta\hat{a}_i^\dagger\psi + \psi^*\delta\hat{a}_j + \text{H.c.} \\
&\approx \psi^*\psi + (\hat{a}_i^\dagger - \psi^*)\psi + (\hat{a}_j - \psi)\psi^* + \text{H.c.} \\
&\approx \hat{a}_i^\dagger\psi + \hat{a}_j^\dagger\psi - \psi\psi^* + \text{H.c.}
\end{aligned}
\tag{2}
$$

The full Hamiltonian is then written as

$$
\hat{H}_{\text{BH}} \approx \hat{H}_{\text{BH}}^{\text{MF}} = \sum_j \left(\hat{h}_j^{(0)} + \hat{V}_j \right),
$$

where $\hat{h}_j^{(0)} = -\mu\hat{n}_j + \frac{U}{2}\hat{n}_j(\hat{n}_j - 1) - Jz\psi^*\psi$ and $\hat{V}_j = -Jz(\psi^*\hat{a}_j + \psi\hat{a}_j^\dagger)$ with z being the coordination number, or the number of sites connected to site j via the hopping term. We then write the mean-field energy as

$$
E_n = E_n^{(0)} + E_n^{(1)} + E_n^{(2)} + \ldots.
$$

By doing perturbation theory with respect to the V-term, the zeroth-order eigenenergy is

$$
E_n^{(0)} = \begin{cases}
0, & \text{for } \mu < 0, \\
-\mu n + \dfrac{U}{2}n(n-1) + Jz\psi^2, & \text{for } U(n-1) < \mu < Un.
\end{cases}
$$

The first-order eigenenergy is zero $E_1^{(1)} = \langle n|\hat{V}_j|n\rangle = 0$. The second-order eigenenergy is

$$
E_n^{(2)} = \psi^2 \sum_{n'} \frac{|\langle n|\hat{V}_j|n'\rangle|^2}{E_n^{(0)} - E_{n'}^{(0)}} = (Jz\psi)^2 \left(\frac{u}{U(n-1) - \mu} + \frac{n+1}{\mu - Un} \right).
$$

The mean-field energy is then $E_n = \text{const} + m^2\psi^2 + \ldots$, where

$$
\frac{m^2}{Jz} = 1 + \frac{n}{\tilde{U}(n-1) - \tilde{\mu}} + \frac{n+1}{\tilde{\mu} - \tilde{U}n},
$$

with $\tilde{\mu} = \mu/Jz$ and $\tilde{U} = U/Jz$.

As shown in fig. 2-c and fig. 2-d, for $m^2 > 0$ E_n, is minimized when $\psi = 0$. Hence the ground state has $U(1)$ symmetry, *i.e.*, invariant under the transformation $\psi \to e^{i\theta}\psi$, and no quantum fluctuation between sites corresponding to the Mott insulating states. For $m^2 < 0$, E_n is minimized when $\psi \neq 0$, implying that the ground state has a broken $U(1)$
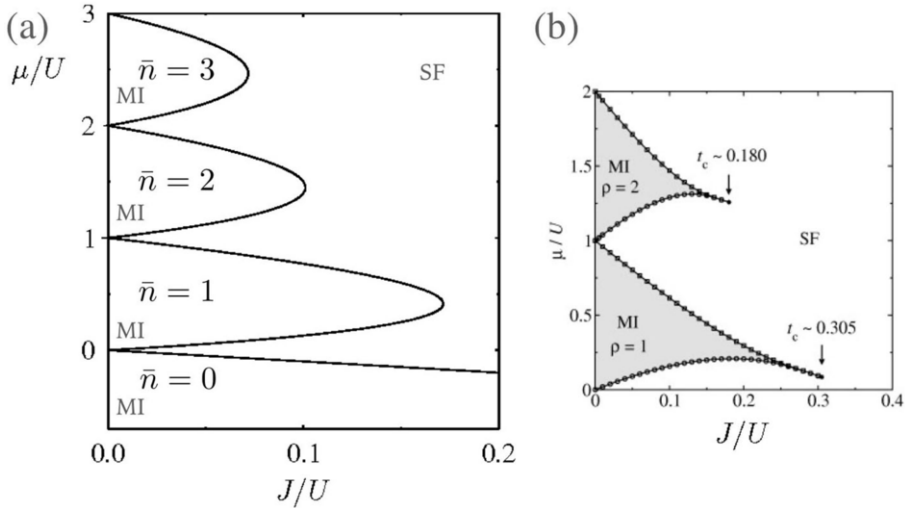
Fig. 3. – Phase diagram of the Bose Hubbard model. The mean-field phase diagram showing the Mott and the superfluid phase is shown in (a). A more exact phase diagram calculated from DRMG for the one-dimensional system is shown in (b). The result is reproduced from ref. [97].

symmetry corresponding to the superfluid state. The phase boundary can be computed by solving the equation $m^2 = 0$. The corresponding mean-field phase diagram is shown in fig. 3-a. Figure 3b shows the phase diagram for a one-dimensional Bose-Hubbard lattice calculated by a more exact density-matrix-renormalization-group (DMRG) technique [97], taking into account correlations between sites. We can see that the mean-field theory can give a qualitative approximation of the phase diagram.

3. – Quantum many-body phases of light

3`1. *Light-matter interaction*. – Having discussed phases of matter, we now turn to the experimental realization of photon-photon interactions and how many-body phases of light can emerge. Engineering strong interactions at progressively low light intensity has been one of the greatest challenges in optical science. In classical regime, photon-photon interaction is achieved by shining an intense light beam to a non-linear material so that the optical properties of the material such as refraction and absorption are modified and, in turn, lead to power-dependent light propagation through the material [98]. Specifically, the polarization **P** of non-linear media, defined as dipole moments per unit volume, can be written as

$$(3) \qquad \mathbf{P}/\epsilon_0 = \chi^{(1)}\mathbf{E} + \chi^{(2)}\mathbf{E}^2 + \chi^{(3)}\mathbf{E}^3 + \dots,$$

where ϵ_0 is the electric permittivity of free space, χ^i is the electric susceptibility of order i-th, and **E** is the input electric field. The higher-order terms account for non-

linear optical phenomena such as second- or higher-harmonic generation, sum-frequency generation, self-focusing, and optical solitons. However, as the light intensity is weaker, the higher-order terms in eq. (3) are suppressed, and eventually, the material only exhibits a linear response, making it difficult to achieve strong interaction at a few photon levels.

Another way to see this is to consider the probability p of one photon getting absorbed by an atom. At resonance, this probability is maximized and proportional to the ratio between the wavelength of light squared (λ^2) and the transverse area of the laser beam (d^2), *i.e.*, $p \sim \lambda^2/d^2$. The number of atoms required to modify one photon is then $N \approx 1/p$. Due to the diffraction limit that prevents the focusing of the light beam below the wavelength, this probability is typically small $p \ll 1$. Recent experiments have achieved $p \approx 0.01$–0.1 by concentrating laser light to a small area [99-102].

In the limit $p \to 1$, the presence of one atom can substantially modify a single incident photon. Since a single two-level atom can only absorb one photon at a time, a pair of incident photons will experience an atomic response that is very different from that of a single photon, hence realizing nonlinearity at the two-photon level. One way to achieve this is to use a reflective cavity that enhances the interaction probability p by the number of bounces, F, that the photon makes inside the cavity before leaking out. The probability p approaches unity when $\eta \gg 1$, where $\eta = F\lambda^2/d^2$ is the cooperativity.

3`1.1. Field quantization: mode of a simple optical resonator. Let us consider an optical cavity consisting of two parallel perfectly reflecting mirrors, lying on the x-y plane at $z = 0$ and $z = L$, see fig. 4. The electric field and the magnetic field inside the cavity take the form

$$\mathbf{E}(\mathbf{r}, t) = \mathbf{e}_x E_x(z, t),$$
$$\mathbf{B}(\mathbf{r}, t) = \mathbf{e}_y B_y(z, t),$$

respectively. By solving Maxwell's equations assuming the boundary conditions $E_x(0, t) = E_x(L, t) = 0$, we get

$$E_x^{(m)}(z, t) = E_0 \sin(\omega_c^{(m)} t) \sin(k_m z),$$
$$B_y^{(m)}(z, t) = B_0 \cos(\omega_c^{(m)} t) \cos(kz),$$

where $k_m = m\pi/L$, m is a positive integer, $\omega_c^{(m)} = ck_m$, c is the speed of light, E_0 is the amplitude of the electric field, and $B_0 = E_0/c$ is the amplitude of the magnetic field. The energy of the electromagnetic field inside the cavity is

$$E^{(m)} = \frac{1}{2} \int \mathrm{d}V \left[\epsilon_0 |E_x^{(m)}(z, t)|^2 + \frac{1}{\mu_0} |B_y^{(m)}(z, t)|^2 \right]$$
$$= \frac{1}{4} \epsilon_0 E_0^2 V \left(\sin^2(\omega_c^{(m)} t) + \cos^2(\omega_c^{(m)} t) \right)$$
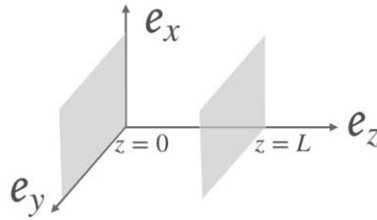$$= \frac{1}{2} \left[(p^{(m)}(t))^2 + (\omega_c^{(m)})^2 (q^{(m)}(t))^2 \right],$$

Fig. 4. – A sketch of a simplified optical cavity consisting of two plane mirrors at $z = 0$ and $z = L$.

where V is the volume of the cavity, $q^{(m)}(t) = \sqrt{\frac{\epsilon_0 V}{2(\omega_c^{(m)})^2}} E_0 \sin(\omega_c^{(m)} t)$, and $p^{(m)}(t) = \sqrt{\frac{V}{2\mu_0}} B_0 \cos(\omega_c^{(m)} t)$. One can see that the energy $E^{(m)}$ takes the form of the energy of a simple harmonic oscillator where $p^{(m)}(t)$ and $q^{(m)(t)}$ are position and momentum coordinates, respectively. From now on we will consider the lowest mode $m = 1$ and drop the superscript (m).

Next, we perform second quantization by promoting $p(t)$ and $q(t)$ to operators, *i.e.*,

$$E^{(m)} \to \hat{H}_{\text{cavity}} = \frac{1}{2} \left(\hat{p}^2 + \omega_c^2 \hat{q}^2 \right),$$

where $[\hat{q}, \hat{p}] = i\hbar$. We then define the ladder operators as

$$\hat{a}^\dagger = \frac{\omega_c \hat{q} - i\hat{p}}{\sqrt{2\hbar\omega_c}},$$

$$\hat{a} = \frac{\omega_c \hat{q} + i\hat{p}}{\sqrt{2\hbar\omega_c}},$$

where $[\hat{a}, \hat{a}^\dagger] = 1$. The Hamiltonian is then written as $\hat{H}_{\text{cavity}} = \hbar\omega_c(\hat{a}^\dagger \hat{a} + \frac{1}{2})$ which is the form of a quantum harmonic oscillator. We will set $\hbar = 1$ from now on for simplicity.

3˙1.2. *The Jaynes-Cummings interaction.* The system consisting of a two-level atom interacting with photons trapped in an optical cavity, as shown in fig. 5, is described by the Hamiltonian

$$\hat{H}_{\text{JC}} = \hat{H}_{\text{cavity}} + \hat{H}_{\text{atom}} + \hat{H}_{\text{int}},$$

where

(4) $$\hat{H}_{\text{cavity}} = \omega_c \left(\hat{a}^\dagger \hat{a} + \frac{1}{2} \right)$$

is the Hamiltonian of the cavity. ω_c is the fundamental frequency of the cavity. The two-level atom is described as

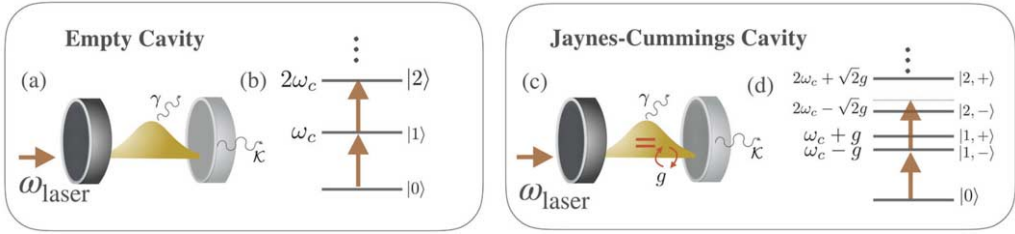$$\hat{H}_{\text{atom}} = \omega_a \hat{\sigma}^+ \hat{\sigma}^-,$$

Fig. 5. – The Jaynes-Cummings model. (a) A sketch of an empty cavity with (b) its linear spectrum. When the modes of the cavity coupled to the two-level system, the total system is described by the Jaynes-Cummings model (c). (d) The resulting energy spectrum has non-linear splitting proportional to $g\sqrt{n}$. An external laser with frequency $\omega_{\mathrm{laser}} = \omega_c - g$ will be resonant with the one-excitation state $|1, -\rangle$ but off-resonant with the two-excitation state $|2, -\rangle$ leading to the photon blockade effect where only one photon can enter the cavity.

where $\hat{\sigma}^+ = |e\rangle\langle g|$ and ω_a is the energy difference between the two eigenstates. The atom interacts with the cavity mode by a dipole transition operator which is defined as $\hat{\mathbf{d}} = \mathbf{d}^*\hat{\sigma}^+ + \mathbf{d}\hat{\sigma}^-$, where $\mathbf{d}$ is the dipole moment. The interaction between the atom and the cavity is described by the dipole interaction:

$$
\begin{aligned}
\hat{H}_{\mathrm{int}} &= -\hat{\mathbf{d}} \cdot \hat{\mathbf{E}}(z, t) \\
&= -E_0(\hat{a} + \hat{a}^\dagger)\sin\left(\frac{\pi z}{L}\right)\hat{d} \\
&= g(\hat{\sigma}^+ + \hat{\sigma}^-)(\hat{a} + \hat{a}^\dagger) \\
&= g(\hat{\sigma}^\dagger\hat{a} + \hat{\sigma}^-\hat{a} + \hat{\sigma}^+\hat{a}^\dagger + \hat{\sigma}^-\hat{a}^\dagger),
\end{aligned}
$$

where $g = -E_0\sin(\frac{\pi z}{L})$ is the light-matter coupling constant. E_0 is the amplitude of the field in the cavity of length L. z is the position in the cavity. We can see that $\hat{H}_{\mathrm{int}}$ contains terms that do not conserve the number of excitation. To see the effect of these terms, we move from the Schrödinger picture into the interaction picture defined by $\hat{H}_{\mathrm{cavity}} + \hat{H}_{\mathrm{atom}}$, *i.e.*,

$$
\begin{aligned}
(5) \qquad \hat{H}_{\mathrm{int}}(t) &= e^{i(\hat{H}_{\mathrm{cavity}} + \hat{H}_{\mathrm{atom}})t}\hat{H}_{\mathrm{int}}e^{-i(\hat{H}_{\mathrm{cavity}} + \hat{H}_{\mathrm{atom}})t} \\
&= g\left(\hat{a}\hat{\sigma}^- e^{-i(\omega_c + \omega_a)t} + \hat{a}\hat{\sigma}^+ e^{i(\omega_a - \omega_c)t} + \mathrm{H.c.}\right).
\end{aligned}
$$

The terms $\hat{a}^\dagger\hat{\sigma}^-$ and $\hat{a}\hat{\sigma}^+$ describe an emission and an absorption process, respectively. They oscillate with a slow frequency $\omega_a - \omega_c$, while the counter-rotating terms $(\hat{a}\hat{\sigma}^- e^{-i(\omega_c + \omega_a)t} + \mathrm{H.c.})$ do not conserve number of excitations and quickly oscillate. When $|\omega_c - \omega_a|, g \ll \omega_c + \omega_a$, the latter terms can be ignored, giving rise to a solvable model known as the Jaynes-Cummings (JC) model [103, 104] first envisioned in 1963. This approximation is known as the rotating-wave approximation. The JC model is then

written as

$$\hat{H}_{\mathrm{JC}} = \omega_a \hat{\sigma}^+ \hat{\sigma}^- + \omega_c \hat{a}^\dagger \hat{a} + g(\hat{a}^\dagger \hat{\sigma}^- + \hat{a} \hat{\sigma}^+).$$

3˙1.3. Eigenstates of the Jaynes-Cummings model. To obtain the eigenstates and the eigenenergies of the JC model, we first notice that the Hamiltonian $\hat{H}_{\mathrm{JC}}$ commutes with the total number excitation operator

$$\hat{N} = \hat{\sigma}^+ \hat{\sigma}^- + \hat{a}^\dagger \hat{a}.$$

For n excitations, there are only two possible states which are i) $|\psi_1\rangle = |n-1, e\rangle$ with $n-1$ photons in the cavity and the atom is in the excited state and ii) $|\psi_2\rangle = |n, g\rangle$ with n photons in the cavity and the atom is in the ground state. The matrix elements of $\hat{H}_{\mathrm{JC}}$ in this subspace,

(6) $$H_{\mathrm{JC},ij}^{(n)} = \langle \psi_i | \hat{H}_{\mathrm{JC}} | \psi_j \rangle$$

for $i, j \in \{1, 2\}$, are written as

$$\hat{H}_{\mathrm{JC}}^{(n)} = \begin{pmatrix} (n-1)\omega_c + \omega_a & g\sqrt{n} \\ g\sqrt{n} & n\omega_c \end{pmatrix}.$$

Diagonalizing this Hamiltonian, we obtain the energy eigenstates as

(7) $$E_\pm(n) = \omega_c \left(n - \frac{1}{2} \right) \pm \frac{1}{2} \sqrt{(\omega_a - \omega_c)^2 + g^2 n}.$$

with the energy eigenstates

$$|n, +\rangle = \cos\left(\frac{\alpha_n}{2}\right) |n-1, e\rangle + \sin\left(\frac{\alpha_n}{2}\right) |n, g\rangle,$$
$$|n, -\rangle = -\sin\left(\frac{\alpha_n}{2}\right) |n-1, e\rangle + \cos\left(\frac{\alpha_n}{2}\right) |n, g\rangle,$$

where $\alpha_n = \tan^{-1}(2g\sqrt{n}/(\omega_a - \omega_c))$. Excitations in $|n, \pm\rangle$ are a collective mode of photonic and atomic excitations called a polariton. The cavity is said to be a non-linear cavity because its eigenenergies now have non-linear dependence in n. The non-linearity becomes maximized at resonance $\omega_a = \omega_c$, i.e., $E_\pm(n) = \omega_c(n-1/2) \pm \frac{1}{2} g\sqrt{n+1}$. In the large detuning limit $|\omega_a - \omega_c| \gg g\sqrt{n}$, the eigenenergies becomes approximately linear in n, i.e.,

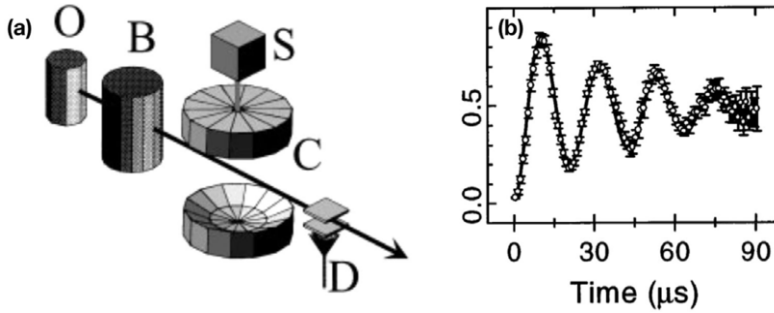$$E_\pm(n) \approx \omega_c n \pm \frac{1}{2} |\omega_a - \omega_c|.$$

Fig. 6. – Quantum Rabi oscillation in a microwave cavity. (a) A simple diagram of the experiment. Rubidium atoms effuse from the oven O and circular Rydberg atoms are prepared in the box B. The atoms cross the cavity C made of two superconducting mirrors. (b) The observed Rabi oscillation according to the Hamiltonian in eq. (6). The result is reproduced from ref. [109].

In this limit, the cavity modes are decoupled from the atom. In addition, the spectrum is also approximately linear for a large number of photons $n \gg 1$, where $\sqrt{n+1} \approx \sqrt{n}$ since the energy gap between adjacent energy levels is approximately the same, *e.g.*

$$E_\pm(n+2) - E_\pm(n+1) \approx E_\pm(n+1) - E_\pm(n) \approx \omega_c \pm \frac{1}{2}g\sqrt{n}.$$

3˙1.4. *Early experimental realizations of strong light-matter coupling.* Signatures of the atom-cavity interaction were first observed in the 1980s via the change in the spontaneous emission rate of an atom when placed in a cavity [105-107]. The cavity mode is said to be "strongly coupled" to the atom when the light-matter coupling is much larger than dissipation rate both to the input and the output waveguides $\mathcal{K}$ and to free space γ, *i.e.*,

$$g^2 > \mathcal{K}\gamma.$$

In this limit, a single photon in the cavity has enough coherent time to allow reversible exchange between the atomic and the photonic excitation before irreversibly leaking out the cavity. Signatures of the strong light-matter interaction were first observed in the optical regime in 1992 via normal mode splitting [108] and in the microwave regime in 1996 via quantum Rabi oscillation [109], see fig. 6. The former led to the first experimental demonstration that single atoms can introduce a phase shift to a single photon by approximately $\pi/10$ [110], while the latter led to the generation of Einstein-Podolsky-Rosen pair of atoms in a controllable manner [111]. In superconducting systems, strong coupling between a single artificial atom and a single microwave photon was later realized in 2004 [83].

3˙1.5. *Photon blockade effect.* Photon blockade refers to a situation in which interaction between photons is so strong that the presence of a single photon in a cavity can
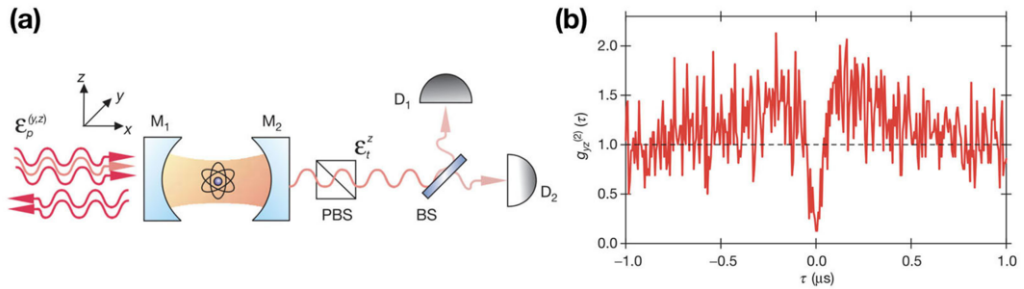
Fig. 7. – Experimental realization of photon blockade. (a) A simple diagram of the experiment. (b) The intensity correlation function $g^{(2)}(\tau)$ as a function of the time delay τ between two photons. $g^{(2)}(\tau)$ drops to near zero at $\tau = 0$, indicating the probability of detecting two photons at the same time is strongly suppressed. The result is reproduced from ref. [113].

completely "block" another photon from entering the cavity. The term is used in analogy to the Coulomb blockade effect [112] where a single electron on a small metallic or semiconductor device can block the flow of another electron when the charging energy is much larger than the thermal energy. To understand photon blockade in the Jaynes-Cummings model, imagine the cavity and the atom is initially in the vacuum state and the ground state, respectively, *i.e.*, $|0, g\rangle$. A laser beam is then shined to the system with the frequency that is resonant with one of the one-excitation eigenstates, *e.g.*,

$$\omega_{\text{laser}} = E_-(1) = \omega_c - \frac{1}{2}g$$

(assuming $\omega_a = \omega_c$). Due to the resonance condition, the first photon that enters the cavity will excite the cavity to the state $|1, -\rangle$. However, the frequency of the second photon is now off-resonant with that of the two-excitation state $|2, -\rangle$,

$$E_\pm(2) - E_-(1) = \omega_c \mp \frac{1}{2}g(\sqrt{2} \mp 1) \neq \omega_{\text{laser}}.$$

Hence the second photon is prevented from entering the cavity and the two photons effectively "repel" each other. The first experimental breakthrough that showed direct signatures of photon blockade was done in 2005 [113], through the anti-bunching statistics of transmitted photons, see fig. 7. The result marks an exciting new era in nonlinear quantum optics.

3˙1.6. *Quantum nonlinear optics with atomic ensembles.* Before moving on to quantum many-body physics with light, we would like to mention an alternative approach to engineer strong light-matter interaction where photons are stored in an ensemble of atoms which exhibits the so-called electromagnetically induced transparency (EIT) [114]. In EIT, the optical response of an otherwise opaque atomic gas is modified by an extra control field. This control field is strong and induces coherent coupling between a weak
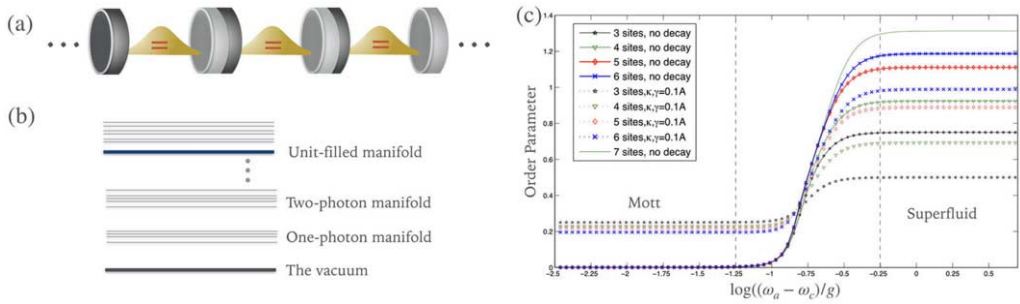
Fig. 8. – The Jaynes-Cummings-Hubbard model (a) A sketch of a coupled cavity array, implementing the Jaynes-Cummings-Hubbard model. (b) Energy spectrum of the JCH model. (c) The order parameter $\mathrm{Var}(N_i)$ of the lowest-energy state in the unit-filled manifold as a function of detuning $(\omega_a - \omega_c)/g$ for sites 3-7 with and without decay. The order parameter exhibits a jump from zero to a finite value, corresponding to the Mott and the superfluid phase, respectively. The transition gets shaper as the system's size is increased as expected from quantum phase transition. The results are reproduced from ref. [59].

probe pulse and atomic states leading to collective light-matter excitations, called polaritons. The latter results in a drastically reduced group velocity of the probe field, much reduced linear susceptibility $\chi^{(1)}$, and greatly enhanced nonlinear susceptibility $\chi^{(3)}$. Effective strong polariton-polariton interaction is then induced by exciting the atoms to the metastable Rydberg state with a high principal quantum number of approximately 100 [115]. The strong interaction between two Rydberg atoms that are separated by less than the blockade radius introduces an energy shift when two of them are excited. This energy shift is maximized when both controlled field and probe field are resonant with the corresponding atomic states. The latter prevents both of them to get excited simultaneously. Effectively, each Rydberg atom behaves like a "superatom" consisting of N_a atoms within the Rydberg radius but only one excitation, resulting in enhanced cooperativity of $\eta = N_a \lambda^2/d^2$.

In addition to the above Rydberg blockade, when the control laser is detuned from resonance, it is possible to use EIT to engineer effective distance-dependent interaction between photons. The attractive interaction between photons has been realized in this way and two-photon bound states have been observed [116]. In the case of repulsive interaction, it is predicted that photon crystallization could be formed [7].

3‘2. Mott-to-superfluid transition of light in coupled resonator arrays. – Having realized strong photon-photon interactions, it is natural to ask if photons can form many-body states in analogy to real atoms in solid state. Pioneer works explored this question by envisioning an array of coupled nonlinear cavities both with the Kerr type [60] and the Jaynes-Cummings type [59,61]. The latter, as shown in fig. 8-a, is described by the

Hamiltonian,

$$\hat{H}_{\text{JCH}} = \sum_{j=0}^{L-1} \left(\omega_a \hat{\sigma}_j^+ \hat{\sigma}_j^- + \omega_c \hat{a}_j^\dagger \hat{a}_j + g \left(\hat{a}_j^\dagger \hat{\sigma}_j^- + \hat{a}_j \hat{\sigma}_j^+ \right) \right) - J \sum_{j=0}^{L-2} \left(\hat{a}_j^\dagger \hat{a}_{j+1} + \text{H.c.} \right),$$

where L is the size of the system, J is the hopping strength of photons between two adjacent cavities, σ_j^+ (σ_j^-) is the raising (lowering) operator for the atom at site j, and $\hat{a}_j$ ($\hat{a}_j^\dagger$) is a bosonic annihilation (creation) operator at site j. The model is known as the Jaynes-Cummings-Hubbard (JCH) model. $\hat{H}_{\text{JCH}}$ commutes with the total number of excitations $\hat{N} = \sum_j \hat{N}_j$, where

$$\hat{N}_j = \hat{a}_j^\dagger \hat{a}_j + \hat{\sigma}_j^+ \hat{\sigma}_j^-.$$

Hence, as shown in fig. 8-b, the eigenspectrum of $\hat{H}_{\text{JCH}}$ are grouped into manifold labeled by the filling factor $\bar{n} = \langle \hat{N} \rangle / L$, where $\langle \ldots \rangle$ denotes an expectation value over a given eigenstate. It is important to recall that when deriving the Jaynes-Cummings interaction we have assumed that ω_a and ω_c are the largest energy scale in the system. This implies that the ground state of $\hat{H}_{\text{JCH}}$ is the vacuum, as depicted in fig. 8-b.

To observe many-body characteristics of $\hat{H}_{\text{JCH}}$, one can consider the lowest-energy state $|G\rangle_{\bar{n}=1}$ in the unit-filled manifold. At resonance and $g \gg J$, photon blockade prevents two photonic excitations at the same cavity, effectively switching off the hopping process and leading to the Mott-like ground state, *i.e.*,

$$|G\rangle_{\bar{n}=1} = |1, -\rangle \otimes |1, -\rangle \ldots \otimes |1, -\rangle.$$

This state can be prepared by sending a $\pi/2$ pulse at frequency $\omega_a - g$ to each cavity to excite the vacuum state $|0, g\rangle$ to the lower polariton state $|-1\rangle$. To observe the superfluid behavior of photonic excitations, one can adiabatically switch on either the coupling g or the detuning $\omega_a - \omega_c$ via, say, a Stark shift from an external field. In this limit, photon blockade is suppressed and the system is effectively described by the tight-binding model

$$\hat{H}_{\text{JCH}} \approx -J \sum_j \left(\hat{a}_j^\dagger \hat{a}_{j+1} + \text{H.c.} \right).$$

The Mott-to-superfluid phase transition can then be probed by measuring the fluctuation of the number of excitations, *i.e.*,

$$\text{Var}(N_i) = \sqrt{\langle \hat{N}_j^2 \rangle - \langle \hat{N}_j \rangle^2},$$

see fig. 8-c. Note that, unlike atoms in the Bose-Hubbard lattice discussed in sect. **2**`1, the number of excitations, in this case, is conserved. Hence the order parameter $\langle a_i \rangle$ always vanishes both in the Mott and the superfluid phase.
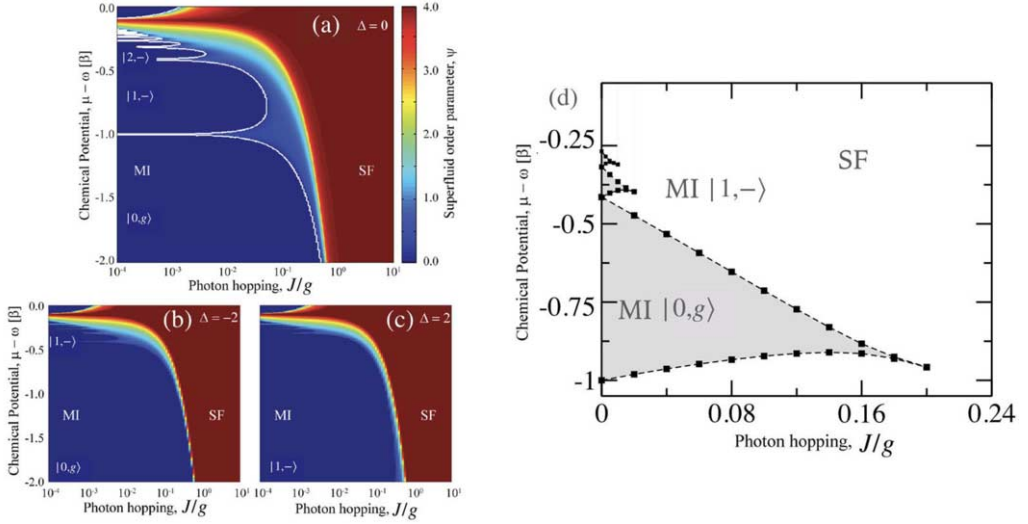
Fig. 9. – Phase diagram of the Jaynes-Cummings-Hubbard model. The mean-field phase diagrams with different detuning $\Delta \equiv \omega_a - \omega_c = 0, -2J, 2J$ are shown in (a)–(c), respectively. The results are reproduced from ref. [61]. The DRMG phase diagram for the one-dimensional system with $\Delta = 0$ is shown in (d). The result is reproduced from ref. [117].

3˙2.1. The mean-field phase diagram. To make a more explicit analogy to the atoms in the Bose-Hubbard lattice, one can introduce the chemical potential term to the JCH model [61]. Note that this is done *by hand* since photons do not naturally have a chemical potential. Nevertheless, a possibility to engineer one has been proposed [118]. The JCH model with the chemical potential is written as

$$\hat{H}_{\text{JCH}}^{\text{GC}} = \hat{H}_{\text{JCH}} - \mu \hat{N},$$

where μ is the chemical potential and the label "GC" stands for the grand canonical potential. $\hat{H}_{\text{JCH}}^{\text{GC}}$ still commutes with $\hat{N}$. However, it is now possible that the ground state of the system is not the vacuum because the chemical potential term introduces an energy shift of $-\mu \bar{n} L$ to the excited states of $\hat{H}_{\text{JCH}}$. This removes the need of restricting ourselves to the $\bar{n} = 1$ manifold as before.

We then proceed to calculate the ground-state phase diagram of $\hat{H}_{\text{JCH}}^{\text{GC}}$ by applying the mean-field approximation $\hat{H}_{\text{JCH}}^{\text{GC}} \approx \sum_j \hat{H}_{\text{JCH}}^{\text{MF}}(j)$, where

$$(8) \qquad \begin{aligned} \hat{H}_{\text{JCH}}^{\text{MF}}(j) = &(\omega_c - \mu)\hat{a}_j^\dagger \hat{a}_j + (\omega_a - \mu)\hat{\sigma}^+ \hat{\sigma}^- + g(\hat{a}^\dagger \hat{\sigma}^- + \hat{a}\hat{\sigma}^+) \\ &- 2J(\psi \hat{a}^2 + \psi^* \hat{a} - |\psi|^2). \end{aligned}$$

To numerically compute the phase diagram, we first write down $\hat{H}_{\text{JCH}}^{\text{MF}}(j)$ in a matrix form, keeping up to $n_{\max}$ excitations. For example, for $n_{\max} = 1$ the matrix takes the

form

$$\hat{H}_{\mathrm{JCH}}^{\mathrm{MF}}(j) = \begin{pmatrix} 0 & 0 & -2J\psi \\ 0 & \omega_a - \mu & g \\ -2J\psi^* & g & \omega_c - \mu \end{pmatrix},$$

where $|g,0\rangle = (1,0,0)$, $|e,0\rangle = (0,1,0)$, and $|e,1\rangle = (0,0,1)$. For $n_{\max} = 2$ the matrix takes the form

$$\hat{H}_{\mathrm{JCH}}^{\mathrm{MF}}(j) = \begin{pmatrix} 0 & 0 & -2J\psi & 0 & 0 \\ 0 & \omega_a - \mu & g & -2J\psi & 0 \\ -2J\psi^* & g & \omega_c - \mu & 0 & -2\sqrt{2}J\psi \\ 0 & -2J\psi & 0 & \omega_a + \omega_c - 2\mu & \sqrt{2}g \\ 0 & 0 & -2J\psi & \sqrt{2}g & 2\omega_c - \mu \end{pmatrix}.$$

The next step is to numerically obtain the ground state energy as a function of the mean-field energy $E[\psi]$ and find ψ_c that minimizes $E[\psi]$. The process is then repeated until ψ_c is converged with $n_{\max}$. The mean-field phase diagram of $\hat{H}_{\mathrm{JCH}}^{\mathrm{GC}}$ as calculated in ref. [61] is shown in fig. 9-a. A more accurate phase diagram was calculated numerically using DMRG in ref. [117] and analytically in ref. [119].

3˙2.2. Existing works on equilibrium many-body phases of interacting photons. Following the pioneer works, there has been several work investigating various aspects of the JCH model including many-body dynamics [120-122], ground-state entanglement [123, 124], critical exponents at the phase transition [125] and its applications for quantum information processing [126, 127]. Phase transitions in the JCH model and the BH model have been shown to be in the same universality class. As shown in [59] in the Mott regime, the JCH model also simulates the standard XY spin model where the presence and the absence of a polariton in each cavity represent the state of spin up and down, respectively. Subsequent works also show that the anisotropic Heisenberg spin model can be simulated using coupled cavity arrays where each cavity contains a three-level system [65-68]. Topological pumping of interacting photons to reliably transport Fock states is discussed in ref. [69]. Artificial gauge field for photons can be engineered in a 2D array using an external drive that controls the hopping phase of photons. When combined with photon blockade, the ground state of the system can be mapped to the Laughlin state, simulating the fractional quantum Hall state of light [62, 63]. Such combination has been realized with two microwave photons in a three-site superconducting circuit chip [64].

3˙2.3. State-of-the-art experiments. Here we briefly review two experimental works that demonstrate exceptional control and a long coherent time of interacting photons in superconducting circuits.

Chiral ground-state currents of interacting photons in a synthetic magnetic field [64]. Using two interacting photons in a three-site superconducting circuit (see fig. 10-a), the authors have realized two basic ingredients for simulating fractional quantum Hall states of light, *i.e.*, large interactions in the presence of a large magnetic field. The resulting ground states exhibit chiral current of two hardcore photons, where the probability of two photons being in the same site is strongly suppressed, see fig. 10-b. The artificial magnetic field is created by periodically modulating the hopping strength between two sites [128], *i.e.*,

$$(9) \qquad \hat{H}^{\mathrm{chiral}}(t) = \sum_{j=1}^{3} \omega_j \hat{n}_j + \sum_{j,k} J_{jk}(t)(\hat{a}_j^\dagger \hat{a}_k + \mathrm{H.c.}) - \frac{U}{2} \sum_{j=1}^{3} \hat{n}_j(\hat{n}_j - 1),$$

where

$$J_{jk}(t) = J_0 \cos(\Delta_{jk} + \phi_{jk}),$$

with $\Delta_{jk} = \omega_j - \omega_k$. J_0 and ϕ_{jk} are constants. To understand how the effective magnetic field is derived, let us consider the Hamiltonian of a pair of qubit

$$\hat{H} = \omega \hat{n}_1 + (\omega + \Delta)\hat{n}_2 + J_0(e^{i\Delta t + i\psi} + e^{-i\Delta - i\phi})(\hat{a}_1^\dagger \hat{a}_2 + \mathrm{H.c.}) - \frac{U}{2} \sum_{j=1}^{2} \hat{n}_j(\hat{n}_j - 1).$$

We then move to a rotating frame via the unitary transformation $e^{-i\Delta \hat{n}_2 t}$. The Hamiltonian in the rotating frame reads

$$\hat{H} = \omega(\hat{n}_1 + \hat{n}_2) + J_0(e^{i\Delta t + i\phi} + e^{-i\Delta - i\phi})(\hat{a}_1^\dagger \hat{a}_2 e^{-i\Delta t} + \mathrm{H.c.}) - \frac{U}{2} \sum_{j=1}^{2} \hat{n}_j(\hat{n}_j - 1).$$

If $J_0 \ll \Delta$, we can apply the rotating-wave approximation and arrive at

$$\hat{H} = \omega(\hat{n}_1 + \hat{n}_2) + J_0(\hat{a}_1^\dagger \hat{a}_2 e^{-i\phi} + \mathrm{H.c.}) - \frac{U}{2} \sum_{j=1}^{2} \hat{n}_j(\hat{n}_j - 1).$$

Hence for a three-site lattice with a periodic boundary condition, the total "artifical" magnetic flux is $\Phi = \phi_{12} + \phi_{23} + \phi_{31}$. In the experiment, the sites in the superconducting chip are inductively coupled to each other and can be tuned in nanosecond timescale using an external (real) magnetic field. The coupling $J_{jk}(t)/2\pi$ can take any value between $-55\,\mathrm{MHz}$ and $+5\,\mathrm{MHz}$, including zero. The initial state is prepared by applying a $\pi/2$ pulse at the first and the second site.

Spectroscopic signatures of localization with interacting photons in superconducting circuits [70]. Statistical thermodynamics is one of the pillars of modern physics in
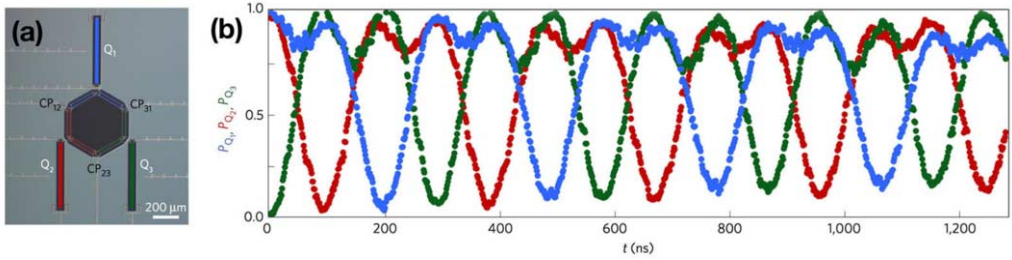
Fig. 10. – Chiral edge states of interacting photons in superconducting circuits. (a) An optical image of the superconducting circuit made by standard nano-fabrication techniques. It can be described by the Bose-Hubbard Hamiltonian as shown in eq. (9). (b) Time evolution showing chiral current of two interacting photons. P_{Q_j} is the probability of finding one photon at site j. Two photons are initialized at sites 1 and 2 by applying a $\pi/2$ pulse to the corresponding sites. The chiral current can be understood by looking at the current of the hole, initially located at site 3. The results are reproduced from ref. [64].

describing physical systems with a large degree of freedom. Its fundamental postulate states that all accessible microstates associated with a given macro-state have equal probability. In quantum physics, it has been observed that quantum many-body systems would often evolve and reach a thermal equilibrium over time, regardless of a starting state. However, disorders can prevent those systems from thermalization. The mechanism is known as many-body localization (MBL) [129, 30, 130-139]. Unlike quantum phase transitions in the equilibrium case such as the Mott to the superfluid phase transition, the thermalized to the MBL phase transition is dynamical and involves all the many-body energy eigenstates of the system.

Signatures of MBL have been observed in cold atoms in optical lattices [44, 140, 141], trapped ions [142] and superconducting qubits [143]. In all cases, a non-thermal evolution is probed by monitoring the time dynamics of an initially localized state. In the thermalized phase, the system spreads throughout the lattice over time leading to zero population imbalance between sites. When the disorder is increased, and the system is in the MBL phase, the system shows traces of the initial state after a long period. Although this technique reveals signatures of MBL, directly probing many-body energy eigenstates is still absent in the previous work.

In ref. [70], the authors observe signatures of the celebrated many-body localization transition using interacting photons in a nine-site superconducting circuit. The measurements of the relevant energy eigenenergies and eigenstates were done by implementing a novel many-body spectroscopy method based on time evolution. The approach was benchmarked by measuring the energy spectrum predicted for the system of electrons moving in two dimensions under a strong magnetic field — the Hofstadter butterfly.

Here we outline the spectroscopy protocol performed in ref. [70], starting with a single photon. We begin by initializing a photon at site p in the superposition state of $|0\rangle$ and

$|1\rangle$, *i.e.*,

$$
|\psi_0\rangle_p = |0\rangle_1 |0\rangle_2 \dots \left(\frac{|0\rangle_p + |1\rangle_p}{\sqrt{2}} \right) \dots |0\rangle_{L-1} |0\rangle_L
$$

$$
= \frac{1}{\sqrt{2}} \left(|\,\mathrm{Vac}\rangle + |\mathbf{1}_p\rangle \right),
$$

$$
= \frac{2}{\sqrt{2}} \left(|\,\mathrm{Vac}\rangle + \sum_{\alpha=0}^{8} C_\alpha^p |E_\alpha^{(1)}\rangle \right),
$$

where $|1_p\rangle = \hat{a}_p^\dagger |\,\mathrm{Vac}\rangle$, $C_\alpha^p = \langle \mathbf{1}_p | E_\alpha^{(1)} \rangle$, $|\,\mathrm{Vac}\rangle$ is the vacuum state, and $|E_\alpha^{(1)}\rangle$ is a one-photon energy eigenstate with eigenenergy $E_\alpha^{(1)}$. The system at time t is given by

$$
|\psi(t)\rangle_p = \frac{1}{\sqrt{2}} \left(|\,\mathrm{Vac}\rangle + \sum_{\alpha} C_\alpha^p e^{-iE_\alpha^{(1)}t} |E_\alpha^{(1)}\rangle \right).
$$

The operator $\hat{a}_p$ is not Hermitian and therefore not observable. Nevertheless, one can measure

$$
\langle \hat{X}_p \rangle \equiv \langle \hat{a}_p^\dagger + \hat{a}_p \rangle,
$$

$$
\langle \hat{Y}_p \rangle \equiv i\langle \hat{a}_p^\dagger - \hat{a}_p \rangle
$$

and compute the expectation value

$$
\langle \hat{a}_p \rangle(t) \equiv \frac{1}{2} \left(\langle \hat{X}_p \rangle - i \langle \hat{Y}_p \rangle \right) = \frac{1}{2} \sum_{\alpha} |C_\alpha^p|^2 e^{-iE_\alpha^{(1)}t}
$$

at different times. The Fourier transform of $\langle \hat{a}_p \rangle(t)$ then reveals the eigenenergies $E_\alpha^{(1)}$ and the overlap $|C_\alpha^p|$. The experiment is then repeated by varying all possible initial configurations $q \in \{1, 2, \dots, L\}$ and calculating

$$
\chi^{(1)}(t) = \sum_{p=1}^{L} \langle \hat{a}_p \rangle(t).
$$

The latter ensures that all peaks will have appreciable amplitudes in the Fourier transform.

To benchmark the method, the authors implement the 1D Harper model with one photon in a nine-site superconducting circuit, *i.e.*,

$$
\hat{H}_{\mathrm{Harper}}^{\text{1-photon}} = \Delta \sum_{j=0}^{8} \cos(2\pi b j) \hat{n}_j - J \sum_{j=0}^{7} \left(\hat{a}_j^\dagger \hat{a}_{j+1} + \mathrm{H.c.} \right).
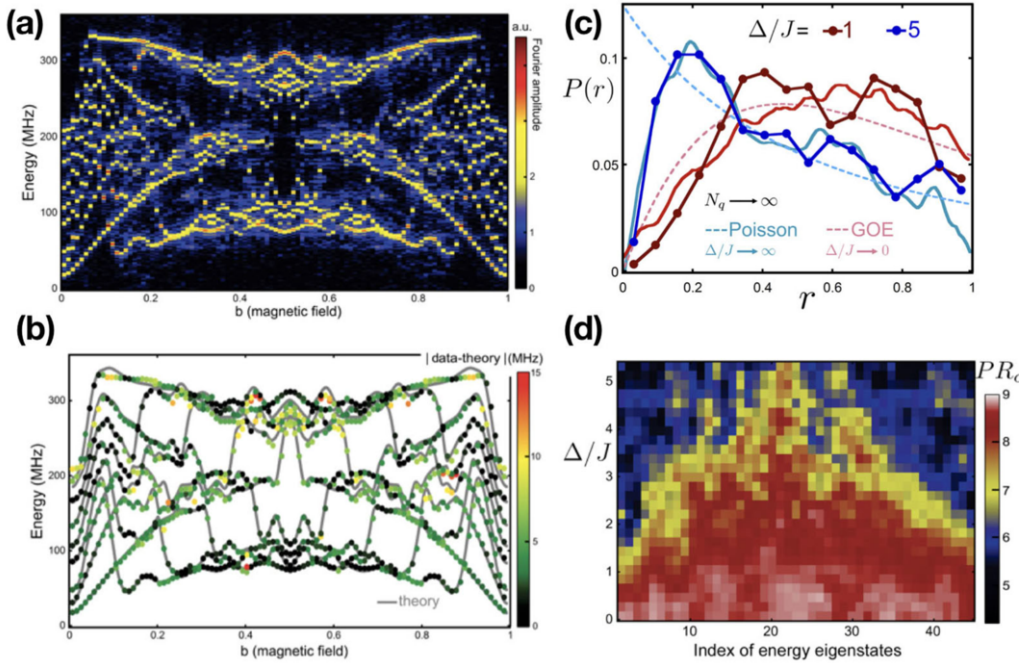$$

Fig. 11. – The Hofstadter butterfly (a) The Fourier transform of $\chi^{(1)(t)}$ is shown for 100 values of dimensionless magnetic field b ranging from 0 to 1. (b) For each b value, we identify 9 peaks and plot their location as a colored dot. The numerically computed eigenvalues of the Harper model are shown with gray lines. The color of each dot is the difference between the measured eigenvalue and the numerically computed one. Spectroscopic signatures of localization with two interacting photons. (c) The measured histogram $P(r)$ of r_β s for $\Delta/J = 1$ and 5. The dashed lines are plots of P_{Poisson} and P_{GOE} according to eq. (10) and eq. (11), and the solid lines are numerical simulations. (d) The participation ration PR_{Space} as a function of Δ/J.

The Harper model can be mapped to the 2D Quantum Hall model where b is mapped to a magnetic flux [144]. The spectrum of the Harper model as a function of b exhibits a butterfly-like structure similar to its 2D counterpart. The structure was first proposed by Hofstadter in 1976 [145]. It is a fractal structure, meaning that small fragments of the structure contain a copy of the entire structure. However, observing the full butterfly in a conventional condensed-matter system requires an unphysically large magnetic field in the order of $\sim 10^5$ tesla that can "squeeze" one flux quantum through a unit cell. Signatures of the butterfly were observed by using a superlattice structure in graphene [146-149].

The authors of ref. [70] realize $\hat{H}_{\text{Harper}}^{\text{1-photon}}$ by setting the cavity's frequency $\omega_j = \Delta \cos(2\pi b j)$. Since b in $\hat{H}_{\text{Harper}}^{\text{1-photon}}$ is not related to a real magnetic flux, it can be easily tuned from 0 to 1 in our setup. Figure 11a shows the Fourier transform of $\chi^{(2)}(t)$ as a function of b. A clear butterfly-like structure is observed as expected since the Fourier

transform represents the eigenspectrum. However there are only nine single-particle eigenenergies for each value of b, the fractal structure of the spectrum is not displayed. In fig. 11-b, the measured peaks in the Fourier transform are compared with exact numerics. The errors in the position of the peaks on average are found to be less than 2%. This result illustrates high controllability and a low error rate of the setup.

By placing two photons into the system, the interacting Harper model is then implemented, *i.e.*,

$$\hat{H}_{\text{Harper}}^{\text{2-photons}} = \Delta \sum_{j=0}^{8} \cos(2\pi bj)\hat{n}_j - \frac{U}{2} \sum_{j=0}^{8} \hat{n}_j (\hat{n}_j - 1) - J \sum_{j=0}^{7} \left(\hat{a}_{j+1}^{\dagger} \hat{a}_j + \hat{a}_j^{\dagger} \hat{a}_{j+1} \right).$$

Four different irrational values of b are chosen from $[0,1]$, and the corresponding observables are averaged. The irrational choice of b ensures that the periodicity of the potential and lattice are incommensurate, mimicking the effect of disorder [150, 151]. In the experiment, $U/2\pi$ and $J/2\pi$ are fixed to $175\,\text{MHz}$ and $50\,\text{MHz}$, respectively (U/J is fixed to 3.5). For this value the ergodic to the localized phase transition of two photons is expected to happen at $\Delta \approx 2J$ [151].

Spectroscopy of the two-photon eigenstates is done in a similar way, *i.e.*, the initial state is prepared as

$$|\psi_0\rangle_{p,q} = |0\rangle_1 |0\rangle_2 \ldots \left(\frac{|0\rangle_p + |1\rangle_p}{\sqrt{2}} \right) \ldots \left(\frac{|0\rangle_q + |1\rangle_q}{\sqrt{2}} \right) \ldots |0\rangle_{L-1} |0\rangle_L$$

$$= \frac{1}{2} \left(|\,\text{Vac}\rangle + |\mathbf{1}_p, \mathbf{1}_q\rangle \right) + \frac{1}{2} \left(|\mathbf{1}_p\rangle + |\mathbf{1}_q\rangle \right),$$

where $p \neq q \in \{1, 2, \ldots, L\}$ and $|\mathbf{1}_p, \mathbf{1}_q\rangle = |0\rangle_1 |0\rangle_2 \ldots |1\rangle_p \ldots |1\rangle_q \ldots |0\rangle_L$ are the two-photon Fock states. Then the measurement at time t reads,

$$\langle \hat{a}_p \hat{a}_q \rangle(t) = \frac{1}{4} \left\langle \hat{X}_p \hat{X}_q - \hat{Y}_p \hat{Y}_q - i\hat{X}_p \hat{Y}_q - i\hat{Y}_p \hat{Y}_q \right\rangle = \frac{1}{4} \sum_{\beta} |C_{\beta}^{p,q}|^2 e^{-iE_{\beta}^{(2)}t}.$$

The experiment is then repeated for all possible pairs of p and q. The following quantity is then calculated:

$$\chi^{(2)}(t) = \sum_{p \neq q} \langle \hat{a}_p \hat{a}_q \rangle(t).$$

The eigenenergies are then obtained from the Fourier transform of $\chi^{(2)}(t)$.

Since the difference between the ergodic and the localized phase is in its dynamics which are determined by eigenenergies, one of the most direct way to probe the transition is to study the distribution of the energy level [152-154]. Using the two-photon protocol, the two-photon eigenenergies $E_{\beta}^{(2)}$ are measured. Then the authors calculate the level

spacing $s_\beta = E^{(2)}_{\beta+1} - E^{(2)}_\beta$ between two adjacent levels and level separation uniformity,

$$r_\beta \equiv \frac{\min\{s_\beta, s_{\beta-1}\}}{\max\{s_\beta, s_{\beta-1}\}}\,.$$

The level statistics is then defined as a histogram $P(r_\beta)$ of r_β. In the localized phase when the disorder is large, the levels are uncorrelated resulting in the Poisson distribution

$$(10) \qquad\qquad P_{\text{Poisson}}(r_\beta) = \frac{2}{(1+r_\beta)^2}\,.$$

In the ergodic phase, it has been postulated that the statistics of energy levels is the same as the ensemble of real random matrices, following the Gaussian orthogonal ensemble (GOE) [154],

$$(11) \qquad\qquad P_{\text{GOE}}(r_\beta) = \frac{27}{4}\frac{r_\beta + r_\beta^2}{(1+r_\beta+r_\beta^2)^{5/2}}\,.$$

The measured level statistics is shown in fig. 11-c. It can be seen that at $\Delta < 2J$ the peak of the distribution $P(r)$ is located away from $r = 0$. As the disorder is increased beyond $2J$, this peak starts to shift towards $r = 0$, as expected from a finite precursor of the thermalized to the MBL phase transition.

The amplitude of the peaks in the Fourier spectrum in the protocol also provides informations about the probability of each energy eigenstate being present at each lattice site $\{P_{\beta,j}\}$. Perhaps, the most common way to quantify the spreading of the eigenstates is to use the participation ratio (PR) [155]

$$(12) \qquad\qquad PR_{\text{Space}}(\beta) = \frac{1}{\sum_j |C^\beta_j|^4}\,.$$

Here $|C^j_\beta|^2$ is the probability of having one or two photons at site j. PR_{Space} indicates the number of lattice sites that are covered by each eigenstate.

The measured PR_{Space} as a function of Δ/J is shown in fig. 11-d. As Δ/J is increased, the eigenstates with the highest and the lowest energies start to shrink, and each eigenstate undergoes a delocalized to a localized transition at different disorder strength. This energy-dependent transition is a finite-size signature of the mobility edge in the thermodynamic limit [156].

3`3. *Driven-dissipative many-body phases of interacting photons*. – Up to now, we have ignored the effect of dissipation by assuming that the dissipation rate is negligibly smaller than a typical energy scale of the system. However, light-matter systems naturally dissipate to the environment. One of the major developments in the field of many-body physics with light is the study of non-equilibrium many-body phases. The latter happens at the steady state where photon losses are compensated by external laser driving. For

example, a coupled resonator array as described by the JCH model can be locally driven by a coherent laser field. The total time-dependent Hamiltonian in the lab frame is written as

$$\hat{H}_{\text{tot}}(t) = \hat{H}_{\text{JCH}} + \sum_{j=0}^{L-1} \Omega_j (\hat{a}_j^\dagger e^{-i\omega_d t} + \hat{a}_j e^{i\omega_d t}),$$

where ω_d is the frequency of the drive, Ω_j is the amplitude of the coherent drive. The time dependence can be removed by going the rotating frame defined by $\hat{U}(t) = \exp[i(\sum_{j=0}^{L-1} \hat{a}_j^\dagger \hat{a}_j)\omega_d t]$, *i.e.*,

$$\hat{H}_{\text{tot}}^{\text{R}} = \hat{U}(t)\hat{H}_{\text{tot}}(t)\hat{U}(t)^{-1} + i\hat{U}(t)\frac{\partial \hat{U}^{-1}(t)}{\partial t}$$
$$= \hat{H}_{\text{JCH}} - \omega_d \sum_{j=0}^{L-1} \hat{a}_j^\dagger \hat{a}_j + \sum_{j=0}^{L-1} \Omega_j (\hat{a}_j^\dagger + \hat{a}_j).$$

The effect of dissipation can be captured by considering the Lindblad master equation

$$(13) \qquad \frac{\partial \hat{\rho}}{\partial t} = \mathcal{L}\hat{\rho} = -i\left[\hat{H}_{\text{tot}}^{\text{R}}, \rho\right] + \frac{\gamma}{2}\sum_{j=0}^{L-1}\left(2\hat{a}_j\hat{\rho}\hat{a}_j^\dagger - \{\hat{\rho}, \hat{a}_j^\dagger \hat{a}_j\}\right),$$

where γ is the loss rate, $\hat{\rho}$ is the density matrix of the system, and $\mathcal{L}$ is the Lindblad superoperator. The master equation is then obtained by first writing down the Schrödringer for the total system and then tracing out the environment, assuming that the system and the environment are initially in a product state and the bath is memoryless [103]. Due to the memoryless bath, the system could reach a non-equilibrium steady state (NESS) that depends on the symmetries of the system, *i.e.*,

$$(14) \qquad \frac{\partial \hat{\rho}_{\text{NESS}}}{\partial t} = 0.$$

Comparison between the NESS of the JCH and the BH model in the driven-dissipative scenario is discussed in ref. [157]. Similarities between the two models are found when NESS contains a few photons per site, and the light-matter coupling is much stronger than the dissipation rate $g/\gamma \sim 10^4$. In 2009, Carusotto *et al.* [72] first showed fermionized photons in a driven-dissipative BH array where the NESS of the system mimics a strongly correlated Tonks-Girardeau gas of impenetrable bosons. In an independent work, Hartmann [73] has studied crystallization of photons at the NESS of a similar dissipative BH array but the with alternating local drive $\Omega_j = -\Omega e^{-i\phi_j}$, where Ω is the amplitude of the drive and $\phi_j = j\pi/2$. Similar behavior is observed in the driven-dissipative JCH array [74]. Signatures of fractional quantum Hall in a 2D driven-dissipative BH array is discussed in [75]. Exotic phases at the NESS includes photon solid phases [77]

and Majorana-like mode of light [76]. The effect of non-linear driving such as parametric down conversion has been discussed in [76, 158]. Probing many-body signatures of non-linear resonator arrays using photon transport has been discussed in ref. [159]. A nonlinear superconducting circuit with up to 72 sites has also been fabricated to study the dissipative phase transition [80]. The role of long-range order and the symmetry in driven-dissipative many-body dynamics will be discussed in ref. [160].

Below we briefly summarize the main results of some of the above proposals and the experiment done in ref. [80, 161].

Fermionized photons in an array of driven-dissipative nonlinear cavities [72]. Here photons blockade is assumed to be strong such that the probability of having two photons at the same site is strongly suppressed. The latter mimics Pauli's exclusion principle of fermionic particles. In this limit, commutation relations of bosonic operators can also be mapped to those of fermionic operators using the Jordan-Wigner transformation. In this work, the authors examine such relation for the steady state of driven-dissipative nonlinear cavities as described by eq. (14). The drive is assumed to be homogeneous. Figure 12a shows the expectation value of the photon number operator $\langle n \rangle$ at NESS for different value of detuning $\Delta\omega_p = \omega_d - \omega_c$. The peaks happen when the frequency of the drive is resonant with the energy of the non-driven system $E(k) = \omega_c - 2J\cos(k)$, where k is the momentum mode. The effect of finite nonlinearities has also been studied.

Polariton crystallization in driven arrays of lossy nonlinear resonators [73]. Here the author considers arrays of nonlinear resonators as described by the Bose-Hubbard model. The drive has an alternating phase, $\Omega_j = -\Omega e^{-i\phi_j}$. The correlation function between site j and l at NESS is defined as

$$g_r^{(2)}(j,l) = \langle \hat{a}_j^\dagger \hat{a}_l^\dagger \hat{a}_l \hat{a}_j \rangle / \langle \hat{a}_j^\dagger \hat{a}_j \rangle \langle \hat{a}_l^\dagger \hat{a}_l \rangle.$$

For strong nonlinearities, $g_r^{(2)}(i,j)$ exhibits density-density correlations indicating crystallization of photons, see fig. 12-b.

Beyond mean-field bistability in driven-dissipative lattices: Bunching-antibunching transition and quantum simulation [162]. Here the authors investigated the existence of multiple non-equilibrium states of a driven-dissipative lattice in the limit $U/J \to \infty$. It was found that a commonly-used mean-field approximation which ignores spatial correlations predicts regimes of bistability at the steady state. However, the matrix-product-state–based analysis reveals that such bistability is an artifact of the mean-field method. The authors also found a bunching-antibunching transition, fig. 12-c, captured by

$$C(j,r) = \frac{\langle \hat{n}_j \hat{n}_{j+r} \rangle}{\langle \hat{n}_j \rangle \langle \hat{n}_{j+r} \rangle},$$

as the detuning Δ changes.

Photon solid phases in driven arrays of nonlinearly coupled cavities [77]. Here the authors considered arrays described by the extended Bose-Hubbard model with cross-Kerr nonlinearities. The mean-field and the matrix-product-state approaches are used
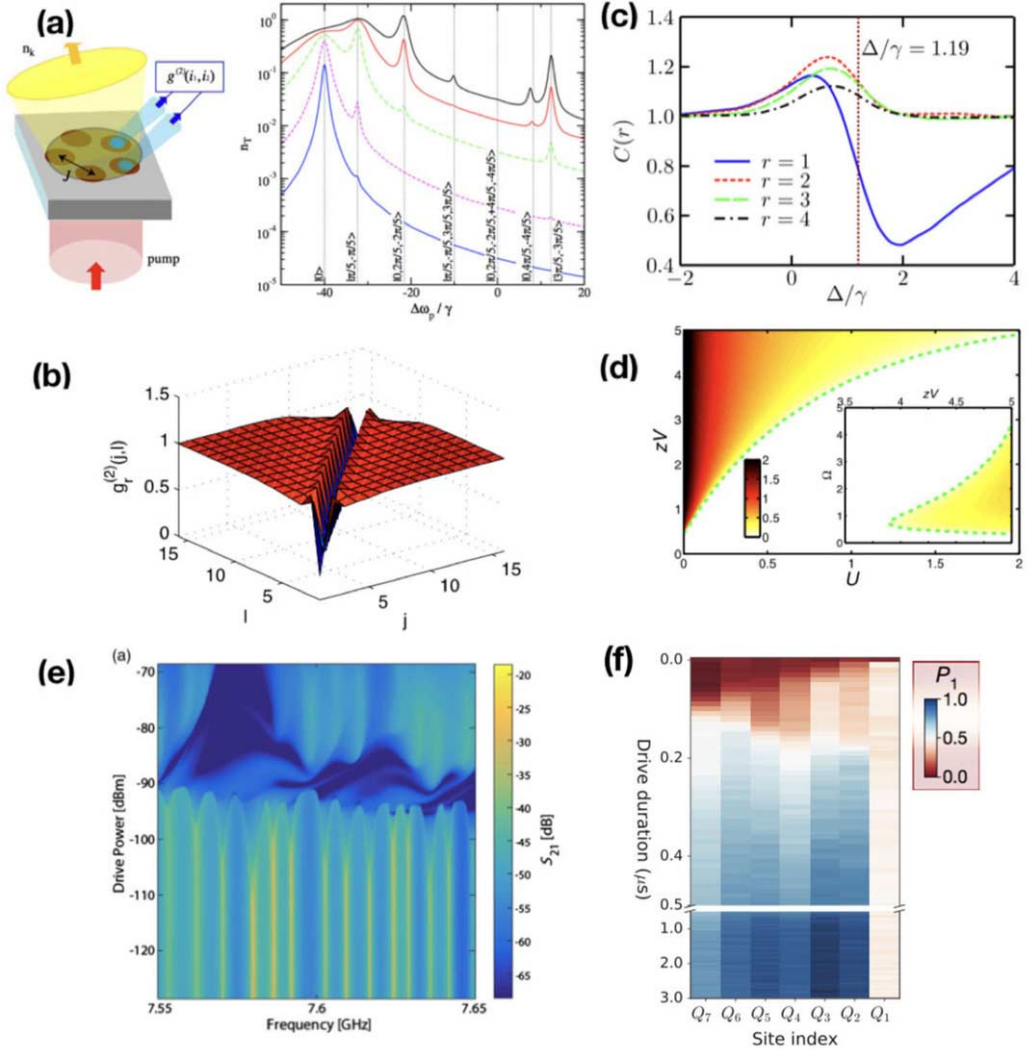
Fig. 12. – Driven-dissipative phases and dissipative phase transitions. (a) fermionized photons at NESS. The plot shows total transmission spectra as a function of the detuning for 5 cavities with $J/\gamma = 20$. Difference curves correspond to the pumping amplitude $\Omega/\gamma = 0.1, 0.3, 1, 2, 3$. (b) Photon crystallization. The figure shows density correlations of the NESS for 16 cavities with $\omega_p = \omega_c$, $U/\gamma = 10$, $\Omega/\gamma = 2$, and $J/\gamma = 2$. (c) Bunching-antibunching transition. Correlations $C(j, r)$ as a function of detuning for $j = 30$, $L = 61$, $J/\gamma = 2$, $\Omega/\gamma = 1$. (d) Photon solid phases. The plot shows population imbalance at NESS for zero-detuning, $J = 0$, and $\Omega = 0.75$. (e) Observation of dissipative phase transitions. The plot shows the transmission as a function of power and driving frequency, exhibiting a transition from a suppressed transmission regime to the regime of dynamical bistability. (f) Dissipatively stabilized Mott Insulator. The plot shows the number of photon, P_1, at each site as a function of time. The results are reproduced from [72, 73, 162, 77, 80, 161], respectively.

to calculate the NESS phase diagram that includes a photon crystal phase, see fig. 12-d. The latter is defined by a non-zero population imbalance between two sub-lattices.

Observation of a dissipative phase transition in a one-dimensional circuit QED lattice [80]. In this work, 72 coupled microwave cavities each coupled to a superconducting qubit was fabricated to study dissipative phase transition. Microwave transmission $\langle \hat{a}_j \rangle$ is measured at the NESS. Figure 12-e shows the transmission as a function of power and driving frequency, exhibiting a transition from a suppressed transmission regime to the regime of dynamical bistability.

A dissipatively stabilized Mott insulator of photons [161]. In this work, the authors engineered a dissipative bath to stabilize the Mott insulating phase of photons in a 8-site superconducting circuit. The bath was done by introducing a lossy cavity attached to the system. When a hole in the Mott insulator happens due to a single photon loss, a coherent drive is autonomously applied to replace the hole with two photons of the same size. The extra photon then coherently hops to the lossy cavity and quickly dissipates away. The resulting Mott insulator is therefore dynamically robust again photon loss.

4. – Strongly interacting photons from superconducting circuits

We now turn our discussion to the implementation of cavity QED and light-matter interactions using superconducting circuits. The idea of quantum phenomena in a macroscopic object is traced back to Josephson in 1962 [163] who predicted quantum tunneling of Cooper pairs between two superconductors separated by a thin insulating barrier known as a Josephson junction. In the late 1990s, quantized charges and Rabi oscillation of a capacitively shunted Josephson junction subjected to a weak microwave field were observed [164, 165], providing evidence that a macroscopic object can behave as an effective quantum two-level system. This "artificial" two-level atom, also known as a superconducting qubit, can then be coupled to modes of a harmonic oscillator such as an LC circuit or a coplanar transmission line. The total system mimics the JC model where a single atom coupled to a cavity. This analogy was put forward in 2004 where strong coupling between a single microwave photon and a superconducting qubit was observed [83], see fig. 13. Since the topology of a circuit can be fabricated almost arbitrarily using the conventional electron-beam lithography, superconducting circuits serves as a scalable platform for quantum simulation with interacting photons. Artificial gauge fields for interacting photons in this system have been realized [64]. A nine-site superconducting circuit with a long coherent time has been fabricated to study signatures of a thermalized to a many-body localized transition [70]. A 72-site superconducting circuit simulating the JCH model has been made to study dissipative phase transition of light as discussed earlier [80].

In the following, we will discuss the standard circuit quantization [166] for an LC circuit as a linear element and a particular type of a superconducting qubit called a transmon qubit as a non-linear element. We conclude the section by reviewing state-of-the-art superconducting chips implementing the BH and the JCH model.
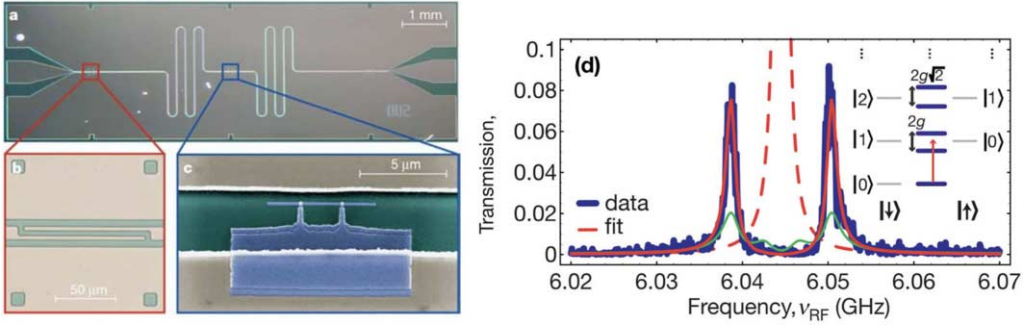
Fig. 13. – Strong coupling of a single microwave photon to a superconducting qubit. (a) The superconducting chip including a coplanar transmission line that acts as a cavity. (b) A capacitor to connect the transmission line to an input and output feed. (c) A superconducting qubit that acts as an artificial atom. (d) Vacuum Rabi mode splitting. The results are reproduced from ref. [83].

4`1. *Microwave photons from an LC circuit*. – An LC circuit is depicted in fig. 14. To write down the Lagrangian for the circuit, we first write down the Kirchhoff's law as

$$(15) \qquad \frac{q}{C} = L\frac{\mathrm{d}I}{\mathrm{d}t},$$

where q is the charge stored in the capacitor, $I = \mathrm{d}q/\mathrm{d}t$ is the current, C is the capacitance, L is the inductance, $\Phi = LI$ is the flux. By differentiating eq. (15) with respect to time, we arrive at an equation of motion for a harmonic oscillator

$$\frac{\mathrm{d}^2}{\mathrm{d}t^2}q + \omega^2 q = 0,$$

where $\omega = \frac{1}{\sqrt{LC}}$ is the frequency of the oscillator. The energies stored in the capacitor and the inductor are

$$E_C = \frac{q^2}{2C} = \frac{1}{2}C\dot{\Phi}^2$$

and

$$E_L = \frac{1}{2}LI^2 = \frac{1}{2L}\Phi^2,$$

respectively, where $\Phi = LI$ is a flux variable. The Lagrangian of the circuit is then defined as

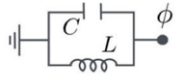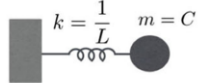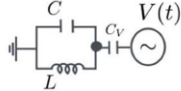$$(16) \qquad \mathcal{L}_{\mathrm{LC}} \equiv E_C - E_L = \frac{1}{2}C\dot{\Phi}^2 - \frac{1}{2L}\Phi^2.$$
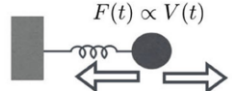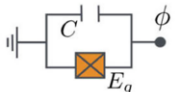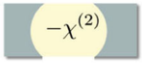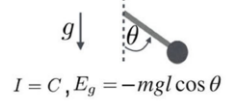
On-site Hamiltonian	Circuit diagram	Equivalent Cavity QED system	Equivalent Mechanical system
(a) Linear resonator ωn	C, L, ϕ		$k = \dfrac{1}{L}$ $m = C$
(b) AC drive $\Omega(a e^{i\omega_p t} + H.c.)$	C, C_v, $V(t)$, L	ω_p	$F(t) \propto V(t)$
(c) Attractive Kerr resonator (a transmon qubit) $\omega n - \dfrac{U}{2} n(n-1)$	C, ϕ, E_g	$-\chi^{(2)}$	$g\downarrow$ θ $I = C, E_g = -mgl\cos\theta$

Fig. 14. – Basic elements in superconducting circuits. Because an LC circuit is a harmonic oscillator, it can be viewed as a linear cavity operating in the microwave regime or a mass attached to a spring. The circuit can be driven coherently by applying an external voltage in the same way that an external laser can drive a cavity. A capacitively-shunted Josephson junction (c) behaves like a $\chi^{(2)}$ nonlinear cavity which has an analogy to a mechanical pendulum.

This Lagrangian can be compared to that of a particle attached to a spring as shown in fig. 14b. The flux Φ corresponds to the position of the particle x. The mass of the particle is $m = C$, while the spring constant is $k = 1/L$. Similar to the harmonic oscillator, the Hamiltonian of the LC circuit takes the form

$$H_{\mathrm{LC}} \equiv \mathcal{L}_{\mathrm{LC}} - \mathcal{Q}\Phi = \frac{\mathcal{Q}^2}{2C} + \frac{\Phi^2}{2L},$$

where

$$\mathcal{Q} = \frac{\partial \mathcal{L}_{\mathrm{LC}}}{\partial \dot{\Phi}} = C\dot{\Phi}$$

is a conjugate momentum. By promoting Φ and Q to operators, we get a commutation relation

$$[\hat{Q}, \hat{\Phi}] = -i.$$

We define an annihilation operator as

$$\hat{a} = i\frac{1}{\sqrt{2C\omega}}\hat{Q} + \frac{1}{\sqrt{2L\omega}}\hat{\Phi},$$

respectively. The final Hamiltonian then takes the form

$$\hat{H}_{\mathrm{LC}} \approx \hbar\omega\left(\hat{a}^\dagger \hat{a} + \frac{1}{2}\right).$$

We note that we choose to discuss an LC circuit here for simplicity. In the experiment, a loss-noise coplanar transmission is usually used as a linear element [81]. We refer the reader to ref. [167] for the detailed derivation of the circuit quantization of the latter.

4`2. *A Kerr resonator from a transmon qubit.* – Josephson junction provides a natural non-linear element for superconducting circuits. A capacitively shunted Josephson junction is described by the Lagrangian

$$(17) \qquad \mathcal{L}_{\text{transmon}} = \frac{1}{2}C\dot{\Phi}^2 + E_J \cos\left(\frac{\Phi}{\Phi_0}\right),$$

where E_J is the Josephson energy and $\Phi_0 = \hbar/2e$ is a flux quanta. As shown in fig. 14, a mechanical analogy of this system is a pendulum where C is the moment of inertia, E_J is the gravitational energy, and Φ is the angle of the pendulum. Let us first understand the harmonic oscillation limit of this system. Imagine the pendulum is initially placed at its minima $\Phi = 0$ and then subjected to a small kick that generates an oscillation around this point. If the gravitational energy is large compared to the initial kinetic energy, then this oscillation has a small amplitude. In the circuit picture, this corresponds to the limit $E_J/E_C \gg 1$ where $E_C = e^2/2C$. Subsequently, the expansion of the cosine function in Φ can be truncated at to a finite order, *i.e.*,

$$(18) \qquad \mathcal{L}_{\text{transmon}} \approx \frac{1}{2}C\dot{\Phi}^2 - \frac{1}{2L_J}\Phi^2 + \frac{E_J}{4\Phi_0^4}\Phi^4 + \dots,$$

where

$$L_J = \Phi_0^2/E_J$$

is an effective linear inductance. When keeping up to the second order, the system reduces to a simple Harmonic oscillator with the frequency

$$\omega = 1/\sqrt{L_J C}.$$

Slightly away from this limit, the nonlinearity arises from the forth-order term. Hence, the system becomes a non-linear oscillator. In the following we will perform the circuit quantization while first keeping infinite orders and only apply truncation after normal ordering of ladder operators. Without truncation, the Hamiltonian can be written as

$$(19) \qquad \mathcal{H}_{\text{transmon}} = \frac{\mathcal{Q}^2}{2C} + \frac{\Phi^2}{2L_J} + \sum_{m=2}^{\infty} \frac{(-1)^m E_J}{(2m)!\Phi_0^{2m}}\Phi^{2m},$$

where

$$\mathcal{Q} = C\frac{\partial \mathcal{L}_{\text{transmon}}}{\partial \dot{\Phi}}$$

is a conjugate momentum. As before, we promote $\mathcal{Q}$ and Φ to operators as

(20)
$$\hat{\Phi} = \sqrt{\frac{L_J\omega}{2}}(\hat{a}^\dagger + \hat{a}),$$

$$\hat{\mathcal{Q}} = i\sqrt{\frac{C\omega}{2}}(\hat{a}^\dagger - \hat{a}),$$

where $\left[\hat{a}, \hat{a}^\dagger\right] = i$. We then apply normal ordering of the operators $\hat{a}$ and $\hat{a}^\dagger$ in $\mathcal{H}_{\text{transmon}}$ using the formula [168]

$$(a + a^\dagger)^{2m} = \sum_{k=0}^{m} \sum_{i=0}^{2m-2k} \frac{(2m)!(a^\dagger)^i a^{2m-2k-i}}{2^k k! i!(2m-2k-i)!}.$$

In the limit $E_J/E_C \approx 50$–100, the higher-order terms in $\mathcal{H}_{\text{transmon}}$ can be truncated up to the forth order. As a result, the final Hamiltonian can be written as

(21)
$$\hat{H}_{\text{transmon}} \approx (\omega + \delta\omega)\hat{n} - \frac{U}{2}\hat{n}(\hat{n} - 1),$$

where $U = -E_J e^{-\lambda^2}\lambda^4/4$ is Kerr nonlinearity, $\delta\omega = \lambda^2 E_J e^{-\lambda^2}$, and $\lambda = (2E_{\tilde{C}}/E_J)^{1/4}$. This Hamiltonian takes the same form of that of a Kerr resonator. Due to the n-dependent nonlinearity, a vacuum state $|0\rangle$ and a one-photon Fock state $|1\rangle$ of the resonator can also be used as a qubit. A capacitively shunted Josephson junction operating at this regime is known as a transmon qubit. Typical values of ω and U are ~ 5–$10\,\text{GHz}$ and ~ 200–$300\,\text{GHz}$, respectively [169]. Typical lifetime of photons in the transmon qubit is 10–$20\,\mu\text{s}$ with the dephasing time around $2\,\mu\text{s}$.

4$\cdot$**3.** *Different types of superconducting qubits*. – For a larger nonlinearity $E_J/E_{\tilde{C}} > 100$, the transmon qubit is also known as a charge or a Cooper-pair-box qubit [164, 165] which was one of the first qubit design invented in early 1990. However, the charge qubit suffers from charge noises and only has a lifetime of a few ns. We note that there are several other designs of superconducting qubits such as flux qubits and phase qubits [170-176] for quantum computing applications [177]. However, only a transmon qubit can be mapped to a Kerr nonlinear resonator.

4$\cdot$**4.** *Nonlinear lattices from arrays of coupled transmon qubits*.

4$\cdot$4.1. The Bose-Hubbard model. Transmon qubits can be coupled in various ways such as a simple use of a capacitor of which we provide details of the circuit quantization below, a transmission line that creates virtual excitation exchange between qubits [179,180], and a pair of Josephson junctions that allow the coupling to be tuned *in situ* using an external flux [181-183]. Arrays of coupled transmon qubits are described by the Bose-Hubbard
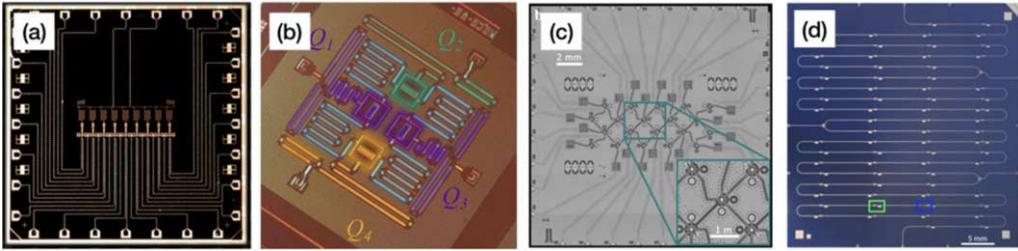
Fig. 15. – Arrays of coupled transmon qubits fabricated by (a) Google with $L = 9$ [178, 70], (b) IBM with $L = 5$ [85], (c) Regetti with $L = 19$ [86]. A 72-site superconducting chip implementing the JCH model to study dissipative phase transition [80] is shown in (d).

Hamiltonian

$$\hat{H}_{\text{BHM}} = \sum_{j=0}^{L-1} \omega_j \hat{n}_j - \frac{U}{2} \sum_{j=0}^{L-1} \hat{n}_j(\hat{n}_j - 1) - \sum_{\langle j,j' \rangle} J_{j,j'} \left(\hat{a}_j^\dagger \hat{a}'_j + \text{H.c.} \right) \tag{22}$$

where $\hat{n}_j = \hat{a}_j^\dagger \hat{a}_j$ is a local number operator, $J_{j,j'}$ is the hopping coefficient between the sites j and j', ω_j is the frequency of the resonator j. State-of-the-art superconducing chips containing arrays of coupled transmon qubits with different topologies are shown in fig. 15. The 9-site one-dimensional chip in fig. 15a was used to implement random circuits for quantum supremacy [178] and to observe stroboscopic signatures of many-body localization [70]. The 5-site chip in fig. 15b and 19-site chip in fig. 15c were used to demonstrate quantum variational-based algorithms for quantum chemistry [85] and quantum machine learning [86].

In the following we will give an example of circuit quantization of capacitively-coupled transmon qubits, the circuit diagram is shown in fig. 16. The flux variable is defined as $\phi_j = -\int V_j \mathrm{d}t$, where V_j is a voltage at the corresponding position. As will be shown below, this quantity can be quantized to the form $\phi_j = \alpha(\hat{a}_j + \hat{a}_j^\dagger)$, where $\hat{a}_j, \hat{a}_j^\dagger$ are bosonic operators at site j and α is some constant that depends on the circuit's elements. As shown in [184], two parallel-connected Josephson junction with a flux bias Φ_g can be thought of as an effective single Josephson junctions E_J where

$$E_J = (E_{J1} + E_{J2}) \cos\left(\frac{\Phi_g}{2\Phi_0}\right) \sqrt{1 + d^2 \tan\left(\frac{\Phi_g}{2\Phi_0}\right)},$$

with $\Phi_0 = \hbar/2e$ and $d = (E_{J2} - E_{J1})/(E_{J2} + E_{J1})$. The resonator's frequency ω_j is related to E_J, hence it can be tuned on the fly, by changing the flux bias Φ_g.

Following the standard circuit quantization procedure [166], we first write down the
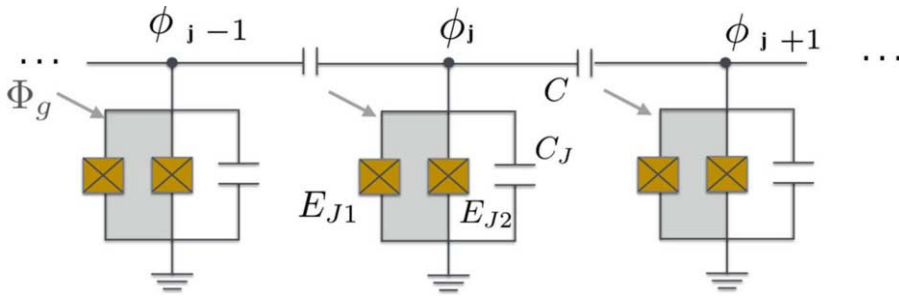
Fig. 16. – Circuit QED diagram showing an implementation of the Bose-Hubbard Hamiltonian.

circuit's Lagrangian as

$$\mathcal{L} = \sum_{j=0}^{L-1} \left(\frac{1}{2} C_J \dot{\phi}_j^2 + E_J \cos\left(\frac{\phi_j}{\phi_0}\right) \right) + \sum_{j=0}^{L-2} \frac{1}{2} C (\dot{\phi}_j - \dot{\phi}_{j+1})^2,$$

Assuming $C/(C_J + 2C) \ll 1$, the Hamiltonian can be obtained using the Legendre transformation [185],

$$(23) \qquad H = \sum_{j=0}^{L-1} \left(\frac{\dot{\phi}_j^2}{2\tilde{C}} + \frac{\phi_j^2}{2\tilde{L}} + \sum_{n=2}^{\infty} \frac{(-1)^n E_J}{(2n)! \Phi_0^{2n}} \phi_j^{2n} \right) + \sum_{j=0}^{L-2} \frac{C}{\tilde{C}^2} q_j q_{j+1},$$

where

$$q_j = \sqrt{2C + C_J} \frac{\partial \mathcal{L}}{\partial \dot{\phi}_j}$$

is a conjugate momentum of ϕ_j, $\tilde{C} = C_J + 2C$ is an effective capacitance and $\tilde{L} = \Phi_0^2/E_J$ is an effective inductance. We then quantized ϕ_j and q_j by defining ladder operators $\hat{a}_j$, $\hat{a}_j^\dagger$ according to

$$(24) \qquad \hat{\phi}_j = (\tilde{L}/4\tilde{C})^{1/4} (\hat{a}_j + \hat{a}_j^\dagger),$$

$$(25) \qquad \hat{q}_j = i(\tilde{C}/4\tilde{L})^{1/4} (-\hat{a}_j + \hat{a}_j^\dagger).$$

The first two terms in eq. (23) become $\sum_j \omega \hat{a}_j^\dagger \hat{a}_j$, where $\omega = 1/\sqrt{\tilde{L}\tilde{C}}$ is a resonator frequency. In addition, the capacitor C leads to the hopping term with $J = -\frac{\omega C}{2\tilde{C}}$. A rotating-wave approximation is assumed, so we ignore the term $(\hat{a}_j^\dagger \hat{a}_{j+1}^\dagger + \text{H.c.})$.

The Josephson junction E_J introduces an anharmonicity to the resonator's frequency. Due to this anharmonicity, a vacuum state $|0\rangle$ and a one-photon Fock state $|1\rangle$ of the resonator can be used as a qubit. A transmon qubit corresponds to the regime with

a large $E_{\tilde{L}}/E_{\tilde{C}} > 1$ where $E_{\tilde{C}} = e^2/2\tilde{C}$ and $E_{\tilde{L}} = \Phi_0^2/\tilde{L}$, such that the terms higher than the forth order can be neglected [184]. Hence, a transmon qubit can be thought of as a resonator with an attractive Kerr nonlinearity $U < 0$. Taking into account the normal ordering [186], we get $U = -E_J e^{-\lambda^2}\lambda^4/4$, where $\lambda = (2E_{\tilde{C}}/E_{\tilde{L}})^{1/4}$. This normal ordering also introduces a small normalization factor $\delta\omega$ to the resonator frequency, with $\delta\omega = \lambda^2 E_J e^{-\lambda^2}$.

4.4.2. *The Jaynes-Cummings Hubbard model*. A single superconducting qubit coupled to a transmission line can be described with the Jaynes-Cummings model, where the transmission line plays a role of a resonator, and a qubit plays a role of an atom. An array of up to 72 coupled Jaynes-Cummings resonators which leads to the JCM model has been implemented in ref. [80] to study dissipative phase transition.

5. – Conclusions and future aspects

Although implementing a universal quantum simulator which requires full control over quantum many-body systems may still be years away, tremendous experimental progress has been made during the past two decades. Two main approaches have emerged. The first approach such cold atom systems provide a global control a large ensemble of quantum particles, with possible local manipulation and measurement in some cases. The second approach such as interacting photons in superconducting circuits provide more flexibility on the local control and measurement while scaling up to 50–100 site are in current progress. For the latter, one needs to develop both new experimental techniques and new theoretical frameworks to maintain such controllability when scaling up. For example, the many-body spectroscopy technique developed in ref. [70] allows one to resolve all energy eigenstates and eigenenergies of the system. This result allows us to benchmark the experiment with the theory and to reconstruct matrix elements of many-body Hamiltonians that a given circuit implements. However, when scaling up eigenenergies of the system will become too dense to be resolved by the current resolution which is limited by the coherence time of the system. Hence, obtaining full information of the Hamiltonian of the circuit is not possible for a large system. To what extent the disregarded information becomes essential to the physics of the system is still an open question. Constructing the Hamiltonian of the system with limited details also require a new theoretical framework. The latter also raises the question of how to systematically benchmark a quantum simulator as it approaches the limit of classical computers. Identifying problems beyond quantum physics that can only be solved with near-term quantum simulators is also an important question that drives the field forwards. With these in mind, we conclude that, due to exceptional local control systems, interacting photons in superconducting circuits, although still in its early state, is one of the promising candidates for quantum simulation.

REFERENCES

[1]   Cirac J. I. and Zoller P., *Nat. Phys.*, **8** (2012) 264
      https://doi.org/10.1038/nphys2275
[2]   Hauke P., Cucchietti F. M., Tagliacozzo L., Deutsch I. and Lewenstein M.,
      Rep. Prog. Phys., **75** (2012) 082401
      http://stacks.iop.org/0034-4885/75/i=8/a=082401
[3]   Johnson T. H., Clark S. R. and Jaksch D., *EPJ Quantum Technol.*, **1** (2014) 10
      https://doi.org/10.1140/epjqt10
[4]   Blatt R. and Roos C. F., *Nat. Phys.*, **8** (2012) 277
      https://doi.org/10.1038/nphys2252
[5]   Gross C. and Bloch I., *Science*, **357** (2017) 995
      http://science.sciencemag.org/content/357/6355/995
[6]   Tosi G., Mohiyaddin F. A., Schmitt V., Tenberg S., Rahman R., Klimeck G. and
      Morello A., *Nat. Commun.*, **8** (2017) 450
      https://doi.org/10.1038/s41467-017-00378-x
[7]   Chang D. E., Vuletić V. and Lukin M. D., *Nat. Photon.*, **8** (2014) 685
      https://doi.org/10.1038/nphoton.2014.192
[8]   Hensgens T., Fujita T., Janssen L., Li X., Van Diepen C. J., Reichl C.,
      Wegscheider W., Das Sarma S. and Vandersypen L. M. K., *Nature*, **548** (2017) 70
      https://doi.org/10.1038/nature23022
[9]   Houck A. A., Türeci H. E. and Koch J., *Nat. Phys.*, **8** (2012) 292
      https://doi.org/10.1038/nphys2251
[10] Yao N. Y., Jiang L., Gorshkov A. V., Maurer P. C., Giedke G., Cirac J. I. and
      Lukin M. D., *Nat. Commun.*, **3** (2012) 800
      https://doi.org/10.1038/ncomms1788
[11] Banks J., Carson J., Nelson B. and Nicol D., *Discrete-Event System Simulation*,
      5th edition (Prentice Hall) 2010.
[12] Stephen N. and Stephen N., *Cancer Drug Design and Discovery*, 1st edition (Academic
      Press) 2007.
[13] Vallespin D., Badcock K., Ronch A. D., White M., Perfect P. and Ghoreyshi
      M., *Prog. Aerospace Sci.*, **52** (2012) 2; *Applied Computational Aerodynamics and High
      Performance Computing in the UK*
      http://www.sciencedirect.com/science/article/pii/S0376042112000139
[14] Gilchrist A., *Nature*, **276** (1978) 342
      https://doi.org/10.1038/276342a0
[15] Carr C. E., Bryan N. C., Saboda K. N., Bhattaru S. A., Ruvkun G. and Zuber
      M. T., *npj Microgravity*, **4** (2018) 14
      https://doi.org/10.1038/s41526-018-0050-3
[16] Benov D., *Monte Carlo Methods and Appl.*, **22** (2016) 73.
[17] Seydel R. U., *Tools for Computational Finance* (Springer International Publishing)
      2006.
[18] Häner T. and Steiger D. S., arXiv e-prints (Preprint 1704.01127) (2017).
[19] Pednault E., Gunnels J. A., Nannicini G., Horesh L., Magerlein T., Solomonik
      E. and Wisnieff R., arXiv e-prints (Preprint 1710.05867) (2017).
[20] Lee P. A., *Rep. Prog. Phys.*, **71** (2008) 012501
      http://stacks.iop.org/0034-4885/71/i=1/a=012501
[21] Hansson T. H., Hermanns M., Simon S. H. and Viefers S. F., *Rev. Mod. Phys.*, **89**
      (2017) 025005
      https://link.aps.org/doi/10.1103/RevModPhys.89.025005

[22] Feynman R. P., *Int. J. Theor. Phys.*, **21** (1982) 467
https://doi.org/10.1007/BF02650179

[23] Lloyd S., *Science*, **273** (1996) 1073
http://science.sciencemag.org/content/273/5278/1073

[24] Carleo G. and Troyer M., *Science*, **355** (2017) 602
http://science.sciencemag.org/content/355/6325/602

[25] Orus R., *Ann. Phys.*, **349** (2014) 117
http://www.sciencedirect.com/science/article/pii/S0003491614001596

[26] Schollwoeck U., *Ann. Phys.*, **96** (2011) 326.

[27] Parr R. G., *Density functional theory of atoms and molecules*, in *Proceedings of Horizons of Quantum Chemistry*, edited by Fukui K. and Pullman B. (Springer Netherlands, Dordrecht) 1980, pp. 5–15.

[28] von der Linden W., *Phys. Rep.*, **220** (1992) 53
http://www.sciencedirect.com/science/article/pii/037015739290029Y

[29] Leggett A. J., *Nat. Phys.*, **2** (2006) 134
https://doi.org/10.1038/nphys254

[30] Nandkishore R. and Huse D. A., *Annu. Rev. Condens. Matter Phys.*, **6** (2015) 15
https://doi.org/10.1146/annurev-conmatphys-031214-014726

[31] Kassal I., Whitfield J. D., Perdomo-Ortiz A., Yung M.-H. and Aspuru-Guzik A., *Annu. Rev. Phys. Chem.*, **62** (2011) 185, pMID: 21166541.
URL https://doi.org/10.1146/annurev-physchem-032210-103512

[32] Lanyon B. P., Whitfield J. D., Gillett G. G., Goggin M. E., Almeida M. P., Kassal I., Biamonte J. D., Mohseni M., Powell B. J., Barbieri M., Aspuru-Guzik A. and White A. G., *Nat. Chem.*, **2** (2010) 106
https://doi.org/10.1038/nchem.483

[33] Bloch I., Dalibard J. and Nascimbène S., *Nat. Phys.*, **8** (2012) 267
https://doi.org/10.1038/nphys2259

[34] Bloch I., Dalibard J. and Zwerger W., *Rev. Mod. Phys.*, **80** (2008) 885
https://link.aps.org/doi/10.1103/RevModPhys.80.885

[35] Greiner M., Mandel O., Esslinger T., Hänsch T. W. and Bloch I., *Nature*, **415** (2002) 39
https://doi.org/10.1038/415039a

[36] Sherson J. F., Weitenberg C., Endres M., Cheneau M., Bloch I. and Kuhr S., *Nature*, **467** (2010) 68
https://doi.org/10.1038/nature09378

[37] Lewenstein M. and Sanpera A., *Science*, **319** (2008) 292
http://science.sciencemag.org/content/319/5861/292

[38] Goldman N., Budich J. C. and Zoller P., *Nat. Phys.*, **12** (2016) 639
https://doi.org/10.1038/nphys3803

[39] Cheuk L. W., Nichols M. A., Okan M., Gersdorf T., Ramasesh V. V., Bakr W. S., Lompe T. and Zwierlein M. W., *Phys. Rev. Lett.*, **114** (2015) 193001
https://link.aps.org/doi/10.1103/PhysRevLett.114.193001

[40] Haller E., Hudson J., Kelly A., Cotta D. A., Peaudecerf B., Bruce G. D. and Kuhr S., *Nat. Phys.*, **11** (2015) 738
https://doi.org/10.1038/nphys3403

[41] Parsons M. F., Huber F., Mazurenko A., Chiu C. S., Setiawan W., Wooley-Brown K., Blatt S. and Greiner M., *Phys. Rev. Lett.*, **114** (2015) 213002
https://link.aps.org/doi/10.1103/PhysRevLett.114.213002

[42] Omran A., Boll M., Hilker T. A., Kleinlein K., Salomon G., Bloch I. and Gross C., *Phys. Rev. Lett.*, **115** (2015) 263001
https://link.aps.org/doi/10.1103/PhysRevLett.115.263001

[43] Zwerger W., *The BCS-BEC Crossover and the Unitary Fermi Gas* (Springer-Verlag Berlin Heidelberg) 2012.

[44] Choi J.-y., Hild S., Zeiher J., Schauss P., Rubio-Abadal A., Yefsah T., Khemani V., Huse D. A., Bloch I. and Gross C., *Science*, **352** (2016) 1547
http://science.sciencemag.org/content/352/6293/1547

[45] Bernien H., Schwartz S., Keesling A., Levine H., Omran A., Pichler H., Choi S., Zibrov A. S., Endres M., Greiner M., Vuletić V. and Lukin M. D., *Nature*, **551** (2017) 579
https://doi.org/10.1038/nature24622

[46] Blatt R. and Roos C. F., *Nat. Phys.*, **8** (2012) 277
https://doi.org/10.1038/nphys2252

[47] Porras D. and Cirac J. I., *Phys. Rev. Lett.*, **92** (2004) 207901
https://link.aps.org/doi/10.1103/PhysRevLett.92.207901

[48] Islam R., Edwards E. E., Kim K., Korenblit S., Noh C., Carmichael H., Lin G. D., Duan L. M., Joseph Wang C. C., Freericks J. K. and Monroe C., *Nat. Commun.*, **2** (2011) 377
https://doi.org/10.1038/ncomms1374

[49] Edwards E. E., Korenblit S., Kim K., Islam R., Chang M.-S., Freericks J. K., Lin G.-D., Duan L.-M. and Monroe C., *Phys. Rev. B*, **82** (2010) 060412
https://link.aps.org/doi/10.1103/PhysRevB.82.060412

[50] Zhang J., Hess P. W., Kyprianidis A., Becker P., Lee A., Smith J., Pagano G., Potirniche I. D., Potter A. C., Vishwanath A., Yao N. Y. and Monroe C., *Nature*, **543** (2017) 217
https://doi.org/10.1038/nature21413

[51] Hffner H., Roos C. and Blatt R., *Phys. Rep.*, **469** (2008) 155
http://www.sciencedirect.com/science/article/pii/S0370157308003463

[52] Schindler P., Nigg D., Monz T., Barreiro J. T., Martinez E., Wang S. X., Quint S., Brandl M. F., Nebendahl V., Roos C. F., Chwalla M., Hennrich M. and Blatt R., *New J. Phys.*, **15** (2013) 123012
http://stacks.iop.org/1367-2630/15/i=12/a=123012

[53] Britton J. W., Sawyer B. C., Keith A. C., Wang C. C. J., Freericks J. K., Uys H., Biercuk M. J. and Bollinger J. J., *Nature*, **484** (2012) 489
https://doi.org/10.1038/nature10981

[54] Debnath S., Linke N. M., Figgatt C., Landsman K. A., Wright K. and Monroe C., *Nature*, **536** (2016) 63
https://doi.org/10.1038/nature18648

[55] Morello A., *Quantum Sci. Technol.*, **3** (2018) 030201
http://stacks.iop.org/2058-9565/3/i=3/a=030201

[56] Watson T. F., Philips S. G. J., Kawakami E., Ward D. R., Scarlino P., Veldhorst M., Savage D. E., Lagally M. G., Friesen M., Coppersmith S. N., Eriksson M. A. and Vandersypen L. M. K., *Nature*, **555** (2018) 633
https://doi.org/10.1038/nature25766

[57] Noh C. and Angelakis D. G., *Rep. Prog. Phys.*, **80** (2017) 016401
http://stacks.iop.org/0034-4885/80/i=1/a=016401

[58] Angelakis D. G., *Quantum Simulations with Photons and Polaritons* (Springer International Publishing) 2007.

[59] Angelakis D. G., Santos M. F. and Bose S., *Phys. Rev. A*, **76** (2007) 031805.

[60] Hartmann M. J., Brandao F. G. S. L. and Plenio M. B., *Nat. Phys.*, **2** (2006) 849.

[61] Greentree A. D., Tahan C., Cole J. H. and Hollenberg L. C. L., *Nat. Phys.*, **2** (2006) 856.

[62] Cho J., Angelakis D. G. and Bose S., *Phys. Rev. Lett.*, **101** (2008) 246809
https://link.aps.org/doi/10.1103/PhysRevLett.101.246809

[63] Nunnenkamp A., Koch J. and Girvin S. M., *New J. Phys.*, **13** (2011) 095008.

[64] Roushan P., Neill C., Megrant A., Chen Y., Babbush R., Barends R., Campbell B., Chen Z., Chiaro B., Dunsworth A., Fowler A., Jeffrey E., Kelly J., Lucero E., Mutus J., O'Malley P. J. J., Neeley M., Quintana C., Sank D., Vainsencher A., Wenner J., White T., Kapit E., Neven H. and Martinis J., *Nat. Phys.*, **13** (2016) 146
https://doi.org/10.1038/nphys3930

[65] Hartmann M. J., Brandão F. G. S. L. and Plenio M. B., *Phys. Rev. Lett.*, **99** (2007) 160501
https://link.aps.org/doi/10.1103/PhysRevLett.99.160501

[66] Kay A. and Angelakis D. G., *EPL*, **84** (2008) 20001
http://stacks.iop.org/0295-5075/84/i=2/a=20001

[67] Li P. B., Gu Y., Gong Q. H. and Guo G. C., *Eur. Phys. J. D*, **55** (2009) 205
https://doi.org/10.1140/epjd/e2009-00188-3

[68] Sarkar S., *Physica B: Condensed Matter*, **407** (2012) 44
http://www.sciencedirect.com/science/article/pii/S0921452611009483

[69] Tangpanitanon J., Bastidas V. M., Al-Assam S., Roushan P., Jaksch D. and Angelakis D. G., *Phys. Rev. Lett.*, **117** (2016) 213603
https://link.aps.org/doi/10.1103/PhysRevLett.117.213603

[70] Roushan P., Neill C., Tangpanitanon J., Bastidas V. M., Megrant A., Barends R., Chen Y., Chen Z., Chiaro B., Dunsworth A., Fowler A., Foxen B., Giustina M., Jeffrey E., Kelly J., Lucero E., Mutus J., Neeley M., Quintana C., Sank D., Vainsencher A., Wenner J., White T., Neven H., Angelakis D. G. and Martinis J., *Science*, **358** (2017) 1175
http://science.sciencemag.org/content/358/6367/1175

[71] Albert V. V. and Jiang L., *Phys. Rev. A*, **89** (2014) 022118
https://link.aps.org/doi/10.1103/PhysRevA.89.022118

[72] Carusotto I., Gerace D., Tureci H. E., De Liberato S., Ciuti C. and Imamoğlu A., *Phys. Rev. Lett.*, **103** (2009) 033601
http://link.aps.org/doi/10.1103/PhysRevLett.103.033601

[73] Hartmann M. J., *Phys. Rev. Lett.*, **104** (2010) 113601
http://link.aps.org/doi/10.1103/PhysRevLett.104.113601

[74] Grujic T., Clark S. R., Jaksch D. and Angelakis D. G., *New J. Phys.*, **14** (2012) 103025
http://stacks.iop.org/1367-2630/14/i=10/a=103025

[75] Umucalilar R. O. and Carusotto I., *Phys. Rev. Lett.*, **108** (2012) 206809
http://link.aps.org/doi/10.1103/PhysRevLett.108.206809

[76] Bardyn C.-E. and İmamoğlu A., *Phys. Rev. Lett.*, **109** (2012) 253606
http://link.aps.org/doi/10.1103/PhysRevLett.109.253606

[77] Jin J., Rossini D., Fazio R., Leib M. and Hartmann M. J., *Phys. Rev. Lett.*, **110** (2013) 163605.

[78] Kessler E. M., Giedke G., Imamoglu A., Yelin S. F., Lukin M. D. and Cirac J. I., *Phys. Rev. A*, **86** (2012) 012116
https://link.aps.org/doi/10.1103/PhysRevA.86.012116

[79] Wilming H., Kastoryano M. J., Werner A. H. and Eisert J., *J. Math. Phys.*, **58** (2017) 033302.

[80] Fitzpatrick M., Sundaresan N. M., Li A. C. Y., Koch J. and Houck A. A., *Phys. Rev. X*, **7** (2017) 011016
https://link.aps.org/doi/10.1103/PhysRevX.7.011016

[81] Underwood D. L., Shanks W. E., Koch J. and Houck A. A., *Phys. Rev. A*, **86** (2012) 023837
https://link.aps.org/doi/10.1103/PhysRevA.86.023837

[82] You J. Q. and Nori F., *Phys. Today*, **58** (2005) 42.

[83] Wallraff A., Schuster D. I., Blais A., Frunzio L., Huang R. S., Majer J., Kumar S., Girvin S. M. and Schoelkopf R. J., *Nature*, **431** (2004) 162
https://doi.org/10.1038/nature02851

[84] Yoshihara F., Fuse T., Ashhab S., Kakuyanagi K., Saito S. and Semba K., *Nat. Phys.*, **13** (2016) 44
https://doi.org/10.1038/nphys3906

[85] Kandala A., Mezzacapo A., Temme K., Takita M., Brink M., Chow J. M. and Gambetta J. M., *Nature*, **549** (2017) 242
https://doi.org/10.1038/nature23879

[86] Otterbach J. S., Manenti R., Alidoust N., Bestwick A., Block M., Bloom B., Caldwell S., Didier N., Schuyler Fried E., Hong S., Karalekas P., Osborn C. B., Papageorge A., Peterson E. C., Prawiroatmodjo G., Rubin N., Ryan C. A., Scarabelli D., Scheer M., Sete E. A., Sivarajah P., Smith R. S., Staley A., Tezak N., Zeng W. J., Hudson A., Johnson B. R., Reagor M., da Silva M. P. and Rigetti C., arXiv e-prints (Preprint 1712.05771) (2017).

[87] Carusotto I. and Ciuti C., *Rev. Mod. Phys.*, **85** (2013) 299
https://link.aps.org/doi/10.1103/RevModPhys.85.299

[88] Carusotto I., Volz T. and Imamolu A., *EPL*, **90** (2010) 37001
http://stacks.iop.org/0295-5075/90/i=3/a=37001

[89] Kasprzak J., Richard M., Kundermann S., Baas A., Jeambrun P., Keeling J. M. J., Marchetti F. M., Szymańska M. H., André R., Staehli J. L., Savona V., Littlewood P. B., Deveaud B. and Dang L. S., *Nature*, **443** (2006) 409
https://doi.org/10.1038/nature05131

[90] Plumhof J. D., Stöferle T., Mai L., Scherf U. and Mahrt R. F., *Nat. Mater.*, **13** (2013) 247
https://doi.org/10.1038/nmat3825

[91] Lagoudakis K. G., Wouters M., Richard M., Baas A., Carusotto I., André R., Dang L. S. and Deveaud-Plédran B., *Nat. Phys.*, **4** (2008) 706
https://doi.org/10.1038/nphys1051

[92] Amo A., Lefrère J., Pigeon S., Adrados C., Ciuti C., Carusotto I., Houdré R., Giacobino E. and Bramati A., *Nat. Phys.*, **5** (2009) 805
https://doi.org/10.1038/nphys1364

[93] Sachdev S., *Quantum Phase Transitions*, 2nd edition (Cambridge University Press, Cambridge, UK) 2011.
URL http://www.cambridge.org/9780521514682

[94] Hubbard J., *Proc. R. Soc. London Ser. A*, **276** (1963) 238
http://rspa.royalsocietypublishing.org/content/276/1365/238

[95] Gersch H. A. and Knollman G. C., *Phys. Rev.*, **129** (1963) 959
https://link.aps.org/doi/10.1103/PhysRev.129.959

[96] Fisher M. P. A., Weichman P. B., Grinstein G. and Fisher D. S., *Phys. Rev. B*, **40** (1989) 546
https://link.aps.org/doi/10.1103/PhysRevB.40.546

[97] Ejima S., Fehske H. and Gebhard F., *EPL*, **93** (2011) 30002
http://stacks.iop.org/0295-5075/93/i=3/a=30002

[98] Boyd R., *Nonlinear Optics* (Elsevier) 2008.

[99] Darquié B., Jones M. P. A., Dingjan J., Beugnon J., Bergamini S., Sortais Y., Messin G., Browaeys A. and Grangier P., *Science*, **309** (2005) 454
http://science.sciencemag.org/content/309/5733/454

[100] Wrigge G., Gerhardt I., Hwang J., Zumofen G. and Sandoghdar V., *Nat. Phys.*, **4** (2007) 60
https://doi.org/10.1038/nphys812

[101] Tey M. K., Chen Z., Aljunid S. A., Chng B., Huber F., Maslennikov G. and Kurtsiefer C., *Nat. Phys.*, **4** (2008) 924
https://doi.org/10.1038/nphys1096

[102] Hétet G., Slodička L., Hennrich M. and Blatt R., *Phys. Rev. Lett.*, **107** (2011) 133002
https://link.aps.org/doi/10.1103/PhysRevLett.107.133002

[103] Walls D. and Milburn G. J., *Quantum Optics* (Springer International Publishing) 2008.

[104] Shore B. W. and Knight P. L., *J. Mod. Optics*, **40** (1993) 1195.

[105] Goy P., Raimond J. M., Gross M. and Haroche S., *Phys. Rev. Lett.*, **50** (1983) 1903
https://link.aps.org/doi/10.1103/PhysRevLett.50.1903

[106] Hulet R. G., Hilfer E. S. and Kleppner D., *Phys. Rev. Lett.*, **55** (1985) 2137
https://link.aps.org/doi/10.1103/PhysRevLett.55.2137

[107] Jhe W., Anderson A., Hinds E. A., Meschede D., Moi L. and Haroche S., *Phys. Rev. Lett.*, **58** (1987) 666
https://link.aps.org/doi/10.1103/PhysRevLett.58.666

[108] Thompson R. J., Rempe G. and Kimble H. J., *Phys. Rev. Lett.*, **68** (1992) 1132
https://link.aps.org/doi/10.1103/PhysRevLett.68.1132

[109] Brune M., Schmidt-Kaler F., Maali A., Dreyer J., Hagley E., Raimond J. M. and Haroche S., *Phys. Rev. Lett.*, **76** (1996) 1800
https://link.aps.org/doi/10.1103/PhysRevLett.76.1800

[110] Turchette Q. A., Hood C. J., Lange W., Mabuchi H. and Kimble H. J., *Phys. Rev. Lett.*, **75** (1995) 4710
https://link.aps.org/doi/10.1103/PhysRevLett.75.4710

[111] Hagley E., Maître X., Nogues G., Wunderlich C., Brune M., Raimond J. M. and Haroche S., *Phys. Rev. Lett.*, **79** (1997) 1
https://link.aps.org/doi/10.1103/PhysRevLett.79.1

[112] Averin D. V. and Likharev K. K., *J. Low Temp. Phys.*, **62** (1986) 345
https://doi.org/10.1007/BF00683469

[113] Birnbaum K. M., Boca A., Miller R., Boozer A. D., Northup T. E. and Kimble H. J., *Nature*, **436** (2005) 87
https://doi.org/10.1038/nature03804

[114] Schmidt H. and Imamoglu A., *Opt. Lett.*, **21** (1996) 1936
http://ol.osa.org/abstract.cfm?URI=ol-21-23-1936

[115] Peyronel T., Firstenberg O., Liang Q.-Y., Hofferberth S., Gorshkov A. V., Pohl T., Lukin M. D. and Vuletić V., *Nature*, **488** (2012) 57
https://doi.org/10.1038/nature11361

[116] Firstenberg O., Peyronel T., Liang Q.-Y., Gorshkov A. V., Lukin M. D. and Vuletić V., *Nature*, **502** (2013) 71
https://doi.org/10.1038/nature12512

[117] Rossini D. and Fazio R., *Phys. Rev. Lett.*, **99** (2007) 186401
https://link.aps.org/doi/10.1103/PhysRevLett.99.186401

[118] Hafezi M., Adhikari P. and Taylor J. M., *Phys. Rev. B*, **92** (2015) 174305
https://link.aps.org/doi/10.1103/PhysRevB.92.174305

[119] Mering A., Fleischhauer M., Ivanov P. A. and Singer K., *Phys. Rev. A*, **80** (2009) 053821
https://link.aps.org/doi/10.1103/PhysRevA.80.053821

[120] Makin M. I., Cole J. H., Hill C. D., Greentree A. D. and Hollenberg L. C. L., *Phys. Rev. A*, **80** (2009) 043842
https://link.aps.org/doi/10.1103/PhysRevA.80.043842

[121] Pippan P., Evertz H. G. and Hohenadler M., *Phys. Rev. A*, **80** (2009) 033612
https://link.aps.org/doi/10.1103/PhysRevA.80.033612

[122] Chakrabarti R. and Sreekumari G., *J. Phys. B*, **44** (2011) 115505
http://stacks.iop.org/0953-4075/44/i=11/a=115505

[123] Huo M. X., Li Y., Song Z. and Sun C. P., *Phys. Rev. A*, **77** (2008) 022103
https://link.aps.org/doi/10.1103/PhysRevA.77.022103

[124] Irish E. K., *Phys. Rev. A*, **80** (2009) 043825
https://link.aps.org/doi/10.1103/PhysRevA.80.043825

[125] Hohenadler M., Aichhorn M., Schmidt S. and Pollet L., *Phys. Rev. A*, **84** (2011) 041608
https://link.aps.org/doi/10.1103/PhysRevA.84.041608

[126] Bose S., Angelakis D. G. and Burgarth D., *J. Mod. Optics*, **54** (2007) 2307.

[127] Hu F. M., Zhou L., Shi T. and Sun C. P., *Phys. Rev. A*, **76** (2007) 013819
https://link.aps.org/doi/10.1103/PhysRevA.76.013819

[128] Kapit E., *Phys. Rev. A*, **87** (2013) 062336
https://link.aps.org/doi/10.1103/PhysRevA.87.062336

[129] Basko D., Aleiner I. and Altshuler B., *Ann. Phys.*, **321** (2006) 1126
http://www.sciencedirect.com/science/article/pii/S0003491605002630

[130] Altman E. and Vosk R., *Annu. Rev. Condens. Matter Phys.*, **6** (2015) 383
https://doi.org/10.1146/annurev-conmatphys-031214-014701

[131] Yao N. Y., Laumann C. R., Gopalakrishnan S., Knap M., Müller M., Demler E. A. and Lukin M. D., *Phys. Rev. Lett.*, **113** (2014) 243002
https://link.aps.org/doi/10.1103/PhysRevLett.113.243002

[132] Pal A. and Huse D. A., *Phys. Rev. B*, **82** (2010) 174411
https://link.aps.org/doi/10.1103/PhysRevB.82.174411

[133] Chandran A., Khemani V., Laumann C. R. and Sondhi S. L., *Phys. Rev. B*, **89** (2014) 144201
https://link.aps.org/doi/10.1103/PhysRevB.89.144201

[134] Serbyn M., Knap M., Gopalakrishnan S., Papić Z., Yao N. Y., Laumann C. R., Abanin D. A., Lukin M. D. and Demler E. A., *Phys. Rev. Lett.*, **113** (2014) 147204
https://link.aps.org/doi/10.1103/PhysRevLett.113.147204

[135] Kjäll J. A., Bardarson J. H. and Pollmann F., *Phys. Rev. Lett.*, **113** (2014) 107204
https://link.aps.org/doi/10.1103/PhysRevLett.113.107204

[136] Serbyn M., Papić Z. and Abanin D. A., *Phys. Rev. X*, **5** (2015) 041047
https://link.aps.org/doi/10.1103/PhysRevX.5.041047

[137] Bahri Y., Vosk R., Altman E. and Vishwanath A., *Nat. Commun.*, **6** (2015) 7341
https://doi.org/10.1038/ncomms8341

[138] Imbrie J. Z., *Phys. Rev. Lett.*, **117** (2016) 027201
https://link.aps.org/doi/10.1103/PhysRevLett.117.027201

[139] Iemini F., Russomanno A., Rossini D., Scardicchio A. and Fazio R., *Phys. Rev. B*, **94** (2016) 214206
https://link.aps.org/doi/10.1103/PhysRevB.94.214206

[140] Schreiber M., Hodgman S. S., Bordia P., Lüschen H. P., Fischer M. H., Vosk R., Altman E., Schneider U. and Bloch I., *Science*, **349** (2015) 842
http://science.sciencemag.org/content/349/6250/842

[141] Kaufman A. M., Tai M. E., Lukin A., Rispoli M., Schittko R., Preiss P. M. and Greiner M., *Science*, **353** (2016) 794
http://science.sciencemag.org/content/353/6301/794

[142] Smith J., Lee A., Richerme P., Neyenhuis B., Hess P. W., Hauke P., Heyl M., Huse D. A. and Monroe C., *Nat. Phys.*, **12** (2016) 907
https://doi.org/10.1038/nphys3783

[143] Xu K., Chen J.-J., Zeng Y., Zhang Y.-R., Song C., Liu W., Guo Q., Zhang P., Xu D., Deng H., Huang K., Wang H., Zhu X., Zheng D. and Fan H., *Phys. Rev. Lett.*, **120** (2018) 050507
https://link.aps.org/doi/10.1103/PhysRevLett.120.050507

[144] Kraus Y. E., Lahini Y., Ringel Z., Verbin M. and Zilberberg O., *Phys. Rev. Lett.*, **109** (2012) 106402
http://link.aps.org/doi/10.1103/PhysRevLett.109.106402

[145] Hofstadter D. R., *Phys. Rev. B*, **14** (1976) 2239
https://link.aps.org/doi/10.1103/PhysRevB.14.2239

[146] Ponomarenko L. A., Gorbachev R. V., Yu G. L., Elias D. C., Jalil R., Patel A. A., Mishchenko A., Mayorov A. S., Woods C. R., Wallbank J. R., Mucha-Kruczynski M., Piot B. A., Potemski M., Grigorieva I. V., Novoselov K. S., Guinea F., Fal'ko V. I. and Geim A. K., *Nature*, **497** (2013) 594
https://doi.org/10.1038/nature12187

[147] Dean C. R., Wang L., Maher P., Forsythe C., Ghahari F., Gao Y., Katoch J., Ishigami M., Moon P., Koshino M., Taniguchi T., Watanabe K., Shepard K. L., Hone J. and Kim P., *Nature*, **497** (2013) 598
https://doi.org/10.1038/nature12186

[148] Hunt B., Sanchez-Yamagishi J. D., Young A. F., Yankowitz M., LeRoy B. J., Watanabe K., Taniguchi T., Moon P., Koshino M., Jarillo-Herrero P. and Ashoori R. C., *Science*, **340** (2013) 1427
http://science.sciencemag.org/content/340/6139/1427

[149] Miyake H., Siviloglou G. A., Kennedy C. J., Burton W. C. and Ketterle W., *Phys. Rev. Lett.*, **111** (2013) 185302
https://link.aps.org/doi/10.1103/PhysRevLett.111.185302

[150] Frahm K. M. and Shepelyansky D. L., *Eur. Phys. J. B*, **88** (2015) 337
https://doi.org/10.1140/epjb/e2015-60733-9

[151] Flach S., Ivanchenko M. and Khomeriki R., *EPL*, **98** (2012) 66002
http://stacks.iop.org/0295-5075/98/i=6/a=66002

[152] Oganesyan V. and Huse D. A., *Phys. Rev. B*, **75** (2007) 155111
https://link.aps.org/doi/10.1103/PhysRevB.75.155111

[153] Atas Y. Y., Bogomolny E., Giraud O. and Roux G., *Phys. Rev. Lett.*, **110** (2013) 084101
https://link.aps.org/doi/10.1103/PhysRevLett.110.084101

[154] Bohigas O., Giannoni M. J. and Schmit C., *Phys. Rev. Lett.*, **52** (1984) 1
https://link.aps.org/doi/10.1103/PhysRevLett.52.1

[155] Iyer S., Oganesyan V., Refael G. and Huse D. A., *Phys. Rev. B*, **87** (2013) 134202
https://link.aps.org/doi/10.1103/PhysRevB.87.134202

[156] De Roeck W., Huveneers F., Müller M. and Schiulaz M., *Phys. Rev. B*, **93** (2016) 014203
https://link.aps.org/doi/10.1103/PhysRevB.93.014203

[157] Grujic T., Clark S. R., Jaksch D. and Angelakis D. G., *New J. Phys.*, **14** (2012) 103025
http://stacks.iop.org/1367-2630/14/i=10/a=103025

[158] Joshi C., Nissen F. and Keeling J., *Phys. Rev. A*, **88** (2013) 063835
http://link.aps.org/doi/10.1103/PhysRevA.88.063835

[159] See T. F., Bastidas V. M., Tangpanitanon J. and Angelakis D. G., arXiv e-prints (Preprint 1807.07882) (2018).

[160] Tangpanitanon J., Clark S. R., Bastidas V. M., Fazio R., Jaksch D. and Angelakis D. G., arXiv e-prints arXiv:1806.10762 (Preprint 1806.10762).

[161] Ma R., Saxberg B., Owens C., Leung N., Lu Y., Simon J. and Schuster D. I., *Nature*, **566** (2019) 51
https://doi.org/10.1038/s41586-019-0897-9

[162] Mendoza-Arenas J. J., Clark S. R., Felicetti S., Romero G., Solano E., Angelakis D. G. and Jaksch D., *Phys. Rev. A*, **93** (2016) 023821
https://link.aps.org/doi/10.1103/PhysRevA.93.023821

[163] Josephson B., *Phys. Lett.*, **1** (1962) 251
http://www.sciencedirect.com/science/article/pii/0031916362913690

[164] Bouchiat V., Vion D., Joyez P., Esteve D. and Devoret M. H., *Phys. Scripta*, **1998** (1998) 165
http://stacks.iop.org/1402-4896/1998/i=T76/a=024

[165] Nakamura Y., Pashkin Y. A. and Tsai J. S., *Nature*, **398** (1999) 786
https://doi.org/10.1038/19718

[166] Devoret M. H., *Les Houches Session LXIII, Quantum Fluctuations* (Elsevier, Amsterdam) 1995, p. 351.

[167] Leib M., Deppe F., Marx A., Gross R. and Hartmann M. J., *New J. Phys.*, **14** (2012) 075024
http://stacks.iop.org/1367-2630/14/i=7/a=075024

[168] Mikhailov V. V., *J. Phys. A*, **18** (1985) 231
http://stacks.iop.org/0305-4470/18/i=2/a=012

[169] Houck A. A., Koch J., Devoret M. H., Girvin S. M. and Schoelkopf R. J., *Quantum Inf. Proc.*, **8** (2009) 105
https://doi.org/10.1007/s11128-009-0100-6

[170] Paik H., Schuster D. I., Bishop L. S., Kirchmair G., Catelani G., Sears A. P., Johnson B. R., Reagor M. J., Frunzio L., Glazman L. I., Girvin S. M., Devoret M. H. and Schoelkopf R. J., *Phys. Rev. Lett.*, **107** (2011) 240501
https://link.aps.org/doi/10.1103/PhysRevLett.107.240501

[171] Orlando T. P., Mooij J. E., Tian L., van der Wal C. H., Levitov L. S., Lloyd S. and Mazo J. J., *Phys. Rev. B*, **60** (1999) 15398
https://link.aps.org/doi/10.1103/PhysRevB.60.15398

[172] Friedman J. R., Patel V., Chen W., Tolpygo S. K. and Lukens J. E., *Nature*, **406** (2000) 43
https://doi.org/10.1038/35017505

[173] Martinis J. M., Nam S., Aumentado J. and Urbina C., *Phys. Rev. Lett.*, **89** (2002) 117901
https://link.aps.org/doi/10.1103/PhysRevLett.89.117901

[174] Martinis J. M., *Quantum Inf. Proc.*, **8** (2009) 81
https://doi.org/10.1007/s11128-009-0105-1

[175] van der Wal C. H., ter Haar A. C. J., Wilhelm F. K., Schouten R. N., Harmans
C. J. P. M., Orlando T. P., Lloyd S. and Mooij J. E., *Science*, **290** (2000) 773
http://science.sciencemag.org/content/290/5492/773

[176] Boixo S., Rønnow T. F., Isakov S. V., Wang Z., Wecker D., Lidar D. A.,
Martinis J. M. and Troyer M., *Nat. Phys.*, **10** (2014) 218
https://doi.org/10.1038/nphys2900

[177] Devoret M. H. and Schoelkopf R. J., *Science*, **339** (2013) 1169
http://science.sciencemag.org/content/339/6124/1169

[178] Neill C., Roushan P., Kechedzhi K., Boixo S., Isakov S. V., Smelyanskiy V.,
Megrant A., Chiaro B., Dunsworth A., Arya K., Barends R., Burkett B.,
Chen Y., Chen Z., Fowler A., Foxen B., Giustina M., Graff R., Jeffrey E.,
Huang T., Kelly J., Klimov P., Lucero E., Mutus J., Neeley M., Quintana C.,
Sank D., Vainsencher A., Wenner J., White T. C., Neven H. and Martinis J. M.,
Science, **360** (2018) 195
http://science.sciencemag.org/content/360/6385/195

[179] Sillanpaa M. A., Park J. I. and Simmonds R. W., *Nature*, **449** (2007) 438
https://doi.org/10.1038/nature06124

[180] Majer J., Chow J. M., Gambetta J. M., Koch J., Johnson B. R., Schreier J. A.,
Frunzio L., Schuster D. I., Houck A. A., Wallraff A., Blais A., Devoret M. H.,
Girvin S. M. and Schoelkopf R. J., *Nature*, **449** (2007) 443
https://doi.org/10.1038/nature06184

[181] Chen Y., Neill C., Roushan P., Leung N., Fang M., Barends R., Kelly J.,
Campbell B., Chen Z., Chiaro B., Dunsworth A., Jeffrey E., Megrant A.,
Mutus J. Y., O'Malley P. J. J., Quintana C. M., Sank D., Vainsencher A.,
Wenner J., White T. C., Geller M. R., Cleland A. N. and Martinis J. M., *Phys.
Rev. Lett.*, **113** (2014) 220502
https://link.aps.org/doi/10.1103/PhysRevLett.113.220502

[182] Geller M. R., Donate E., Chen Y., Fang M. T., Leung N., Neill C., Roushan
P. and Martinis J. M., *Phys. Rev. A*, **92** (2015) 012320
https://link.aps.org/doi/10.1103/PhysRevA.92.012320

[183] Kafri D., Quintana C., Chen Y., Shabani A., Martinis J. M. and Neven H., *Phys.
Rev. A*, **95** (2017) 052333
https://link.aps.org/doi/10.1103/PhysRevA.95.052333

[184] Koch J., Yu T. M., Gambetta J., Houck A. A., Schuster D. I., Majer J., Blais
A., Devoret M. H., Girvin S. M. and Schoelkopf R. J., *Phys. Rev. A*, **76** (2007)
042319
http://link.aps.org/doi/10.1103/PhysRevA.76.042319

[185] Nunnenkamp A., Koch J. and Girvin S. M., *New J. Phys.*, **13** (2011) 095008.

[186] Leib M., Deppe F., Marx A., Gross R. and Hartmann M. J., *New J. Phys.*, **14**
(2012) 075024
http://stacks.iop.org/1367-2630/14/i=7/a=075024

This page intentionally left blank

Nano-optomechanics

Ewold Verhagen(*)

Center for Nanophotonics, AMOLF - Science Park 104,
1098 XG Amsterdam, The Netherlands

Summary. — This tutorial presents a brief introduction to the physical principles
of cavity optomechanics. When light and mechanical motion are both confined in
nanoscale structures, they can effectively couple through radiation pressure. This
lecture discusses the quantum limits to optical measurement of mechanical motion
and the basic physics of optomechanical interactions between photons and phonons.
It reviews several recent developments in the field that exploit state transfer, break-
ing of time-reversal symmetry, and nonlinearities to develop new ways to control
both light and motion in the classical and quantum domains.

1. – Introduction: coupling light and motion

The field of *optomechanics* studies the interaction between light — or, more broadly,
electromagnetic fields — and the mechanical motion of objects. This interaction, me-
diated by optical radiation pressure forces, occurs naturally in systems where a me-
chanical deformation alters the optical response of the system. The mechanical motion
that is considered is typically that of high-quality mechanical resonators. Such devices
find application in various contexts, due to their high spectral purity and susceptibility

---

(*) E-mail: verhagen@amolf.nl

to tiny disturbances: in atomic-force microscopes, gravitational-wave detectors, time-keeping (*e.g.* quartz oscillators in wrist watches) and signal processing (*e.g.* filtering high-frequency electronic signals in modern cell phones).

Light provides excellent means to read out the motion of a mechanical resonator, due to the wide abundance of high-quality laser sources and photodetectors, and because it is a probe that introduces no more extra noise than fundamental quantum (shot) noise, even at room temperature. Optical detection of motion can happen in various ways: For example, by monitoring the phase of light reflected from a mirror that is free to move, or that of light passing through an optical fiber whose refractive index is locally changed due to strain associated with a deformation of the fiber.

Indeed, a plethora of systems has been developed in recent years in which optomechanical coupling is exploited, ranging from single nanoscale beads trapped in focused laser fields, through on-chip integrated devices, all the way to the km-scale interferometers that are used to detect gravitational waves. The scientific drive to develop those systems not only lies in advancing mechanical-sensing performance, but in particular also in the possibilities offered by optical forces. These principles allow new ways to control mechanical systems with light, *e.g.* to create special quantum states of motion. Optomechanical systems thus provide a test bed for quantum physics in massive mechanical systems, for example to study potential decoherence mechanisms acting on such "macroscopic" entities. The developed control methods allow adding mechanical resonators to the "quantum technology toolbox", leveraging their long lifetimes and capability to couple to a variety of other (quantum) systems. In fact, through such couplings one thus also gains new ways of optical control over other degrees of freedom *via* the mechanical resonator, including over light itself. The field of optomechanics thus studies a range of phenomena from both fundamental and technological standpoints, at the intersection of quantum optics, nano- and micro-electromechanical systems (NEMS/MEMS), and photonics. It draws inspiration from related developments for gravitational-wave detection, quantum information technology, and the control of cold ions and atoms with light fields.

To maximize optomechanical interactions, systems have been continuously improved along two lines: On the one hand, minimizing optical and mechanical losses — confining photons in optical cavities and phonons in mechanical resonators for the longest possible times — effectively increases their interaction. On the other hand, co-localizing light and motion in the smallest possible systems leads to large optomechanical coupling, as mechanical displacements yield larger effects on small optical cavities, and as low mass makes mechanical resonators more susceptible to optical forces. Thus, significant attention is given to *nano-optomechanical systems* that couple photons and phonons in small, on-chip architectures. In this lecture, we will introduce the basic physical description of optomechanical interactions at a tutorial level, and highlight several directions of current research. For a much more elaborate introduction to the field, including historical context, overviews of the studied systems, and in-depth theoretical descriptions, we refer the reader to several excellent other texts, including the review on "Cavity optomechanics" by M. Aspelmeyer, T. J. Kippenberg, and F. Marquardt [1], and the book "Quantum optomechanics" by W. P. Bowen and G. J. Milburn [2].
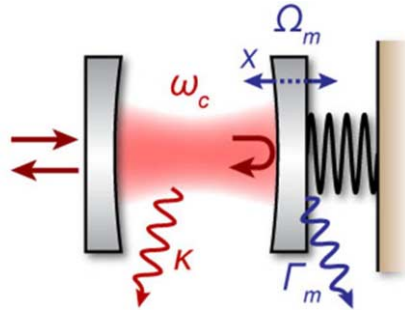
Fig. 1. – A typical cavity optomechanical system, with a cavity whose optical length (and thus its frequency ω_c) is subject to the harmonic motion x of a mechanical resonator with frequency Ω_m. Optical and mechanical damping rates are κ and Γ_m, respectively.

1˙1. *The canonical cavity optomechanical resonator*. – Although optomechanical systems take many forms, a simple model system serves to describe many of the observed phenomena in all of them. It is depicted in fig. 1 and comprises an optical cavity of which the length can change through the motion $x(t)$ of a mechanical resonator — in this picture formed by the mass of the end mirror, whose motion is harmonically constrained by a spring. We will briefly discuss the observable (classical) effects here, before turning to a quantum description. For now, we will consider only a single optical mode (and likewise, only a single mechanical mode). This is in many cases a valid approach, when the damping of individual modes is small enough such that their resonant responses are clearly separated in frequency, and a drive laser can be tuned to interact with effectively only one cavity mode.

The cavity resonance frequency $\omega_c/2\pi$ depends on the position x as

$$(1) \qquad \omega_c(x) = \omega_c + x\partial\omega_c/\partial x + \dots.$$

We define the frequency shift per displacement as $G = -\partial\omega_c/\partial x$, which can be shown to be ω_c/L for our model system, where L is the length of the Fabry-Pérot cavity. The cavity is driven by a laser through the partially transparent left mirror. This means that light must also be able to leak out of the cavity. The rate at which energy is lost from the cavity is $\kappa/2\pi$; it is equal to the spectral linewidth of the cavity's response. The mechanical oscillator has resonance frequency $\Omega_m/2\pi$, typically in the Hz to GHz range, and in any case much smaller than $\omega_c/2\pi$. The damping rate (linewidth) of the mechanical oscillator is $\Gamma_m/2\pi$. Several effects can be discerned:

- When the frequency of a laser impinging on the cavity is tuned across its resonance, the phase of the reflected light changes by 2π over a bandwidth of $\sim \kappa$. On resonance, this extra phase shift is π (as compared to an off-resonant laser). If the mechanical oscillator moves, the resulting change of the resonance frequency is imprinted as a phase change on the reflected light of monochromatic laser of fixed

frequency. The reflected phase is thus directly proportional to mirror displacement, and small motion can be read out with quantum-limited sensitivity, *e.g.* using homodyne interferometry.

- The light in the cavity exerts a radiation pressure force on the mechanical oscillator, which displaces it slightly in proportion to the laser power. But this changes the cavity length, and thus the cavity's optical response. As such, the optomechanical interaction can be seen as an effective optical (χ_3) nonlinearity. Moreover, as the force strongly depends on the oscillator position (for some given laser frequency), it effectively alters the restoring force that the mechanical oscillator feels, leading to "softening" or "stiffening" and an associated change of the mechanical resonance frequency (the "optical spring" effect).

- If the laser is slightly detuned from the cavity resonance, a mechanical position change will lead to a change of the light intensity in the cavity. But because of the finite response time of the cavity (given by $1/\kappa$) this change will not be instantaneous. As a result, the force on the oscillator will change — with some delay — upon a change of oscillator position. Depending on the conditions, this can lead to "automatic" *damping* or *amplification* of the oscillator's motion. These effects, summarized under the term *dynamical backaction*, are especially pronounced in systems with small optical damping κ and small mechanical damping Γ_{m}. They are at the basis of optical cooling of the mechanical resonator, for example.

In the following, we will first discuss how quantum mechanics limits the accuracy with which the mechanical motion can be measured. We will then introduce a quantum optical description of the system, and use it to describe radiation pressure effects. We will in particular discuss optical cooling and state transfer. We conclude with reviewing several research activities that exploit multimode optomechanical systems and nonlinearities to develop new ways to control light and motion in the classical and quantum domains.

2. – Quantum measurements of motion with light

2˙1. *Measuring motion with a cavity*. – The position of the mirror in fig. 1 determines the cavity frequency, and through that the phase of an intracavity field. This, in turn, can be detected by monitoring the light leaking out of the cavity. For a laser tuned to resonance, a small displacement δx imparts a phase shift

$$(2) \qquad\qquad \delta\phi = 4\frac{G}{\kappa}\delta x$$

on the outgoing laser beam. One can see the effect of cavity enhancement by comparing this shift to the $4\pi\delta x/\lambda$ phase shift that a light beam acquires by direct reflection off of a single mirror: For the Fabry-Pérot cavity, the phase shift per unit displacement is enhanced by a factor $2c/L\kappa$, which is equal to the cavity *Finesse* (the number of roundtrips light can make in the cavity before it decays) multiplied by a factor $2/\pi$.
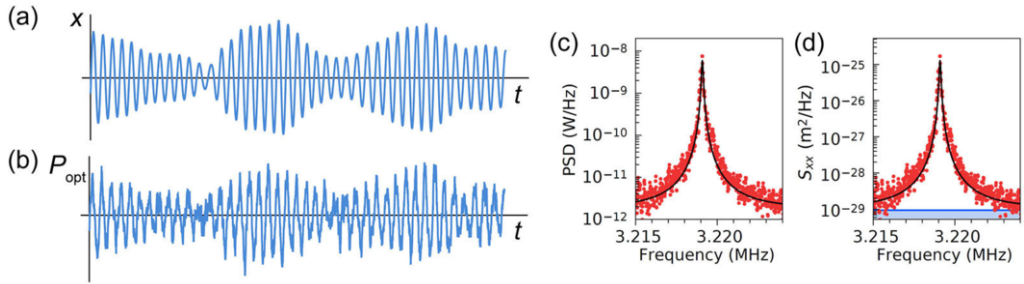
Fig. 2. – (a) The amplitude and phase of the mechanical resonator's oscillations are fluctuating at a typical time scale $1/\Gamma_m$ due to Brownian motion and quantum fluctuations. (b) A measurement of $x(t)$ through detecting optical power fluctuations P_{opt} will add imprecision noise. (c) Fourier-transforming the measured fluctuations using an electronic spectrum analyzer to show the electronic power spectral density (PSD) reveals the Lorentzian mechanical resonance with linewidth Γ_m. (d) With the equipartition theorem, the spectrum can be calibrated to yield the displacement spectral density S_{xx}. The constant background (blue) is the measurement imprecision.

2˙2. Mechanical frequency response. – So what is the motion that one typically wants to detect? A mechanical resonator is of course most likely to oscillate with a frequency near its natural resonance frequency. There, its susceptibility to external forces is highest. This susceptibility $\chi(\omega)$ specifies the displacement $x = \Re\{\tilde{x}\}$ induced by a harmonic force $\Re\{\tilde{F}_0 e^{-i\omega t}\}$ with frequency ω and (complex) amplitude $\tilde{F}_0$ through

$$\tag{3} \tilde{x}(t) = \tilde{x}_0 e^{-i\omega t} = \chi(\omega)\tilde{F}_0 e^{-i\omega t}.$$

Note that we have introduced complex representations $\tilde{x}$ and $\tilde{F}$ of position and force, respectively, for mathematical convenience. The susceptibility is that of a damped harmonic oscillator and reads

$$\tag{4} \chi(\omega) = \frac{1}{m}\frac{1}{\Omega_m^2 - \omega^2 - i\Gamma_m\omega},$$

where m is the mass of the mechanical resonator. Near resonance of a high-Q resonator, it can be approximated as a Lorentzian response:

$$\tag{5} \chi(\omega) \approx \frac{i}{2m\Omega_m}\frac{1}{-i(\omega - \Omega_m) + \Gamma_m/2}.$$

2˙3. Mechanical fluctuation spectra and sidebands. – This sharply-peaked susceptibility thus also determines the spectrum of *fluctuations* that the resonator exhibits when it is driven by a stochastic force that itself has a relatively flat spectrum. These can be both vacuum fluctuations, giving rise to zero-point motion, or thermal noise leaking into the resonator from its environment at elevated temperatures, giving rise to Brownian

motion. The fluctuations are spread over a bandwidth $\sim \Gamma_{\mathrm{m}}$ around the mechanical frequency. It causes the mechanical resonator's amplitude and phase to vary randomly within a typical time scale $1/\Gamma_{\mathrm{m}}$ (see example in fig. 2(a)). By measuring the phase fluctuations of the optical output field, one gains a record of the mechanical fluctuations $x(t)$. The fluctuation spectrum can then be obtained through a Fourier transform. We define a "gated" Fourier transform for a single record of measurement duration τ as [3]

$$(6) \qquad x_\tau(\omega) = \frac{1}{\sqrt{\tau}} \int_{-\tau/2}^{\tau/2} \mathrm{d}t e^{\mathrm{i}\omega t} x(t).$$

Averaging many such measurements yields a smooth noise power spectrum $\langle |x_\tau(\omega)|^2 \rangle$, which approximates the *noise spectral density* $S_{xx}(\omega)$ as

$$(7) \qquad \lim_{\tau \to \infty} \langle |x_\tau(\omega)|^2 \rangle = S_{xx}(\omega).$$

This is the so-called Wiener-Khinchin theorem, which relates measurable noise spectra to the Fourier transform of the autocorrelation function of $x(t)$, which is the formal definition of $S_{xx}(\omega)$ [3].

The total size of the fluctuations is determined by the equipartition theorem, *i.e.* $m\Omega_{\mathrm{m}}^2 \langle x^2 \rangle / 2 = k_B T/2$ in the limit of large temperature T, where k_B is the Boltzmann constant. For negligible temperature, only vacuum fluctuations remain, with $\langle x^2 \rangle = x_{\mathrm{zpf}}^2$ and

$$(8) \qquad x_{\mathrm{zpf}} = \sqrt{\frac{\hbar}{2m\Omega_{\mathrm{m}}}} .$$

When one measures these fluctuations at frequency Ω_{m}, for example using an electronic spectrum analyser that analyses the detected photocurrent of a detector in the output of an interferometer (see fig. 2(c)), one is essentially probing the beat of an optical field at the input laser frequency ω_{l} and that of *optical sidebands* at frequencies $\omega_{\mathrm{l}} \pm \Omega_{\mathrm{m}}$. The fact that the mechanical motion induces such optical sidebands is entirely equivalent to Stokes and anti-Stokes Raman scattering, which produces down- or upconverted photons by giving off or taking up a quantum of energy (phonon) from a mechanical resonator. This notion is very useful, for example to distinguish quantum from classical (thermal) fluctuations: If a mechanical resonator is in its ground state, it is incapable of providing energy to upconvert a photon to higher energy. Thus, the fluctuation spectrum is necessarily asymmetric. This asymmetry can be shown to be a direct consequence of the commutation relations and can be observed *e.g.* by distinguishing Stokes and anti-Stokes photons through judicious spectral filtering. Indeed, such tests of *sideband asymmetry* are now standard ways to determine that a resonator has been prepared in its ground state [4].

2˙4. *Imprecision and backaction; the Standard Quantum Limit*. – What is the smallest motion that can be resolved? In order to evaluate sensitivity, we need to consider the *noise added by the measurement*. A practical measurement of $x(t)$ suffers from noise, such that a recorded trace looks more like fig. 2(b). As a result, the observed noise spectral densities are larger than the actual fluctuations in the absence of a measurement. Even if one works hard to remove all sources of technical noise, one is left with unavoidable quantum uncertainty, related to the fact that 1) the probe — light in this case — suffers from quantum uncertainty, and 2) measurements tend to act back on the object under study. Here we will qualitatively discuss these two factors and show how they are related.

On the one hand, the shot noise of the light carrying the measured signal to the detector will produce fluctuations of the detected photocurrent. This produces a white (frequency-independent) noise "background" in the spectra of $S_{xx}(\omega)$ that we derive from the measurement, which is called the *measurement imprecision* (fig. 2(d)). Since the amount of shot noise (as apparent on the photocurrent spectral density) scales linearly with the light intensity and the signal we seek to detect quadratically, the measurement imprecision (expressed as apparent displacement fluctuations $S_{xx}(\omega)$) reduces when we increase the laser power. In other words, we can detect phase fluctuations more accurately if we use a larger number of photons; a direct consequence of the number-phase uncertainty relationship.

However, this reduction of the measurement imprecision with increasing laser power does not come without a price. For large enough power, the shot noise of the light in the cavity starts to significantly affect the mechanical oscillator by exerting a stochastic radiation pressure force. This *measurement backaction* causes extra mechanical fluctuations $S_{xx}^{\mathrm{ba}}(\omega) = |\chi_{\mathrm{m}}(\omega)|^2 S_{FF}^{\mathrm{ba}}(\omega)$, where $S_{FF}^{\mathrm{ba}}(\omega)$ is the spectral density of the radiation pressure force fluctuations. If the cavity lifetime is shorter than the mechanical period, $S_{FF}^{\mathrm{ba}}(\omega)$ can be considered to be white noise (flat spectrum), as it originates in delta-correlated shot noise. It scales linearly with optical power, *increasing* fluctuations of the mechanical resonator even if the imprecision goes down. The total noise added by the measurement, $S_{xx}^{\mathrm{add}} = S_{xx}^{\mathrm{imp}} + S_{xx}^{\mathrm{ba}}$, evaluated at the resonance frequency of the mechanical oscillator, has a minimum for a certain optical power. This is called the *Standard Quantum Limit* (SQL). Figure 3 shows the different contributions to the noise spectra for varying probe power. It can be shown that the minimum noise is precisely equal to the spectral density of the zero-point fluctuations,

$$(9) \qquad \bar{S}_{xx}^{\mathrm{add}}(\Omega_{\mathrm{m}}) \leq \bar{S}_{xx}^{\mathrm{zpf}}(\Omega_{\mathrm{m}}) = 2\frac{x_{\mathrm{zpf}}^2}{\Gamma_{\mathrm{m}}} = \frac{\hbar}{m\Omega_{\mathrm{m}}\Gamma_{\mathrm{m}}} \,.$$

Here, the horizontal bars denote that we are comparing "symmetrized" spectral densities, averaged over positive and negative frequencies:

$$(10) \qquad \bar{S}_{xx}(\omega) \equiv \left(S_{xx}(\omega) + S_{xx}(-\omega)\right)/2.$$

The appearance of the SQL is directly related to Heisenberg's uncertainty principle. As we are continuously monitoring the trajectory $x(t)$ in time, we gain knowledge about
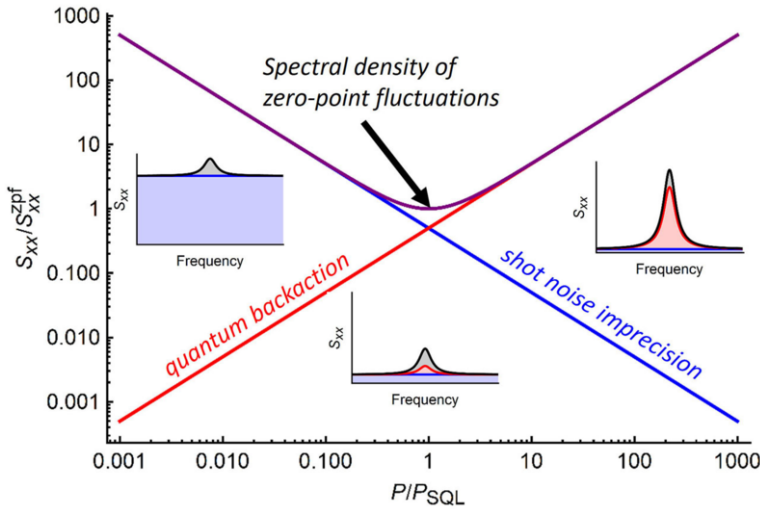
Fig. 3. – Total displacement noise added by a measurement (purple) as a function of laser power. It is a combination of imprecision (blue) and backaction (red). Insets depict the measured spectra in three power regimes, when measuring zero-point fluctuations (grey).

the oscillator's position *and* momentum. The uncertainty principle of course forbids to do this with arbitrary accuracy on both degrees of freedom. However, several clever measurement schemes exist to reduce the noise on the measurement of one of the quadratures of motion (so-called "back-action evading" measurements) [5-7]. These include the possibility to take pulsed, "snap-shot" measurements of displacement — which naturally gain no information on momentum — and also provide routes to creating squeezed states of the mechanical resonator, which exhibit reduced fluctuations in one of its quadratures [8-10]. Moreover, squeezed light can be used to shift the SQL to a different power for a chosen range of frequencies. Such methods are crucial to the working of the next-generation gravitational-wave detectors, which will operate at conditions close to the quantum limit [11].

We note that many optomechanical systems can now operate at measurement strengths way beyond the standard quantum limit power P_{SQL}. That does not automatically mean that radiation-pressure-induced fluctuations dominate the resonator's motion: After all, since for most systems $k_B T \gg \hbar \Omega_{\mathrm{m}}$, thermal fluctuations typically dwarf quantum motion. However, several optomechanical experiments achieved the regime where quantum backaction induces fluctuations of comparable size to thermal motion [12-14].

3. – A quantum optical description of cavity optomechanics

3`1. *The optomechanical Hamiltonian*. – In the preceding section, we already recognized the (back)action of optical forces in optomechanical systems. The interactions mediated by these forces lead to rich behaviour. To introduce this, we will now discuss

the basic cavity optomechanical system in terms of the annihilation operators $\hat{a}$ and $\hat{b}$ of the optical cavity and mechanical resonator modes, respectively. The Hamiltonian of the combined oscillators can be written as

$$(11) \qquad \hat{H} = \hbar\omega_{\rm c}(\hat{x})\hat{a}^\dagger\hat{a} + \hbar\Omega_{\rm m}\hat{b}^\dagger\hat{b} = \hbar\omega_{\rm c}\hat{a}^\dagger\hat{a} + \hbar\Omega_{\rm m}\hat{b}^\dagger\hat{b} - \hbar G\hat{x}\hat{a}^\dagger\hat{a},$$

where we recognized that the optical frequency depends linearly on the position $\hat{x}$ as $\omega_{\rm c}(\hat{x}) = \omega_{\rm c} - G\hat{x}$. We choose the origin of x such that the mean position $\bar{x} = \langle\hat{x}\rangle = 0$. From the interaction term on the right, we immediately recognize the radiation pressure force

$$(12) \qquad F_{\rm rp} = \hbar G\hat{a}^\dagger\hat{a}.$$

Since $\hat{x}$ can be expressed in terms of the phonon ladder operators as $\hat{x} = x_{\rm zpf}(\hat{b} + \hat{b}^\dagger)$, we can write the cavity optomechanical Hamiltonian as

$$(13) \qquad \hat{H} = \hbar\omega_{\rm c}\hat{a}^\dagger\hat{a} + \hbar\Omega_{\rm m}\hat{b}^\dagger\hat{b} - \hbar g_0\hat{a}^\dagger\hat{a}(\hat{b} + \hat{b}^\dagger),$$

where we have introduced the *vacuum optomechanical coupling rate* $g_0 = Gx_{\rm zpf}$. This parameter signifies the optical frequency shift for a displacement by the size of the quantum ground state, and is a general measure of photon-phonon coupling strength, ignorant of *e.g.* the arbitrariness in defining x. Significant advances have been made towards optimizing this parameter, especially in nanoscale devices. In electromechanical systems, mechanical motion is coupled to the GHz-frequency electromagnetic modes of on-chip superconducting LC-resonators. Especially large coupling strengths are obtained by letting the motion of thin micron-scale aluminum drums affect the capacitance across a gap of few tens of nm [15]. Largest coupling strength are achieved in nanophotonic systems, such as high-index ring resonators where light is coupled to breathing motion of the ring [16], and especially photonic crystal cavities [17-21]. There, light trapped in nanobeam cavities within wavelength-scale mode volumes interacts with localized mechanical vibrations, either flexural beam vibrations at MHz frequencies or breathing motion of the beam at GHz frequencies. In such systems, coupling rates $g_0/2\pi$ up to a few tens of MHz have been achieved [22]. Optomechanical shifts are optimized through design, and originate in the movement of dielectric boundaries near large field concentrations (akin to an optical gradient force) [23] or in strain-induced changes of the refractive index (electrostriction) [24].

3˙2. The linearized Hamiltonian. – Interestingly, the interaction term in Hamiltonian (13) is cleary nonlinear; it contains products of more than two operators. This in principle can lead to very interesting quantum behaviour, including the generation of nonclassical states of motion and light and single-quantum interactions [25, 26]. This nonlinearity can be seen, for example, in a simple thought experiment: A photon entering the cavity on resonance exerts a force, displacing the resonator. This, in turn, shifts the cavity frequency such that a second photon of the same frequency can no longer enter the

cavity, establishing a form of single-photon blockade. However, for any such effect to be observable, the cavity linewidth — which the Hamiltonian ignored — should be smaller than the mechanical frequency and the photon-phonon coupling rate; $g_0 > \Omega_{\mathrm{m}} > \kappa$. This is so far out of reach for solid-state optomechanical systems, by about two orders of magnitude.

While it is conceivable that the single-quantum nonlinear regime of optomechanics is reached in the future, a great degree of quantum control is still achievable for interaction strengths reachable today, by enhancing the interaction through suitable laser drive fields [1, 2]. To see how this comes about, we first transform the Hamiltonian (13) to a frame rotating at the laser frequency ω_{l}. A transformation is performed through a unitary operator $\hat{U}$, which changes the Hamiltonian $\hat{H}$ as

$$(14) \qquad \hat{H} \rightarrow \hat{U}\hat{H}\hat{U}^{\dagger} - \hat{U}\mathrm{i}\hbar\partial\hat{U}^{\dagger}/\partial t.$$

To shift to a rotating frame, we take $\hat{U} = \exp(\mathrm{i}\omega_{\mathrm{l}}\hat{a}^{\dagger}\hat{a}t)$[1], to arrive at

$$(15) \qquad \hat{H} = -\hbar\Delta\hat{a}^{\dagger}\hat{a} + \hbar\Omega_{\mathrm{m}}\hat{b}^{\dagger}\hat{b} - \hbar g_0\hat{a}^{\dagger}\hat{a}(\hat{b} + \hat{b}^{\dagger}),$$

where we introduced the *laser detuning* $\Delta \equiv \omega_{\mathrm{l}} - \omega_{\mathrm{c}}$. We note that in the Heisenberg picture, this Hamiltonian now describes the evolution of slowly varying operators $\hat{a}$ (analogous to the light field in the cavity), etc.

We now consider that the cavity is driven by a coherent laser to large amplitude. It then makes sense to write $\hat{a} = \alpha + \delta\hat{a}$, where $\alpha \equiv \langle\hat{a}\rangle = \sqrt{\bar{n}_c}$ is the (complex) amplitude of the light field in the cavity expressed as the square root of the mean number of photons $\bar{n}_c$, and all fluctuations of the optical field are contained in $\delta\hat{a}$. Thus, when expanding the photon number, we get

$$(16) \qquad \hat{a}^{\dagger}\hat{a} = |\alpha|^2 + \alpha^*\delta\hat{a} + \alpha\delta\hat{a}^{\dagger} + \delta\hat{a}^{\dagger}\delta\hat{a}.$$

We now insert this in eq. (15) and neglect all terms with $\delta\hat{a}^{\dagger}\delta\hat{a}$ assuming large drive $|\alpha| \gg 1$. The interaction part of the Hamiltonian (last term in eq. (15)) then reads

$$(17) \qquad \hat{H}_{\mathrm{int}} \approx -\hbar g_0|\alpha|^2(\hat{b} + \hat{b}^{\dagger}) - \hbar g_0(\alpha^*\delta\hat{a} + \alpha\delta\hat{a}^{\dagger})(\hat{b} + \hat{b}^{\dagger}).$$

The first term corresponds to a constant shift of the mechanical displacement due to the radiation pressure of the classical drive field. We can omit it by implementing an appropriate shift of the displacement's origin and then in the following always use a new detuning with respect to the (shifted) cavity resonance $\Delta \rightarrow \Delta - 2g_0^2|\alpha|^2/\Omega_{\mathrm{m}}$. Moreover, for a single optical mode we can always choose an appropriate gauge of intracavity phase such that α is real. The interaction then becomes

$$(18) \qquad \hat{H}_{\mathrm{int}} \approx -\hbar g(\delta\hat{a} + \delta\hat{a}^{\dagger})(\hat{b} + \hat{b}^{\dagger}).$$

---

[1] For this transformation, $\hat{U}\hat{a}\hat{U}^{\dagger} = e^{-\mathrm{i}\omega_{\mathrm{l}}t}\hat{a}$, $\hat{U}\hat{a}^{\dagger}\hat{U}^{\dagger} = e^{\mathrm{i}\omega_{\mathrm{l}}t}\hat{a}^{\dagger}$, and $\hat{U}\mathrm{i}\hbar\partial\hat{U}^{\dagger}/\partial t = \hbar\omega_{\mathrm{l}}\hat{a}^{\dagger}\hat{a}$.

Here we have introduced the *linearized coupling rate* $g = g_0\alpha$. This Hamiltonian describes two *linearly coupled harmonic oscillators* at resonance frequencies $-\Delta$ and Ω_{m}, coupled at a rate g that is controllable with the external laser drive. Note that the optical-cavity mode $\delta\hat{a}$ is the displaced field, describing the *fluctuations* of the light field, *i.e.* the photons in sidebands of the drive field α. All dynamics of the system can be deduced from the full Hamiltonian, by retrieving the evolution of an operator $\hat{A}$ in the Heisenberg picture through $\dot{\hat{A}} = \frac{\mathrm{i}}{\hbar}[\hat{H}, \hat{A}]$ [1].

This interaction Hamiltonian describes many phenomena in optomechanics: it shows how mechanical position fluctuations $(\hat{b} + \hat{b}^\dagger)$ are transduced to the optical phase quadrature $(\delta\hat{a} + \delta\hat{a}^\dagger)$ to facilitate motion measurement. And just like in classical coupled oscillators, or atom-light coupling in cavity QED, we can distinguish weak- and strong-coupling regimes when $2g < \{\kappa, \Gamma_{\mathrm{m}}\}$ and $2g > \{\kappa, \Gamma_{\mathrm{m}}\}$, respectively. In the strong-coupling regime, fluctuation spectra display normal mode splitting and Rabi oscillations between photons and phonons occur [27, 28, 15, 29]. In the weak-coupling regime, the optical cavity (plus the bath it decays to) can be considered to influence the decay rate of the mechanical resonator in processes analogous to the Purcell effect in cavity QED. This is in fact the source of optical cooling and amplification, effects known as dynamical backaction [1, 30, 31].

4. – Optomechanical cooling and state transfer

4˙1. *The resolved sideband regime*. – If the optical (and mechanical) damping is smaller than the mechanical frequency, the two oscillators are only coupled efficiently when they are tuned to resonance, *i.e.* for $\Delta \approx \pm\Omega_{\mathrm{m}}$. To see what effect this has, we first shift to an interaction picture by applying a new unitary (rotating frame) transformation

$$(19) \qquad \hat{U} = e^{-\mathrm{i}\Delta\delta\hat{a}^\dagger\delta\hat{a}t + \mathrm{i}\Omega_{\mathrm{m}}\hat{b}^\dagger\hat{b}t},$$

such that the Hamiltonian becomes

$$(20) \qquad \hat{H}_{\mathrm{int}} = -\hbar g \left(\delta\hat{a}\hat{b}^\dagger e^{\mathrm{i}(\Delta+\Omega_{\mathrm{m}})t} + \delta\hat{a}^\dagger\hat{b}e^{-\mathrm{i}(\Delta+\Omega_{\mathrm{m}})t} + \delta\hat{a}\hat{b}e^{\mathrm{i}(\Delta-\Omega_{\mathrm{m}})t} + \delta\hat{a}^\dagger\hat{b}^\dagger e^{-\mathrm{i}(\Delta-\Omega_{\mathrm{m}})t} \right).$$

Provided that $(\kappa, \Gamma_{\mathrm{m}}) < \Omega_{\mathrm{m}}$, the so-called *resolved sideband regime*, and likewise $g < \Omega_{\mathrm{m}}$, we can apply the *rotating wave transformation* to neglect some terms in the above Hamiltonian. In particular, if the laser is detuned to the red mechanical sideband of the cavity ($\Delta = -\Omega_{\mathrm{m}}$), we can neglect the last two terms in the interaction Hamiltonian on the basis that they are oscillating very fast (at $\pm 2\Omega_{\mathrm{m}}$) compared to the slowly varying (resonant) first two terms and the cavity dynamics. For that detuning,

$$(21) \qquad \hat{H}_{\mathrm{int}} = -\hbar g(\delta\hat{a}^\dagger\hat{b} + \delta\hat{a}\hat{b}^\dagger).$$

The evolution that this "beam-splitter" Hamiltonian describes corresponds to a continuous swapping of the states between the optical and mechanical degrees of freedom at a
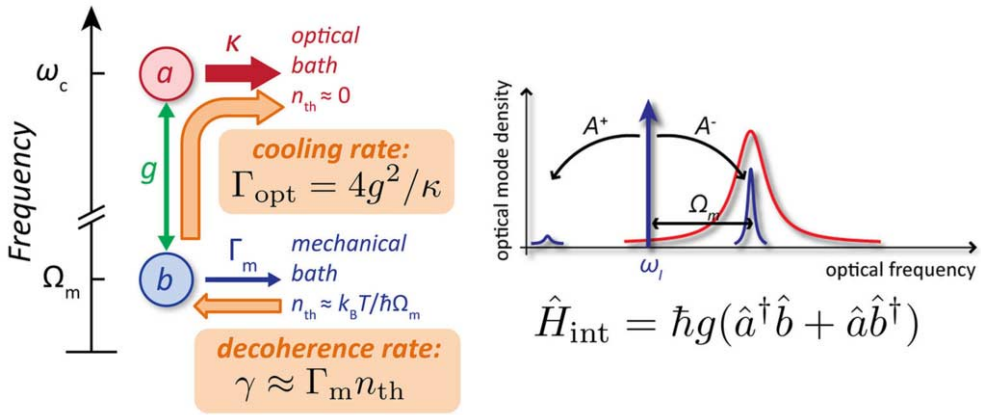
Fig. 4. – Left: Schematic of optical cooling as a competition between different environments. The mechanical resonator "b" is coupled at rate g to an optical mode a. Decay to the optical bath thus competes with the intrinsic mechanical bath, characterized by a much larger thermal occupancy n_{th}. Thus, thermomechanical fluctuations entering the mechanical mode at rate γ can be quickly dissipated in the optical bath, which is carrying no more than quantum fluctuations, leading to a net cooling of the mechanical oscillator. Right: The cooling can be seen as a cavity enhancement of anti-Stokes scattering processes A^-. In the resolved sideband regime $\Omega_{\text{m}} > \kappa$ the Stokes scattering A^+ is sufficiently suppressed to not imprint excess backaction fluctuations.

rate $2g$. It thus enables *state transfer* between the optical and mechanical modes. For a coherent drive, the optical field $\delta\hat{a}$ corresponds to the vacuum, such that transfer of this state to the mechanical mode naturally cools it. This is the principle of *resolved sideband cooling* [32, 33].

For blue detuning ($\Delta = \Omega_{\text{m}}$), a similar argument selects the last two terms:

$$(22) \qquad \hat{H}_{\text{int}} = -\hbar g(\delta\hat{a}^\dagger\hat{b}^\dagger + \delta\hat{a}\hat{b}).$$

With this "two-mode squeezing" Hamiltonian, the simultaneous creation of a photon and a phonon can lead to entanglement between the light field and the mechanical motion, as well as the aforementioned amplification and self-oscillations.

4`2. *Cooling rate and engineered reservoir*. – Particular attention has been given to optomechanical cooling, as it provides a way to prepare macroscopic resonators, which normally suffer from significant thermal fluctuations, to their quantum ground state [32, 33]. Laser cooling happens most effectively in the weak-coupling regime at detuning $\Delta = -\Omega_{\text{m}}$, where the state transfer Hamiltonian (21) applies. Without cooling, a mechanical resonator in equilibrium with a bath at temperature T, to which it is coupled with rate Γ_{m}, is typically in a large thermal state with mean phonon occupation $\bar{n}_{\text{th}} = k_{\text{B}}T/\hbar\Omega_{\text{m}}$. The cooling process can be pictured hand-wavingly as follows: under the influence of the interaction, the displaced optical field $\delta\hat{a}$ is swapped to the mechanical resonator,

bringing it to its ground state. In turn, the thermal phonons are swapped to the optical mode, from which they rapidly dissipate in the cold bath that the optical mode is coupled to with decay rate κ. Thus, the optical cavity provides a path of decay for the mechanical resonator, in addition to the intrinsic mechanical decay Γ_m (see fig. 4). It introduces a reservoir to the mechanical resonator that is intrinsically cold. The rate of decay via the cavity is

$$(23) \qquad\qquad \Gamma_\mathrm{opt} = \frac{4g^2}{\kappa} \,.$$

Provided that the total mechanical damping rate $\Gamma_\mathrm{eff} = \Gamma_\mathrm{opt} + \Gamma_\mathrm{m}$ remains smaller than the cavity decay rate κ, the cooling rate can be increased by ramping up the laser intensity. When the red-detuned cooling laser is applied, the total damping rate of the resonator changes to $\Gamma_\mathrm{eff} = \Gamma_\mathrm{opt} + \Gamma_\mathrm{m}$, and the fluctuations are reduced. In a classical theory, the effective temperature of the mechanical mode could go to zero, according to $T_\mathrm{eff} = T\Gamma_\mathrm{m}/\Gamma_\mathrm{eff}$. This is however only true for narrow-linewidth cavities, such that Stokes processes, described by the interaction terms in eq. (22), are suppressed. If not, these interactions — which are essentially the aforementioned quantum backaction — add more phonons to the resonator than can be cooled. It can be shown that the minimum achievable phonon number (in the limit of large laser power) is $\bar{n}_\mathrm{min} = (\kappa/4\Omega_\mathrm{m})^2$ [32,33].

In conclusion, in the resolved sideband regime the phonon number can become smaller than 1 and the system can be cooled close to the mechanical ground state. This has been achieved in 2011 for the first time at NIST in a nanoscale electromechanical system, and since then reached in various other systems [34-36].

5. – Controlling photons and phonons

The above dynamics reveal a glimpse into the effects that are studied in optomechanics research which is by no means exhaustive. The interactions in these relatively simple systems have sparked a wide variety of pursuits towards controlling both photons and phonons in new ways, in both quantum and classical contexts. The latter includes applications within time-keeping and signal synthesis and processing that exploit the generation of narrow-band mechanical oscillations. Indeed, in the standard optomechanical system a blue-detuned laser drive induces mechanical amplification through dynamical backaction, *i.e.*, enhancement of the Stokes scattering process. For high enough optical power, this negative Γ_opt overcomes intrinsic dissipation, resulting in a net mechanical gain. Laser powers above this parametric instability threshold thus drive the mechanical resonator into a regime of large self-oscillations reminiscent of lasing behaviour. The amplitude of these oscillations is limited through nonlinear effects.

$5^.1$. *Optomechanically-induced transparency and cooperativity*. – Moreover, the coupling between optical and mechanical modes, induced by a detuned drive laser, also provides a way to control the propagation of optical signals. An example is the effect of optomechanically-induced transparency (OMIT): If a cavity is critically coupled to an

input/output channel, an optical "probe" laser field tuned to cavity resonance ω_c is normally absorbed. But in the presence of a red-detuned drive at $\omega_c - \Omega_m$, the beat of drive and probe can resonantly induce mechanical vibrations. These in turn stimulate the creation of a modulation sideband of the drive laser at ω_c — which can destructively interfere with the probe field in the cavity. The result is a narrow frequency window of finite optical transparency. In essence, the two-way optomechanical coupling described by eq. (21) provides an extra path photon-phonon-photon that excitations can take in the system, and that can interfere with other paths. Similar effects of optomechanically-induced absorption and amplification arise in the red-detuned regime due to the interaction in eq. (22).

The OMIT window can be controlled by the drive laser, and leads to near-ideal transmission at high drive power. The transparency becomes significant (exceeding 1/4) if the so-called optomechanical *cooperativity* C exceeds unity. The cooperativity is defined as

$$(24) \qquad\qquad\qquad C = \frac{4g^2}{\kappa \Gamma_m} \,.$$

This quantity, which combines coupling strength and dissipation, describes the strength of many other optomechanical effects as well. For example, the condition $C = 1$ also defines the optical field strength at which the standard quantum limit is reached.

A related quantity of importance is the *quantum cooperativity* $C_q = C/\bar{n}_{th}$, which is effectively the cooperativity with mechanical dissipation rate replaced by thermal decoherence rate $\gamma = \Gamma_m \bar{n}_{th}$. Reaching $C_q > 1$ is a general condition for achieving optomechanical control in the quantum regime: It enables laser cooling to thermal occupancies below 1 (either through sideband or active feedback cooling) [34, 35, 14], the observation of radiation pressure shot noise at equal level as thermal fluctuations [12], effects such as optical and mechanical quantum squeezing [37, 38], quantum-coherent transfer of signals [29, 39], etc.

5`2. *Beyond single-mode interactions.* – A wide array of possibilities emerges when extending optomechanical systems beyond the single optical and single mechanical modes that compose the model system we discussed so far. For example, if two mechanical modes are both coupled to a single optical-cavity mode, as depicted in fig. 5(a), a laser field can lead to mechanical coupling: If the laser is detuned from cavity resonance, the motion of one resonator will lead to a change of the intracavity photon number and thus a change of the force on the other resonator, and vice versa. The condition for strong mechanical coupling is $C > 1$ [40], and if the coupling exceeds decoherence (for $C_q > 1$), the light field entangles the mechanical resonators [41]. Moreover, when combined with self-oscillation and mechanical amplification, such systems allow the control and study of synchronization of (nano)mechanical oscillators [42-44].

Conversely, if two optical modes are coupled to a single mechanical mode, as depicted in fig. 5(b), optical control fields can stimulate coupling of the two optical modes *via* the mechanical resonator. The state-transfer Hamiltonian (21) can be straightforwardly
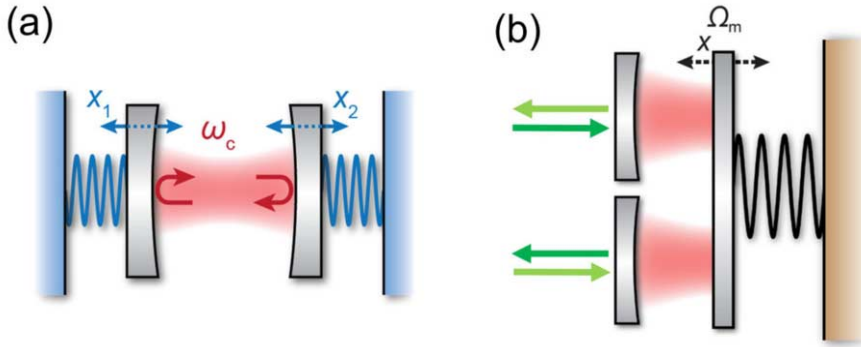
Fig. 5. – Examples of multimode optomechanical systems. (a) Two mechanical resonators can be coupled via radiation pressure of a single cavity mode. (b) Two optical resonators interacting with a single mechanical resonator facilitate state transfer from one cavity to the other via the mechanical resonator.

extended to two optical modes if they are both excited by suitably red-detuned drive fields. For large — and matched — cooperativities, probe light entering one cavity on resonance will exit via the other. This mode conversion process preserves quantum coherence if $C_q > 1$ [45-47].

Interestingly, the two cavity modes do not need to be at equal frequency, as long as they are driven with suitable drive fields that create the couplings (fig. 6(a)). In fact, the parametric optomechanical coupling even allows state transfer from microwave to optical signals [48]. This provides a promising technological opportunity, as such a quantum-

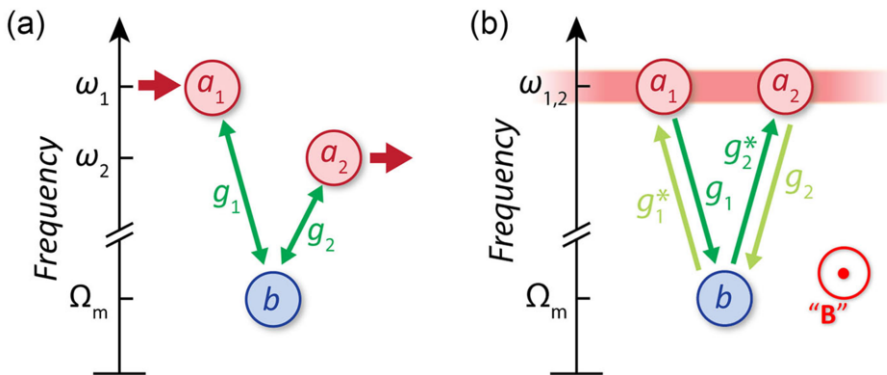Fig. 6. – Wavelength conversion and nonreciprocity using optomechanical coupling. (a) Two drive fields mediate conversion of an optical signal from one cavity mode to another, via the mechanical resonator. (b) As the phases of drive fields are imprinted on the photon-phonon transfer in a nonreciprocal fashion, mechanically-mediated mode conversion can lead to effective magnetic fields for light and sound.

coherent link would be a nice way to connect optical photons — which can transport quantum information virtually decoherence free at room temperature — to quantum computers based on superconducting circuits that operate at GHz frequencies. Multiple groups are thus pursuing the creation of such interfaces, by suitably combining optical and microwave cavities with nanomechanical resonators [49-53].

5˙3. *Beyond reciprocity*. – The fact that the parametric coupling mechanisms we discussed provide conversion between optical and mechanical excitations at different frequencies offers more interesting opportunities. These relate to the notion that optomechanical interactions can effectively break time-reversal symmetry for light or sound. For charged particles such as electrons, magnetic fields can break time-reversal symmetry and induce rich physical behaviour, from cyclotron orbits that depend on propagation direction, to the Aharonov-Bohm effect which imprints a direction-dependent phase on the wave function of a particle traversing a loop that encloses a magnetic flux, and one-way transport in topologically protected edge states of quantum Hall insulators. These effects have in common that they break reciprocity: If source and detector are exchanged, transport amplitude and phase is not preserved.

Photons and phonons, in contrast, do not interact with magnetic fields (except very weakly in magneto-optic materials). To create on-chip nonreciprocal and topological components that break time-reversal symmetry in a similar way, optomechanical interactions in multimode systems provide an interesting toolbox. When going from eq. (17) to eq. (18), we ignored the phase of the drive field α. This was possible for a single optical mode through an appropriate change of gauge. But in multimode systems, the phase *difference* of drive fields cannot be generally gauged away, such that we should remember to describe the coupling rates g for all modes as complex quantities, with phases directly related to those of the optical drive fields. For example, for red detuned drives the interaction Hamiltonian is generally of the form $-\hbar(g\delta\hat{a}^\dagger\hat{b} + g^*\delta\hat{a}\hat{b}^\dagger)$ for each coupling. Here we see that the optical drive phase is imprinted nonreciprocally on the photon-phonon transfer: If the creation of a phonon upon annihilation of a photon gains a positive phase, the reverse path creating a photon in the same mode gains a negative phase. This is reminiscent of the Peierls phase that electron wave functions gain as they travel in a magnetic vector potential. So if a photon transferred from mode 1 to mode 2 via a mechanical resonator acquires a phase $\Delta\phi = \arg(g_1) - \arg(g_2)$ (where g_i defines the drive-induced coupling rate of the resonator to each mode i), the reverse process from mode 2 to 1 acquires a phase $-\Delta\phi$. In analogy to the electronic Aharonov-Bohm effect, this becomes observable when a path with such a nonreciprocal phase is interfered with a different path (see fig. 6(b)). In suitably driven optomechanical systems, this has been used to create nonreciprocal optical and microwave elements such as isolators and circulators, by implementing constructive interference of paths from one port to another, but destructive in the opposite direction [54-63]. Similar mechanisms can also be used to break reciprocity for optically-mediated mechanical mode transfer [64,65].

These effects rely on optical and mechanical resonances, and are thus inherently

limited in bandwidth. The bandwidths can exceed the mechanical linewidth, as often the optically damped linewidth Γ_{eff} is the relevant bandwidth over which transport can be controlled. Nonetheless, also those are typically limited fundamentally by the cavity linewidth and/or the mechanical frequency. Various schemes seek to control photon and phonon transport over larger bandwidths, by exploiting propagating light and sound waves in waveguides rather than cavities. While the absence of resonant enhancement makes cavity-less approaches challenging, promising results have been achieved [66, 67].

Extending the creation of effective magnetic fields for optical or mechanical transport to large numbers of modes in optomechanical lattices provides many opportunities. These include in particular the creation of topological insulators for light and sound [68], with intriguing properties such as one-way conduction of signals along the edge of the array, topologically protected against backscattering. A flexible platform towards such goals is offered by periodically structured dielectric slabs: Suitable patterns can offer simultaneous two-dimensional bandgaps for both light and sound at the nanoscale, with point or line defects in the structure serving as optomechanical resonators and waveguides connecting them [69]. While the control over fabrication disorder makes the implementation of such arrays challenging, continuous technical improvements could bring it into reach in the near future.

5˙**4.** *Beyond linearity*. – To create nonclassical states of light or motion, a certain resource of nonlinearity is needed. Although the intrinsic nonlinearity of the optomechanical Hamiltonian (13) can have pronounced effects on thermal fluctuations with $\bar{n}_{\text{th}} \gg 1$ [22], the regime where this nonlinearity is significant at the single-quantum level is still out of reach for massive mechanical resonators.

Various techniques are however pursued to introduce nonlinearity in different ways. A straightforward strategy to create a Hamiltonian describing a nonlinear coupling between optical fields and motion is to enhance so-called *quadratic coupling* through design. If a system is designed such that the linear term in the relation between optical frequency and position in eq. (1) vanishes, the first leading term will likely be quadratic ($\omega_c \propto x^2$). In the resolved sideband regime, this leads to a Hamiltonian that directly couples phonon number $\hat{b}^\dagger \hat{b}$ to the light field. This naturally occurs for example when a vibrating membrane is placed exactly in the middle of a Fabry-Pérot cavity [70]. Especially if the reflectivity of the membrane is high, the quadratic variation with position can be pronounced [71, 72]. Quadratic coupling can in principle lead to the creation of nonclassical states (*e.g.* resembling superpositions of x and $-x$), and to the detection of quantum jumps when single mechanical quanta enter or exit the mechanical mode [70, 73]. However, careful analysis shows that sufficient cancellation of linear coupling puts stringent demands on loss and fabrication precision that are equivalent to those to reach single-photon strong coupling $g_0 > \kappa$ [74] — although nanoscale confinement in specific electromechanical systems may somewhat relax those demands [75].

Thus, a multitude of efforts aim to couple intrinsically nonlinear quantum systems to mechanical resonators in one way or another. An interesting approach is to leverage

the fact that *single-photon detectors* are inherently nonlinear [76-78]. For a laser tuned to the blue sideband of an optical cavity, the detection of a single photon emitted on cavity resonance (in the Stokes sideband) "heralds" the presence of a single phonon if the resonator was initially cooled to its ground state, as the phonon and Stokes photon must have been created as a pair through the $\hat{a}^\dagger \hat{b}^\dagger$ term in the Hamiltonian. A subsequent "click" that detects an anti-Stokes photon for a red-detuned laser can prove the presence of that phonon — as long as it was performed within a mechanical decoherence time. Such protocols have been used for example to study entanglement between mechanical vibrations of distant photonic crystal nanobeams, and nonclassical states of motion that are conditioned on the detection of single photons [79, 80]

To introduce quantum nonlinearity in a more deterministic fashion, researchers strive to couple mechanical resonators to two-level systems, creating mechanical analogues of cavity or circuit quantum electrodynamics — or the motion of trapped ions coupled to two-level transitions [81]. For example, it has been proposed and demonstrated that mechanical motion can influence the transition frequencies of semiconductor quantum dots and nitrogen vacancy centers [82-86], or coupled to the latter via a magnetic field gradient [86]. Moreover, optical emitters placed in suitable laser-driven optomechanical systems can lead to phonon-emitter interactions [87, 88]. At this moment the most advanced demonstrations have been provided using the techniques of circuit QED, coupling superconducting qubits based on Josephson junctions to high-frequency bulk or surface acoustic wave resonators through piezo-electric interactions, achieving high levels of control over the quantum motion of resonators involving billions to trillions of moving atoms [89-92].

6. – Conclusions

The field of cavity optomechanics, and in particular nano-optomechanics, has proven a fertile ground to explore various intriguing physical concepts and develop technology that could impact classical and quantum information processing as well as sensing and metrology. Spectacular advances in system performance and control techniques, as well as interfacing with other (quantum) systems in hybrid architectures, continue to show the ability of optomechanics to create new scientific opportunities.

* * *

REFERENCES

[1] Aspelmeyer M., Kippenberg T. J. and Marquardt F., *Rev. Mod. Phys.*, **86** (2014) 1391.

[2] Bowen W. P. and Milburn G. J., *Quantum Optomechanics* (CRC Press) 2015.

[3] Clerk A. A., Devoret M. H., Girvin S. M., Marquardt F. and Schoelkopf R. J., *Rev. Mod. Phys.*, **82** (2010) 1155.

[4] Safavi-Naeini A. H., Chan J., Hill J. T., Alegre T. P. M., Krause A. and Painter O., *Phys. Rev. Lett.*, **108** (2012) 033602.

[5] Clerk A. A., Marquardt F. and Jacobs K., *New J. Phys.*, **10** (2008) 095010.

[6] Hertzberg J. B., Rocheleau T., Ndukum T., Savva M., Clerk A. A. and Schwab K. C., *Nat. Phys.*, **6** (2010) 213.

[7] Suh J., Weinstein A. J., Lei C. U., Wollman E. E., Steinke S. K., Meystre P., Clerk A. A. and Schwab K. C., *Science*, **344** (2014) 1262.

[8] Vanner M. R., Pikovski I., Cole G. D., Kim M. S., Brukner Č., Hammerer K., Milburn G. J. and Aspelmeyer M., *Proc. Natl. Acad. Sci. U.S.A.*, **108** (2011) 16182.

[9] Vanner M. R., Hofer J., Cole G. D. and Aspelmeyer M., *Nat. Commun.*, **4** (2013) 2295.

[10] Muhonen J. T., La Gala G. R., Leijssen R. and Verhagen E., *Phys. Rev. Lett.*, **123** (2019) 113601.

[11] Aasi J. *et al.*, *Nat. Photon.*, **7** (2013) 613.

[12] Purdy T. P., Peterson R. W. and Regal C. A., *Science*, **339** (2013) 801.

[13] Wilson D. J., Sudhir V., Piro N., Schilling R., Ghadimi A. and Kippenberg T. J., *Nature*, **524** (2015) 325.

[14] Rossi M., Mason D., Chen J., Tsaturyan Y. and Schliesser A., *Nature*, **563** (2018) 53.

[15] Teufel J. D., Li D., Allman M. S., Cicak K., Sirois A. J., Whittaker J. D. and Simmonds R. W., *Nature*, **471** (2011) 204.

[16] Ding L., Baker C., Senellart P., Lemaitre A., Ducci S., Leo G. and Favero I., *Phys. Rev. Lett.*, **105** (2010) 263903.

[17] Eichenfield M., Camacho R., Chan J., Vahala K. J. and Painter O., *Nature*, **459** (2009) 550.

[18] Eichenfield M., Chan J., Camacho R. M., Vahala K. J. and Painter O., *Nature*, **462** (2009) 78.

[19] Gavartin E., Braive R., Sagnes I., Arcizet O., Beveratos A., Kippenberg T. J. and Robert-Philip I., *Phys. Rev. Lett.*, **106** (2011) 203902.

[20] Safavi-Naeini A. H., Alegre T. P. M., Chan J., Eichenfield M., Winger M., Lin Q., Hill J. T., Chang D. E. and Painter O., *Nature*, **472** (2011) 69.

[21] Leijssen R. and Verhagen E., *Sci. Rep.*, **5** (2015) 15974.

[22] Leijssen R., La Gala G. R., Freisem L., Muhonen J. T. and Verhagen E., *Nat. Commun.*, **8** (2017) 16024.

[23] Johnson S. G., Ibanescu M., Skorobogatiy M. A., Weisberg O., Joannopoulos J. D. and Fink Y., *Phys. Rev. E*, **65** (2002) 066611.

[24] Chan J., Safavi-Naeini A. H., Hill J. T., Meenehan S. and Painter O., *Appl. Phys. Lett.*, **101** (2012) 081115.

[25] Rabl P., *Phys. Rev. Lett.*, **107** (2011) 063601.

[26] Nunnenkamp A., Børkje K. and Girvin S. M., *Phys. Rev. Lett.*, **107** (2011) 063602.

[27] Dobrindt J. M., Wilson-Rae I. and Kippenberg T. J., *Phys. Rev. Lett.*, **101** (2008) 263602.

[28] Gröblacher S., Hammerer K., Vanner M. R. and Aspelmeyer M., *Nature*, **460** (2009) 724.

[29] Verhagen E., Deléglise S., Weis S., Schliesser A. and Kippenberg T. J., *Nature*, **482** (2012) 63.

[30] Kippenberg T. J., Rokhsari H., Carmon T., Scherer A. and Vahala K. J., *Phys. Rev. Lett.*, **95** (2005) 033901.

[31] Kippenberg T. J. and Vahala K. J., *Science*, **321** (2008) 1172.

[32] Wilson-Rae I., Nooshi N., Zwerger W. and Kippenberg T. J., *Phys. Rev. Lett.*, **99** (2007) 093901.

[33] Marquardt F., Chen J. P., Clerk A. A. and Girvin S. M., *Phys. Rev. Lett.*, **99** (2007) 093902.

[34] Teufel J. D., Donner T., Li D., Harlow J. W., Allman M. S., Cicak K., Sirois A. J., Whittaker J. D., Lehnert K. W. and Simmonds R. W., *Nature*, **475** (2011) 359.

[35] Chan J., Alegre T. P. M., Safavi-Naeini A. H., Hill J. T., Krause A., Gröblacher S., Aspelmeyer M. and Painter O., *Nature*, **478** (2011) 89.

[36] Peterson R. W., Purdy T. P., Kampel N. S., Andrews R. W., Yu P.-L., Lehnert K. W. and Regal C. A., *Phys. Rev. Lett.*, **116** (2016) 063601.

[37] Safavi-Naeini A. H., Gröblacher S., Hill J. T., Chan J., Aspelmeyer M. and Painter O., *Nature*, **500** (2013) 185.

[38] Wollman E. E., Lei C. U., Weinstein A. J., Suh J., Kronwald A., Marquardt F., Clerk A. A. and Schwab K. C., *Science*, **349** (2015) 952.

[39] Palomaki T. A., Harlow J. W., Teufel J. D., Simmonds R. W. and Lehnert K. W., *Nature*, **495** (2013) 210.

[40] Shkarin A. B., Flowers-Jacobs N. E., Hoch S. W., Kashkanova A. D., Deutsch C., Reichel J. and Harris J. G. E., *Phys. Rev. Lett.*, **112** (2014) 013602.

[41] Ockeloen-Korppi C. F., Damskägg E., Pirkkalainen J.-M., Asjad M., Clerk A. A., Massel F., Woolley M. J. and Sillanpää M. A., *Nature*, **556** (2018) 478.

[42] Heinrich G., Ludwig M., Qian J., Kubala B. and Marquardt F., *Phys. Rev. Lett.*, **107** (2011) 043603.

[43] Zhang M., Wiederhecker G. S., Manipatruni S., Barnard A., McEuen P. and Lipson M., *Phys. Rev. Lett.*, **109** (2012) 233906.

[44] Bagheri M., Poot M., Fan L., Marquardt F. and Tang H. X., *Phys. Rev. Lett.*, **111** (2013) 213902.

[45] Tian L. and Wang H., *Phys. Rev. A*, **82** (2010) 053806.

[46] Safavi-Naeini A. H. and Painter O., *New J. Phys.*, **13** (2011) 013017.

[47] Hill J. T., Safavi-Naeini A. H., Chan J. and Painter O., *Nat. Commun.*, **3** (2012) 1196.

[48] Regal C. A. and Lehnert K. W., *J. Phys.: Conf. Ser.*, **264** (2011) 012025.

[49] Bochmann J., Vainsencher A., Awschalom D. D. and Cleland A. N., *Nat. Phys.*, **9** (2013) 712.

[50] Bagci T., Simonsen A., Schmid S., Villanueva L. G., Zeuthen E., Appel J., Taylor J. M., Sørensen A., Usami K., Schliesser A. and Polzik E. S., *Nature*, **507** (2014) 81.

[51] Andrews R. W., Peterson R. W., Purdy T. P., Cicak K., Simmonds R. W., Regal C. A. and Lehnert K. W., *Nat. Phys.*, **10** (2014) 321.

[52] Balram K. C., Davanço M. I., Song J. D. and Srinivasan K., *Nat. Photon.*, **10** (2016) 346.

[53] Forsch M., Stockill R., Wallucks A., Marinkovic I., Gärtner C., Norte R. A., van Otten F., Fiore A., Srinivasan K. and Gröblacher S., arXiv:1812.07588 (2018).

[54] Hafezi M. and Rabl P., *Opt. Express*, **20** (2012) 7672.

[55] Metelmann A. and Clerk A. A., *Phys. Rev. X*, **5** (2015) 021025.

[56] Shen Z., Zhang Y.-L., Chen Y., Zou C.-L., Xiao Y.-F., Zou X.-B., Sun F.-W., Guo G.-C. and Dong C.-H., *Nat. Photon.*, **10** (2016) 657.

[57] Ruesink F., Miri M.-A., Alù A. and Verhagen E., *Nat. Commun.*, **7** (2016) 13662.

[58] Fang K., Luo J., Metelmann A., Matheny M. H., Marquardt F., Clerk A. A. and Painter O., *Nat. Phys.*, **13** (2017) 465.

[59] Bernier N. R., Tóth L. D., Koottandavida A., Ioannou M. A., Malz D., Nunnenkamp A., Feofanov A. K. and Kippenberg T. J., *Nat. Commun.*, **8** (2017) 604.

[60] Peterson G. A., Lecocq F., Cicak K., Simmonds R. W., Aumentado J. and Teufel J. D., *Phys. Rev. X*, **7** (2017) 031001.

[61] Barzanjeh S., Wulf M., Peruzzo M., Kalaee M., Dieterle P. B., Painter O. and Fink J. M., *Nat. Commun.*, **8** (2017) 953.

[62] Ruesink F., Mathew J. P., Miri M.-A., Alù A. and Verhagen E., *Nat. Commun.*, **9** (2018) 1798.

[63] Shen Z., Zhang Y.-L., Chen Y., Sun F.-W., Zou X.-B., Guo G.-C., Zou C.-L. and Dong C.-H., *Nat. Commun.*, **9** (2018) 1797.

[64] Xu H., Jiang L., Clerk A. A. and Harris J. G. E., *Nature*, **568** (2019) 65.

[65] Mathew J. P., del Pino J. and Verhagen E., arXiv:1812.09369 (2018).

[66] Sohn D. B., Kim S. and Bahl G., *Nat. Photon.*, **12** (2018) 91.

[67] Kittlaus E. A., Otterstrom N. T., Kharel P., Gertler S. and Rakich P. T., *Nat. Photon.*, **12** (2018) 613.

[68] Peano V., Brendel C., Schmidt M. and Marquardt F., *Phys. Rev. X*, **5** (2015) 031011.

[69] Safavi-Naeini A. H., Hill J. T., Meenehan S., Chan J., Gröblacher S. and Painter O., *Phys. Rev. Lett.*, **112** (2014) 153603.

[70] Thompson J. D., Zwickl B. M., Jayich A. M., Marquardt F., Girvin S. M. and Harris J. G. E., *Nature*, **452** (2008) 72.

[71] Sankey J. C., Yang C., Zwickl B. M., Jayich A. M. and Harris J. G. E., *Nat. Phys.*, **6** (2010) 707.

[72] Ludwig M., Safavi-Naeini A. H., Painter O. and Marquardt F., *Phys. Rev. Lett.*, **109** (2012) 063601.

[73] Vanner M. R., *Phys. Rev. X*, **1** (2011) 021011.

[74] Miao H., Danilishin S., Corbitt T. and Chen Y., *Phys. Rev. Lett.*, **103** (2009) 100402.

[75] Dellantonio L., Kyriienko O., Marquardt F. and Sørensen A. S., *Nat. Commun.*, **9** (2018) 3621.

[76] Vanner M. R., Aspelmeyer M. and Kim M. S., *Phys. Rev. Lett.*, **110** (2013) 010504.

[77] Cohen J. D., Meenehan S. M., MacCabe G. S., Gröblacher S., Safavi-Naeini A. H., Marsili F., Shaw M. D. and Painter O., *Nature*, **520** (2015) 522.

[78] Galland C., Sangouard N., Piro N., Gisin N. and Kippenberg T. J., *Phys. Rev. Lett.*, **112** (2014) 143602.

[79] Riedinger R., Hong S., Norte R. A., Slater J. A., Shang J., Krause A. G., Anant V., Aspelmeyer M. and Gröblacher S., *Nature*, **530** (2016) 313.

[80] Riedinger R., Wallucks A., Marinković I., Löschnauer C., Aspelmeyer M., Hong S. and Gröblacher S., *Nature*, **556** (2018) 473.

[81] Leibfried D., Blatt R., Monroe C. and Wineland D., *Rev. Mod. Phys.*, **75** (2003) 281.

[82] Wilson-Rae I., Zoller P. and Imamoḡlu A., *Phys. Rev. Lett.*, **92** (2004) 075507.

[83] MacQuarrie E. R., Gosavi T. A., Jungwirth N. R., Bhave S. A. and Fuchs G. D., *Phys. Rev. Lett.*, **111** (2013) 227602.

[84] Yeo I., de Assis P.-L., Gloppe A., Dupont-Ferrier E., Verlot P., Malik N. S., Dupuy E., Claudon J., Gérard J.-M., Auffèves A., Nogues G., Seidelin S., Poizat J.-P., Arcizet O. and Richard M., *Nat. Nanotechnol.*, **9** (2014) 106.

[85] Ovartchaiyapong P., Lee K. W., Myers B. A. and Jayich A. C. B., *Nat. Commun.*, **5** (2014) 4429.

[86] Teissier J., Barfuss A., Appel P., Neu E. and Maletinsky P., *Phys. Rev. Lett.*, **113** (2014) 020503.

[87] Arcizet O., Jacques V., Siria A., Poncharal P., Vincent P. and Seidelin S., *Nat. Phys.*, **7** (2011) 879.

[88] Cotrufo M., Fiore A. and Verhagen E., *Phys. Rev. Lett.*, **118** (2017) 133603.

[89] O'Connell A. D., Hofheinz M., Ansmann M., Bialczak R. C., Lenander M., Lucero E., Neeley M., Sank D., Wang H., Weides M., Wenner J., Martinis J. M. and Cleland A. N., *Nature*, **464** (2010) 697.

[90] Chu Y., Kharel P., Renninger W. H., Burkhart L. D., Frunzio L., Rakich P. T. and Schoelkopf R. J., *Science*, **358** (2017) 199.

[91] Satzinger K. J., Zhong Y. P., Chang H.-S., Peairs G. A., Bienfait A., Chou M.-H., Cleland A. Y., Conner C. R., Dumur E., Grebel J., Gutierrez I., November B. H., Povey R. G., Whiteley S. J., Awschalom D. D., Schuster D. I. and Cleland A. N., *Nature*, **563** (2018) 661.

[92] Chu Y., Kharel P., Yoon T., Frunzio L., Rakich P. T. and Schoelkopf R. J., *Nature*, **563** (2018) 666.

Photostable molecules on chip: a scalable approach to photonic quantum technologies

M. Colautti, G. Mazzamuto and F. S. Cataliotti

LENS and Università di Firenze - Via N. Carrara 1, 50019 Sesto Fiorentino (FI), Italy

P. Lombardi and S. Pazzagli

CNR-INO, Istituto Nazionale di Ottica - Via Carrara 1, 50019 Sesto Fiorentino (FI), Italy

A. P. Ovvyan, N. Gruhler and W. H. P. Pernice

Physikalisches Institut, Westfälische Wilhelms-Universität Münster
Heisenbergstrasse 11, 48149 Münster, Germany

G. Kewes, O. Neitzke and O. Benson

Institut für Physik, Humboldt-Universität - Newtonstrasse 15, 12489 Berlin, Germany

C. Toninelli(*)

LENS and Università di Firenze - Via N. Carrara 1, 50019 Sesto Fiorentino (FI), Italy
CNR-INO, Istituto Nazionale di Ottica - Via Carrara 1, 50019 Sesto Fiorentino (FI), Italy

Summary. — In this manuscript we demonstrate the potential of a hybrid technology which combines single organic molecules as quantum light sources and dielectric chips. In particular, we discuss our approach based on evanescent coupling of dibenzoterrylene molecules to silicon nitride waveguides and show a coupling efficiency of up to $42 \pm 2\%$ over both propagation directions. Our results open a novel path towards a fully integrated and scalable photon processing platform.

(*) E-mail: toninelli@lens.unifi.it

1. – Introduction

Reliable and bright non-classical light sources are a fundamental ingredient for many quantum technologies, such as sensing, imaging and metrology applications [1]. In the last years single quantum emitters under pulsed excitation have been presented as deterministic sources of indistinguishable single photons [2]. Among them, solid-state emitters such as quantum dots [3], color centres in diamond [4] and single molecules [5] are particularly suitable for integration into photonic chips [6]. In particular, direct coupling of single emitters to optical waveguides (WGs) is a powerful strategy to collect single photons in well-defined propagating modes [7].

In this work, we present the design and characterization of the evanescent coupling between Dibenzoterrylene (DBT) molecules and a ridge WG made of silicon nitride [8]. Room temperature measurements demonstrate competitive results with the state-of-the-art [6,9], with an overall molecule-to-WG coupling efficiency up to $(42\pm2)\%$ and evidence of low multi-photon probability inside the WG. The advantages of our approach include an all-solid-state platform, a small footprint, simple fabrication methods and scalability.

2. – Evanescent coupling of single molecules to a nearby dielectric waveguide

Efficient light-matter interaction can be achieved placing a quantum emitter in the strong evanescent field of optical dielectric waveguides on-chip [7]. Here we discuss the design and the realization of a hybrid molecules-nanophotonic system made of spincoated DBT:Ac crystals ($n = 1.8$) on Si_3N_4 ($n = 2$) WGs.

2˙1. *Single-molecule quantum emitters*. – Dibenzoterrylene molecules embedded in Anthracene (Ac) crystals (DBT:Ac) have key advantages for the coupling to photonic structures, due to the wavelength of its main optical transition centerd at 785 nm, to its photostability also at room temperature [10], and to the easy fabrication method which allows to obtain few tens of nanometer films of DBT:Ac crystal via spin-coating.

The Jablonski diagram of a DBT molecule is depicted in fig. 1a. It shows the singlet (S_0, S_1) and triplet (T_1) electronic states with the relative vibrational multiplets. DBT quantum yield results close to unity due to the small inter-system crossing probability (10^{-4}) to the rapidly decaying triplet state, and the zero-zero phonon line (00-ZPL) is lifetime-limited at liquid helium temperature ($\simeq 40$ MHz) [11]. The radiative (solid arrows) and non-radiative decay processes (dashed arrows) are shown in the diagram. In this work we show room temperature measurements where we use a non-resonant 767 nm laser to pump the molecule to a vibrational level of a higher excited electronic state. The single-molecule red-shifted emission at 785 nm can be measured by out-filtering the pump.

2˙2. *Design and fabrication of the hybrid photonic chip*. – We have designed the guiding structure such to have an important evanescent field at the emitter position, and to simultaneously achieve a strong mode confinement and low losses. A rendering of the nanophotonic circuit is sketched in fig. 1b. It consists of a glass substrate with a 500 nm-wide single-mode optical WG, and focusing grating couplers. Gratings are buried
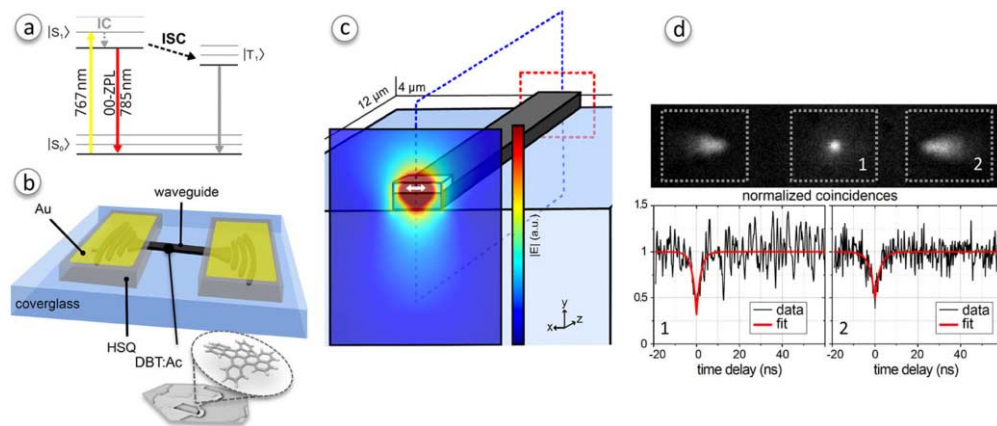
Fig. 1. – Evanescent coupling of DBT molecules to a ridge WG. a) Jablonski diagram of the DBT:Ac system showing the singlet (S) and triplet (T) electronic states. Radiative (non-radiative) transitions are represented by solid (dashed) arrows. b) Rendering of the silicon nitride WG with grating outcouplers, coated with HSQ and gold. A zoom-in shows a thin DBT:Ac crystal which is spin-coated onto the WG. c) Layout of the 3D numerical simulations. A dipolar emitter (white arrow) mimicking a single molecule is placed in a 100 nm thick Ac crystal. The transverse section shows the normalized electric field on the dipole plane. d) The top panel displays the fluorescence map measured with the EMCCD camera, showing signal both from the molecule position (region 1) and from the grating out-couplers. In the bottom panel, the antibunching dips relative to the molecule position (1) and to the coupler area (2) are displayed. Panels b, c, d were adapted with permission from P. Lombardi, *et al.*, *ACS Photonics*, **5** (1) (2018), pp. 126-132 DOI: 10.1021/acsphotonics.7b00521. © 2017 American Chemical Society.

with a hydrogen silsequioxane (HSQ) buffer layer to prevent the formation of crystals on the couplers and consequent scattering, and a gold mirror is deposited on top to enhance directionality. DBT single molecules embedded in thin Ac crystals are then drop casted on the chip. The geometric parameters of the WG, *i.e.* a width of 500 nm and a thickness of 175 nm, are optimized for single-mode operation at 785 nm and in order to maximize the electric field of this fundamental mode at the position of the emitter. The grating coupler is designed to fulfil mode-matching with a Gaussian-like mode, and to obtain maximum out-coupling efficiency at the central emission wavelength of DBT (up to 90%, according to finite elements simulations).

Figure 1c displays the layout of 3D numerical simulations for the estimation of the emitter-WG coupling efficiency, *i.e.* $\beta = \frac{\Gamma_{WG}}{\Gamma_{tot}}$, being Γ_{WG} the emission rate into the WG mode and Γ_{tot} the total decay rate in the presence of the WG. A dipolar emitter oriented along the y-axis is placed inside an Ac crystal to model a single molecule. The β-factor is calculated as the Poynting vector flux through the detected area, delimited by the red dashed line which surrounds the WG section, and is then normalized with the total power flow radiated through a volume containing the emitter. Taking into account the intrinsic variability imposed by the spin-coating of DBT:Ac on the chip, the optimal

$\beta \sim 50\%$ is obtain for a $180\,\mathrm{nm}$ thick Ac crystal, and for a distance of the emitter from the surface of $10\,\mathrm{nm}$.

2˙**3. Experimental results.** – The experimental set-up is a two channel confocal microscope, which allows to focus at the same time both the off-resonant excitation beam ($767\,\mathrm{nm}$) through the substrate onto the WG area and the resonant reference laser ($785\,\mathrm{nm}$) onto the grating couplers for the throughput characterization. A Hanbury Brown and Twiss (HBT) set up allows to take measurements of the second-order correlation function ($g^2(\Delta t)$) of the fluorescence light.

An example of fluorescence map is shown in the top panel of fig. 1d. The emission is partially lost in free space (bright spot at the molecule position in the center) and partially coupled throughout the WG towards the couplers, in both directions (bright lateral spots). The emitter-WG coupling efficiency is estimated by comparing the fluorescence intensity on the EM-CCD camera in the couplers areas, S_c, with the molecule residual emission into the free space, S_f, after appropriate background subtraction. Accounting for the corresponding collection efficiencies η_c and η_f, the coupling probability to the WG can be calculated as

$$(1) \qquad \beta_{\mathrm{meas}} = \frac{S_c/\eta_c}{S_c/\eta_c + S_f/\eta_f}\,.$$

The out-coupling efficiency (η_c) of the WG is estimated with transmission measurements. The resonant reference laser is focused into one of the couplers and light from the other coupler is imaged, integrated over the coupler area and normalized to the same signal obtained for reflection of the laser spot on a silver mirror (after background subtraction on both images). The square root of this value corresponds to the single-coupler efficiency, which is found to be $\eta_c = 35 \pm 5\%$, where the difference from the simulated value is ascribed to a non-optimal HSQ thickness.

The collection efficiency η_f is estimated via 3D numerical simulations, as Poynting vector flux through an area corresponding to the objective collection capacity. The value is then normalized with the overall non-guided power flow and yields $\eta_f = (5.1 \pm 1.5)\%$. Therefore, β_{meas} can be determined by direct confocal excitation of the molecule and collection from the EM-CCD image. Integration of the signal in the respective regions S_f and S_c (from both couplers) yields an average value of $\beta_{\mathrm{meas}} = 20\%$ and a peak value of $\beta_{\mathrm{meas}} = (42 \pm 2)\%$, which is correctly described by the theoretical model when accounting for possible different dipole positions.

To conclude, the quantum nature of the WG-coupled light is analyzed by measuring the $g^2(\Delta t)$ off-chip, collecting light either from the illumination point or from one coupler, i.e. the regions in the top panel of fig. 1d labelled with 1 and 2, respectively. The bottom panel displays the correspondent measurements and fits, which yield $g^2_{\mathrm{off}}(0) = 0.33 \pm 0.09$ and $g^2_{\mathrm{off}}(0) = 0.50 \pm 0.05$. After accurate background correction for the non-guided laser scattering from the illumination point (see ref. [8] for details), we evaluate an on-chip single-photon purity $g^2_{\mathrm{on}}(0) = 0.01 \pm 0.10$, which indicates a low multi-photon probability inside the WG.

3. – Conclusions

In this manuscript we discuss a possible platform to integrate single-molecule–based quantum emitters into dielectric WGs, aiming at efficient emission, control and collection of single photons on-chip. We use DBT molecules embedded in Ac crystals as reliable sources of single photons, owing to their purity, brightness and photostability at room temperature. We present the design and characterization of efficient evanescent coupling between a single molecule and a ridge WG made of silicon nitride. Room temperature measurements show competitive results with the state-of-the-art with a molecule-to-WG coupling efficiency up to $(42 \pm 2\%)$ and evidence of single-photon-source purity on-chip. The advantages of our approach include an all-solid-state platform, a small footprint, simple fabrication methods and scalability.

REFERENCES

[1] Dowling J. P. and Seshadreesan K. P., *J. Light. Technol.*, **33** (2015) 2359.
[2] Lounis B. and Moerner W. E., *Nature*, **407** (2000) 491.
[3] Buckley S., Rivoire K. and Vučović, *Rep. Prog. Phys.*, **75** (2012) 126503.
[4] Doherty M. W., Manson N. B., Delaney P., Jelezko F., Wrachtrup J. and Hollenberg L. C., *Phys. Rep.*, **528** (2013) 1.
[5] Kiraz A., Hellerer Th., Müstecaplioğlu Ö. E., Bräuchle C. and Zumbusch A., *Phys. Rev. Lett.*, **94** (2005) 223602.
[6] Zadeh, Elshaari A. W., Jons K. D., Fognini A., Dalacu D., Poole P. J., Reimer M. E. and Zwiller V., *Nano Lett.*, **16** (2016) 2289.
[7] Hwang J. and Hinds E., *New J. Phys.*, **13** (2011) 085009.
[8] Lombardi P., Ovvyan A., Pazzagli S., Mazzamuto G., Kewes G., Neitzke O., Gruhler N., Benson O., Pernice W., Cataliotti F. and Toninelli C., *ACS Photon.*, **5** (2017) 126.
[9] Davanco M., Liu J., Sapienza L., Zhang C.-Z., Cardoso J. V. D. M., Verma V., Mirin R., Nam S. W., Liu L. and Srinivasan K., *Nat. Commun.*, **8** (2017) 889.
[10] Toninelli C., Early K., Bremi J., Renn A. and Sandoghdar V., *Opt. Express*, **18** (2010) 6577.
[11] Nicolet A. A., Hofmann C., Kol'chenko M. A., Kozankiewicz B. and Orrit M., *Chem. Phys. Chem.*, **8** (2007) 1215.

This page intentionally left blank

Environment spectroscopy with an NV center in diamond

S. Hernández-Gómez, F. Poggiali and N. Fabbri

LENS European Laboratory for Non linear Spectroscopy, Università di Firenze
I-50019 Sesto Fiorentino (FI), Italy

P. Cappellaro

Department of Nuclear Science and Engineering, Massachusetts Institute of Technology
Cambridge, MA 02139, USA

Summary. — Nitrogen-vacancy (NV) centers in diamond have emerged in the last decade as a prominent platform for quantum technologies. As for any qubit system, a good understanding of their local environment is crucial to build quantum devices protected from detrimental noise. Here, we describe in detail a method to spectroscopically characterize the spin bath around an NV center, even when the NV coherence time is short, and identify the coherent coupling with the nearest nuclear spins. In the regime of weak qubit-bath coupling, the acquired knowledge of the bath reliably predicts the qubit dynamics under different controls.

1. – Introduction

Characterizing the environment surrounding a qubit is important for quantum technologies, since it enables the development of strategies to increase coherence [1,2]. Moreover, the controlled and coherent coupling of a quantum sensor with its environment has
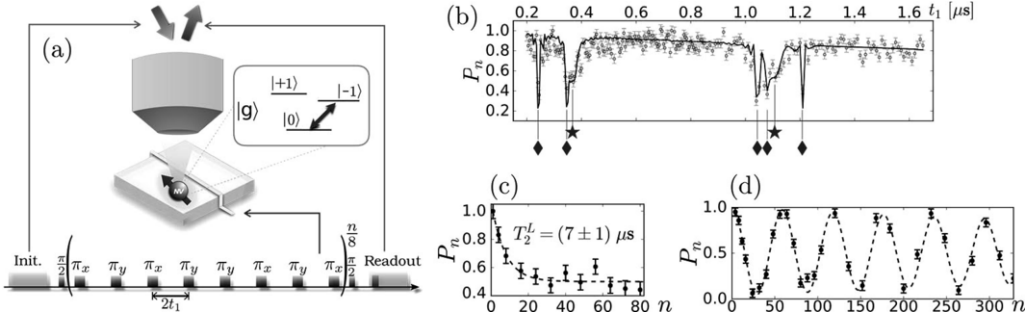
© Società Italiana di Fisica

Fig. 1. – (a) Scheme of the experimental setup. (b-d) Evolution of P_n under an XY-8 sequence. (b) Varying the time between pulses, with $n = 40$. (c)-(d) Varying the number of pulses, fixing t_1 to the center of a ★ collapse (c) and a ♦ collapse (d).

been proposed as a potential resource also for sensing and computing [3, 4]. Here we present an experimental procedure to perform spectroscopy of a spin bath, sensed by the electronic spin of a nitrogen-vacancy (NV) center in diamond. We also give a brief description of the procedure to characterize the coupling with single nearby nuclear spins. Once the environment has been fully characterized, we discuss the predictive power of the obtained noise model, a crucial requirement for quantum devices.

2. – Effect of the environment on the NV center

2'1. *Spectroscopy method*. – We explore the complex environment of the NV spin qubit, formed by an ensemble of natural abundance (1%) ^{13}C nuclear spins $I = 1/2$ randomly distributed in the lattice. The experimental setup is shown in fig. 1(a). We use a home-built confocal microscope to initialize an NV center into the spin state $m_s = 0$, and read out its final state after manipulation. An antenna next to the diamond delivers microwave pulses used to coherently control the NV electronic spin. A permanent magnet generates a magnetic field which we align with the NV quantization axis [5]. The spectroscopy protocol is based on dynamical decoupling (DD) sequences composed by a variable number n of π pulses, as explained in the next section. Each sequence is enclosed in a Ramsey interferometer to map coherence into residual population P_n of $m_s = 0$.

In fig. 1(b) we present the time evolution of P_n under an XY-8 sequence of $n = 40$ pulses as a function of the time between pulses, $2t_1$ (total measurement time $T = 2nt_1$). There are two different kinds of loss (collapses) of the electronic spin coherence. The collapses due to the interaction with the spin bath are the broad ones and go down to $P_n = 0.5$ (marked with ★ in fig. 1(b)). The analysis of these collapses gives access to the noise spectral density (NSD) modeling the large spin bath, as shown in the next section. Narrow collapses (marked with ♦ in fig. 1(b)) can reach $P_n < 0.5$ and originate from the interaction with individual strongly coupled nuclear spins. Characterizing the two contributions to the signal loss gives us a full picture of the spin environment.

The difference between the two interactions is even more evident when we fix t_1 and observe the behavior of the coherence in terms of the number of pulses. While the collective spin bath induces an exponential decay of P_n, the coherent coupling to nearby nuclei generates coherent oscillations, as shown in fig. 1(c)-(d), respectively.

In the presence of a classical stationary noise, the coherence function $W(t)$ of the qubit decays as

$$(1) \qquad W(t) = e^{-\chi(t)} \quad \text{with } \chi(t) = \int \frac{d\omega}{\pi\omega^2} S(\omega)|Y(\omega)|^2,$$

where $Y(\omega)$ is the filter function [6] describing the used DD sequence, and $S(\omega)$ is the NSD, which models the collective effect of the spin bath. When using an equispaced DD sequence with large number of pulses [7] the filter function can be approximated by a δ-function centered at $\omega = \pi/(2t_1)$, and we can approximate the coherence as $W(nt_1) \simeq \exp(-\frac{2nt_1}{T_2^L})$. To characterize the NSD we extract the generalized coherence time T_2^L from experimental data, as exemplified in fig. 1(c).

Although we could use the approximated expression $S(\omega) \simeq \frac{\pi^2}{8 T_2^L}$ to obtain the NSD from the first collapse, this approximation is only valid for a large number of pulses, whereas the coupling with the spin bath leads to a very fast decay ($n < 8$) for t_1 around the first collapse. This induces an artificial broadening on the NSD peak and leads to an incorrect estimate of its maximum amplitude. To overcome the problem of strong decoherence around the Larmor frequency $\omega = \omega_L$ of the nuclear spin bath, we take advantage of the fact that the filter function of an equidistant sequence has harmonics at $\omega_l = (2l + 1)\omega_L$, affecting T_2^L [7, 8],

$$(2) \qquad \frac{1}{T_2^L(\omega)} = \frac{8}{\pi^2} \sum_{l=0}^{\infty} \frac{1}{(2l + 1)^2} S(\omega_l).$$

In practice, we center the higher-order harmonics of the filter function around the expected NSD peak, to extract the different harmonic contributions and combine them to obtain a faithful estimate of the NSD. By fitting the experimental data to eq. (2) we estimate the NSD, as shown in fig. 2(a). As detailed below, we find that the NSD lineshape can be reliably extracted from a Gaussian fit of $1/T_2^L$ around the 1st- and 2nd-order collapses ($l = 1$ and $l = 2$), without the need to measure even higher harmonics.

We demonstrate self-consistency of the method, and show that while the first collapse of the signal does not provide reliable information to obtain the NSD, the analysis of 1st- and 2nd-order collapses enables a correct reconstruction of the NSD. In our calculations we assumed instantaneous π pulses, this approximation is better verified for the higher harmonics, which are associated to lower frequencies.

To model the NSD we use a Gaussian noise peak centered at $750\,\text{kHz}$, shown as a dashed line in fig. 2(b). Using eq. (1) we simulate the coherence of the qubit under a DD sequence with equidistant pulses, and analyze the result to extract T_2^L and reconstruct the original NSD peak. The dark-gray shaded area in fig. 2(b) corresponds to the NSD
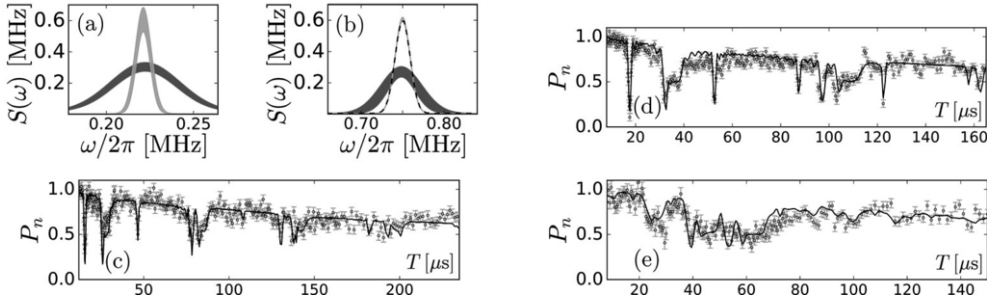
Fig. 2. – (a-b) NSD obtained with the 1st- and 2nd-order harmonics (light-gray), and with the 0th-order harmonic (dark-gray). The shaded areas include the error on the fit. (a) Result from experimental data with $B = 208(1)$ G. (b) Reconstruction of a model NSD used to proof self-consistency of the method. The black dashed line (overimposed with the light-gray area) is the original model NSD. (c)–(e) Dynamics of the electronic spin under different conditions. Points represent the experimental data, and solid line the evolution predicted from the characterized environment. (c)-(d) XY-8 sequence with $n = 24$ pulses at $310(1)$ G and $394(1)$ G, respectively. (e) A XY-4 at $B = 205(1)$ G, with $n = 20$ pulses at positions $t_{ij} = \frac{T}{80}(20i + 3j - 19)$, with $i = 1 \ldots 4$ and $j = 1 \ldots 5$ [9].

reconstructed from the simulation of the first collapse, while the light-gray shaded area represents the result of the reconstruction of the NSD using the $l = 1, 2$ harmonics. Width and amplitude obtained with 0th-harmonic collapse are very different from the original ones. On the other hand, using the first two harmonics allows us to reproduce the original parameters of the Gaussian peak with less than 0.2% error.

The hyperfine interaction with a nearby nuclear spin induces modulations of the coherence of the NV electronic spin in terms of the number of pulses [10-12], which can be isolated from detrimental noise using equidistant DD sequences. In fig. 1(d) we show an example of this coherent oscillation, together with the fit to a theoretical function, calculated using conditional evolution operators, from which we extract the components of the coupling strength between the NV spin and the nearby nuclear spin. More details are reported in ref. [9].

**2`2. *Predictive power of the characterization.* – In order to corroborate the predictive power of the reconstructed environment model, we use the information to simulate the evolution of the electronic spin for different magnetic fields and under different DD sequences, and compare the results to corresponding new measurements. In fig. 2(c)-(d) we present the spin coherence under an XY-8 sequence of 24 equidistant pulses for two different strengths of the external magnetic field, in the regime of weak qubit-bath coupling. The model successfully predicts the qubit evolution under sequences with non-equidistant pulses, as shown in fig. 2(e) where we used an adaptive XY-4 [13] sequence (more details in Supplementary materials of [9]). In all cases we verify a very good agreement between data and simulation. We have also tested the model for adaptive XY-8 and Uhrig sequences [9], with similar results.

By varying the magnetic-field strength, we tune the bath internal energy compared to its coupling with the NV spin [9,14]. At a low magnetic field (~ 150 G or below) we find that the controlled NV spin dynamics affects the spin bath [9]. Since the bath is no longer independent from the NV, it is not possible to find a single NSD that would correctly describes the evolution of the electronic spin.

3. – Conclusions

In conclusion, we have described a method to fully characterize the environment comprising nuclear spins in diamond, using as a probe the electronic spin of an NV center. We characterize both the spin bath and the nearby nuclear spins. By using higher harmonics of the DD-sequence filter functions applied on the qubit, we overcome the problem of short coherence time, and reconstruct a reliable environment model. We find that this model predicts the dynamics of the NV spin under various DD sequences and for different external magnetic fields, in the regime of weak qubit-bath coupling.

$$* * *$$

REFERENCES

[1] Poggiali F., Cappellaro P. and Fabbri N., *Phys. Rev. X*, **8** (2018) 021059.
[2] Layden D. and Cappellaro P., *npj Quantum Inf.*, **4** (2018) 30.
[3] Goldstein G., Cappellaro P., Maze J. R., Hodges J. S., Jiang L., Sorensen A. S. and Lukin M. D., *Phys. Rev. Lett.*, **106** (2011) 140502.
[4] Cappellaro P., Jiang L., Hodges J. S. and Lukin M. D., *Phys. Rev. Lett.*, **102** (2009) 210502.
[5] Poggiali F., Cappellaro P. and Fabbri N., *Phys. Rev. B*, **95** (2017) 195308.
[6] Degen C. L., Reinhard F. and Cappellaro P., *Rev. Mod. Phys.*, **89** (2017) 035002.
[7] Yuge T., Sasaki S. and Hirayama Y., *Phys. Rev. Lett.*, **107** (2011) 170504.
[8] Álvarez G. A. and Suter D., *Phys. Rev. Lett.*, **107** (2011) 230501.
[9] Hernández-Gómez S., Poggiali F., Cappellaro P. and Fabbri N., arXiv:1808.08222 (2018).
[10] Taminiau T. H., Wagenaar J. J. T., van der Sar T., Jelezko F., Dobrovitski V. V. and Hanson R., *Phys. Rev. Lett.*, **109** (2012) 137602.
[11] Kolkowitz S., Unterreithmeier Q. P., Bennett S. D. and Lukin M. D., *Phys. Rev. Lett.*, **109** (2012) 137601.
[12] Zhao N., Honert J., Schmid B., Klas M., Isoya J., Markham M., Twitchen D., Jelezko F., Liu R.-B., Fedder H. and Wrachtrup J., *Nat. Nanotechnol.*, **7** (2012) 657.
[13] Casanova J., Wang Z.-Y., Haase J. F. and Plenio M. B., *Phys. Rev. A*, **92** (2015) 042304.
[14] Reinhard F., Shi F., Zhao N., Rempp F., Naydenov B., Meijer J., Hall L. T., Hollenberg L., Du J., Liu R.-B. and Wrachtrup J., *Phys. Rev. Lett.*, **108** (2012) 200402.

This page intentionally left blank

Ultrafast photonic quantum correlations mediated by individual phonons

S. Tarragó Vélez and Christophe Galland

Institute of Physics, Ecole Polytechnique Fédérale de Lausanne (EPFL)
CH-1015 Lausanne, Switzerland

Summary. — This contribution to the proceedings describes a new technique to prepare and measure the lifetime of the first phonon Fock state in diamond using single-photon time-correlated Raman spectroscopy. By using a pair of ultrafast laser pulses of two different colors we can spectrally distinguish the Stokes photons created during the first pulse from the anti-Stokes photons created during the second pulse. Single-photon detection on the Stokes signal acts as a projective measurement preparing the phonon in an energy eigenstate. During the lifetime of the phonon, the second pulse, which arrives after a controllable delay, has a higher probability of emitting an anti-Stokes photon than allowed by classical mechanics. Two-photon quantum correlations between Stokes and anti-Stokes can therefore be used to map the phonon decay.

1. – Description

This contribution to the proceeding was originally shown as a poster presentation in the school. This poster explained our group's recent work in developing a method to probe phonon states by measuring photon correlations, which was recently published in [1].

251

2. – Experimental method

The aim of our experiment was to measure the dynamics of the first phonon Fock state in diamond. Broadly speaking, our method is the following: First, a 100 fs laser pulse interacts with the sample, creating with a low probability (typically < 1%) a perfectly correlated pair of one optical phonon and one Stokes-shifted photon. The photon is filtered from the laser and detected by an avalanche photodiode operated in Geiger mode. Successful detection projects the state of the phonon into the first Fock state (energy eigenstate). The phonon mode freely evolves for some time before a second laser pulse interacts with the sample, which can annihilate the phonon (if present) and in the process emits an anti-Stokes photon, which is filtered and detected using another single-photon detector. In other words, one laser pulse first writes the state (together with the measurement process), the phonon mode evolves for a certain amount of time, and a second laser pulse reads the state. The scheme is therefore similar to the one proposed in 2001 for atomic ensembles by Duan, Lukin, Cirac and Zoller [2], and can therefore be used for a wide range of quantum information processing tasks.

To interact with the phonon mode of frequency ω_{ph} we use the Raman effect, where the inelastic scattering of a laser of frequency ω_0 gives rise to a signal at frequency $\omega_0 - \omega_{ph}$, called the Stokes (S) signal, and a signal at frequency $\omega_0 + \omega_{ph}$, called the anti-Stokes (aS). The emission of a Stokes photon is accompanied by the creation of a phonon, while the emission of an anti-Stokes photon is accompanied by the annihilation of a phonon.

In order to investigate the dynamics, we use two lasers, one of which has an adjustable delay line along its path. We then look at the Stokes signal from one of the lasers, and at the anti-Stokes from the other. Phonons typically decay in pico-second time scales. For that reason, our experiments use ~ 100 fs pulses from a mode-locked Ti:Sapph oscillator and a synchronously pulsed OPO being pumped by part of the TiSa's output.

Two lasers beams at different frequencies are used in order to spectrally distinguish the Stokes from the anti-Stokes photons. The TiSa emits pulses centered on ~ 810 nm, while the OPO emits pulses centered on ~ 690 nm. This wavelength configuration is chosen purely for convenience, as the only requirement on the wavelengths is that the Stokes and anti-Stokes should be distinguishable, and noise from the sample (*e.g.* from photoluminescence) should be avoided.

The correlation between the S and aS photons are investigated using Time Correlated Single-Photon Counting (TCSPC). Start-stop measurements are done, where the detection of a S photon triggers the start of a measurement, and the detection of an aS photon triggers the stop. By doing this multiple times a histogram is built, from which the second order cross correlation between the S and aS ($g_{S,aS}^{(2)}$) can be calculated. In the histogram shown in fig. 1, the peak at $t = 0$ corresponds to the events where both a S and aS photons were detected during the same repetition rate of the lasers, while the side peaks come from the events where the detectors clicked during different repetitions. The value of $g_{S,aS}^{(2)}$ is then calculated as the ratio of the $t = 0$ peak to the average of the side peaks.
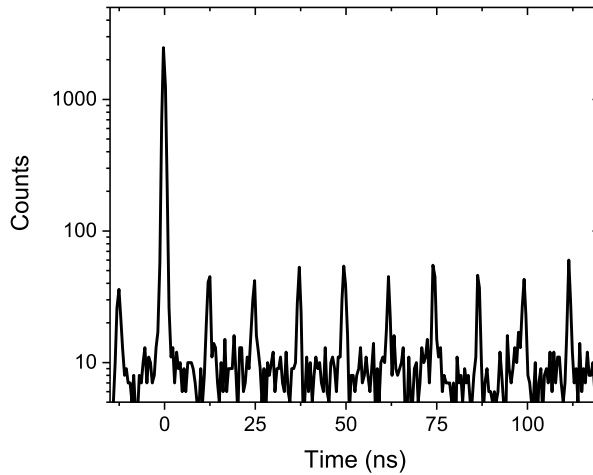
Fig. 1. – S-aS coincidence histogram measured for 20 minutes, with both *write* and *read* pulse arriving at the sample simultaneously. The peak at time $t = 0$ represents the correlated events, while the other peaks show accidental coincidences.

3. – Results

The classical limit for the S-aS correlations, found by applying the Cauchy-Schwarz inequality to classical fields [3,4], is given by $g_{S,aS}^{(2)}(0) \leq \sqrt{g_{S,S}^{(2)}(0) g_{aS,aS}^{(2)}(0)}$, where $g_{S,S}^{(2)}(0)$ and $g_{aS,aS}^{(2)}(0)$ are the Stokes and anti-Stokes auto-correlation functions, respectively. Both of these functions follow thermal statistics, giving an upper bound on the maximum classical value of $g_{S,aS}^{(2)}(0) = 2$. When both lasers overlap in time, as shown in fig. 1, we find $g_{S,aS}^{(2)}(0) = 63.4 \pm 9.7$, breaking the classical limit by 6 standard deviations.

The photon correlation is mediated by a phonon, which the *write* pulse creates and the *read* pulse annihilates. As such, if the phonon has time to decay before the *read* pulse arrives, the signal from the two lasers will no longer be correlated. Because of this, measuring the S-aS correlations as a function of the delay between *write* and *read* lets us measure the decay of the phonon mode, as shown in fig. 2. The correlations show an exponential decay, where we measure the phonon lifetime to be $\tau = 3.9 \pm 0.7\,\text{ps}$, which is consistent with other measurements in the literature [5].

4. – Conclusion

Here we have demonstrated a method to prepare and measure the dynamics of the first phonon Fock state. There's nothing that depends on the specific properties of diamond, so this method can be directly applied to other high-frequency phonon modes in different types of systems. The wavelength tunability means that it can also be used to address electronic or engineered transitions, giving the signal a resonant enhancement.
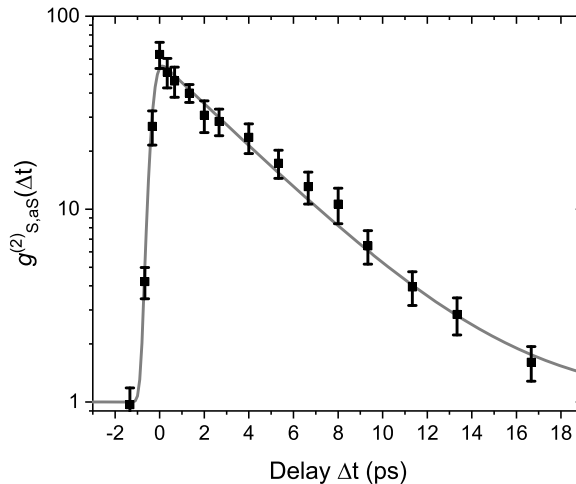
Fig. 2. – Delay dependence of the S-aS correlations, with the measured correlations (black squares) fitted with an exponential decay convoluted with the instrument response (grey line), with a time constant of $\tau = 3.9 \pm 0.7$ ps.

This method can also be extended to multi-photon correlations in order to study higher-order Fock states, or modified to start and stop on different Raman lines to study phonon-phonon coupling.

$* * *$

REFERENCES

[1] Mitchell D. Anderson, Santiago Tarrago Velez, Kilian Seibold, Hugo Flayac, Vincenzo Savona, Nicolas Sangouard and Christophe Galland, "Two-Color Pump-Probe Measurement of Photonic Quantum Correlations Mediated by a Single Phonon", *Phys. Rev. Lett.*, **120** (2018) 233601.
[2] Duan L.-M., Lukin M. D., Ignacio Cirac J. and Peter Zoller, "Long-distance quantum communication with atomic ensembles and linear optics", *Nature*, **414** (2001) 413.
[3] Reid M. D. and Walls D. F., "Violations of Classical Inequalities in Quantum Optics", *Phys. Rev. A*, **34** (1986) 1260.
[4] Kuzmich A., Bowen W. P., Boozer A. D., Boca A., Chou C. W., Duan L.-M. and Kimble H. J., "Generation of Nonclassical Photon Pairs for Scalable Quantum Communication with Atomic Ensembles", *Nature*, **423** (2003) 731.
[5] Lee K. C., Sussman B. J., Sprague M. R., Michelberger P., Reim K. F., Nunn J., Langford N. K., Bustard P. J., Jaksch D. and Walmsley I. A., "Macroscopic Non-Classical States and Terahertz Quantum Processing in Room-Temperature Diamond", *Nat. Photon.*, **6** (2012) 41.

International School of Physics "Enrico Fermi"

Villa Monastero, Varenna

Course 204

23 – 28 July 2018

Nanoscale Quantum Optics

Directors

Mario Agio
University of Siegen
and CNR-INO
Laboratory of Nano-Optics
Walter-Flex-Str. 3
57072 Siegen
Germany
`mario.agio@uni-siegen.de`

Irene D'Amico
Univeristy of York
Department of Physics
York YO10 5DD
UK
`irene.damico@york.ac.uk`

Rashid Zia
Brown University
School of Engineering
Box D
182 Hope St.
Providence, RI 02912
USA
`rashid_zia@brown.edu`

Scientific Secretary

Costanza Toninelli
CNR-INO and LENS
Via Nello Carrara 1
50019 Sesto Fiorentino (FI)
Italia
`toninelli@lens.unifi.it`

Lecturers

Dimitris Angelakis
Technical University of Crete
and Center for Quantum Technologies
(Singapore)
School of Electronic and
Computer Engineering
University Campus
731 00, Chania
Greece
`angelakis@ece.tuc.gr`

Lee Bassett
University of Pennsylvania
Department of Electrical
and Systems Engineering
200 South 33rd Street
Philadelphia, PA 19104-6314
USA
`lbassett@seas.upenn.edu`

Nathalie De Leon
Princeton University
Department of Electrical Engineering
E-Quad B320
Olden Street
Princeton, NJ 08540
USA
`npdeleon@princeton.edu`

Niek van Hulst
ICFO
Institute of Photonic Sciences
Av. Carl Friedrich Gauss 3
08860 Castelldefels
Barcelona
Spain
`niek.vanhulst@icfo.es`

Friedemann Reinhard
Technical University of Munich
Walther Schottky Institute
Am Coulombwall 4
85748 Garching
Germany
`friedemann.reinhard@wsi.tum.de`

Fabio Sciarrino
University of Roma "La Sapienza"
Dipartimento di Fisica
Piazzale Aldo Moro 5
00185 Roma
Italia
`fabio.sciarrino@uniroma1.it`

Jelena Vuckovic
Stanford University
Ginzton Laboratory
348 Via Pueblo Mall
Stanford, CA 94305-4088
USA
`jela@stanford.edu`

Seminar Speakers

Mete Atatüre
University of Cambridge
Department of Physics
Cavendish Laboratory
JJ Thomson Avenue
Cambridge, CB3 0HE
UK
`ma424@cam.ac.uk`

Mohammad Hafezi
Univeristy of Maryland
Joint Quantum Institute
2017 Atlantic Bldg.
College Park, MD 20742
USA
`hafezi@umd.edu`

Ewold Verhagen
AMOLF
Center for Nanophotonics
Science Park 104
1098 Amsterdam
The Netherlands
`verhagen@amolf.nl`

Students

Sebastian Andersen	University of Southern Denmark, Denmark
Akshay Balgarkashi	EPFL, Switzerland
Sabyasachi Barik	University of Maryland, USA
Mariana Barros	Federal University of Minas Gerais, Brazil
Caue Carvalho	Universidade Estadual de Campinas, Brazil
Alessia Castellini	Università di Palermo, Italy
Carlotta Ciancico	Institute of Photonic Sciences, Spain
Dario Cilluffo	Università di Palermo, Italy
Marco Clementi	Università di Pavia, Italy
Maja Colautti	LENS, Italy
Andrea Cordaro	AMOLF, The Netherlands
Marija Curcic	Institute of Physics, Serbia
Yunyun Dai	Aalto University, Finland
Isabella De Bellis	LENS, Italy
Martino De Carlo	Politecnico di Bari, Italy
Huang Ding	Princeton University, USA
Subhojit Dutta	University of Maryland, USA
Saverio Francesconi	University Paris Diderot, France
Gabriele Frigenti	LENS, Italy
Morgane Gandil	Universität des Saarlandes, Germany

Sijia Gao	Univeristy of Glasgow, UK
Andrea Geraldi	Università di Roma "La Sapienza", Italy
Jodok Happacher	University of Basel, Switzerland
Sahar Hejazi	Okinawa Institute of Science and Technology, Japan
Santiago Hernandez Gomez	LENS, Italy
Xuerong Hu	Aalto University, Finland
Parvez Islam	Johannes Gutenberg-Universität Mainz, Germany
Yaseera Ismail	University of KwaZulu-Natal, South Africa
Haritha Kambalathmana	University of Siegen, Germany
Friederike Klauck	Universität Rostock, Germany
Irina Komen	Kavli Institute of Nanoscience, The Netherlands
Zhe Xian Koong	Heriot-Watt University, UK
Antonio Alessio Leonardi	Università di Catania, Italy
Maki Maeda	Okinawa Institute of Science and Technology, Japan
Mattia Mantovani	Universität Konstanz, Germany
Niccolò Michieli	Università di Padova, Italia
Monika Mycroft	University of Warsaw, Poland
Mackrine Nahra	University of Technology of Troyes, France
Richard Nelz	Saarland University, Germany
Alvaro Nodar Villa	Materials Physics Center-CFM, Spain
Jan Olthaus	Institut for Solid State Theory, Germany
Gerard Queralto	VAB Grup d'Optica, Spain
Priscila Romagnoli	Okinawa Institute of Science and Technology, Japan
Federico Andrea Sabattoli	Università di Pavia, Italy
Jake Southall	The University of Leeds, UK

TETYANA SHALOMAYEVA	University of Stuttgart, Germany
AMY SKELT	University of York, UK
HENK SNIJDERS	Leiden University, The Netherlands
SANTIAGO TARRAGO VELEZ	Ecole Polytechnique Fédérale de Lausanne, Switzerland
MIKKO TURUNEN	Aalto University, Finland
FRANCESCA URBAN	Università di Salerno, Italy
MAURO VALERI	Università di Roma "La Sapienza", Italy
REINIER VAN DER MEER	University of Twente, The Netherlands
THIJS VAN GOGH	TU Delft, The Netherlands
SIMONE VARO	Tyndall National Institute, Ireland
YADONG WANG	Aalto University, Finland
LORENZ WEISS	Max Planck Institute of Quantum Optics, Germany
DANIEL WHITE	Heriot-Watt University, UK

This page intentionally left blank

Finito di stampare
nel mese di settembre 2020

This page intentionally left blank